Study of the Arctic mixed-phase clouds observed in June 2017 duringthe ACLOUD campaign using the WRF atmospheric model

Diana Arteaga

UNIVERSITÉ CLERMONT AUVERGNE

ÉCOLE DOCTORALE DES SCIENCES FONDAMENTALES

THÈSE

présentée pour obtenir le grade de

DOCTEUR D'UNIVERSITÉ

Spécialité : Sciences de l'Atmosphère

par **ARTEAGA Diana**

Diplômée du Master Sciences de la Terre et des Planètes, Environnement

spécialité Sciences de l'Atmosphère et du Climat

Étude des nuages arctiques en phase mixte observés en juin 2017 lors de la campagne ACLOUD à l'aide du modèle atmosphérique WRF

Soutenue publiquement le 28 juin 2023, devant la commission d'examen :

Présidente du jury	
Andrea FLOSSMANN	*Professeure d'université, Université Clermont Auvergne, LaMP*
Rapporteurs	
Jean Christophe RAUT	*Maitre de conférences – HDR, Sorbonne Université, LATMOS*
Dominique BOUNIOL	*Chercheure chargée de recherches – HDR, CNRM, Météo France*
Examinateurs	
Céline CORNET	*Professeure d'université, Université Lille 1, LOA*
Gwendal RIVIÈRE	*Directeur de recherche CNRS, ENS Paris, LMD*
Directrice de thèse	
Céline PLANCHE	*Maitresse de conférences – HDR, Université Clermont Auvergne, LaMP*
Co-directeur de thèse	
Olivier JOURDAN	*Maitre de conférences – HDR, Université Clermont Auvergne, LaMP*
Invité *(direction)*	
Wolfram WOBROCK	*Professeur d'université, Université Clermont Auvergne, LaMP*

Université Clermont Auvergne
Ecole Doctorale des Sciences Fondamentales
8 avenue Blaise Pascal
63178 Aubière Cedex

Laboratoire de Météorologie Physique
UMR6016 CNRS – INSU
4 avenue Blaise Pascal
63178 Aubière Cedex

Remerciements

Tout d'abord, je voudrais remercier mes parents qui m'ont toujours apportée leur soutien inconditionnel même avec la distance afin que je puisse atteindre tous mes objectifs personnels et académiques. Ce sont eux qui, par leur affection, m'ont toujours encouragée à poursuivre mes objectifs et à ne jamais baisser les bras. Je voudrais remercier aussi mon chéri d'amour qui a été mon support inconditionnel, merci pour ton amour et ta patience pendant toutes ces années. Je remercie également ma belle-mère ou deuxième maman pour son amour et soutien pendant cette période de ma vie.

Je suis très reconnaissante envers mes encadrants de thèse, Céline Planche, Olivier Jourdan et Wolfram Wobrock, merci pour votre disponibilité et votre accompagnement. Trois points de vue diffèrents qui, des fois, ne pas très facile à mettre d'accord, mais ils m'ont appris à voir les choses avec différentes perspectives et à trouver un bon équilibre entre la réalité (observations) et les calculs (simulations). Merci à Wolfram qui a partagé avec moi ses connaissances sur le code du model WRF et qui a pris le temps de m'expliquer et de trouver des réponses très importantes pour l'avancement et l'argumentation de ma thèse. Merci à Olivier d'avoir partagé avec moi toute son expertise sur l'Arctique et de m'avoir aidée dans la compréhension du fonctionnement des instruments que j'ai dû utiliser. Un merci spécial à Céline qui m'a non seulement initiée à la modélisation depuis mon stage de master, elle m'a aussi donné le goût pour comprendre et apprendre à simuler, merci pour tous tes conseils, je m'en souviendrai toujours dans mon avenir professionnel.

Je tiens à remercier tous les membres composant mon jury de thèse : à la présidente, Andrea Flossmann, aux rapporteurs, Jean-Christophe Raut et Dominique Bouniol ainsi qu'aux examinateurs Céline Cornet et Gwendal Rivière. Merci d'avoir accepté de faire partie de mon jury et pour vos remarques et questions qui m'ont poussée à aller plus loin dans mon analyse et ainsi à améliorer mon manuscrit.

J'exprime ma gratitude à Sandra Banson et Edouard Bray, qui m'ont bien aidée avec tout le support informatique. Merci Sandra pour ta disponibilité et ta réactivité. Je tiens à remercier Jean-Luc Baray d'avoir pris le temps de m'expliquer le fonctionnement de CAT et qui m'a permis de faire l'analyse des trajectoires des particules d'aérosol et de la situation synoptique. Aussi, un merci à Guillaume Mioche qui m'a aidée avec PYTHON au début de ma thèse et aussi avec ses informations ponctuelles sur la campagne ACLOUD. Egalement, merci à Régis Dupuy qui m'a fournie les données ACLOUD et qui m'a donnée des explications claires et utiles. Je remercie également Frédéric Tridon d'avoir partagé avec moi ses connaissances sur le modèle SSRGA et son aide avec toute l'analyse de la réflectivité.

Un grand merci aussi à tous les membres du laboratoire pour leur bienveillance,

spécialement à Ariane et Mathilde, merci pour les repas de midi partagés entre filles, j'ai bien apprécié ces petits moments avec vous. Merci également à Véronique et Marlène pour leur aide au niveau des formalités administratives.

Je voudrais remercier Nadège pour ses conseils pour la préparation de ma présentation finale et pour mon avenir professionnel. Merci aussi à mes collègues doctorants pour leur soutien pendant la préparation de ma soutenance, vous avez été vraiment "le team thèse" avec en tête Angelica, la directrice de pot.

Enfin je voudrais remercier mon petit Arthur, mon bébé tu es arrivé dans ma vie à la moitié de ma thèse, et tu m'as donné le courage et l'inspiration pour l'amener jusqu'au bout avec détermination et persévérance. J'espère que tu auras hérité un peu du côté curieux et scientifique de ta maman et qu'un jour tu pourras voir les nuages d'une autre façon ...

À mon petit Arthur

A mi pequeño Arthur

Contents

List of Figures

List of Tables

Introduction

Polar regions are more sensitive to climate change than any other region of the world (Screen and Simmonds, 2009; Serreze and Barry, 2011). During the last decades, the Arctic region has warmed three times faster than the rest of the globe (phenomenon which is called Arctic amplification) and has shown acute visible signs such as the retreat of summertime sea-ice (Serreze and Barry, 2011; Stroeve et al., 2007; Overland et al., 2019). Among the mechanisms contributing to this Arctic amplification is the reduction of surface albedo with the melting of snow and ice (Serreze and Barry, 2011; Taylor et al., 2013), changing the surface energy balance. As temperature rises, the atmosphere-surface energy balance is modified. But all consequences of changes in the energy balance are difficult to access as significant uncertainties remain. An example, is the increasing atmospheric moisture content which can affect seasonal cloud properties and feedback on the surface (Middlemas et al., 2020), as well as the transport of moisture within, into, and out of the Arctic region (Mellat et al., 2021). Similarly, projected increases in evaporation and precipitation could play amplifying roles, depending on when and where they occur (Bintanja et al., 2020).

Clouds are an important component in the Arctic climate system as they play a key role in the radiation budget (Curry, 1995; Curry et al., 1996; Garrett et al., 2009; de Boer et al., 2014). They can cool or warm the surface and the atmosphere depending on their macrophysical and microphyical properties. The predominant longwave radiative effect in the Arctic (Lubin and Vogelmann, 2006), which tend to a regional net warming effect, is caused by different aspects, as the low sun elevation in summer and the lack of solar radiation during the winter polar night, the presence of supercooled water, temperature gradients, etc. The ice/snow cover has a pronounced effect on the turbulent and heat surface fluxes. During winter, snow-covered ice insulates the atmosphere from the high heat capacity of the ocean. Combined with longwave radiative cooling and the absence of solar forcing during the Arctic winter, this gives rise to persistent stable stratification in the Arctic boundary layer about 75% of the time (Persson, 2002). Turbulence in very stable conditions is poorly understood (Mahrt et al., 1998; Grachev et al., 2005). During summer, melting ice and snow regulates the low-level temperature; additional energy input enhances melting rather than heating the surface, while energy loss results in freezing, rather than a cooling. Long periods of stable boundary layer conditions are interspersed with shorter periods with near-neutral conditions. This is forced by longwave radiation (Persson, 2002) and directly related to boundary layer clouds, which are difficult to handle in atmospheric models.

The occurrence of clouds in Arctic is important (anual mean is $\approx 67\%$) throughout the year (Ruiz-Donoso et al., 2020; Mioche et al., 2017, 2015; Intrieri et al., 2002a), especially close to the Svalbard archipelago. Several studies have highlighted a seasonal

variability in cloud cover with a minimum in winter (65%) and a maximum in autumn (90%) (Maillard et al., 2021; Cesana et al., 2012; Nomokonova et al., 2019; Liu et al., 2017; Shupe et al., 2006; Mioche et al., 2015; Yeo et al., 2018). This variability can be explained by the intrusion of wet air from the Atlantic in autumn (Maillard et al., 2021). The greater concentration of moisture in summer and autumn, is attributed to the increase of open water by melting sea ice that increases latent and sensitive heat fluxes (Nomokonova et al., 2019; Abe et al., 2016). However other studies came to opposite results. Morrison et al. (2019) used a coupled ocean/sea-ice/atmosphere model (CESM1-CAM5),and showed that cloud occurrence should not increase in summer with decrease of sea ice. In the Arctic, 30% to 60% of clouds are mixed phase clouds (MPCs), *i.e.,* composed of both ice crystals and supercooled liquid water (Mioche et al., 2015; Shupe et al., 2011; McFarquhar et al., 2007). These have a strong radiative impact due to their persistence during all seasons and their particular microphysical properties (Curry et al., 1996; Intrieri et al., 2002a; Eastman and Warren, 2010; Shupe et al., 2015).

The complex system of interactions between numerous local and large-scale processes greatly complicate their understanding and modelling (Klein et al., 2009; Morrison et al., 2012). The ice crystal number concentration controls the liquid/ice partitioning and hence the maintenance of the MPCs. An inaccurate small increase of the predicted ice crystal number concentration can lead to a substantially reduced liquid water path, a rapid glaciation and a dissipation of the cloud (Morrison et al., 2012; Prenni et al., 2007). However, previous model intercomparisons (Klein et al., 2009) clearly highlighted large discrepancies in the simulated liquid water content (LWC) and ice water content (IWC) and even wider differences in the predicted ice crystal number concentrations, emphasising that our understanding of ice formation processes within MPCs is far from complete (Korolev et al., 2017). Clouds containing liquid water have more effect on radiative fluxes (longwave and shortwave) than a cloud containing only ice crystals. Although liquid water is present in clouds in an important fraction even at very low temperatures (Beesley, 2000; Intrieri et al., 2002b) throughout the year, the proportion of liquid water and ice crystals in the cloud varies with the season (Ebell et al., 2020; Nomokonova et al., 2019; Morrison et al., 2012). A study of the annual variability of MPCs was performed during the *Surface HEat Budget of the Arctic ocean* experiment (SHEBA; Uttal et al. (2002)), showing, that in summer, liquid-containing clouds over the Beaufort sea reach more than 90%. In winter ice crystals are dominant in the cloud, water represent about 40% of the clouds. To maintain the unstable equilibrium between liquid droplets and ice crystals within MPCs, the coupling of various processes is necessary. This may explain the longevity of MPCs, which can last up to several days or weeks as has been frequently observed (Shupe et al., 2011; Verlinde et al., 2007; Morrison et al., 2012). Sedlar et al. (2020) found that some models did not correctly simulate the occurrence of clouds also causing bad radiation flux representation.

The connection of cloud effects to aerosol particles and cloud microphysics is discussed by Curry (1986); McFarquhar et al. (2011); Solomon et al. (2015, 2018); Young et al. (2017). Aerosol particles, which are necessary for the formation of cloud condensation nuclei (CCN), regulates the radiative characteristics of the clouds, providing possible complications to the ice-albedo feedback. There are considerable variations in the concentrations and composition of arctic aerosols. Shaw (1982) first identified the arctic haze associated with the transport of aerosols from Europe and Asia. During summer, with the increase of open water due to melting, trans-Arctic shipping is

also projected to increase, exerting local aerosol perturbations (Hobbs et al., 2000; Khon et al., 2010; Peters et al., 2011). There is an increased availability of CCN resulting from both sea salt and dimethyl sulfide emissions (Leck and Persson, 1996) which is released by sea ice algae and phytoplankton (*e.g.* Gourdal et al. (2019)) from the ocean, and predicted ship emissions. This may lead to increased cloud formation and a net surface cooling during summer, as projected by global climate and Earth system models (Gilgen et al., 2018; Stephenson et al., 2018). In the summer, the influence of long-range transport on the near-surface aerosol population may be limited, since the transport tends to occur above the boundary layer (Stohl, 2006; Thomas et al., 2019; Shindell and Faluvegi, 2009; Sand et al., 2017). Igel et al. (2017) found that entrainment of aerosols from the free troposphere into the boundary layer represents an important source of aerosol particles for Arctic MPCs, also shown by Tjernström et al. (2014) from observations and LES experiments as part of the *Arctic Summer Cloud Ocean Study* (ASCOS). In contrast, in winter, continental and anthropogenic aerosol may have a larger influence at the surface (*e.g.,* in Freud et al. (2017) and Shupe et al. (2022)). Another primary aerosol source over sea ice in the polar regions is particle generation from drifting or blowing snow (Frey et al., 2020; Yang et al., 2008). As for secondary aerosol sources, precursor gases can be transported over the pack ice and both continental and marine sulphate has been observed in aerosol particles over the pack ice (Chang et al., 2011). Christensen et al. (2014) and Possner et al. (2017) found that, locally, aerosols released in ship tracks alone can change cloud liquid and ice water contents. This may increase the reflectivity and change the lifetime of Arctic clouds and this would constitute a negative feedback to climate change. Equivalently, a reduction in the ambient CCN and hence cloud droplet number concentration (N_{drops}) could induce cloud dissipation (Mauritsen et al., 2011; Loewe et al., 2017; Stevens et al., 2018). Therefore, significant impacts on aerosol concentrations in the Arctic could be generated by future changes in non-local sources of aerosol and long-range transport. Furthermore, an increase in shipping traffic is expected once the Arctic becomes seasonally ice free, further increasing aerosol concentrations (Peters et al., 2011). This increase in shipping traffic would also be expected to yield an increased demand for accurate weather forecasts over the Arctic region (Stevens et al., 2018). However, disentangling the competing effects environmental conditions and aerosol disturbances appears challenging (Jackson et al., 2012).

There is a real need to better understand the MPCs lifecycle: a combination of local and large-scale processes control formation, development, persistence and dissipation of MPCs (Morrison et al., 2012). Previous studies from Korolev et al. (2003); Korolev and Isaac (2003); Korolev (2007) show that the lifetime of MPCs depend of several aspects. At the small scale, the ice crystal production is controlled by heterogeneous ice nucleation given the temperature range observed in MPCs, where ice crystals grow at the expense of supercooled water droplets (Bergeron, 1935; Findeisen, 1938; Wegener, 1911). This mechanism leads to a rapid glaciation of the MPCs. On the other hand, dynamical processes, such as turbulence or entrainment may facilitate the formation of new supercooled water droplets. For example, liquid droplets can be formed by resupply of water vapour from the surface or from entrainment of moisture above the clouds. The evolution of MPCs, however, is closely related to local thermodynamical conditions or local and long-range dynamic processes (aerosol, heat and moisture transport) which have a significant impact on Arctic MPCs formation and properties (Cesana et al., 2012; Morrison et al., 2012; Shupe and Intrieri, 2004). The limited measurements capabilities, the

complexity of interactions between all these processes and to assert which of them play a key role in the MPCs evolution, make understanding difficult (Harrington et al., 1999; Morrison et al., 2012). This translates into inaccurate model parameterisations to compute ice crystal concentrations and makes difficult to understand the lifecycle of MPCs (Heymsfield et al., 2017; Korolev et al., 2017; Field et al., 2017). The hypothesis given by Solomon et al. (2018) is that, for given meteorological conditions, the relative impact of CCN and INP (ice nucleating particles) on the phase partitioning is not accurately represented in models leading to an incorrect prediction of ice crystal concentrations. Another hypothesis given by Lenaerts et al. (2017) is that, the small scale variability of the thermodynamics properties as humidity, vertical velocity, temperature, controls the droplets and the ice crystal concentrations and their spatial distribution within MPCs. This non linear response of the microphysical properties to atmospheric conditions is inaccurately represented in regional models with potential large impacts on the MPCs lifetime.

Furthermore, knowledge of cloud-radiation interactions and cloud properties in the Arctic remains one of the main source of uncertainties in predicting future climate by numerical models (Solomon et al., 2007; Stephens, 2005). Several observations, as well as numerical modelling focused on MPCs (Verlinde et al., 2007; De Boer et al., 2009; Gayet et al., 2009a; Jourdan et al., 2010; McFarquhar et al., 2011, among others), show that there are still many uncertainties in the results and important discrepancies are observed between observations and simulations (Chernokulsky and Mokhov, 2012; Klein et al., 2009; Morrison et al., 2009b; Thomas et al., 2004). In particular, thermodynamical properties are crucial for assessing the cloud radiative impact as well as their influence on the radiation budget and climate feedbacks (Choi et al., 2014; Komurcu et al., 2014). Ice-albedo feedback also impact largely cloud interactions, warming reduces the ice and snow cover reducing the surface albedo, thus, enhancing the warming. How climate models handle sea ice and snow, and the energy exchange at the surface is critical. Battisti et al. (1997) showed that a lack of physical detail in describing ice processes inhibits a realistic representation of natural variability in the Arctic climate. It also causes significant errors in global weather forecast models (Beesley, 2000).

Some studies have found that climate models tend to underpredict the formation of optically thin liquid clouds with supercooled water (*e.g.*, Cesana et al. (2012)). Large differences in the seasonal cloud fraction between Coupled Model Intercomparison Project phase 3 (CMIP3) models are shown by Vavrus et al. (2009). All models suppose that liquid water and ice are uniformly mixed throughout the model grid boxes (Tan et al., 2016; Komurcu et al., 2014; Morrison et al., 2012; Klein et al., 2009; Prenni et al., 2007). However, MPCs seem to be more likely composed of an inhomogeneous mixture of ice particles and liquid droplets clustered in single-phase liquid or ice cloud regions (Korolev et al., 2017). The MPCs simulated by the model will be referred to as 'genuine' mixed-phase and the real MPCs as 'conditional' mixed phase. In the conditionally MPCs, the interaction between ice crystals and liquid droplets is hindered because of their spatial separation. As a result, the thermodynamic and radiative properties of genuine and conditional MPCs might be different (Lance et al., 2011). Consequently, these uncertainties in cloud simulations with climate models cause a greater variability in the temperature forecast for Arctic latitudes than for lower latitudes (Chapman and Walsh, 2007). Low-level clouds especially contribute to model uncertainty (Williams and Webb, 2009). Multiple observational programs within the past two decades have

sought to address the Arctic cloud challenges (*e.g.*, Uttal et al. (2002); Verlinde et al. (2007); McFarquhar et al. (2011); Tjernström et al. (2014); Smith et al. (2017)). Efforts continue to implement more advanced cloud representations within models (Morrison et al., 2005; Luo et al., 2008; Morrison and Gettelman, 2008; Gettelman et al., 2010; Lim and Hong, 2010; Liu et al., 2012; English et al., 2014; Forbes and Ahlgrimm, 2014; Park et al., 2014; Thompson and Eidhammer, 2014). While these efforts are not necessarily all targeted for polar clouds, it is hoped that improved physics will ultimately produce better representations of regional characteristics. Yet, existing schemes are still not sufficiently tested against Arctic data, and many cloud schemes are developed based upon observations of midlatitude and tropical cloud properties (Randall et al., 1998; Tjernström et al., 2014).

The ability of models to describe the evolution of climate over time depends on the parameterisation of physical processes. In turn, the reliability of the parameterisations depends on the degree of scientific understanding of the underlying processes. Climate models alone will not resolve the Arctic climate issue because they often use simple parameterisations that need to be verified, tested, and/or improved. Nevertheless, modelling associated to observations will help to improve our understanding of the different components of the Arctic region and their interactions. The ice cover is also a reason for a relative lack of in situ observations. It produces a difficult and hostile environment for observational studies: fixed permanent sites for long-term measurements cannot be established due to the ice drifts. Consequently, the ensemble of observations used for the development of reliable parameterisations may be inadequate. This may be one reason for the difficulties in modelling the Arctic climate, and the only realistic way to rectify this is to obtain detailed observations of climate-related processes in the Arctic. Even if several campaigns have already been organised over the Arctic region (as described in Chapter 1), the required observations are still sparsely distributed across this region. As a consequence further data have to be collected in well-planned and dedicated campaigns to better document and understand the Arctic climate changes.

Building on existing research and motivated to better understand the role of clouds for climate change in the Arctic, we will apply in this study the *Weather Research and Forecasting* (WRF) model at regional scale to simulate two MPCs systems observed during the ACLOUD (*Arctic CLoud Observations Using airborne measurments during polar Day*) campaign which took place at the North-West of the Svalbard archipelago during spring 2017. WRF has already been used in previous studies on the Svalbard archipelago, in the area of Ny-Ålesund and Longyearbyen (Kilpelainen et al., 2012a,b; Makiranta et al., 2011; Claremar et al., 2012; Young et al., 2016). However, significant uncertainties in model simulations were reported by these authors for atmospheric processes (cloud evolution and persistence, turbulence, radiation) and variables (LWC, IWC), near-surface wind characteristics in particular. Our modeling study with WRF has three objectives:

- To use the detailed in-situ measurements from the ACLOUD campaign which took place in the transition zone of the Greenland Sea and the Arctic Ocean (between open ocean and sea ice) to test the ability of WRF mesoscale model to reproduce two MPCs observed on the 17 June 2017.
- To evaluate the impact of different surfaces (sea ice and open ocean) on MPCs microphysical properties

- To investigate how the response to increased CCN concentrations may differ for different cloud regimes and impact the MPCs' properties.

All of these objectives are highly related and are addressed to better understand the physical processes responsible for the spatial distribution of the water and ice phases within the MPCs and to better identify the weaknesses of the WRF model in such Arctic clouds. Models are most useful when they reproduce observations for the right physical reasons. Thus, we must ensure that the model reproduces observed relationships clouds-atmosphere-surface for the right physical reasons, before using the model to understand future clouds' interactions and to assess the sign of future cloud feedback.

The present thesis is organised in four chapters. Chapter 1 introduces the Arctic region and describes in detail the different elements impacting the Arctic climate and the Arctic amplification phenomenon. Chapter 1 also provides information about the past Arctic instrumental expeditions and about past studies on modelling performances for representating the Arctic clouds' properties at climate and weather forecasting scales. Chapter 2 presents observational results of the ACLOUD campaign. Moreover, Chapter 2 describes the properties of the two MPCs observed over sea ice or open ocean on the 17 June 2017 with cloud radar, dropsondes and in situ microphysics probes deployed by airborne measurements. A complete description of the different modelling tools used throughout this thesis are presented in Chapter 3. Chapter 4 presents the different results obtained comparing ACLOUD observations and WRF simulations for both MPCs studied in this thesis. Sensitivity studies of MPC microphysics properties to thermodynamics, boundary layer and microphysics parameterised schemes, and aerosols loadings are also presented in Chapter 4. The last Chapter will summarise the conclusions on the Arctic MPCs and will provide several perspectives to this work.

Chapter 1

The Arctic region and its climate

1.1 The Arctic region

1.1.1 Definition

The Arctic region is often delimited by the Arctic Circle (66.5°N) (Figure 1.1), which corresponds to the southern boundary of the midnight sun. However, such a definition is too simplistic and does not take into account the physical and geographical characteristics of this region: variations in temperature, presence of mountain ranges, and surface properties. Therefore, no simple delimitation of the Arctic region is applicable and different possible boundaries can be identified for this region depending on the prevailing criterion considered.

- On the basis of temperature, the Arctic is defined as the area north of the 10°C July isotherm, *i.e.* North of the region which has a mean July temperature of 10°C (Woo and Gregor, 1992). Figure 1.1 shows that in the Atlantic Ocean West of Norway, the heat transport of the Gulf Stream extension deflects this isotherm northward including only the northernmost parts of Scandinavia within the Arctic region. In the opposite, cold water and air from the Arctic Ocean push the 10°C isotherm southward taking in the north-eastern Labrador and including much of the Bering Sea (see Figure 1.1).

- A floristic boundary such as the treeline can be used to delimit the terrestrial Arctic region (Linell and Tedrow, 1981). By definition, the treeline is simply the northern limit beyond which trees do not grow. This limit corresponds to a transition zone between continuous boreal forest and tundra, with isolated stands of trees. As shown in Figure 1.1, the treeline roughly coincides with the 10°C July isotherm with few exceptions such as over the Northern Canada.

- Based on oceanographic properties, the marine boundary of the Arctic is located along the convergence of cool, less saline surface waters from the Arctic Ocean and warmer, saltier waters from oceans to the South (Stonehouse, 1989). Figure 1.1 shows that the marine boundary of the Arctic region is highly variable in latitude over the region studied throughout this thesis. Indeed, the warming effect of the

North Atlantic current deflects this boundary north of 80°N west of the Svalbard archipelago, while it moves southward in the Barents Sea to 76°N.

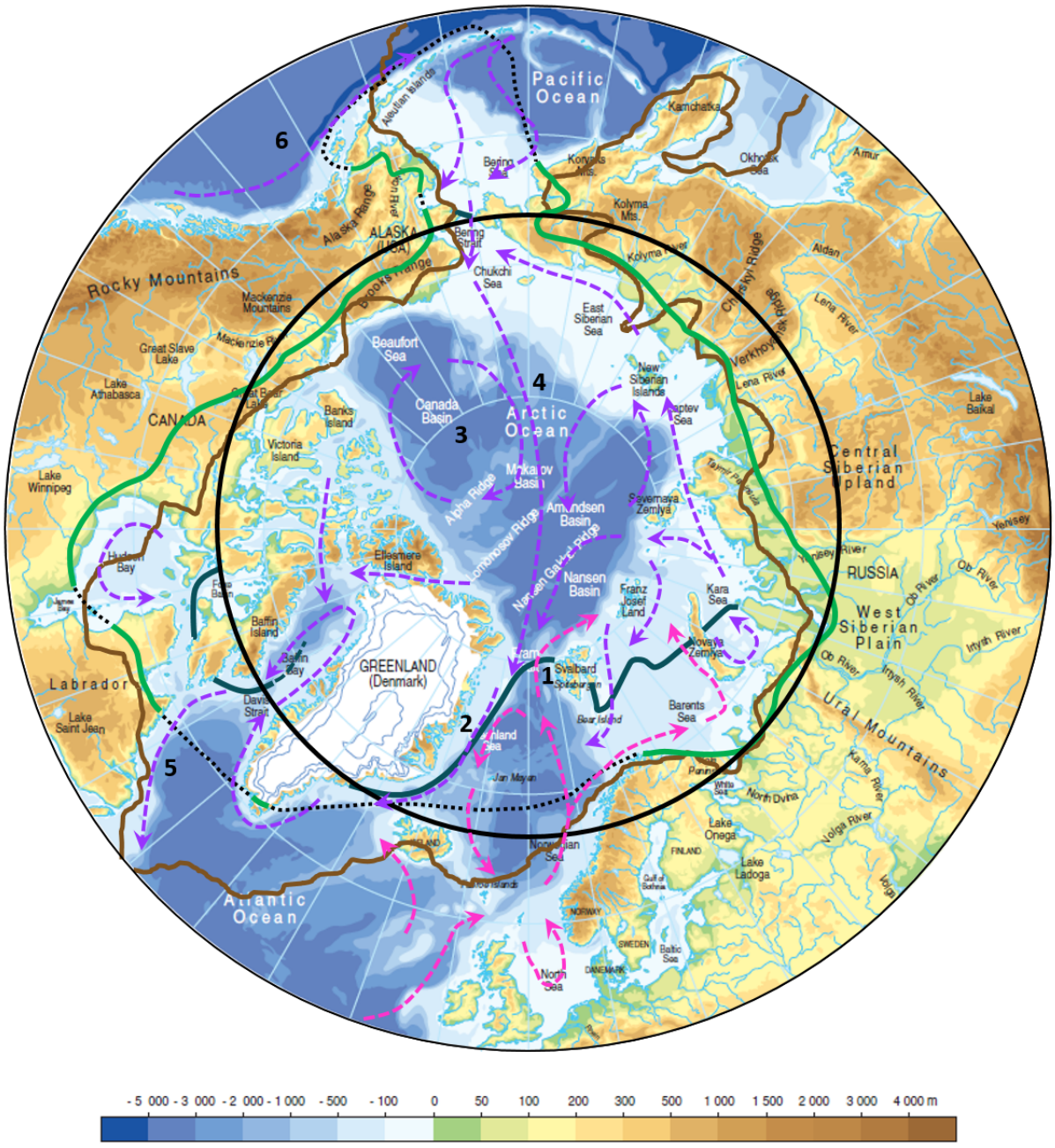

Figure 1.1: Bathymetric and topographic map (over Greenland, the topography lines are given every 1000 m) with the possible boundaries of the Arctic region: Arctic Circle at 66°N (black solid line), the 10°C July isotherm (brown solid line), the treeline (green solid line) and the marine boundary (dark blue solid line). The arrows with dashed lines represent the surface ocean currents: Atlantic currents (and Gulf Stream extension) in pink and other currents in purple. The numbers in black indicate the main others currents: 1: West Svalbard Current, 2: East Greenland Current, 3: Beaufort Gyre, 4: Transpolar Drift, 5: Labrador Current, and 6: Alaska Current. Figure adapted from AMAP (1998).

Regardless the definition used to determine this region, the Arctic covers a vast area of approximately 21.03×10^6 km^2 with diverse surface categories: ocean, sea ice, glaciers,

permafrost, tundra ... and is comprised of numerous mountainous lands (see Figure 1.1). These mountains at high latitudes can impede the atmospheric flow, especially between the mid-latitudes and the Arctic. Moreover, as suggested before, the energy received from the sun by the diverse terrestrial and marine surfaces varies with the latitude.

Therefore, the distribution of the surface categories: land, sea and mountains, the variation of the energy received from the sun, and the atmospheric and oceanic circulation characterise the regional and local climatic and meteorological conditions in the Arctic. Nevertheless, these different factors interact with each other's making more complicated the prediction of the Arctic climate feedbacks and weather patterns in the current context of global warming.

1.1.2 Arctic climate and meteorology

On an annual basis, the Arctic receives less solar (or shortwave (SW)) radiation than other parts of the globe. However, the level of SW radiation varies a lot according to the season since there is a total lack of incoming solar radiation in winter months, whereas the poles receive higher levels of solar radiation in summer months, due to the length of polar days. The annual amount of solar radiation received is lower than that lost to space by terrestrial (or longwave (LW)) radiation since a large part of the solar radiation that reaches the Earth is reflected by clouds, snow and ice cover, as well as the sea surface. This radiative imbalance produces low air temperatures next to the surface and results in a redistribution of heat from southern latitudes via atmospheric and oceanic currents.

a) Atmospheric circulation

The frequency and the preferred tracks of the persistent Pacific and Atlantic low-pressure systems and the position of the persistent high-pressure systems play an important role on the regional and local climates in the Arctic (AMAP, 1998). However, the positions of these organised pressure systems are different according to the seasons. Thus, the redistribution of heat as well as the transport of humidity and pollution between the Arctic and the southern latitudes is different in winter and summer months.

In winter months (November through February, when there is no solar radiation), the lower tropospheric circulation of the Arctic region is dominated by the two low-pressure systems located over the northern Pacific Ocean[1] (the "Aleutian Low" which is blocked by the mountains of Alaska and northeast Siberia) and over the northern Atlantic Ocean (the "Icelandic Low" whose influence extends to the North Pole) and by the high pressure areas over the continents (over North America and Siberia). Thus, the prevailing winds are westerly or south-westerly between Iceland and Scandinavia, transporting warm and humid air from lower latitudes toward the Arctic. Farther north, the circulation is generally anticyclonic around the pole with easterly and north-easterly prevailing winds.

In summer months (June to August), the continental high-pressure systems disappear, and the oceanic low-pressure systems weaken: the Aleutian Low disappears and

[1]Note that the positions of the different pressure systems can be easily located using the Figure 1.1.

the low-pressure system close to Iceland shifts to southern Baffin Island (becoming the "Canadian Low"). A weak ridge of high pressure present over the Arctic Ocean separates this low-pressure system from low pressure areas present at the south of the Lake Baikal in Russia. Accordingly the northward transport from mid-latitudes decreases and the mean circulation in the lower atmosphere gives way to a more circular clockwise flow around the pole.

b) Oceanic circulation

As already mentioned in Section 1.1.1, waters flowing north to the Arctic regions are comprised of warm currents originating from the Atlantic and Pacific Oceans, while cold currents flow out of the Arctic. Atlantic water enters the Arctic Ocean through Fram Strait (*i.e.* at the west of the Svalbard archipelago) and the Barents Sea, while Pacific water enters via Bering Strait (see Figure 1.1). Nevertheless, most of the water in the Arctic Ocean originates from the Atlantic Ocean. Water leaves the Arctic largely via Fram Strait, but also through the Canadian Arctic Archipelago (*i.e.* close to the Ellesmere, Banks and Victoria Islands) (Timmermans and Marshall, 2020). The contributions of heat to the atmosphere due to oceanic transport have a major impact on the geographical distribution of cloud cover in the Arctic.

The Greenland Sea is thereby an area where the oceanic circulation is quite complex and the different currents involved can impact the surface properties. The western part of the Greenland Sea has perennial ice cover (see sea ice edge in Figure 1.2a), due to ice formed locally as well as ice advected from the Arctic Basin through the Fram Strait (see Figure 1.1). At about 74°N, the Jan Mayen Gyre (see Figure 1.1) entrains some ice from the East Greenland Current ($T < 0$°C) into the centre of the sea (Parkinson et al., 1987). The ice extent reaches its maximum in February-March and its minimum in August-September on the Greenland Sea or on the entire Arctic region (see Figure 1.2b for the latter one). On the contrary, the eastern part of the Greenland Sea is kept free of ice by the warm waters of the West Svalbard Current ($T > 3$°C) (Figure 1.2a), *i.e.* one extension of the Arctic Currents (Hopkins, 1991).

c) Arctic energy budget

The Arctic energy budget depends on the complex interactions between the radiation fluxes, the atmospheric and oceanic currents and the surface properties which are all greatly affected by seasonal variations (Walden et al., 2017; Mayer et al., 2019). In this framework, the Arctic energy budget can be defined by the following components (see the coloured arrows in Figure 1.3):

- the atmospheric energy convergence (AEC) that corresponds to the energy (heat and moist) coming from lower latitudes via the atmospheric currents described in Section 1.1.2(a), as well as the oceanic energy convergence (OEC),
- the top of atmosphere (TOA) net radiation flux that corresponds to the balance between incoming SW and outgoing LW radiations at the top of the atmosphere,
- and the net surface energy flux (Surf.) which characterises the energy transfers associated to the ocean-surfaces-atmosphere interactions.

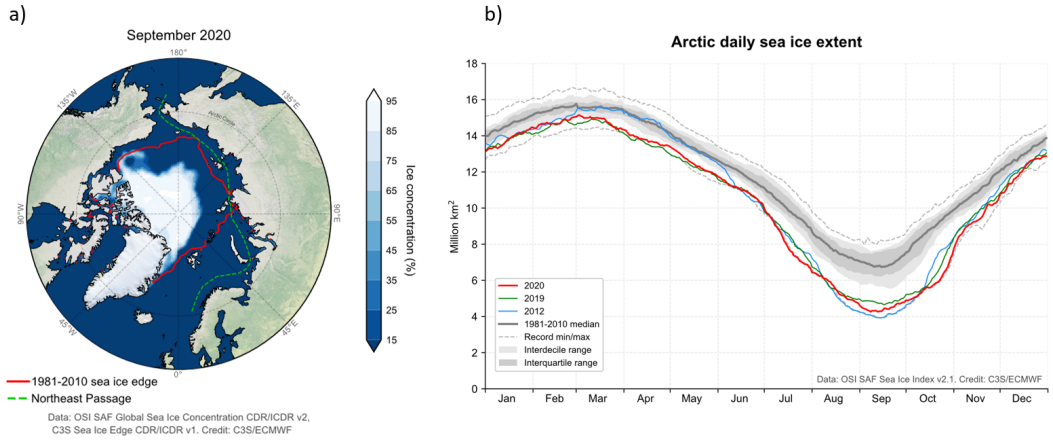

Figure 1.2: a) Monthly average sea ice concentration in September 2020. The red line shows the median ice edge position in September for 1981-2010 and the dashed green line shows the Northeast Passage shipping route. b) Time series of Arctic daily sea ice extent for 2012 (blue), 2019 (green) and 2020 (red). The plot shows in grey shades the daily median (solid line), interdecile range (light shading) and interquartile range (dark shading) during 1981-2010, as well as the daily minimum and maximum during 1981-2010 (dashed lines). Figure adapted from ESOTC (2020).

According to the work of Mayer et al. (2019), where they use a combination of the fifth-generation European Re-Analysis (ERA5; Hersbach et al. (2018c)) and the Ocean Re-Analysis System 5 (ORAS5; Zuo et al. (2019)) associated with a novel observational product (the Japan Meteorological Agency (JMA) 55-year Re-Analysis (JRA-55); Kobayashi et al. (2015)), in order to provide an updated estimate of the coupled atmosphere-ocean-sea ice Arctic energy budget (including flux and storage terms) for the 2001-2017 period, they found that on an annual average basis over the Arctic Ocean, the TOA net radiation[2] is equal to -115.8 W m^{-2} meaning that there is more LW radiation emitted upward ($LW_{u,TOA}$) than SW coming down ($SW_{d,TOA}$). Also, the AEC is +99.6 W m^{-2} whereas the oceanic energy convergence (OEC) (associated to the oceanic currents described in Section 1.1.2(b)) is equal to +16.9 W m^{-2}, which is much smaller (but not insignificant). On an annual average basis, the net surface energy flux is -16.2 W m^{-2} indicating a transfer of energy from the ocean into the atmosphere. The negative value at the TOA, is induced by the AEC which brings in energy from lower latitudes to the Arctic region. Therefore, the atmospheric energy storage is close to zero, *i.e.* the atmospheric incoming and outgoing energy transfers balance. The atmospheric component is not losing or gaining energy on an annual average basis over the Arctic Ocean. On the opposite, the oceanic energy storage is slightly unbalanced since it is equals to +0.3 W m^{-2} indicating that the ocean is slightly warming (Mayer et al., 2019).

However, as mentioned before, the Arctic energy budget is greatly impacted by the seasons. In winter months, the absence of the SW radiation involves a dominant LW flow (Walden et al., 2017) and a strongly negative TOA radiation budget (-176.9 W m^{-2}) (Mayer et al., 2019). The AEC is really high (+123.3 W m^{-2}) and even if the OEC is fairly small (+21.4 W m^{-2}) its role is significant. The net surface flux is equal to

[2]All energy fluxes discussed in this Section are defined to be positive if they are directed toward the ground.

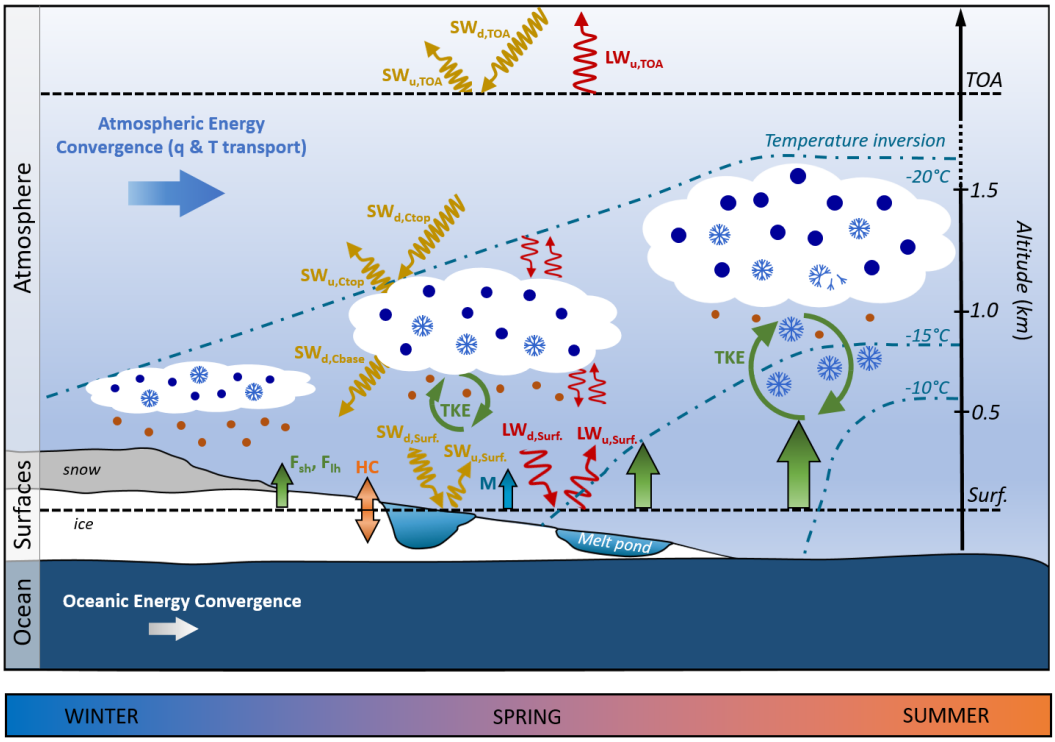

Figure 1.3: Schematic summarising the components of the Arctic energy budget: SW and LW are the shortwave (yellow arrows) and longwave (red arrows) radiations, F_{sh} and F_{lh} are the sensible and latent heat fluxes (green arrows) at the surface, HC is the heat conduction (orange arrows) through the surface, and M is the energy flux of the ice melting. The subscripts $_d$ and $_u$ denote downward and upward directions whereas the subscripts $_{TOA}$ and $_{Surf.}$ denote the "top of the atmosphere" and the "mean surface" reference altitudes (dashed black lines) used in the text. Note that the intensity of each flux are variable according to the season; more details in the text. The schematic also illustrates the development of clouds and thermodynamic properties across the transition from sea ice to ocean: aerosol particles, cloud droplets and ice particles (cloud ice and snowflakes) are represented with brown circles, dark blue circles and light blue crystals respectively. Note that the size of the green vertical arrows which depict F_{sh} and F_{lh} is proportional of the increase in strength of these fluxes according to the surface properties. The curled green arrows represent the development of the turbulent kinetic energy (TKE) below the clouds. Temperature isotherms (turquoise dashed lines) illustrate the changing in the boundary layer structure over the transition from the cold sea ice to the warm ocean. Lastly, the schematic indicates the dominant surface structure present in winter, spring or summer. Figure adapted from Young et al. (2016).

-59.9 W m^{-2} meaning there is a huge transfer of energy from the ocean into the atmosphere. Therefore, the atmospheric energy storage is positive (+5.9 W m^{-2}) entailing a warm up of the atmosphere although the temperatures are cold in winter. On the opposite, the ocean energy storage is negative (-14.3 W m^{-2}) showing its loss of energy (Mayer et al., 2019). In summer months, the SW flux becomes dominant and the TOA net radiation becomes slightly positive (+12,4 W m^{-2}). The AEC becomes smaller than in winter (+87.9 W m^{-2}) (as already explained in Section 1.1.2(a)) whereas the OEC remains equivalent (+21.4 W m^{-2}). Compared to the winter conditions, the net surface flux varies a lot since it becomes highly positive (+94.4 W m^{-2}). Therefore, considering all the incoming and outgoing radiations, the atmospheric component is gaining energy (+5.8 W m^{-2}) as well as the ocean (+47.2 W m^{-2}). During summer months, the ocean

warms up implying the melting of the sea ice and heating flux uppermost levels of the ocean. Then, as the surface temperature increases, the LW radiation becomes more intense (Walden et al., 2017). The atmospheric energy available reaches its maximum in summer months while the atmospheric energy tendency (*i.e.* the change in the energy storage) is the most positive already during the spring because the sun is rising higher in the sky and more energy penetrates to the surface (which is greatly evolving).

d) Surface energy fluxes

The net surface energy flux (Surf.) permits to quantify the energy received and lost by the surface and to understand the exchanges between the evolving surface and the atmosphere. Ultimately, it determines the growth and decay of sea ice, as well as the melting and freezing of snow cover. It is a major driver of many important processes in the Arctic such as the stability properties of the lower troposphere. The net surface energy flux can be described by the Equation 1.1 (as *e.g.* in Lesins et al. (2012)) (the parameters are explained in Figure 1.3) that corresponds to the sum of all the vertical energy fluxes at the atmosphere-surface interface:

$$SW_{d,Surf.} + SW_{u,Surf.} + LW_{d,Surf.} + LW_{u,Surf.} + F_{sh} + F_{lh} + HC + M = Surf. \quad (1.1)$$

when $Surf. = 0$, the surface temperature remains the same and if $Surf.$ is positive or negative, the surface temperature increases or decreases respectively.

Moreover, as defined by Stull (1988), the atmospheric boundary layer (ABL) is the lower part of the troposphere directly affected by the surface properties and the surface forcing occurring within an hour maximum timestep. Then, the surface can generate turbulence that vertically transports heat, moisture and momentum impacting the BL temperature and stability. According to the strength of these fluxes, the thickness of the atmospheric BL could be affected.

As explained in Sections 1.1.2(b)-(c), the Arctic Ocean is covered by sea ice whose extent and thickness vary according to the seasons (Figure 1.2b). In winter, with the absence of sunlight ($SW_{d,Surf.}+SW_{u,Surf.} = 0$), the mean surface air temperature decreases up to ≈ 240 K (Figure 1.4) and sea ice forms reaching its annual maximum extension in March (Figure 1.2b). Turbulent fluxes are relatively weak and the atmosphere is mainly stable over the winter except if synoptic scale systems occur (Walden et al., 2017). As the ocean is warmer than the ice surface, the HC flux remains positive during all this season. In spring, with the return of sunshine ($SW_{d,Surf.} \neq 0$), the snow begins to melt (Figure 1.2b) and melt ponds form (as illustrated in Figure 1.3) (Webster et al., 2015). In summer, when the surface air temperature is ≈ 273 K (Figure 1.4) and the sunshine period is maximal, the sea ice continues to melt (*i.e.* the M flux is still effective) and reaches its annual minimum in September (Figure 1.2b). The appearance of melting ponds and ice-free regions on the surface increases the intensity of the turbulent kinetic energy (TKE) and the sensible and latent heat fluxes (F_{sh}, F_{lh}; see bigger green arrows in Figure 1.3). With the increase of the surface temperature, the HC flux becomes negative (*i.e.* the ocean receives energy) and more SW radiation penetrates into the ocean (Mayer et al., 2019). Note that these changes in surface properties highly impact radiative parameters such as the surface albedo (α) which varies from $\alpha_{ice} > 0.65$ to $\alpha_{ocean} \leq 0.2$ when the surface is bright ice or darker ocean respectively.

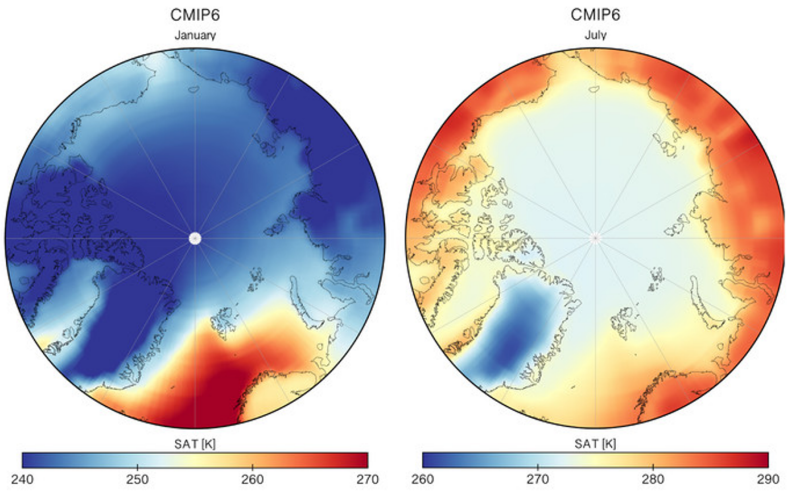

Figure 1.4: The climatological mean surface air temperature (SAT) from the CMIP6 (Coupled Model Intercomparison Project Phase 6) ensemble mean for the months of (left) January and (right) July. The panels are plotted on different colour scales to ensure the spatial details are visible. Figure from Davy and Outten (2020).

Over the Arctic region, in winter months, due to the sea ice surface the atmosphere is often stable (Overland, 1985; Lüpkes et al., 2011; Young et al., 2016). Even if the atmosphere is under stable conditions, the thermodynamical properties are favourable to the cloud formation (as described in the Section 1.1.2(e)). This can be due to synoptic scale events that bring in warmer and moister air (Walden et al., 2017). In summer months, due to the melting of the sea ice and the presence of more oceanic surfaces, the BL becomes more unstable (Lüpkes et al., 2011). These unstable summer atmospheric conditions are mainly present due to local origins (increase in the concentration of aerosols from local biogenic sources), as synoptic scale disturbances have less effect (Tjernström et al., 2004) (the forcing of the atmospheric currents are less intense in summer, as described in Sections 1.1.2(a)-(c)).

Temperature inversions in the lower troposphere occur frequently in the Arctic region, especially in winter months (Tjernström and Graverson, 2009). The strength of these inversions can influence gas and other pollutants' concentrations in the BL (Barrie et al., 1988; Bridgman et al., 1989). In addition, there is a strong interaction between Arctic clouds and the vertical temperature structure (Schweiger et al., 2008; Qiu et al., 2015; Young et al., 2016) (as illustrated in Figure 1.3). Thus, the temperature inversions (see Figure 1.3) play a key role in the Arctic climate system. Note that specific humidity inversions have also been observed over the Arctic Ocean (Sedlar and Tjernström, 2009; Solomon et al., 2011; Tjernström et al., 2012) and on the Svalbard archipelago (Treffeisen et al., 2007; Vihma et al., 2011) and also impact the cloud properties.

Hereinabove, the variations in the surface properties and their impacts on the net surface energy flux and the atmospheric boundary layer have been described according to the seasons. All these key trends remain the same if we focus on a geographical area characterised by a transition from sea ice to open ocean via a marginal ice zone (both seasonal and geographical transitions are illustrated in Figure 1.3). Several Arctic expeditions (see Section 1.3) were organised during spring to focus observations on this transitional phase, such as ACCACIA campaign (*Aerosol-Cloud Coupling And Climate*

Interactions in the Arctic; Young et al. (2016)) which took place in spring 2013 close to the Svalbard archipelago, and during the ACLOUD campain (Wendisch et al., 2019)) organised over the Greenland Sea in spring 2017 (more details in Chapter 2) which is the framework of this thesis.

e) Arctic mixed-phase clouds (MPCs)

Arctic clouds, which play a major role in the evolution of the Arctic climate (Curry et al., 1996), have a significant impact on the Arctic energy exchange and surface energy budget.

In the Arctic region, the cloud cover is important (anual mean ≈ 67%) throughout the year (Ruiz-Donoso et al., 2020; Mioche et al., 2017, 2015; Intrieri et al., 2002a), especially close to the Svalbard archipelago. Figure 1.5a represents the mean seasonal occurrence of clouds (F_{CLOUDS}) referring to time and shows that F_{CLOUDS} values are ranged from 80% to nearly 100% close to the Svalbard. Clouds then offer a significant area to interact with sun radiation (see $SW_{d,Ctop}$ and $SW_{u,Ctop}$ illustrated in Figure 1.3). The clouds disperse the SW radiation ($SW_{d,Cbase}$) decreasing the SW striking on the surface ($SW_{d,Surf.}$). The LW emitted by the earth ($LW_{u,Surf.}$) and the lower atmosphere is absorbed by the clouds and these in turn emit LW radiation depending on their own temperature. The cloud radiative forcing (CRF) is calculated by making the difference between the energy balance in clear sky and with clouds ($F_{net} - F_{net}^{cf}$), which depends on the microphysical, macrophysical, and optical properties of the clouds (Shupe and Intrieri, 2004). The CRF informs on the ability of the clouds to cool or warm the surface. Nevertheless, the cloud interactions with the surface and the energy balance are still poorly understood and poorly represented in climate and weather prediction models (Lacour et al., 2017) (see Section 1.4).

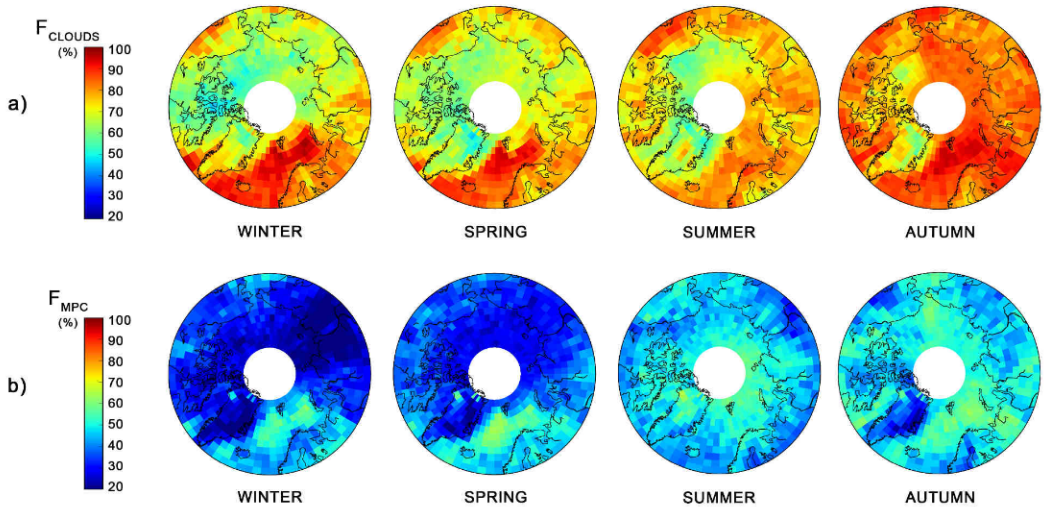

Figure 1.5: Stereographic projections of the seasonal occurrences of: (a) all clouds (referring to time) and (b) mixed-phase clouds (MPCs) (referring to clouds). Occurrences are computed taking into account the 500-12 000 m altitude range. Figure from Mioche et al. (2015).

Numerous observational studies suggest that boundary layer mixed-phase clouds (MPCs, mixture of supercooled liquid droplets and ice) are ubiquitous in the Arctic

and persist for several days under a variety of meteorological conditions (see Ruiz-Donoso et al., 2020; Mioche et al., 2017, 2015; Morrison et al., 2012; Shupe et al., 2011; McFarquhar et al., 2007; Shupe and Intrieri, 2004; Intrieri et al., 2002a, among others). Figure 1.5b shows the MPC occurrences where F_{MPC} refers to time where clouds occur. The MPCs are encountered in all seasons: in winter and early spring, about 30% of the clouds over the entire Arctic region are MPCs and F_{MPC} reaches about 50% of the clouds from May to October. However, the spatial and temporal distribution of MPCs is highly inhomogeneous. For example, larger occurrences (up to 60%) are present over the Canadian Basin and the Chukchi Sea in autumn, and over the Greenland Sea throughout the year. Over the Svalbard region, F_{MPC} is even equal or larger compared to the Arctic average (Mioche et al., 2015).

The persistence of the MPCs in the lower troposphere under a variety of atmospheric conditions for periods of days to weeks is surprising considering the fact that the mixture of supercooled liquid droplets and ice is microphysically unstable, due to the Wegener-Bergeron-Findeisen mechanism (WBF) (Pruppacher and Klett, 1997). A complex web of interactions between various physical processes exists within MPCs making the comprehension of these clouds and their impacts still difficult. Based on a review of many previous studies, Morrison et al. (2012) have proposed a conceptual diagram summarising the various physical processes (radiative cooling, microphysics, dynamics, and surface properties) involved in the development and the evolution of the MPCs (see Figure 1.6).

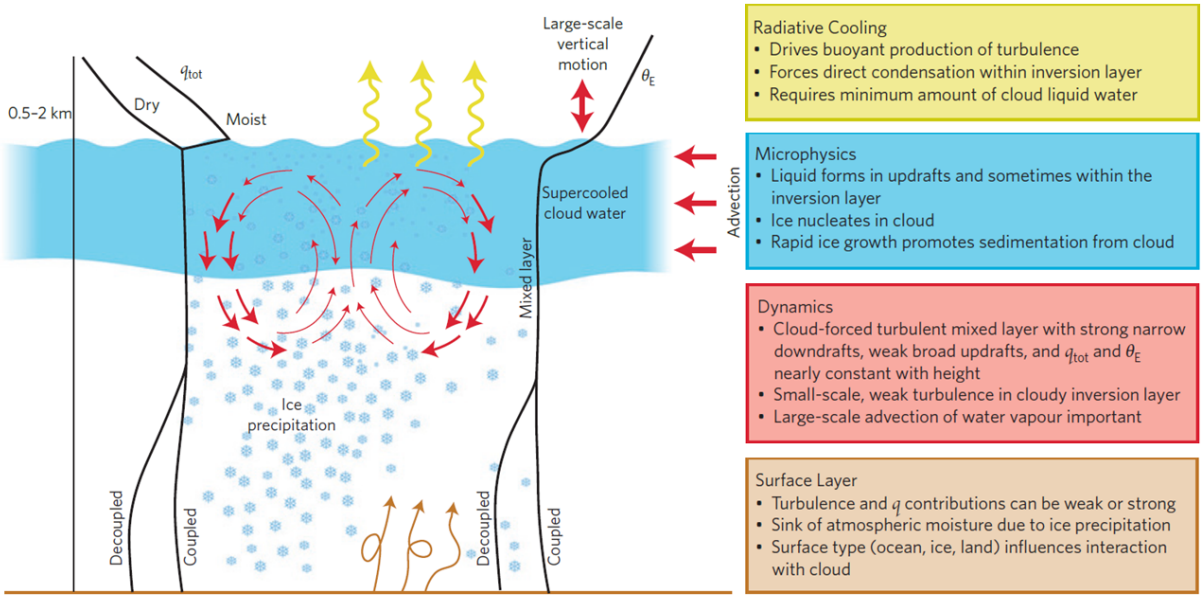

Figure 1.6: Basic physical structure of Arctic MPCs. The main features are described in text boxes, which are colour-coded for consistency with elements shown in the diagram. Characteristic profiles are provided of total water (vapour, liquid and ice) mixing ratio (q_{tot}) and equivalent potential temperature[3] (θ_e). These profiles may differ depending on local conditions, with dry *vs.* moist layers/moisture inversions above the cloud top, or coupling[4] *vs.* decoupling of the cloud mixed layer with the surface. Cloud-top height is 0.5-2 km. Figure from Morrison et al. (2012).

Figure 1.6 illustrates that the MPC top height can range between 0.5-2 km since the cloud base and thickness depend on the atmospheric thermodynamical and stability conditions, and the surface properties (Young et al., 2016; Morrison et al., 2012) (see also Section 1.1.2(d)). Turbulence and cloud-scale upward air motion are very important in maintaining MPCs under weak synoptic-scale forcing (Shupe et al., 2008). The updrafts can induce supersaturated conditions with respect to the liquid water leading to growth of ice crystals and supercooled liquid droplets simultaneously. Thus, the clouds can be made up of a single layer of supercooled water droplets at the top from which ice crystals form and precipitate. This supercooled liquid layer is responsible for a significant part of the CRF as downward LW fluxes increase and then warm the surface (Wang et al., 2001). On the other hand near the cloud top, a LW radiative cooling is present leading to decreased static stability, buoyant production of turbulent updrafts, and condensational growth of droplets (Luo et al., 2008). A moisture inversion (see Figure 1.6) is also frequently produced near the cloud top by large-scale advection, moistening the cloud layers thanks to the turbulent entrainment of air from above the clouds (Solomon et al., 2011). These complex feedbacks between turbulence, radiation and cloud droplets, in association with moisture inversions near the cloud top and surface fluxes whose magnitude depends on the surface type, can lead to the persistence of MPCs in various environmental conditions (Morrison et al., 2012).

Also, the atmospheric aerosol particles can influence the evolution of the MPCs by affecting cloud microphysical properties. Indeed, aerosol particles with heterogeneous ice-nucleating properties are involved in the ice formation (Cantrell and Heymsfield, 2005; Fridlind et al., 2007). The concentration of INP and hence ice crystals is critical for MPCs (as mentioned in Figure 1.6) because it impacts the WBF mechanism and so the liquid/ice partitioning. The liquid phase has also a role on the ice phase in the MPCs since several observation studies indicate that ice crystal concentration and the presence of supercooled liquid droplets are correlated (Lance et al., 2011; de Boer et al., 2011). However, the concentration and size of the cloud droplets are linked to the aerosol particles (*i.e.* the CCN) via the droplet heterogeneous nucleation process. The increase in the aerosol loading with transport from mid-latitudes (see Section 1.1.2(a)) or with higher emissions due to the evolving surface type (see Section 1.1.2(d)) impact the cloud droplet concentration (Abbatt et al., 2019); thus, the supercooled liquid phase can impact not only the ice crystal properties but also the CRF resulting in a surface warming, which may then affect the surface fluxes (Garrett and Zhao, 2006).

As described before, the strong impact of the MPCs on the energy budget is caused by their persistence and microphysical properties, causing a net warming effect of the surface which result from a complex web of interactions between numerous local and larger scale processes (see Figure 1.6) that greatly complicate their understanding and modelling (Klein et al., 2009; Morrison et al., 2012). Major uncertainties limit our understanding of the interactions and feedbacks between the physical processes involved in the MPC lifecycle. This complexity translates into the large discrepancies that can be found in numerical models to represent the cloud formation and persistence (Wesslén

[3] θ_e is the temperature a parcel of air would reach if all its water vapour condenses (releasing latent heat) and then it is adiabatically brought to the 1000 hPa standard reference pressure level. Under stably stratified conditions where vertical motions are suppressed $\frac{\partial \theta_e}{\partial z} > 0$ whereas when $\frac{\partial \theta_e}{\partial z} < 0$ the atmosphere is unstable and convection is likely.

[4] Surface-coupled clouds were identified by a quasi-constant potential temperature profile (*i.e.* close to adiabatic conditions) from the surface up to liquid layer (Gierens et al., 2020; Griesche et al., 2021).

et al., 2014), the interactions between sea ice and MPCs (Palm et al., 2010; Liu et al., 2012) as well as the energy balance and variability in the BL, which in turn impacts their capability of the models to forecast cloud properties in the Arctic.

1.2 Climate evolution: Arctic amplification

The global temperature of the planet increases as a result of greenhouse gas emissions from anthropogenic activities (IPCC, 2018). Recently, observations confirmed that the Arctic has warmed three times faster than the rest of the globe during the last few decades as shown in the Figure 1.7 (ESOTC, 2020), with a very pronounced seasonality as winter warming far exceeds summer warming (AMAP, 2021), in conjunction with sea ice retreat (ESOTC, 2020). This increase in temperature, is responsible for the phenomenon called "Arctic amplification", often attributed to the decrease in the size and thickness of ice and the snow that covers it. Sea ice decreased by 40% in September and 10% in March compared to 1975 (ESOTC, 2020) (see Figure 1.2b). Several physical processes have a role in explaining this phenomenon, including the radiative forcing of clouds, aerosols particles, the heat carried by ocean currents, changes in atmospheric circulation, disturbances of heat and moisture transport to the Arctic (Cohen et al., 2018; Previdi et al., 2020).

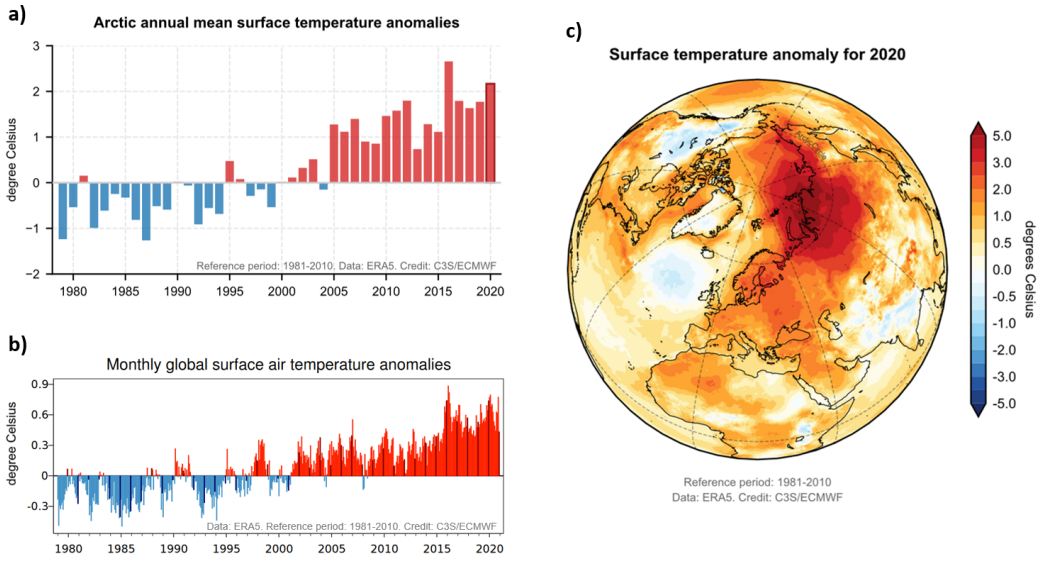

Figure 1.7: Time series of (a) Arctic annual mean surface temperature anomalies (averaged over 66.6°N-90°N) and of (b) monthly global-mean surface air temperature anomalies, both from 1979 to 2020. (c) Map of the annual mean surface temperature anomaly in 2020. All anomalies are calculated relative to the 1981-2010 mean. Figure adapted from ESOTC (2020).

Figures 1.7a and b show that the global temperatures on the 2000-2020 period were on average about 0.6°C higher than they were on the 1981-2010 reference period whereas over the Arctic region the temperatures on the 2000-2020 period were $\approx$ 1.6°C warmer than the ones measured during the same reference period. This more pronounced warming present over the Arctic region appears to be mainly a surface-based feature, especially in the non-summer seasons, even though there is also evidence of summer warming aloft

according to Graversen et al. (2007). Also, Screen and Simmonds (2009) suggested that the Arctic warming is mainly linked to the sea ice decline that evolves at a rate of 13% per decade. Moreover, as suggested by Zhang et al. (2008), changes in atmospheric and oceanic heat and moisture transports also play a role in the Arctic warming. So, despite the profound impacts of temperature changes on the Arctic ecosystems (ACIA, 2005), the main causes of the Arctic amplification are not fully understood due to the complex interactions between the surfaces, the atmospheric and oceanic currents (AEC, OEC), the radiative fluxes, the cloud cover and the atmosphere pollution. Indeed, as indicated in Wendisch et al. (2017): "*there is not yet a consensus in the Arctic research community about the dominant mechanisms leading to Arctic amplification*".

Figure 1.8 describes several feedback mechanisms which are effective in the Arctic region and involved in the Arctic amplification phenomenon (Wendisch et al., 2017).

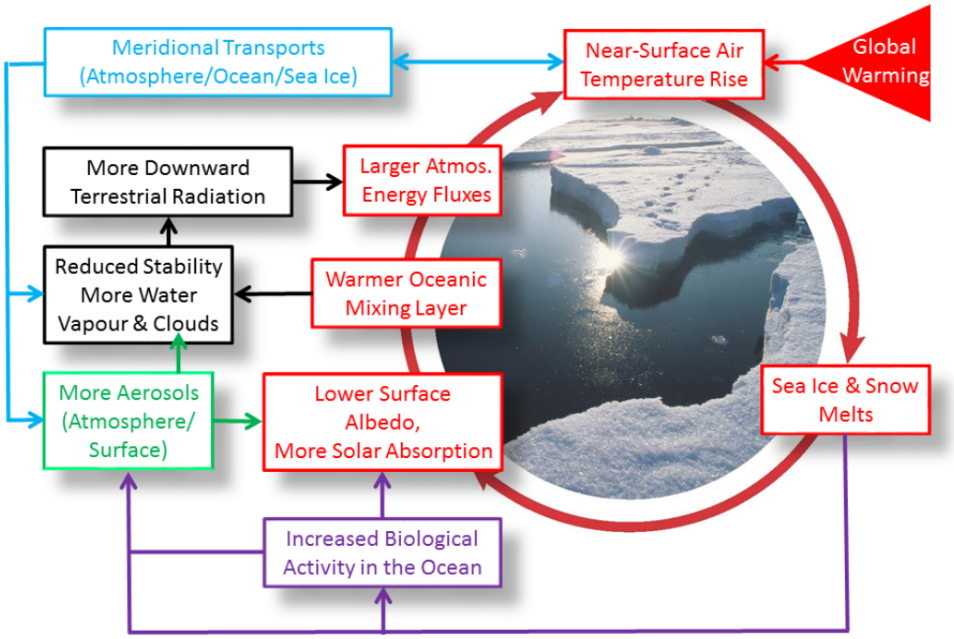

Figure 1.8: Scheme of important feedback mechanisms and processes involved in the Arctic amplification phenomenon. Red: surface albedo effect; Black: water vapour, cloud, and lapse rate feedback mechanisms; Green: aerosol effect; Purple: increased oceanic biological activity; Blue: modifications in the atmospheric and oceanic transports (remote processes). Figure from Wendisch et al. (2017).

The Figure 1.8 taken from Wendisch et al. (2017) illustrates that, due to the global warming, the atmospheric temperatures near the surface increase impacting the surface properties since the melting of the sea ice and snow becomes more efficient. Then, due to less reflective surfaces, the albedo decreases and the ocean heat storage becomes more important (due to more solar absorption by the upper oceanic layer). Thus, the energy fluxes from the surface to the atmosphere are enhanced, which increases the air temperature near the surface even further. A warmer ocean surface could also increase the atmospheric water vapour amount impacting the stability of the atmosphere and thus cloud development. Moreover, the increase in ocean temperatures and in the ocean ice-free surface can produce a rise not only in the oceanic biological activity but also

in the aerosol emissions (which can also affect the cloud properties and their associated radiative impacts). All of these mechanisms can locally be modified by the wind fields and can be affected by atmospheric and oceanic transports from larger scales.

Historically, regions of open ocean and newly formed thin ice growing to sea ice at a rapid rate, a strong negative radiative feedback which tended to overwhelm other Arctic processes. Arctic changes observed in recent years, however, are likely due to an underestimated connectivity in multiple atmosphere-sea ice-ocean processes (Wendisch et al., 2017).

In fact, the ice albedo feedback (Deser et al., 2010; Hall, 2004) has long been considered as the primary contributor to Arctic warming. This feedback mechanism operates primarily in summer when insolation is highest, and is absent in winter. It can affect wintertime temperatures by seasonal storage and release of energy (Screen and Simmonds, 2009; Serreze and Francis, 2006), but the actual energy going into summer ocean warming and into ice melt and how much both contribute to heat release in Arctic winter warming remains unclear. Also, the warming of the Arctic atmosphere has been found to increase downwelling infrared radiation mainly through changes in cloud cover (Screen and Simmonds, 2009) and their properties (Francis and Hunter, 2007), BL inversion strength (Bintanja et al., 2012, 2011) and moisture content (Lu and Cai, 2009). The water vapour feedback involves either increased local evaporation owing to the retreating sea ice (Graversen and Wang, 2009) or increased poleward latent heat transport (Lu and Cai, 2009).

Aerosol particles also impact the climate both directly (aerosol-radiation-interactions) and indirectly (aerosol-cloud-interactions)(Wendisch et al., 2019). The indirect effect is the most important in the total aerosol radiative forcing, and the net effect is a cooling of the atmosphere. Aerosol-cloud-radiation interactions vary significantly, not only spatially but also seasonally, due to presence of a diverse environment around Arctic Circle (containing pack-ice, glaciers, mountains) and also to arrived of different air masses. On Svalbard, there are many potential aerosol sources and the aerosol particle population follows a seasonal cycle. In winter and spring the aerosol population is dominated by the Arctic haze period, which is a phenomenon due to the accumulation of anthropogenic particles (diameters from $\approx$ 70 nm to 1 μm) in the atmosphere. A major characteristic of Arctic haze is the ability of its chemical components to persist in the atmosphere for significantly longer than other pollutants. This aerosols arrived on Svalbard via long-range atmospheric transport (Tunved et al., 2013). They are transported from Northern Europe, but also from the lower Arctic, e.g. Siberia one of the major sources of black carbon and sulphate aerosol in the Arctic (Hirdman et al., 2010; Huang et al., 2015). In summer, due to different atmospheric transport patterns (Stohl, 2006) and more efficient wet scavenging (Browse et al., 2012) the accumulation of particles is lower than spring. In summer, the aerosol population is dominated by smaller particles (Aitken mode) obtained from local secondary aerosol formation (Tunved et al., 2013), from vapors of both terrestrial and nearby marine origin (Beck et al., 2021; Dall'Osto et al., 2017). Other potential aerosol sources coming from Svalbard itself include glacial dust, which has the ability to act as INP (Tobo et al., 2019).

In order to better identify the dominant mechanisms leading the Arctic amplification and disentangle them, several observational campaigns have been organised in the Arctic region focussing on the atmosphere-surface-radiation interactions.

1.3 Arctic expeditions

During the last decades, several observational campaigns were performed over various parts of the Arctic region (*e.g.* the Greenland Sea, the Beaufort Sea, the Norwegian Sea and the Barents Sea; see Figure 1.1 for localisations) in order to study the atmosphere-surface-radiation complex interactions of the Arctic climate and better understand the Arctic amplification phenomenon. These past campaigns generally highlighted the important role that clouds can play in that changing system and in the manifestation of Arctic amplification. However, there is still a basic lack of understanding of the interplay between aerosol particles, clouds, and surface properties, as well as turbulent and radiative fluxes with dynamical processes.

Tables 1.1-1.2 give a (non-exhaustive) list of the major airborne measurement campaigns, organised since the 2000s, which were focussing on the microphysical properties of the clouds present in different regions of the Arctic.

In autumn 2004, the *Mixed-Phase Arctic Cloud Experiment* (M-PACE) that was organised in the North of Alaska merged the observations from four surface-based sites (Barrow, Atqasuk, Oliktok Point, and Toolik Lake) and two aircrafts equipped with the microphysical and radiation instruments to document the cloud properties between these four points (Verlinde et al., 2007). Using the complementary of in-situ instruments, remote sensing facilities and radiosondes, the main objectives of this campaign were to study the dynamical and physical (including microphysics and radiative) processes in the Arctic MPCs (Verlinde et al., 2007). Within the international ASTAR (*Arctic Study of Tropospheric Aerosols, clouds and Radiation*) project, series of airborne campaigns which were organised in spring 2004 (Schwarzenboeck et al., 2009; Gayet et al., 2007) and spring 2007 (Gayet et al., 2009a,b; Ehrlich et al., 2009) were devoted to study the MPCs present in another region of the Arctic: over the Greenland and Barents Seas. From Longyearbyen (Svalbard), airborne in-situ and remote sensing instruments were deployed to investigate the aerosol-cloud interactions and the resulting modifications of radiative properties of the clouds. In spring 2008, the aerosol-cloud interactions in the Arctic boundary layer were also investigated during the *Indirect and Semi-Direct Aerosol Campaign* (ISDAC, McFarquhar et al. (2011)) in the vicinity of Barrow, Alaska (*i.e.* the ARM permanent observational facilities). Other experiments were conducted at the same time as ISDAC which also contributed to a better understanding of the MPCs over the Beaufort Sea and the North of Alaska, such as the *Aerosol, Radiation and Cloud Processes affecting the Arctic Climate* experiment (ARCPAC, Lance et al. (2011); Warneke et al. (2009)) and the *Arctic Research of the Composition of the Troposphere from Aircraft and Satellites* experiment (ARCTAS, Jacob et al. (2010)). ARCPAC was an airborne campaign coordinated with the POLARCAT experiment (*Polar study using aircraft, remote sensing, surface measurements and models of climate chemistry, aerosols and transport*); it was closely collocated with remote sensing and in-situ observations from the ARM ground site of Barrow, Alaska. One of the main objectives of POLARCAT was the development of an instrumental synergy to retrieve cloud properties and to characterise the cloud phase at scales smaller than a kilometre (Delanoë et al., 2013). As visible in Table 1.1, international and collaborative efforts with intensive research focus on the polar regions were made in 2008 within the framework of the *International Polar Year* (IPY) programme sponsored by the International Council for Science (ICSU) and the World Meteorological Organization (WMO).

Year	Period	Acronym	Campaign	Localisation	References
2004	Sept-Oct	M-PACE	Mixed-Phase Arctic Clouds experiment	North of Alaska	Verlinde et al. (2007)
2004	May-June	ASTAR 2004	Arctic Study of Tropospheric cloud, Aerosol and Radiation	Greenland Sea Barents Sea	Schwarzenboeck et al. (2009) Gayet et al. (2007)
2007	April	ASTAR 2007	Arctic Study of Tropospheric Aerosol, cloud and Radiation	Greenland & Barents Sea Svalbard	Gayet et al. (2009a,b) Ehrlich et al. (2009)
2008	March-April	POLARCAT Spring	POLar study using Aircraft, Remote sensing surface measurements and models of Climate chemistry, Aerosols and Transport	Sweden Greenland	Delanoë et al. (2013)
2008	August	AMISA	Arctic Mechanisms of Interaction between the Surface and Atmosphere	Arctic Ocean North of Svalbard	Persson (2010)
2008	April	ISDAC	Indirect and Semi-Direct Aerosol Campaign	Beaufort Sea, North of Alaska	McFarquhar et al. (2011) Jackson et al. (2012)
2008	April	ARCPAC	Aerosol, Radiation and Cloud Processes affecting the Arctic Climate	North of Alaska	Lance et al. (2011)
2010	April-May	SORPIC	Solar Radiation and Phase Discrimination of Arctic Clouds	Greenland and Barents Seas Svalbard	Bierwirth et al. (2013)
2012	April-May	VERDI	Vertical Distribution of Ice in Arctic Clouds	Beaufort Sea	Klingebiel et al. (2015)
2013	March-April & July	ACCACIA	Aerosol-Cloud Coupling And Climate Interactions in the Arctic	Greenland Sea	Lloyd et al. (2015) Young et al. (2016)
2014	April-May	RACEPAC	Radiation-Aerosol-Cloud Experiment in the Arctic Circle	Beaufort Sea	Costa et al. (2017)
2017	May-June	ACLOUD	Arctic CLoud Observations Using airborne measurements in polar Day conditions	Greenland Sea North of Svalbard	Wendisch et al. (2019) Ehrlich et al. (2019a) Ruiz-Donoso et al. (2020)
2018	March-April	PAMARCMiP	Polar Airborne Measurements and Arctic Regional Climate Model Simulation Project	Arctic Ocean	Ohata et al. (2021) Herber (2019)
2019	March-April	AFLUX	Airborne measurements of radiative and turbulent FLUXes in the cloudy atmospheric boundary layer	Greenland Sea North of Svalbard	Lüpkes et al. (2019) Mech et al. (2022)

Table 1.1: Non-exhaustive list of major airborne measurement campaigns performed in the Arctic region from 2004 to 2019, during which in-situ observations on microphysical properties of the MPCs were conducted. Adapted from Mioche and Jourdan (2018) and Jourdan (2022)

In April-May 2010, the aircraft campaign SoRPIC (*Solar Radiation and Phase Discrimination of Arctic Clouds*) was held in Svalbard (Arctic Norway). More than 10 re-

Year	Period	Acronym	Campaign	Localisation	References
2020	August-Sept	MOSAiC-ACA	Atmospheric airborne observations in the Central Arctic	Greenland Sea North of Svalbard Central Arctic	Herber et al. (2020) Shupe et al. (2022)
2022	March-April	HALO(AC)^3	HALO(AC)^3	Greenland Sea Arctic Ocean Svalbard	Wendisch et al. (2019)
2022	August	RALI-THINICE	RALI-THINICE	Greenland Sea Svalbard	Rivière et al. (2022)
2022	March-April	ISLAS	Isotopic links to atmospheric water's source	Norwegian Sea	

Table 1.2: As for Table 1.1 but for the 2020-2022 period.

search flights were conducted out of Svalbard's main settlement (Longyearbyen) with the Polar 5 aircraft (of Alfred Wegener Institute for Polar and Marine Research; Germany) over the Greenland, Norwegian and Barents Seas (Bierwirth et al., 2013). The aircraft was equipped with a combination of remote sensing and cloud particle in-situ instruments to study the properties of the different cloud phases and their radiative impacts. During VERDI (*Vertical Distribution of Ice in Arctic Clouds*), the airborne observations were conducted inside and above low-level Arctic clouds from Inuvik (northern Canada) in April-May 2012 in order to improve our knowledge about the cloud effects in the Arctic climate system (Klingebiel et al., 2015). The RACEPAC (*Radiation-Aerosol-Cloud Experiment in the Arctic Circle*) campaign which was organised in April-May 2014 took place at the same place as VERDI (Costa et al., 2017). The several flights of both VERDI and RACEPAC covered the region of the Arctic Beaufort Sea coast with its retreating sea ice in spring (Young et al., 2016). Although both campaigns took place at the same period of the year, the different synoptic conditions led to different cloud properties: stable anticyclonic periods allowing the formation of strong inversions in the boundary layer with persisting stratus were observed during VERDI, whereas the frequent frontal systems observed during RACEPAC induced more variable and short-lived cloud situations (Costa et al., 2017). To study the Arctic seasonality, the two campaigns of the ACCACIA project took place during March-April and then in July 2013 over the region between Greenland and Norway (mainly in the vicinity of the Svalbard) (Young et al., 2016; Lloyd et al., 2015). The main objective of this project was to reduce the large uncertainty in the effects of aerosols and clouds on the Arctic surface energy balance and climate, and in particular obtain a better understanding of the microphysical properties of Arctic clouds and their dependence on aerosol properties. Both the FAAM BAe-146 (British Aerospace-146 of the Facility for Airborne Atmospheric Measurements) and the BAS (British Antarctic Survey) Twin Otter aircrafts performed several flights incorporating profiled ascents, descents and constant altitude runs below, within and above cloud to measure the vertical structure of the cloud microphysics and the aerosol properties inside and outside clouds (Lloyd et al., 2015).

Since January 2016, the German Research Foundation launched a new Transregional Collaborative Research Centre called *ArctiC Amplification: Climate relevant Atmospheric and surfaCe processes, and feedback mechanisms* (AC)^3 (Wendisch et al., 2017). In this framework, one of the objectives is to embed the short-term measurements

from several intensive field campaigns (organised in different seasons and meteorological conditions, covering a suitable wide range of spatial and temporal scales) in longer-term data sampling programs (*i.e.* the past 30 years) to identify trends in the spatiotemporal variability of the Arctic climate parameters. Four airborne campaigns were performed using the German research aircrafts Polar 5 and Polar 6 of the Alfred-Wegener-Institute (AWI; Wesche et al. (2016)): ACLOUD in May-June 2017 (which is the framework of this PhD and will be described in details in Chapter 2) (Wendisch et al., 2019), PAMARCMiP (*Polar Airborne Measurements and Arctic Regional Climate Model Simulation Project*) in March-April 2018, AFLUX (*Airborne measurements of radiative and turbulent FLUXes in the cloudy atmospheric boundary layer*) in March-April 2019, and MOSAiC-ACA (*Atmospheric airborne observations in the Central Arctic* organised to complement the MOSAiC mission (*Multidisciplinary drifting Observatory for the Study of Arctic Climate*; Shupe et al. (2022))) in August-September 2020. The first $(AC)^3$ results achieved since 2016 on the atmospheric and surface processes, and the feedback mechanisms determining the Arctic amplification are presented in Wendisch et al. (2022).

More recently (*i.e.,* March-April 2022), an additional $(AC)^3$ campaign called HALO$(AC)^3$ was organised in the vicinity of the Svalbard (Wendisch et al., 2021). During this campaign, a novel form of observation was used in order to follow air masses to and from the Arctic region thanks to three aircrafts: the AWI Polar 5 and Polar 6 as well as the HALO Gulfstream G-550 aircraft (*High Altitude and Long Range Research Aircraft* funded by the DFG, German Research Foundation), allowing a better understanding of the meridional transport and linkages between the Arctic and the midlatitudes. Additionally, airborne observations were organised during the international RALI-THINICE field campaign in Svalbard in August 2022 involving American, French and British teams. The field campaign involved two instrumented research aircrafts: the French ATR42 aircraft operated by SAFIRE (*the French facility for airborne research*) that was dedicated to study atmospheric dynamics and cloud microphysics in the middle troposphere, and the Twin Otter aircraft deployed by the British Antarctic Survey (BAS) to identify the interactions between atmospheric dynamics and sea ice. The main goal of RALI-THINICE was to study the interactions between atmospheric dynamics, cloud microphysics and sea ice near summertime Arctic cyclones (Rivière et al., 2022).

All these campaigns help to provide a better knowledge of the complex processes involved in the Arctic amplification and they should improve climate and weather numerical forecasts in the Arctic region which are still difficult.

1.4 Modelling of the Arctic clouds

The performance of climate and weather models has improved considerably in recent years, allowing models to perform calculations at finer resolutions. However, models still have difficulties in correctly representing Arctic weather variables (Sedlar et al., 2020). Numerous studies are trying to improve models operating in the Arctic region by considering different processes of local scale. Observational studies have shown that MPCs are common in the Arctic (*e.g.* Mioche et al. (2017); Verlinde et al. (2007)). The life cycle of MPCs results from a complex web of interactions between local dynamical, radiative and microphysical processes as well as larger scale environmental conditions

(illustrated in Figure 1.6; Morrison et al. (2012); Solomon et al. (2011); Klein et al. (2009)). MPCs are therefore challenging to model from local to global scales (Pithan et al., 2016; de Boer et al., 2014), and over simplified assumptions in the representation of the microphysical processes are required.

As described in Figure 1.5, cloud cover is close to 67% throughout the year in the Arctic. These cloud fields have been observed to persist for ≈ 12 h (Shupe et al., 2006) with some persisting longer than 100 h (Shupe et al., 2011). Climate and meteorological models generally have great difficulty in correctly representing cloud occurrences and their microphysical properties, and this is an important source of bias on the surface energy balance. Clouds in Arctic typically maintain a liquid layer at cloud top which facilitates ice formation and precipitation during all year (Morrison et al., 2012; Jackson et al., 2012; McFarquhar et al., 2011; Verlinde et al., 2007; Shupe et al., 2006; Rangno and Hobbs, 2001) and models have difficulties in representing them correctly (Ebell et al., 2020; Morrison et al., 2012). Liquid water and ice are uniformly mixed throughout the model grid boxes (Tan et al., 2016; Komurcu et al., 2014; Morrison et al., 2012; Klein et al., 2009; Prenni et al., 2007). However, MPCs seem to be more likely composed of an inhomogeneous mixture of ice particles and liquid droplets clustered in single-phase liquid or ice cloud regions (Korolev et al., 2017). The significant uncertainties associated with global climate model (GCM) predictions may be largely attributed to the inadequate treatment of sub-grid scale (such as cloud microphysics) parameterisations, and it has strong consequences on the droplet-ice interactions and hence on the persistence of MPCs (IPCC, 2013). These uncertainties are predicted to enhance discrepancies in temperature forecasts in the polar regions (IPCC, 2013; Serreze and Barry, 2011; ACIA, 2005). The accuracy of these forecasts can be improved by developing the representation of the physical processes involved through the comparisons with observations from *e.g.,* in-situ or remote sensing instruments (Curry et al., 1996).

Finer scale models also show that the cloud structure and longevity are very sensitive to the phase partitioning (Solomon et al., 2018; Pithan and Mauritsen, 2014; Ovchinnikov et al., 2011; Fan et al., 2009). Greater ice number concentrations (N_{ice}) enhance the efficiency of the WBF process – leading to the depletion of liquid water within the cloud – whilst lower number concentrations allow liquid droplets to persist under moderate vertical motions (Morrison et al., 2012; Prenni et al., 2007). The ice crystal number concentration controls the liquid/ice partitioning and hence the maintenance of the MPCs. However, previous model intercomparisons (Klein et al., 2009) clearly highlighted large discrepancies in the simulated LWC and IWC and even wider differences in the predicted N_{ice} (five orders of magnitude). The discrepancies can be attributed to ice formation processes within MPCs in the model, due to the representation of different microphysical processes and properties result from interactions between atmospheric dynamics, thermodynamics and aerosol particles, which can act as CCN or INP (see Figure 1.6). Heterogeneous ice nucleation is the key process that controls the ice crystal production in MPCs (and hence the phase partitioning). However measurements capabilities of this process are still limited. This translates into inaccurate model parameterisations to compute N_{ice} and hinders our understanding of the life cycle of MPCs (Heymsfield et al., 2017; Korolev et al., 2017; Field et al., 2017).

The seasonal variability of cloud cover and cloud microphysical properties and sea ice cover regulates the temporal evolution of the ABL energy fluxes (turbulent and radiative), which interact with the cloud layers (Young et al., 2016; de Boer et al.,

2014; IPCC, 2013). Cloud top radiative cooling and local dynamical processes such as turbulence and cloud-scale upward air motion also influence the microphysical properties and are critical in maintaining MPCs (Solomon et al., 2011). The surface properties (Renfrew et al., 2020) and the ABL (Sedlar et al., 2020; Wesslén et al., 2014; Liu et al., 2012; Palm et al., 2010) are poorly represented by climate and weather models and heat exchange coefficients are generally overestimated in the ABL (Sedlar et al., 2020), leading to poor representation of energy balance on the surface.

The work described in the following chapters aims to evaluate the WRF mesoscale model (Skamarock et al., 2008) to reproduce the MPCs and to analyse their properties, for two situations observed during the ACLOUD airborne campaign in spring over sea ice and over open ocean. Before describing the characteristics of the WRF model, the following chapter presents the ACLOUD campaign, the observations and instrumentation used to record the both studied situations.

Chapter 2

ACLOUD campaign, observations and case studies

As mentioned in the Chapter 1, we are currently witnessing drastic climate changes in the Arctic that are unprecedented in the history of mankind (Jeffries et al., 2013). NASA data shows the Arctic warmed a little less than three times as fast as the rest of the globe over the past 30 years (Serreze and Barry, 2011). Unfortunately, we neither fully comprehend these striking climate changes in the Arctic nor well understand why they happen so fast. Therefore, several international efforts are underway to better understand the various mechanisms that occur in this specific area in order to improve model projections of the Arctic climate. Climate models alone will not resolve the Arctic climate issue because they often use simple parameterizations that need to be verified, tested, and/or improved. Nevertheless, modelling associated to observations will help to improve our understanding of the different components of the Arctic region and their interactions. Even if several campaigns have already been organised over the Arctic (see Chapter 1), the required observations are still sparsely distributed across this region. As a consequence further data have to be collected in well-planned and dedicated campaigns to better document and understand the Arctic climate changes.

This chapter presents the ACLOUD campaign, performed during the spring 2017 at the North-West of the Svalbard archipelago, *i.e.* region of the Arctic where environmental conditions are complex (this region is subject to different types of air masses likely to be affected by pollution from mid-latitudes, oceanic currents influencing the sea ice cover as detailed in Chapter 1). Different objectives have been identified for this campaign, among which the characterisation of the boundary layer clouds in mixed phase from in-situ and remote sensing measurements, which provide the framework of the present thesis. After a brief description of the ACLOUD campaign, the instrumentation used to characterise the two selected case studies are being presented. Afterwards, the case studies are described along with each its unique feature, synoptic conditions, thermodynamical, radiation, and microphysical cloud properties.

2.1 ACLOUD campaign (Spring 2017)

The ACLOUD field study was conducted jointly with the PASCAL (Physical feedbacks of Arctic planetary boundary level Sea ice, Cloud and AerosoL) ship cruise campaign (Macke and Flores, 2018) in May and June 2017 (Wendisch et al., 2019). Both campaigns were conducted within the framework of the $(AC)^3$ project (Wendisch et al., 2022, 2017).

Collocated, process-oriented observations of a diversity of atmospheric and surface parameters were collected by instrumentation installed on the Polar 5 and Polar 6 aircrafts of the German Alfred Wegener Institute (AWI) (Wesche et al., 2016) (ACLOUD), an ice floe station including a tethered balloon, the research vessel and AWI icebreaker Polarstern, and from the ground-based site in Ny-Ålesund on Svalbard (Norway) (PASCAL). The archipelago of Svalbard (stretching from 76-81°N and from 10-28°E; see Figure 2.1) is a special location due to its high latitude, where there are frequent intrusions of warm air from the south and cold air from the Arctic Ocean. Also, this is an area where the climate is less cold than other Arctic regions.

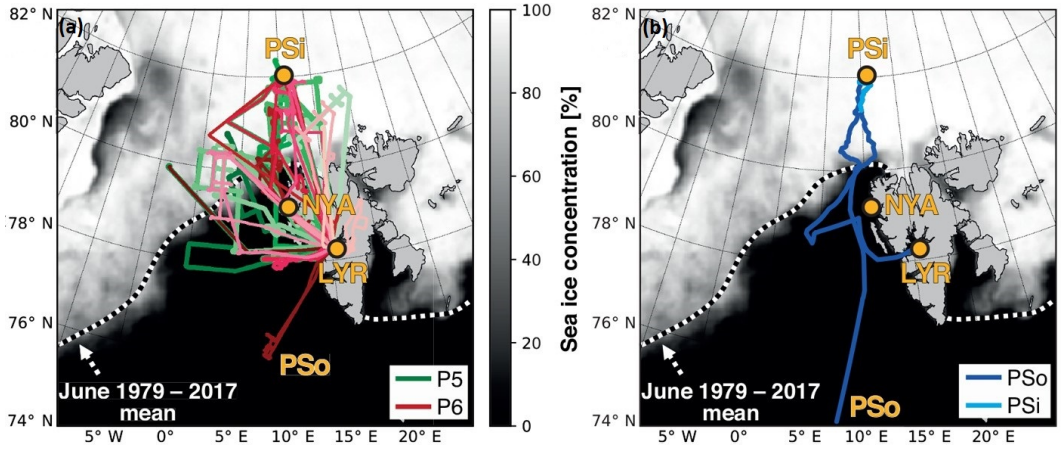

Figure 2.1: Overview of ACLOUD/PASCAL observations. (a) Tracks of the aircraft Polar 5 (green) and Polar 6 (red) flights during ACLOUD (23 May-26 June 2017), with later dates in brighter colours. (b) Track of icebreaker Polarstern: dark and bright colours indicate ocean-cruising (PSo; 30 May-5 June and 17-18 June 2017) and ice-attached (PSi; 6-16 June 2017) positions, respectively. LYR and NYA show the positions of Longyearbyen (LYR) and Ny-Ålesund (NYA) stations on Svalbard. The shading and the dashed line represent the average sea ice concentration over the ACLOUD/PASCAL measurement period and edge (defined by 15% concentration) over the 1979-2017 climatological period, respectively. Figure adapted from Knudsen et al. (2018).

The ACLOUD/PASCAL campaigns took place in the transition zone of the Greenland Sea and the Arctic Ocean between open ocean and sea ice. As the period of the campaigns was the spring period, the significant snow melt began impacting the radiative balance at the surface. Figure 2.1 shows the average sea ice concentration over the ACLOUD/PASCAL region during the measurement period (23 May-26 June 2017). Figure 2.1 also provides an overview of the tracks of the icebreaker Polarstern during PASCAL and of the Polar 5 and Polar 6 flights during ACLOUD. The area of flight activities extended to Ny-Ålesund and the marginal ice zone West of Svalbard, which were in reach of the aircraft. Within this area, five flights with Polar 5 and Polar 6 were

coordinated with A-Train satellite constellation overpasses to characterise the vertical structure of clouds (Stephens et al., 2002).

Using near-surface and upper-air meteorological observations, satellite, and ECMWF (European Centre for Medium-Range Weather Forecasts; Dee et al. (2011)) reanalysis data, Knudsen et al. (2018) provide an overview of the synoptic conditions during the ACLOUD/PASCAL measurement period. Relative to the long-term averages, three key periods representative of the distinct synoptic states were identified: a 7-days cold period (CP; 23-29 May), a 14-days warm period (WP; 30 May-12 June), and a 14-days normal period (NP; 13-26 June). During the CP, the Svalbard region was affected by a northerly cold air outbreak, which led to the development of low-level clouds over the warm open ocean. Over the Fram Strait (see Figure 1.1 for localisation), these clouds were organised in a roll convective structure, forming typical cloud streets. During the WP period a high pressure system south of Svalbard advected warm air from the south over the archipelago, leading to the development of a low-level, optically thick, and homogeneous stratocumulus (Ruiz-Donoso et al., 2020). Cold air outbreaks and warm air advections are phenomena often affecting the Arctic regions (Kolstad et al., 2009; Woods et al., 2013; Fletcher et al., 2016; Sedlar and Tjernström, 2017; Pithan et al., 2018). The NP is characterised by close-to-average temperate and moist air from a mixture of regions but dominated by adiabatically warmed air from the West. Figure 2.2 shows the temporal evolution of the vertical profiles of the temperature and the specific humidity for the three key periods of the campaign.

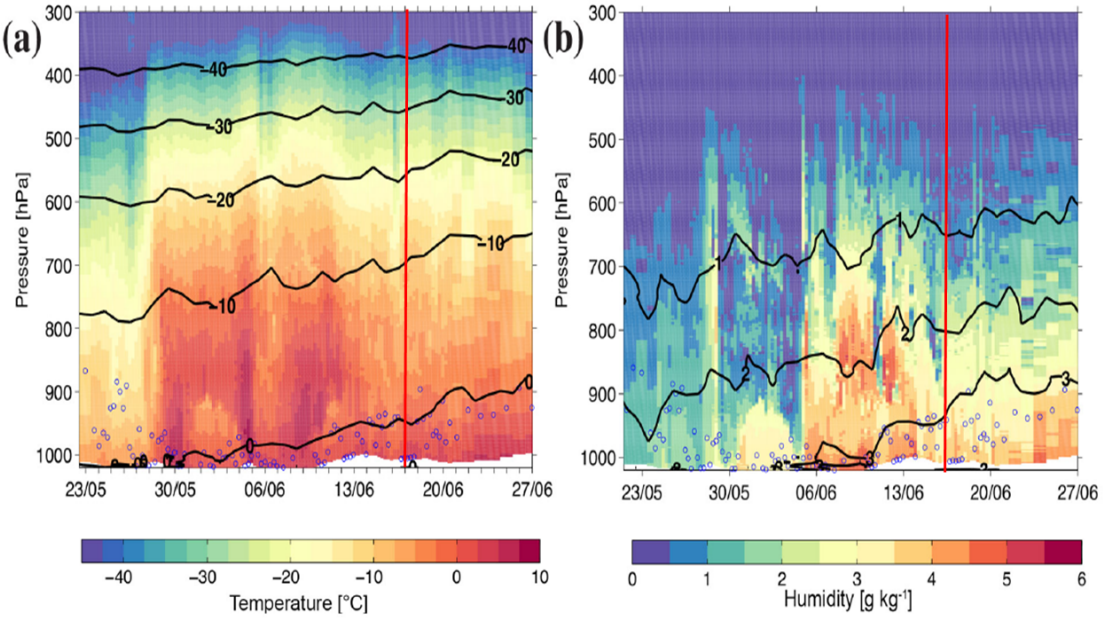

Figure 2.2: Vertical profiles of the temperature (a) and the specific humidity (b) measured at Ny-Ålesund over the ACLOUD measurement period (23 May-26 June). Black contour lines represent the respective 1993-2016 averages. Blue circles indicate an estimated of the height of the atmospheric boundary layer (Knudsen et al., 2018). The vertical red line represents the thermodynamical conditions for the cases studied hereafter. Figure adapted from Knudsen et al. (2018).

According to Knudsen et al. (2018), the marine cold air outbreak (MCAO) index, which is defined as the difference between the potential temperature at the surface and

at 850 hPa (Papritz et al., 2015; Kolstad, 2017), offers arguably a good understanding of the local weather. Figure 2.3 shows the temporal evolution of the MCAO index over the Eastern Greenland Sea obtained for the ACLOUD/PASCAL measurement period. A comparison with the MCAO index for the 1979-2016 climatological period illustrates the extreme variations in the weather conditions met during the 3 first weeks of the campaign.

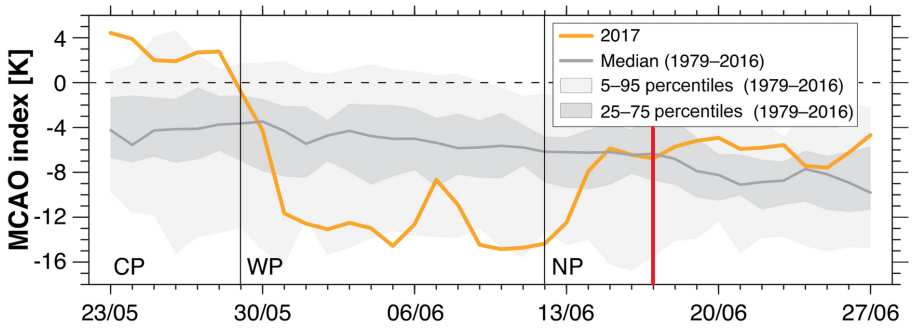

Figure 2.3: Marine cold air outbreak (MCAO) index for the Eastern Greenland Sea (75.00-80.25°N, 4.50-10.50°E) over the ACLOUD/PASCAL measurement period, based on Era-Interim reanalysis data (Dee et al., 2011) from the ECMWF. The grey median line and percentile shading refer to the climatology over 1979-2016, while the black vertical lines separate the three key periods (CP, WP, and NP) in 2017. The vertical red line represents the meteorological situation for the cases studied hereafter. Figure adapted from Knudsen et al. (2018).

During the CP, the values of the MCAO index mostly exceed the 95^{th} percentile of the climatology whereas they significantly drop below the median (even below the 25^{th} percentile of the climatology) during the WP. Note that the values of the MCAO are higher during the CP, showing a stable atmosphere with cold air mass intrusions. As one of the main objectives of this work is to analyse the cloud properties and improve cloud mesoscale modelling within the Arctic under regular conditions, the cases studied in this work (see Section 2.3) were chosen during the NP when measurements were available. The others periods have been studied recently by Moser et al., [submitted]; Zanatta et al., [submitted], Järvinen et al. [submitted]. Moreover, in order to study the possible impact of the surface type on the cloud properties, the observation data analysed throughout this thesis were collected during the ACLOUD flight 19 on the 17^{th} of June 2017 (see Figure 2.3), over sea ice as well as open ocean surfaces.

2.2 Instrumentation

This section presents the instruments used throughout this thesis. Observational data as provided as a function of time (in UTC), longitude, latitude, altitude and aircraft speed relative to the ground, by GPS (Global Positioning System) and the Inertial Navigation System (INS) of the aircraft. Sections 2.2.1 and 2.2.2 describe the instruments used within this work that were deployed on the Polar 5 and the Polar 6 aircraft, respectively.

2.2.1 Polar 5 aircraft

The Polar 5 aircraft was primarily operated as a remote sensing aircraft. Active radar and lidar observations were combined with passive spectral solar and microwave sensors. Profiles of meteorological parameters were collected by dropsondes. Technical details about the used instruments are given below:

AVAPS: The Advanced Vertical Atmospheric Profiling System was operated to release dropsondes of type RS904 (Ikonen et al., 2010). The dropsondes measure ***the vertical profiles of air temperature, humidity, pressure, and the horizontal wind vector*** between typical flight altitude of 3-4 km and the surface. The vertical resolution of the profiles is about 5 m, determined by the fall velocity of about 10 m s^{-1} and the sampling frequency of 2 Hz. A detailed overview of the specifications, data processing, and data are published in the World Data Centre PANGAEA (Ehrlich et al. (2019b)).

MiRAC: The MiRAC (Figure 2.4) radar package is composed of an active (MiRAC-A) and a passive (MiRAC-P) part for remote sensing: a single vertically polarised frequency-modulated continuous wave (FMCW) cloud radar (MiRAC-A) manufactured by RPG (Radiometer Physics GmbH; Küchler et al. (2017)) that provides the reflectivity factor Z_e (in mm^6 m^{-3}) at 94 GHz with an uncertainty of 0.5 dBZ (Mech et al., 2019) and a passive channel radiometer at 89 GHz (MIRAC-P) which allows to measure the radiance and the brightness temperature. Thus, the MiRAC-A permits to document the ***macrophysical structures of the sampled clouds (height, thickness)*** whereas the 89 GHz channel of the MiRAC-P, which is especially sensitive to the emissions of the surface and liquid clouds, can be used to retrieve the ***liquid water path*** over the open ocean, *i.e.* where the emissivity of the surface is low. The processed data of MiRAC-A was published in a combined data set (Kliesch and Mech (2019), https://doi.org/10.1594/PANGAEA.899565).

Figure 2.4: Left: MiRAC-A with opened belly pod below the research aircraft Polar 5. Figure adapted from Mech et al. (2019). Right: The AMALi system in zenith-pointing airborne configuration on board the Polar 5 aircraft. Figure adapted from Stachlewska et al. (2010).

AMALi: The active microwave profiling by MiRAC-A was complemented by the Airborne Mobile Aerosol Lidar (AMALi) system (Stachlewska et al., 2010) (Fig-

ure 2.4). This backscatter lidar has three channels: one unpolarised channel in the ultraviolet at 355 nm and two channels in the visible spectral range at 532 nm (perpendicular and a parallel polarised). The lidar has a vertical resolution of 7.5 m and a measuring frequency of 1 Hz averaged over a period of 5 s for a horizontal resolution of 375 m for a typical aircraft flight speed of 270 km h^{-1}. AMALi provides cloud features such as ***the height of the cloud top*** which can be identified as the attenuated backscatter channel at 532 nm.

2.2.2 Polar 6 aircraft

The Polar 6 aircraft was primarily equipped with in-situ instruments characterising aerosol particles, cloud droplets, ice crystals, and trace gases. Descriptions of the in-situ probes that provide the data analysed throughout this thesis are given below:

CDP-2: The Cloud Droplet Probe (CDP) is composed of a direct diffusion optical spectrometer (between 2 and 5 μm) using a 0.658 μm wavelength laser diode (Figure 2.5) and anti-shattering tips to avoid artefacts caused by the shattering of large ice crystals on the instruments tips. The sampling frequency is 1 Hz. The instrument counts and sizes individual water droplet, sizes are accumulated in 30 bins with variable widths. For ACLOUD, a 1 μm bin width was chosen for small droplet sizes from 2 to 14 μm, while larger cloud droplets with a diameter from 16 to 50 μm were collected in 2 μm bins. The diameter of the droplets is deduced from the theory of Mie (scattering cross section to diameter relationship) and ***droplet number size distribution (DSD)*** is corrected using a Monte Carlo inversion method (see details in Ehrlich et al. (2009)). Microphysical quantities such as the ***LWC***, the ***concentration of droplets*** N_{drop} and the ***effective droplet diameter*** D_{eff} can be derived from the DSD.

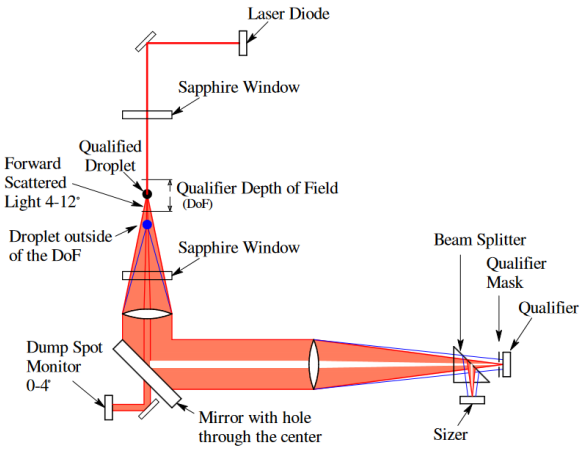

Figure 2.5: Optical schematic of the CDP. Light rays coloured in red indicate the scattering signal for a droplet within the qualifier DoF (Depth of Field), whereas blue light rays indicate a droplet outside of the qualifier DoF. For the qualified droplet, the scattered light is focused through the slit of the qualifier mask, allowing the qualifier signal to be great enough such that the particle is counted. Figure from Lance et al. (2010).

CIP: The Cloud Imaging Probe (CIP), which is an optical array probe (OAP, Knollenberg (1976)), measures the size and the shape of cloud particles (Baumgardner et al., 2011) providing the ***particle size distribution (PSD)*** as well as the ***ice concentration*** N_{ice}. It has a sampling frequency of 1 Hz. The CIP has nominal size range of 25 to 1550 μm with a resolution of 25 μm. An assumed a relationship (given by (Brown and Francis, 1995)) between the diameter (D) and the mass (m) of the crystals [$m(D) = aD^b$ where m is given in kilograms, D in m, and the constants a and b are respectively equal to 0.0185 and 1.9] allows the ***IWC*** to be deduced using the Equation 2.1, where the summation is over the range of particle sizes recorded by the CIP (Brown and Francis, 1995).

$$IWC = \sum_{D_{min}}^{D_{max}} n(D)m(D) \tag{2.1}$$

Non-spherical ice crystals were separated from liquid droplets based on their circularity parameter (circularity larger than 1.25 and image area larger than 16 pixels) following the approach developed by Crosier et al. (2011). Only these non-spherical particle images were used for the computation of the ice phase properties. Possible contamination of shattering and splashing of ice and liquid particles on the instruments' tips have been identified and removed using interarrival time statistics and image processing (Field et al., 2006).

Depending on the application, different definitions of the particle diameters can be applied when calculating the PSD. Figure 2.6 displays several possible diameters that can be used. For example, using the binary image of the measured crystals, two simple dimensions can be derived from the dimensions of a rectangular box that fully encloses the particle image (Lawson, 2011): the size D_y is the box dimension along the direction of the photodiode array and D_x is the box dimension along the perpendicular direction (along the axis of the forward movement of the aircraft). The resulting mean of the box lengths D_x and D_y, $D_m = (D_x + D_y)/2$, is called the mean chord length. In this study, D_{max} is used (Figure 2.6, in red), which is the maximum dimension originating from the image centre of gravity (see Leroy et al., 2016). It was used in previous studies performed over the Arctic region (*e.g.* as in Jourdan et al., 2010). Others diameters can be used as the equivalent diameter (D_{eq}) which corresponds to the diameter of the circle that has the same surface as the particle image, $A = (\pi/4)D_{eq}^2$ (McFarquhar and Heymsfield, 1996). Vaillant de Guélis et al. (2019) show that D_{eq} is the least subjected to error in sizing due to out-of-focus deformation of the image. Also there is the circumpolar diameter (D_{cc}) which is the diameter of the circle encompassing the particle image. This is the diameter used in the Brown and Francis (1995) mass-diameter relationship. Ehrlich et al. (2019a) showed using a comparison of averaged PSD calculated using the three different options for the assumed particle diameter that there are no significant differences between each calculated PSD.

A complete description of the data processing, including a discussion of the applied mass-diameter relationships can be found in Leroy et al. (2016). In the CDP-2 and CIP data sets published in the PANGAEA database (Dupuy et al. (2019), https://doi.org/10.1594/PANGAEA.899074), the PSDs of all instruments are stored separately.

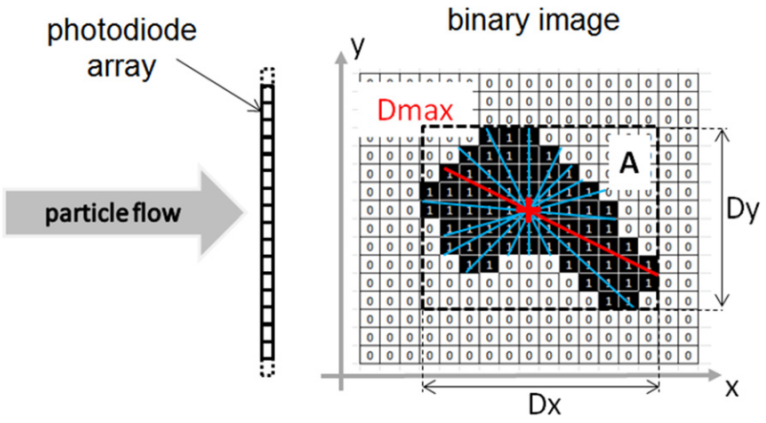

Figure 2.6: Definition of particle dimensions that are extracted from OAP (Optical Array Probe) binary images. Blue lines illustrate some possible diameters passing through the centre of the image, whereas the red line highlights the longest one, which is defined in this study as the maximum dimension (D_{max}). Figure from Leroy et al. (2016).

Moreover, in order to study the aerosol-cloud interactions, several instruments were deployed on-board the Polar 6 aircraft. These instruments provide the aerosol particle size distributions (APSDs) and concentrations. The ***CCN and INP concentrations*** are also available. All aerosol particle sizes measured during ACLOUD refer to dry aerosol because most particulate water evaporates in the sampling lines connecting the inlets and the instruments due to the higher temperature inside the aircraft cabin. Details about the instruments are given below:

UHSAS: The ultra-high sensitivity aerosol spectrometer (UHSAS) measures the number size distribution of particles (Cai et al., 2008) with diameters between 60 and 1000 nm, by detecting scattered laser light divided in 100 user-specified size bins of variable size (2-30 nm resolution). From these measurements, the mean particle diameter and the particle number concentration of a defined size range can be derived. During ACLOUD, two UHSAS were operated either at different inlets (for simultaneous measurements) or at the same inlet (for intercomparison), the UHSAS-1 and the UHSAS-2 could reliably detect particles larger than 60 and 80 nm, with a sampling frequency of 3 s and 1 s, respectively. The flow rate was set to 50 mL min^{-1}.

CPC: The condensation particle counter (CPC TSI-3010) measures the total particle number concentration (Mertes et al., 1995), via a light-scattering technique after creating aerosol droplets inside the instrument large enough for detection (using butanol to make the drops grow and detectable). In this way, number concentration of particles down to diameters of 10 nm and up to 3 μm (limit of the CPC) were measured at a sample flow of 1 L min^{-1}.

CVI: The counterflow virtual impactor (CVI) was applied to capture exclusively non-precipitating cloud particles inside the cloud and to release their cloud residual particles for aerosol analysis (Ogren et al., 1985; Twohy et al., 2003), which are the dry particles that remain after the evaporation or sublimation of cloud droplets or ice particles, respectively. They are closely related to the CCN and INP that form the clouds. The cloud particle collection is achieved by blowing a so-called counter-

flow out of the CVI inlet tip. As a consequence, interstitial gases are completely deflected from the inlet and smaller interstitial particles that are not activated to cloud droplets or did not nucleate ice particles are considerably decelerated, stopped, and blown out of the inlet. Only larger particles could overcome the counterflow and are sampled by the CVI. The minimum cloud particle size that is collected by the CVI is determined by the air velocity at the inlet tip (true air speed of Polar 6) and the amount of the counterflow. Due to the rather low air speed of Polar 6, the adjustment of the counterflow to about 2 L min^{-1} could minimize the lower cut-off diameter to only 8 μm, which is slightly higher than reported in previous operations of the CVI inlet (Schwarzenboeck et al., 2000). Therefore, the cloud droplet residuals (CDR) could not be sampled for the complete cloud droplet population (Mertes et al., 2005). From time to time the counterflow was raised to 12 L min^{-1}, in order to sample only the large hydrometeors in the cloud, which increased the lower cut-off size between 22 and 24 μm (more details in Ehrlich et al. (2019a)).

The CVI only provides particle separation but does not directly measure aerosol concentrations. The UHSAS or CPC are connected to CVI in order to measure the aerosol concentrations.

CMP 22 Pyranometers and CGR4 Pyrgeometers: pairs of CMP 22 pyranometers and CGR4 pyrgeometers were used to measure upward and downward broadband irradiances, covering the solar (0.2 - 3.6 μm) and thermal-infrared (4.5 - 42 μm) wavelength range, respectively. Both aircraft, Polar 5 and 6, were configured with an identical set of instruments and sampled with a frequency of 20 Hz. In stationary operation, the uncertainty of the sensors is less than 3% (Grobner et al., 2014).

2.3 One flight, two case studies

According to Young et al. (2016) the microphysics of single-layer mixed-phase stratiform clouds can significantly change over the transition from sea ice to ocean (see Figure 1.3). In this framework, two case studies were chosen to investigate cloud properties developing over sea ice as well as over open ocean using cloud scale modelling. We choose to analyse the cloud properties observed on the 17^{th} of June in 2017 during the Arctic regular conditions (during the normal period (NP) defined by Knudsen et al. (2018); see Section 2.1) which corresponds to the ACLOUD flight 19. Note that this flight was not coordinated with the A-Train satellite constellation and the Polarstern was far from the flight trajectory (see Figure 2.7a). However, this flight has the benefit of cover both sea ice and open ocean surfaces (see Figure 2.7a). Figure 2.7a illustrates the flights paths in red and yellow for Polar 5 and Polar 6, respectively. Moreover, the Figure 2.7a shows the positions of the different dropsondes released from the Polar 5 during the flight 19. The analyses of the modelled cloud properties described in the chapters hereafter will be done on two specific domains which cover the two flight parts of interest: one domain over sea ice area (hereafter called SI) defined between 80.25°N - 80.38°N and 1.0°E-3.0°E (blue rectangle in Figure 2.7), and one domain over open ocean (hereafter called OO) defined between 78.21°N - 78.33°N and 5.34°E - 7.15°E (green rectangle in Figure 2.7). Note that dropsondes were also released in the vicinity of both considered domains.

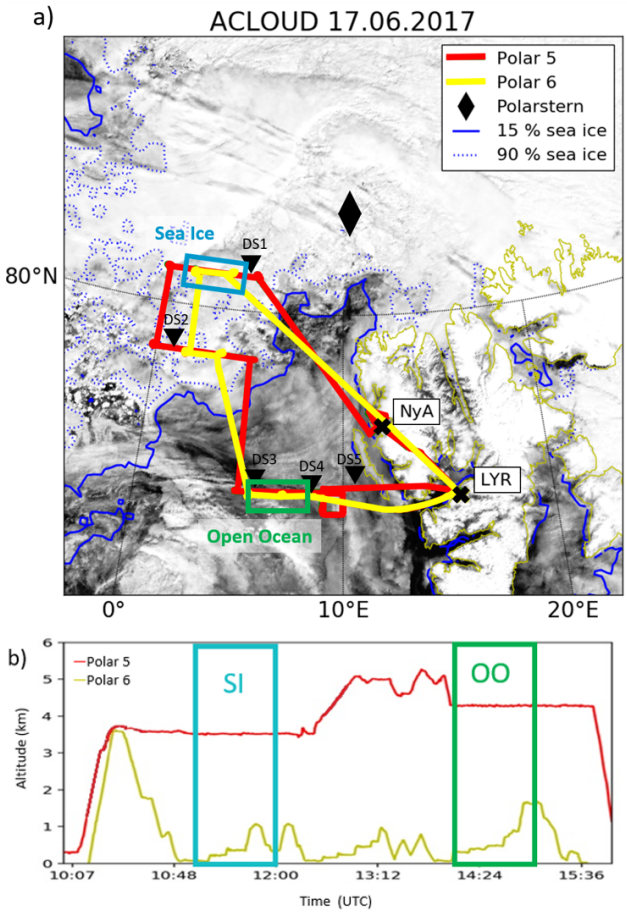

Figure 2.7: Flight paths (a) and altitudes (b) for the Polar 5 aircraft (in red) and for the Polar 6 aircraft (in yellow) done on the 17^{th} of June 2017, *i.e.* ACLOUD flight 19. The rectangles in blue and in green represent the domain analyses for, respectively, the SI case study and the OO case study described in chapters hereafter. On panel a), the solid and dotted blue lines indicate the 15% and the 90% sea ice concentration (derived from the AMSR2 measurements (Ludwig et al., 2019)), the shading represents the cloud cover (visible image from MODIS), the locations where the dropsondes (DS) were released are marked thanks to the black triangles, and the position of the Polarstern is represented by the black diamond. Figure adapted from the ACLOUD flight report.

Figure 2.7b shows the flight altitudes for both Polar 5 and Polar 6 aircrafts on the 17^{th} of June in 2017. During the whole flight, the Polar 5 flew at higher altitudes than the Polar 6, with an average altitude of 3.5 km or 4.5 km for the two regions of interest (rectangles in green (OO) and in blue (SI) in Figure 2.7b). Note that during both periods, the Polar 5 performed round-trips over the SI and the OO domains. In addition to the dropsondes, as the remote sensing instruments were on-board the Polar 5, the available observations will allow us to characterise the vertical thermodynamical properties of the atmosphere (dropsondes) and the vertical structure of the clouds (lidar and radar).

Polar 6 aircraft flew at altitudes lower than 1.5 km for both regions of interest (see Figure 2.7b). In order to well sample the profiles of clouds formed close to the surface, the Polar 6 aircraft realised horizontal paths (of approximately 15 Nautical Miles (NM)) at several constant altitude steps called horizontal legs or staircase patterns

(see Figures 2.8a and b for SI and OO situations, respectively). According to the chosen legs, the distribution of measurements is not homogeneous on the height of the cloud. Thus, many measurement points are available along the legs whereas it is not the case for the parts where the aircraft changes its altitude.

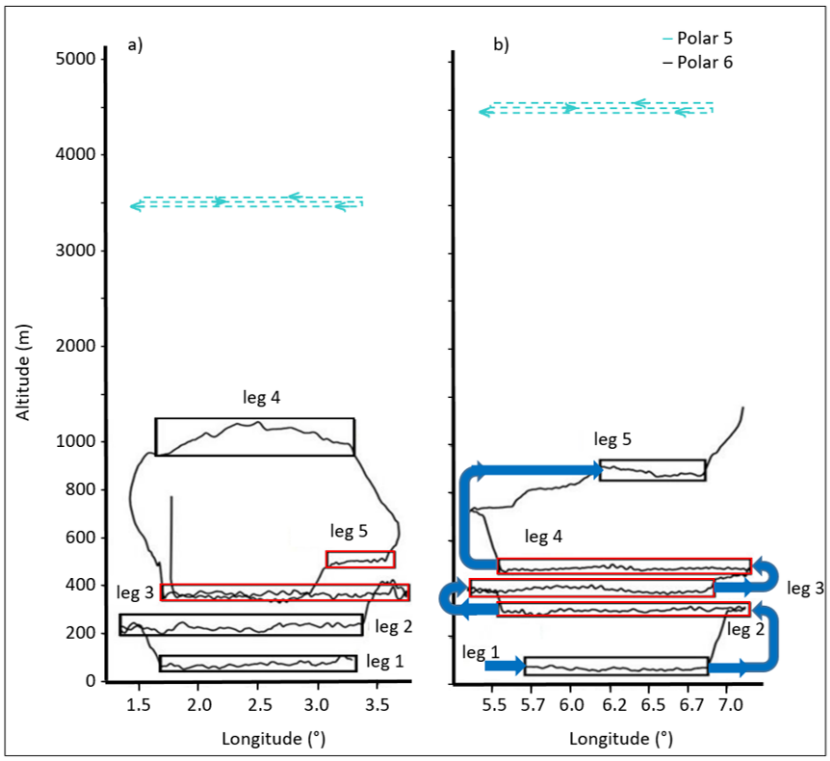

Figure 2.8: The racetrack flight pattern of the aircraft Polar 5 and Polar 6 over: a) sea ice (SI) and b) open ocean (OO) domains. Cyan lines correspond to the three horizontal paths (back and forth) performed by the Polar 5 aircraft at several constant altitudes. Black lines correspond to horizontal paths realised by the Polar 6 aircraft. The red rectangles correspond to the legs which were performed inside the clouds whereas the others legs were performed above clouds top or within the precipitation layer according to the flight reports.

To better characterise the surface type (and so identify the surface properties for both the SI and the OO cases), a cloud-free surface albedo α_{cf} was calculated based on solar radiation (SW) (Stapf et al., 2020, 2019a,b). Figure 2.9 shows the derived cloud-free surface albedo for the coordinates of the ACLOUD flight 19. The cloud-free surface albedo is quite variable according to the type of the surface. Over sea ice, where $SW_{u,Surf.}$ is important, the values for α_{cf} vary between 0.5 and 0.9 whereas over the ocean (where more $SW_{d,Surf.}$ is absorbed), they drop between 0.15 and 0.4. Moreover, if we focus on the modelling domains used in the following chapters, the surface albedo is on average equal to 0.72 over the SI domain (blue rectangle) and to 0.21 over the OO domain (green rectangle). Also, note that the mean albedo calculated over sea ice surface ($\approx$ 0.79) (grey area in Figure 2.9) of the ACLOUD flight 19 is smaller than the mean albedo observed over the same surface type ($\approx$ 0.82) during the N-ICE (*Norwegian Young Sea Ice*) campaign which took place in January-June 2015 at the North of the Svalbard archipelago (Walden et al., 2017). Seasonal and geographical variations associated to the reduction of the extent of sea ice and local phenomena such as different meteorological conditions (*e.g.* snowfalls) could explain the difference

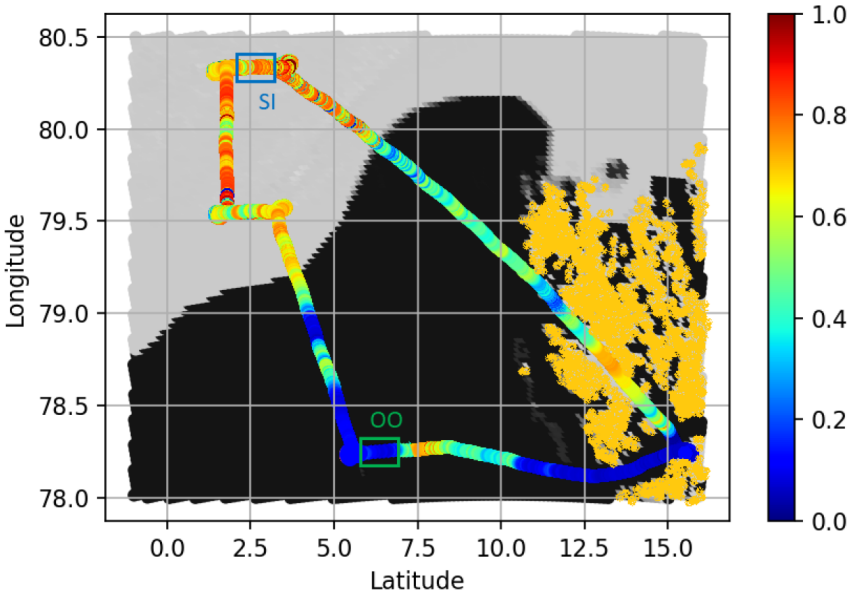

Figure 2.9: Cloud-free surface albedo α_{cf} calculated for the coordinates of the ACLOUD flight 19 from the upward- and downward-looking pyranometers and pyrgeometers. The processed data were merged and published in a combined data set (Stapf et al. (2019a), https://doi.org/10.1594/PANGAEA.900442). The black and grey backgrounds correspond to, respectively, the open ocean and the sea ice cover whereas the rectangles in blue and in green represent the modelling domains of both the SI and the OO cases.

obtained in the surface albedo between ACLOUD and N-ICE.

2.3.1 Synoptic conditions of both case studies

The synoptic situation was analysed for both case studies, based on the operational reanalysis data of the ECMWF ERA-5 were used (Copernicus Climate Change Service (C3S), 2017). These data are provided on a 0.25° × 0.25° horizontal grid. To illustrate the synoptic conditions for the 17 June 2017, weather charts are shown in Figures 2.10 and 2.11 for key heights at 12:00 UTC.

Figure 2.10 presents the sea surface pressure in addition to the 750 hPa geopotential height. Three low (L) pressure systems are present over the region: the first one centred over Iceland, the second one (less intense) on the Baffin Sea at the West of Greenland, and the third one at the North-East of the Svalbard archipelago. A little marked high (H) pressure system is also present on Northern Europe. Figure 2.10 permits to identify the main air masses close to these different pressure systems at 750 hPa: a polar air mass descending from the North Pole towards the Svalbard latitudes (blue arrows), and a temperate air mass coming from the North Atlantic Ocean via the Norwegian Sea (red arrows).

Figure 2.11 shows weather charts for temperature (T) and relative humidity with respect to liquid water (RH) also obtained thanks to the ECMWF ERA-5 operational reanalysis data at different geopotential heights. Note that in January, during the Arctic night (or winter), the temperature close to the surface is in average equal to 255 K which is much lower than the spring temperatures observed during the ACLOUD campaign. In

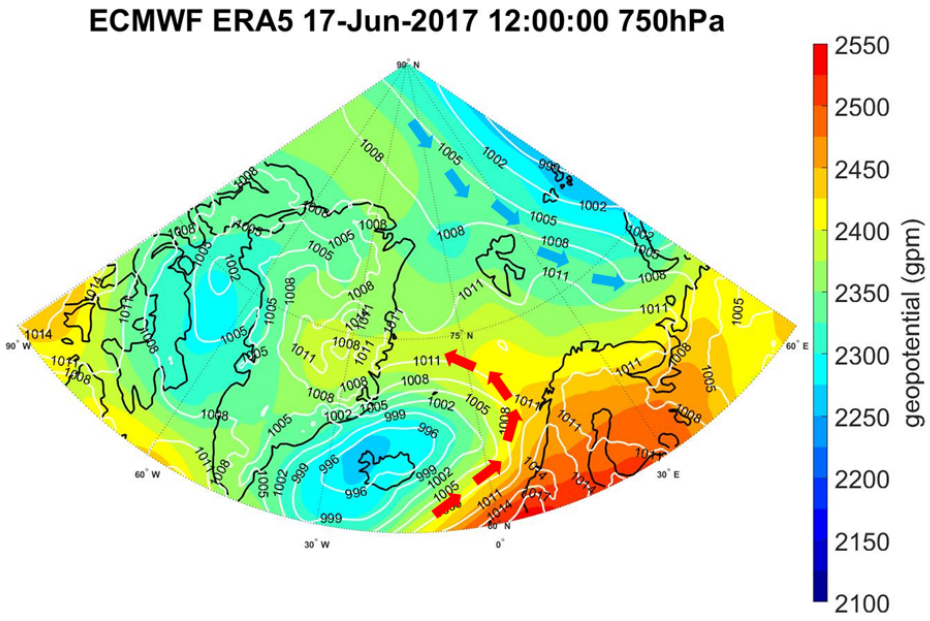

Figure 2.10: ECMWF ERA-5 at 750 hPa geopotential height (in meters; shading) on 17 June 2017 at 12:00 UTC. The figure also presents the sea level pressure (in hPa; white contours). Blue and red arrows represents air masses coming from the North Pole and the North Atlantic Ocean, respectively.

fact, the temperature at 1000 hPa is relatively uniform and equals to ≈ 272 K on average over the ACLOUD flight 19 area (see white rectangle in Figure 2.11a). Figures 2.11a-c show that the temperature at 1000 hPa, 950 hPa, and 750 hPa becomes colder in average when the latitude increases (*i.e.* towards the North Pole). However, higher temperatures can be locally visible around the ACLOUD flight 19 area compared to the mean temperature present in the surrounding area, such as over the North of the Greenland and at the North of the Svalbard archipelago, where the increase in the temperature field can reach up to 7 K. Also, cooler air can locally be present as at 750 hPa within the ACLOUD flight 19 area (Figure 2.11c).

Figures 2.11d-f show that the relative humidity (RH) field is not very variable at 950 hPa and 1000 hPa, but it becomes more variable and heterogeneous at 750 hPa. Above sea ice or open ocean (*i.e.* zones without any reliefs), the RH is more uniform over the Northern Arctic than over the Southern parts of the Arctic both at 1000 hPa and 950 hPa. At 750 hPa, the variabilities in the RH field are more marked. For example, the RH is in average equals to 85% over the ACLOUD flight 19 area and decrease sharply around this area (*e.g.* to $\approx$ 40% or $\approx$ 50% at the South or the North, respectively). Humidity differences are associated with synoptic situation shown in Figure 2.10. Note that the warmer local temperatures identified over the North of the Greenland and at the North of the Svalbard archipelago are associated to dry conditions at 1000 hPa, 950 hPa and 750 hPa. Far from the area of study, the RH can decrease to lower values, as *e.g.* over Northern Europe where RH values drop to 20% at 1000 hPa and 950 hPa (Figures 2.11d-e). Figures 2.11d-f permit to identify saturation spots (where $RH = 100\%$) within the ACLOUD flight 19 area at 950 hPa and 750 hPa suggesting the presence of clouds at these levels.

According to Figures 2.10 and 2.11, the synoptic conditions for the 17^{th} of June at

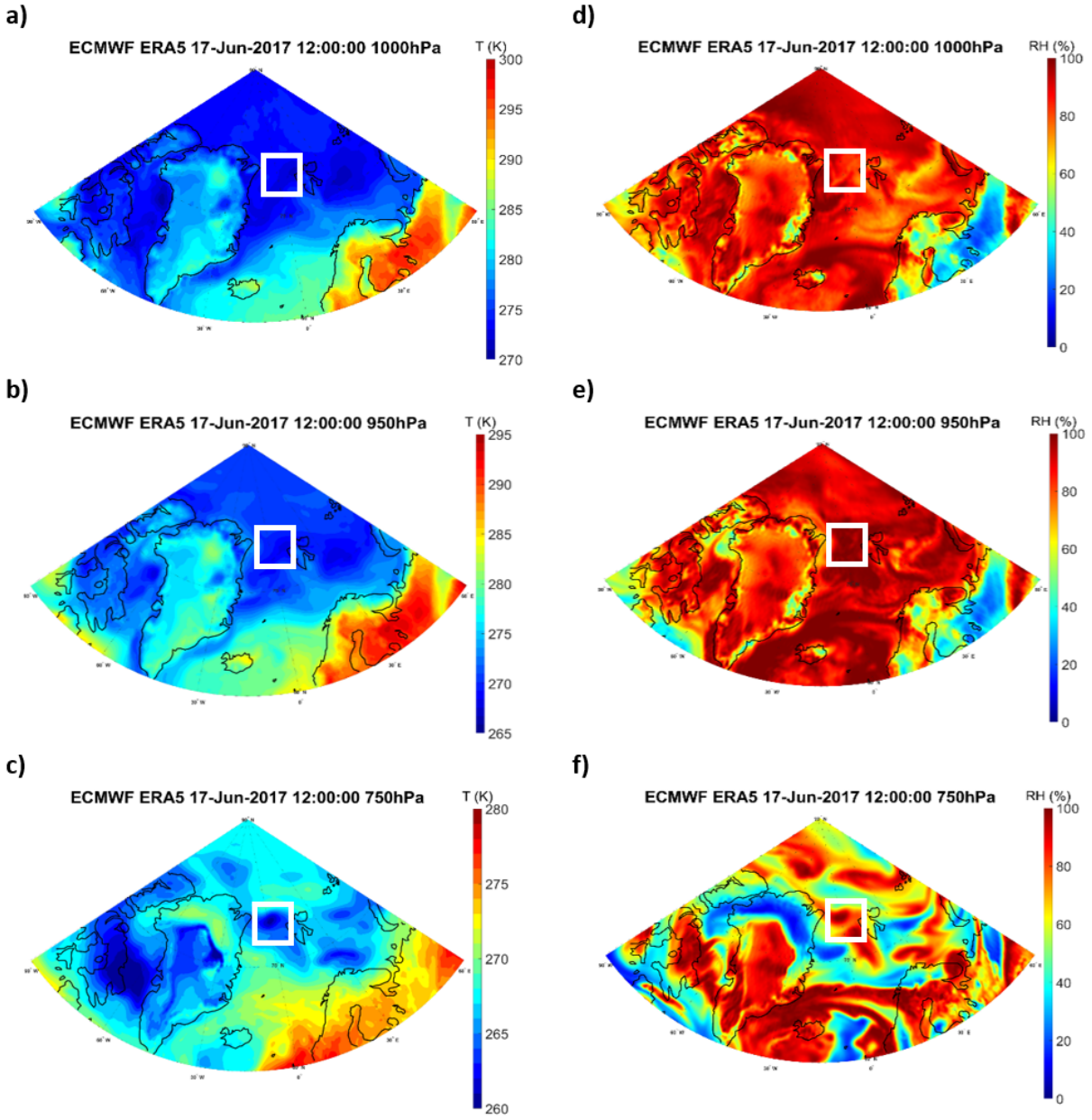

Figure 2.11: Temperature (in K) (a-c) and relative humidity with respect to liquid water (RH) (in %) (d-f) at the 1000 hPa (a,d), the 950 hPa (b,e) and the 750 hPa (c,f) geopotential heights.

12:00 UTC reveal the presence of two main air masses around the Svalbard archipelago: one cold air mass coming from the North and the other one from the South (*i.e.* from the North Atlantic Ocean). The latter air mass regularly observed (Tjernström and Graverson, 2009; Yu et al., 2019) brings moisture and heat (Dufour et al., 2016; Sorteberg and Walsh, 2008; Woods et al., 2013) causing temperature and humidity variations, instabilities and weather changes which promote cloud formation and persistence on the Svalbard region (Savre et al., 2015). However, the analyses of the synoptic conditions also reveal a particular situation for this date. A local cool area is visible in Figure 2.11c within the ACLOUD flight 19 zone as well as a warm and dry air at the North of the Svalbard; conditions that are not very common in the region and which could impact the cloud formation and evolution.

2.3.2 Sea Ice (SI) case study

Observations obtained from instruments on-board the Polar 5 and Polar 6 aircraft (described in Section 2.2) over the SI domain (see blue rectangles in Figure 2.7) are discussed in this section. We recall that the Polar 5 aircraft flew at higher altitudes than the Polar 6 aircraft. The Polar 5 aircraft made return-trips over the domain whereas the Polar 6 flight was composed of 5 legs within the sampled clouds (see flight schematic in Figure 2.8a). The in-situ observations of Polar 5 and Polar 6 presented hereafter focus on the legs 3 and 5, which were done inside of cloud. According to the flight reports, legs 1 and 2 were done inside a precipitation layer, and the leg 4 was done above the clouds.

a) Thermodynamic and macrophysical properties

As described in the Section 2.2.1, the dropsondes released from the Polar 5 aircraft permit to characterise the vertical thermodynamic properties. During the flight 19, several dropsondes were launched. One of them was released over sea ice surface, close to the SI domain. The position of this dropsonde is approximately at 80.3°N and 4.6°E, and the corresponding time is 11:20 UTC (see DS1 position in Figure 2.7a). Figure 2.12 presents the skew-T log-P diagram obtained with the DS1 measurements, *i.e.* the profiles of the dew point temperature T_d (in blue dashed line), the temperature T (in red line), and the horizontal wind v_h properties (barbs).

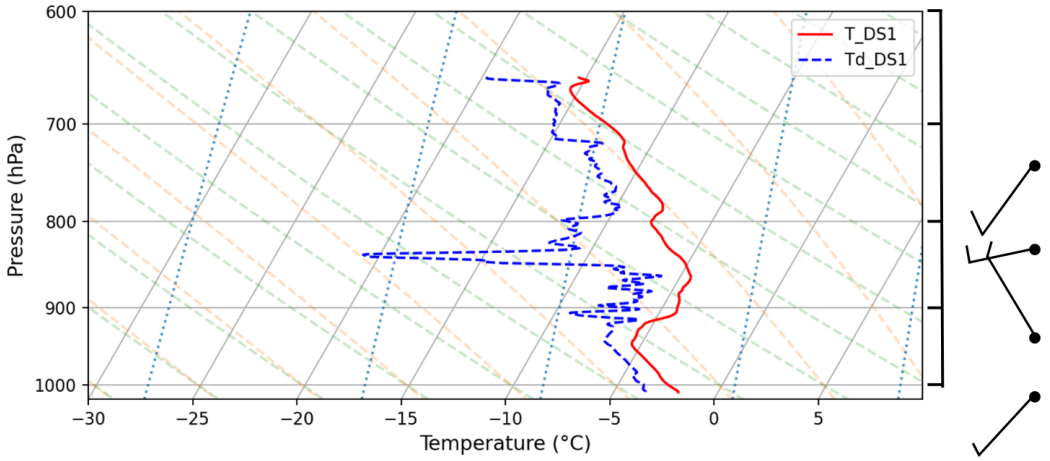

Figure 2.12: Temperature T (red solid line) and dew point temperature T_d (blue dashed line) profiles from the dropsonde (DS1) released during flight 19 over sea ice (SI) at 11:20 UTC(see DS1 position in Figure 2.7a). The barbs show the vertical properties of the wind speed and direction.

Figure 2.12 shows that the temperature close to the surface is equal to -2.5°C. Then the temperature decreases with the altitude up to 950 hPa (≈ 500 m) where, at this level, there is a temperature inversion until approximately 875 hPa (≈ 1200 m), with an isotherm condition ($T \approx$ -6°C) between 950 hPa and 925 hPa (*i.e.* 500-750 m). At altitudes above the 875 hPa level, the temperature decreases with the altitude except for the 800-775 hPa layer (at about 2000 m altitude) where a second temperature inversion is observed. This latter temperature inversion is nevertheless less intense than the one

present at lower altitudes. The dew point temperature is equal to -4°C at the surface. Then all along the profile, the dew point temperature follows closely the temperature of the air, except between 870 hPa and 800 hPa (≈ 1250-1950 m). Thus, the atmosphere is quite humid on almost all the profile (also reproduced within the ERA-5 product at 1000 hPa, 950 hPa and 750 hPa; see Figures 2.11d-f). Using this skew-T log-P diagram, the Lifting Condensation Level (LCL) can be estimated at approximately 980 hPa, *i.e.* at ≈ 200 m altitude. Due to the temperature inversion at 950 hPa, we can assume that low-level thin clouds could be present over the SI surface, which is confirmed by the radar reflectivity measurements in Figure 2.13. Moreover, according to the humid conditions (95%) observed at the highest altitudes of the DS1, we can suppose a second cloud layer for this case study at levels above 800 hPa (≈ 2000 m altitude).

In this framework, thanks to the reflectivity[1] field (Z) obtained using the 94 GHz MIRAC-A radar that was on-board the Polar 5 aircraft permits to identify clearly the two cloud layers (Figure 2.13). Indeed, Figure 2.13 which presents the temporal evolution of the vertical profile of the radar reflectivity shows two types of clouds: low-level clouds (200-600 m) with precipitating ice and maybe droplets close to the cloud top and mid-level clouds (1500-3500 m) with vertical bands of Z which could be associated to precipitating ice crystals. Figure 2.13 also illustrates the observations obtained by the AMALi Lidar (see Section 2.2.1), which gives the altitude of the cloud top.

b) Air mass origin and aerosols properties

As described by Gultepe et al. (2000) and Gultepe and Isaac (2002), Arctic cloud properties are strongly linked to the air mass origin. For these reasons, we also studied the air mass origin for the two different cloud layers occurring in the SI case. This study was performed using a 3D kinematic trajectory code, the CAT model (Computing Advection-interpolation of atmospheric parameters and Trajectory tool; Baray et al. (2020)). This model can be used in a backward mode that permits back-trajectory analysis. CAT is initialised with the wind fields from the ERA-5 reanalysis data provided by the ECMWF organisation (Hersbach et al., 2018a,b) and generated using the Copernicus Climate Change Service information. The back-trajectories are calculated over 72 hours using this dynamical product over a topography matrix with a horizontal grid resolution of ≈ 10 km, and a spatial resolution of 0.25° in latitude and longitude, calculated every 3 hours. The number of vertical levels were 20 between 1000 hPa and 300 hPa.

To perform this back-trajectory study, a suitable start point in time and space have to be chosen for the two cloud layers. The spatial and temporal coordinates were defined according to the flight trajectory, and the radar observations where the altitudes of both cloud layers are visible (see Figure 2.13). In this way, two sets of back-trajectories were performed: one set to study the low-level cloud layer using as start point the position of the Polar 5 aircraft at 11:00 UTC and an altitude of 500 m and another set to study the mid-level cloud layer using the same position but with a higher vertical coordinate, *i.e.* 2800 m.

For the SI case, the air masses at the origin of the both cloud layers are from

[1]The radar reflectivity Z in dBZ is obtained using the Z_e in mm^6 m^{-3} via the following expression: $Z = 10\ log_{10} Z_e$.

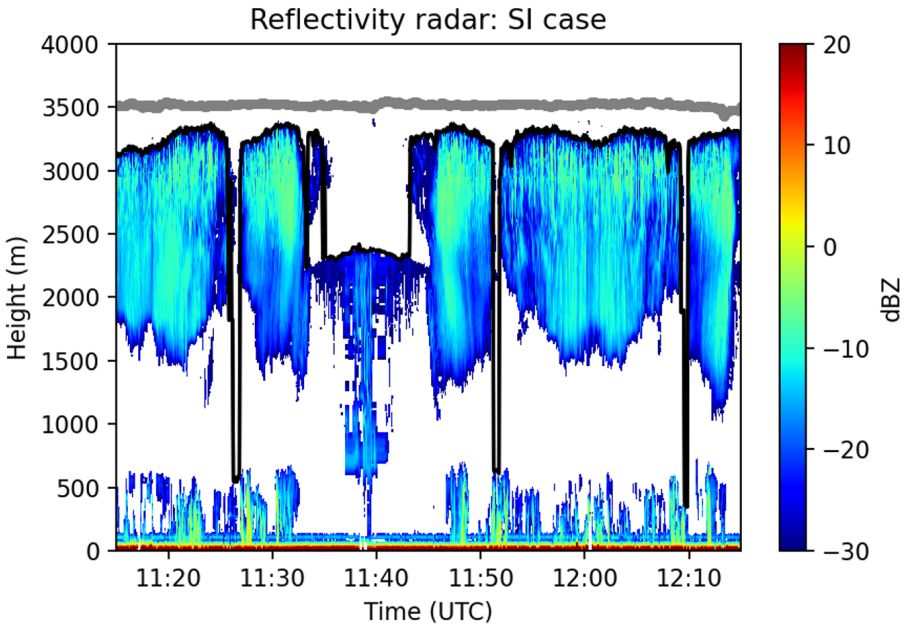

Figure 2.13: Temporal evolution of the profile of the radar reflectivity obtained with the 94 GHz MIRAC-A cloud radar system (in dBZ; colour scale) and of the cloud top determined by means of the AMALi lidar system (black solid line represents the altitude of the cloud top) over the SI surface. These both remote sensing systems were on-board the Polar 5 aircraft whose flight altitude is described with the grey solid line. Note that the Polar 5 aircraft performed a round-trip over the SI domain (see Figures 2.7 and 2.8a for the Polar 5 and Polar 6 flight paths). The processed data of MiRAC-A and AMALi were merged and published in a combined data set: https://doi.org/10.1594/PANGAEA.899565 (Kliesch and Mech, 2019), and https://doi.org/10.1594/PANGAEA.899962 (Neuber et al., 2019), respectively.

the North and the North-North-East of the Svalbard (Figures 2.14a and d) following approximately a constant altitude for each cloud layer. Figure 2.14b shows that the temperature of the air mass at the origin of the low-level clouds decreases due to a mixture with another air mass, meaning that at 500 m altitude the air is warmer close to the North Pole (274 K) than close to the Svalbard archipelago (270 K). This trend reflects the particular situation already identified during the analyses of the synoptic conditions (see Figure 2.10). Figure 2.14e shows that at 2800 m the temperature of the air mass at the origin of the mid-level clouds follows the same trend: the temperature decreases from 268 K to 263 K towards the Svalbard archipelago. Figure 2.14c shows that at 500 m the humidity of the air mass is constant during all trajectory, instead at 2800 m in Figure 2.14f we can see an increase of humidity from 40% to 90% towards the Svalbard archipelago.

The back-trajectories analysis permits to show that the northerly air masses at the origin of both cloud layers pass neither over industrial areas nor over land surfaces, but stay over sea ice surfaces (see Figure 2.7a). This can explain the quite clean atmospheric properties observed for the SI case (Figure 2.15) with the CPC instrument (*i.e.* particles > 10 nm) deployed on-board the Polar 6 aircraft (see Section 2.2). Figure 2.15a shows that the temporal evolution of the aerosol particle (AP) concentration $N_{AP,SI}$ is quite variable, by about 4 orders of magnitude, for the SI case. The median value for the $N_{AP,SI}$ is equal to 13 cm^{-3}, which is smaller than the median obtained for the whole campaign (240 cm^{-3}) (Wendisch et al., 2019).

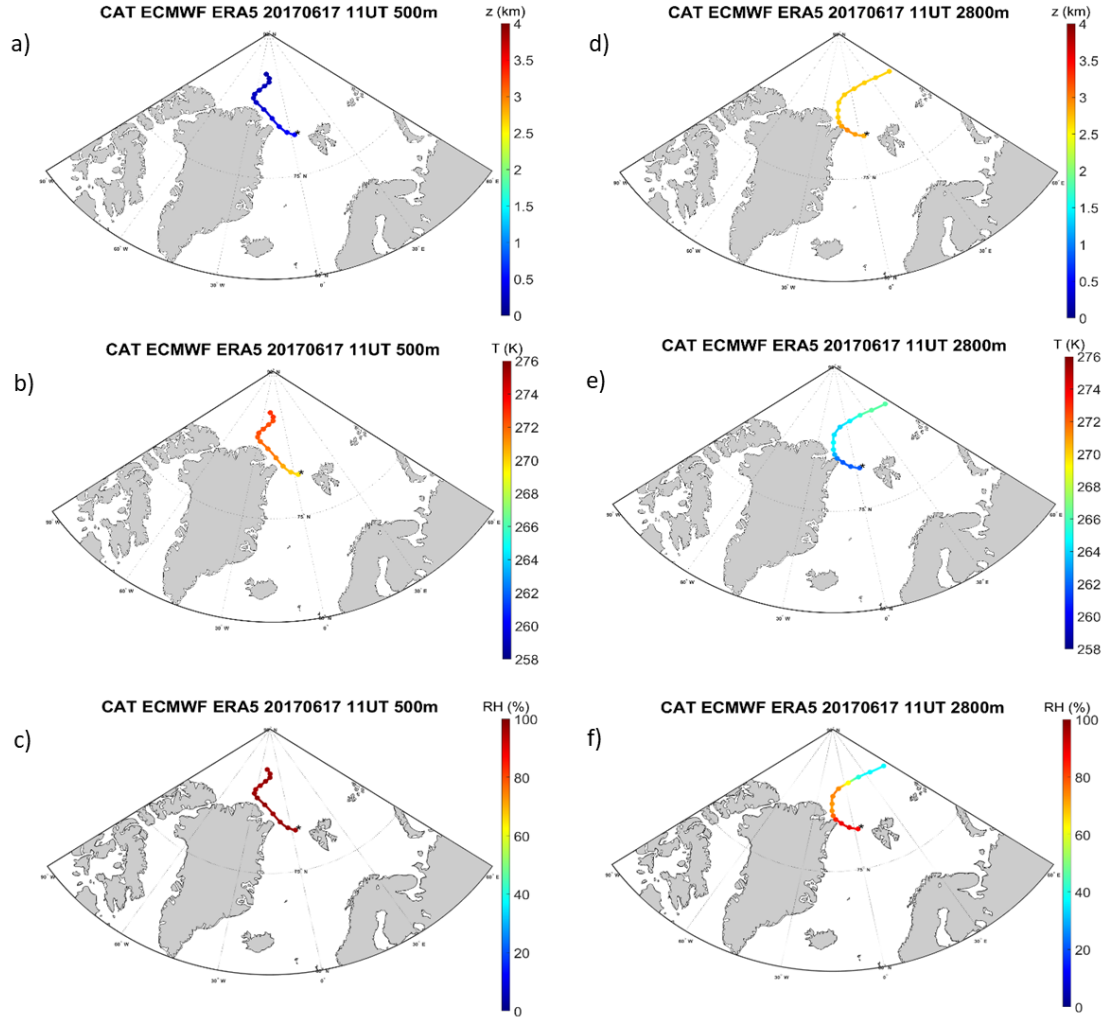

Figure 2.14: 72 hours mean mass back-trajectories calculated for the a)-c) low-level clouds (start point at 500 m altitude) and for the d)-f) mid-level clouds (start point at 2800 m altitude) of the SI case. The panels a) and d) give the 3D air mass evolution whereas the panels b), e) give the temporal evolution of the air mass temperature and c), f) give the temporal evolution of the air mass RH for both cloud layers.

Figure 2.15 also shows the temporal evolution of the CCN concentration ($N_{CCN,SI}$), which was derived from CPC using the CVI inlet resulting in a cut-off diameter of 12 μm (see Section 2.2). The aerosols measured are the CPRs (cloud particle residues) inside the cloud, which are the dry particles that remain after evaporation or sublimation of cloud droplets (CCN). For the $N_{CCN,SI}$, the median value is equal to 9 cm^{-3} which is comparable with the median during all the normal period (NP period identified in Figure 2.3) over SI (11 cm^{-3}) (Baudoux, 2022). The low CCN concentrations measured during ACLOUD are comparable with the observations performed during ASCOS (*Arctic Summer Cloud Ocean Study* at the North of the Svalbard archipelago, Tjernström et al. (2014)) since during this campaign the observed CCN concentrations were between about 10 and 100 cm^{-3} most of the time, with occasional values near or below 1 cm^{-3} (Martin et al., 2011; Mauritsen et al., 2011; Tjernström et al., 2014; Leck and Svensson, 2015).

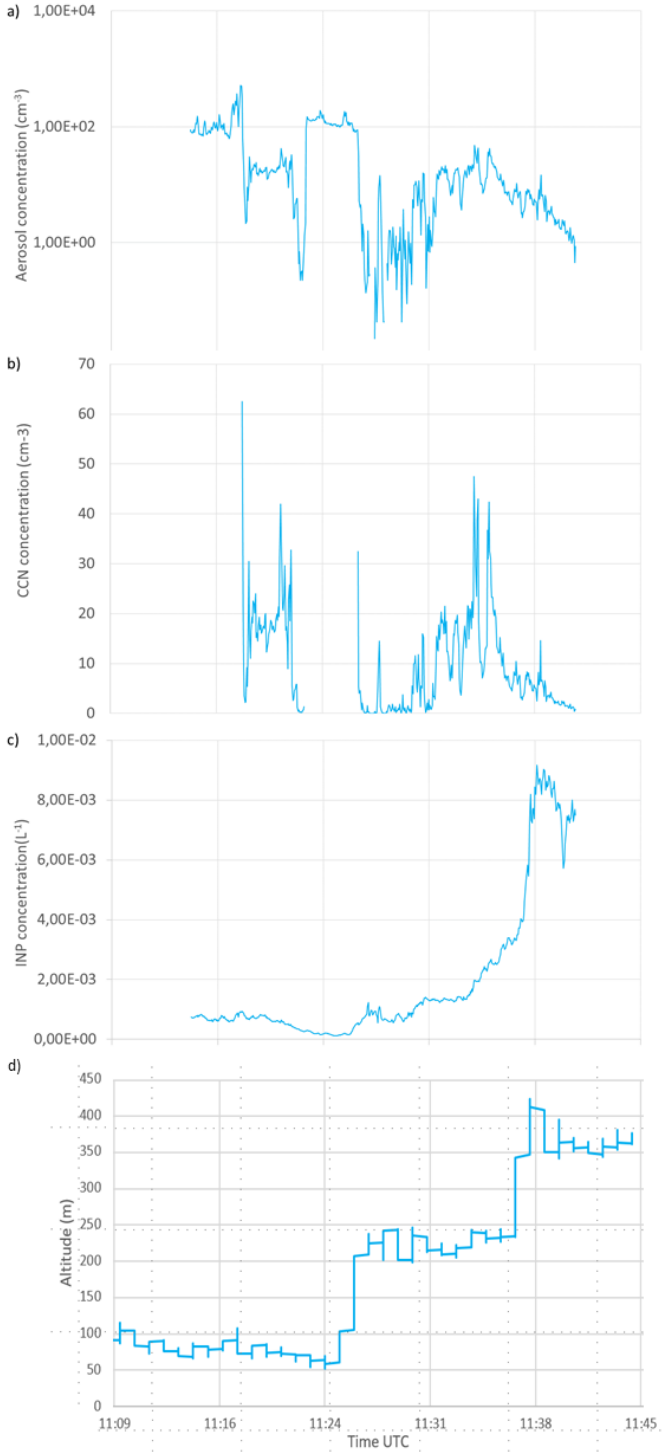

Figure 2.15: Temporal evolutions of a) total aerosol particle number concentration $N_{AP,SI}$ for the SI case in the diameter range from 10 nm to 3 μm, b) CCN concentration derived $N_{CCN,SI}$, c) INP concentration $N_{INP,SI}$ derived from the DeMott et al. (2010) parameterisation and d) flight altitudes for Polar 6 aircraft.

Regarding the INP, the temporal evolution of the INP concentrations ($N_{INP,SI}$) can be calculated using the parameterisation of DeMott et al. (2010). This parameterisation relates the INP number concentration N_{INP} (in L^{-1}) to the temperature T (in K), and

the number concentration of the aerosol particles with diameters larger than 0.5 μm $N_{AP,0.5}$ (in cm^{-3}) according to the Equation 2.2:

$$N_{INP} = 5.94 \times 10^{-5} \times (273.15 - T)^{3.33} \times (N_{AP,0.5})^{\{0.0264 \times (273.15-T)+0.0033\}} \quad (2.2)$$

Figure 2.15c shows the INP concentrations derived using the Equation 2.2, and the observations for $N_{AP,0.5}$ and the temperature. The uncertainty attributed to the parameterisation is approximately of an order of magnitude. Note that the median value for the $N_{AP,0.5}$ measured over the SI domain is equal to 0.7 cm^{-3} and the associated value for the $N_{INP,SI}$ is equal to 8.19 $\times$ 10^{-4} L^{-1}. This value is much smaller than the mean N_{INP} concentration obtained for that day ($\approx$ 1.25 $\times$ 10^{-2} L^{-1}) as presented in Wendisch et al. (2019). The lower values in the INP concentrations obtained with the parameterisation could be explained by the fact that Wendisch et al. (2019) present the INP concentrations at a temperature T = -22.5°C derived from measurements of polycarbonate filters deployed on the Polarstern, *i.e.* at the surface where the aerosol particle concentrations N_{AP} are more important.

c) Radiative properties

The radiative fluxes play a significant role in the Arctic energy budget and the surface energy fluxes which then impact the boundary layer properties (see Sections 1.1.2(c)-(d)). Clouds are also an essential component since they interact with solar (SW) and terrestrial (LW) radiations (see Section 1.1.2(e)). During ACLOUD, measurements of various radiative parameters were performed by Polar 5 and Polar 6 aircrafts, in order to better characterise different radiation fluxes and the interactions between the surface and the clouds (*i.e.* with flight legs performed just above or below the clouds; see Figure 2.8). In order to compare both case studies SI and OO, according to available data, only data from Polar 5 are analysed. Instruments and data (Stapf et al., 2020, 2019a,b) used hereafter are the same than those used in the determination of the cloud-free surface albedo presented in Section 2.3. The processing of the pyranometer and pyrgeometer data is detailed in Ehrlich et al. (2019a). In this section, shortwave and longwave upward and downward broadband irradiance measurements are analyzed (measurements from Polar 5 aircraft done at $\approx$ 3.5 km altitude).

Figures 2.16a-c present the probability density functions (PDF) of the observed upward, downward and net fluxes (identified by the following subscripts $_u$, $_d$ and $_{net}$ respectively) for the solar (SW), terrestrial (LW) and total radiation. The shortwave net (SW_{net}) and longwave net (LW_{net}) terms are respectively given by the Equations 2.3 and 2.4. The analysis was made taking into account all sky conditions:

$$F_{SW,net} = (SW_d - SW_u) \quad (2.3)$$

$$F_{LW,net} = (LW_d - LW_u) \quad (2.4)$$

Figure 2.16a shows that an important fraction of the energy emitted by the sun is reflected by the clouds and the ice surface since the median of the SW_u and SW_d are equal to 446 W m^{-2} and 646 W m^{-2} respectively. The median of the SW_{net} radiation is equal to 200 W m^{-2}. Figure 2.16b shows that almost all the energy emitted by the Earth is trapped by the clouds and then re-emitted, as the median of LW_u and LW_d are equal

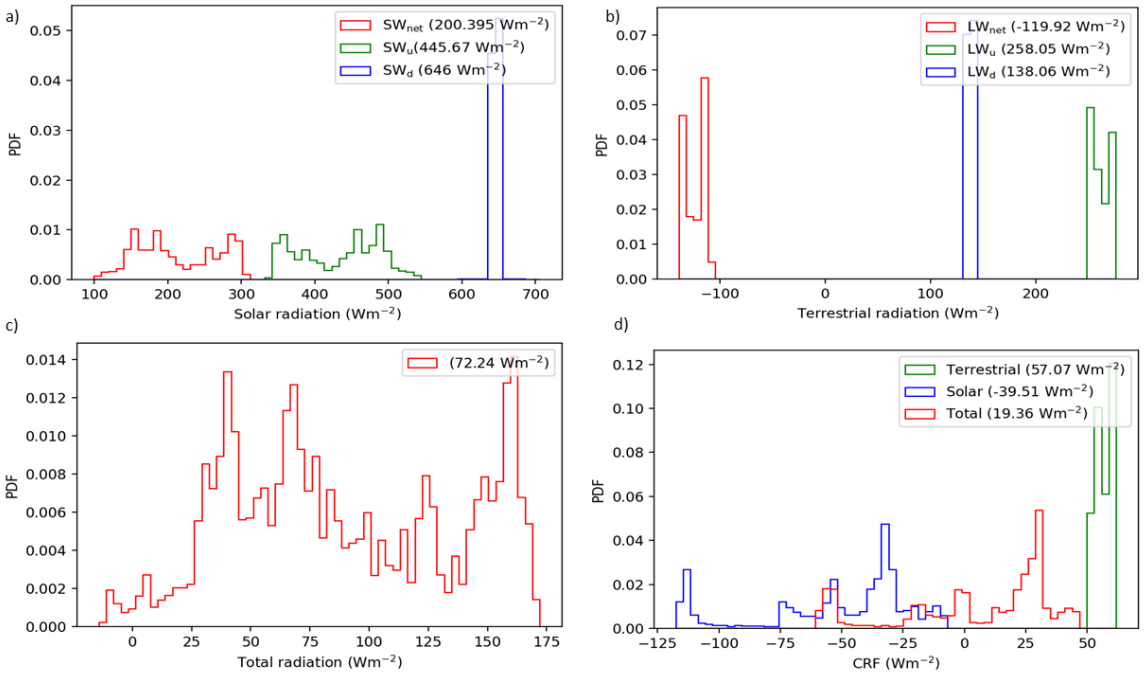

Figure 2.16: Probability density function (PDF) of observed a) upward, downward and net solar (SW) radiation, b) upward ($_u$), downward ($_d$) and net ($_{net}$) terrestrial (LW) radiation, and c) total radiation ($SW_{net} + LW_{net}$), obtained from Polar 5 aircraft at ≈ 3.5 km altitude over SI. Panel d) shows the PDF of the solar (in blue), the terrestrial (in green) and the total (in red) CRF. Values in legends indicate the median of the respective variables. The analysis was made taking into account all sky conditions.

to 258 W m^{-2} and 138 W m^{-2} respectively. The median of the total radiation is equal to 72 W m^{-2} for the SI case (see Figure 2.16c), showing that net surface irradiance is mainly mediated by its solar component. Note that the median values for SW_{net}, LW_{net} and the total radiation are higher than the values found during the whole ACLOUD campaign, which is related to varying sea ice albedo during the campaign. Additionally, the incoming solar radiation varied between research flights as they took place a different times of the day which also introduces further variability.

To better understand the behaviour of clouds and their interactions with the surface, we analysed the surface CRF according to Stapf et al. (2020). The CRF (defined in Chapter 1) is calculated at the flight altitude of the Polar 5 (≈ 3500 m; as visible in Figure 2.7b). The surface CRF is defined by the Equation 2.5:

$$CRF = F_{net} - F_{net}^{cf} \tag{2.5}$$

$$CRF = (F_{SW,net} + F_{LW,net}) - (F_{SW,net}^{cf} + F_{LW,net}^{cf}) \tag{2.6}$$

where the superscripts ^{cf} denote the cloud-free conditions (Ramanathan et al., 1989) and the parameters without superscripts correspond to all-sky conditions (analysed in Figure 2.16).

For practical reasons, it is impossible to simultaneously measure in cloudy and in cloud-free conditions at the same time and location. Therefore, the approach used in Stapf et al. (2020) is to measure net irradiances in cloudy conditions and estimate the respective net irradiances in an assumed cloud-free atmosphere with radiative-transfer

simulations (more details in Stapf et al., 2020). Figure 2.16d shows the LW, SW and total CRF obtained for the SI case. The median values for ΔF_{LW} and ΔF_{SW} are respectively 57.07 W m^{-2} (warming effect) and -39.51 W m^{-2} (cooling effect) over sea ice surface. In total, ΔF is equal to 19.36 W m^{-2} (the total CRF is positive) meaning that a warming effect is produced in this case.

In addition, the sensible heat flux, which shows the ability of the surface to exchange heat with the atmosphere while its temperature is changing, can be determined thanks to the observations. Also, using the eddy covariance method (Foken et al., 2012) and the Reynolds decomposition (which is used to break an observed variable (u) into means ($\overline{u}$) and deviations (u'): $u = \overline{u} + u'$), the sensible heat flux can be defined as:

$$F_{sensible} = \overline{\rho} c_p \overline{w'\theta'} \tag{2.7}$$

with $\overline{\rho}$ the air density, calculated using the perfect gas law with the temperature and pressure for dry air, c_p the heat capacity of dry air, w' and θ' the perturbation in vertical wind speed and in potential temperature respectively. This calculation is applied only to the different horizontal legs of Polar 6 aircraft (see Figure 2.8a) because the flight changes in altitude are responsible for significant potential temperature and vertical velocity variations that cause outliers for the sensible heat flux.

Figure 2.17 shows the sensible heat flux for the different legs of the SI case, *i.e.* it provides an estimation of the vertical profile of the sensible heat fluxes. The chosen

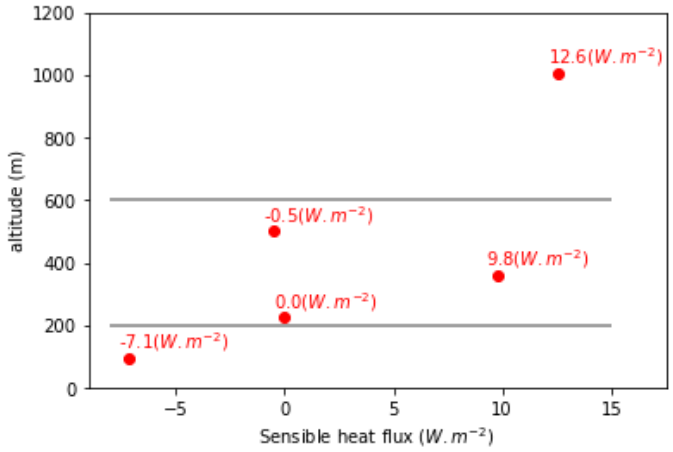

Figure 2.17: Vertical profile of the sensible heat fluxes for the SI case. Values in red correspond to the sensible heat flux obtaines for each horizontal leg of the flight ($\approx$ 10 minutes for each leg). The gray lines indicate the cloud base and top in accordance with reflectivity radar measurements.

convention entails that the negative values are when the atmosphere loses energy in favour of the cloud and positive values are when the opposite occurs. We can note that there are large flux variations inside the cloud layer. Moreover, the negative value obtained for the sensible heat flux suggests vertical wind transport below the cloud layer. Whereas the positive value located above the cloud layer, suggests the presence of turbulence caused by the radiative cooling of supercooled water at the top of the clouds (see Section 2.3.2(d)).

Moreover, we can identify the influence of the surface on the clouds, following the methodology defined by Gierens et al. (2020); Griesche et al. (2021), which analyse the

behavior of potential temperature (θ) between the surface and the cloud base. For the SI case, the vertical variation of θ is equal to 0.34 K (which is lower than the 0.5 K threshold value defined in Gierens et al. (2020); Griesche et al. (2021), meaning that we we have a coupled cloud-surface system.

d) Microphysical cloud properties

The microphysics probes on-board the Polar 6 aircraft permit to characterise the in-cloud properties over SI surface (see Section 2.2.2). However, this characterisation is only possible within the low-level cloud layer since in-situ microphysics observations are only available at altitudes lower than 1500 m as shown in Figures 2.7b and 2.8a.

Figure 2.18 shows the mean PSD and the mean DSD derived from CIP and CDP data. As explained in Section 2.2.2, several assumptions can be made to compute the PSD. Hereafter, the diameter used to determine the PSD is the maximum diameter (D_{max}) (Leroy et al., 2016) which corresponds to the maximum dimension originating from the gravity centre of the image (see red segment in Figure 2.6).

The PSDs and DSDs shown in Figure 2.18a, are averaged on 480 seconds for each leg of the flight (see Figure 2.8a) improving their representativeness. In addition, the spread of the measurements for each leg permits to quantify cloud horizontal heterogeneities. Figure 2.18b presents the DSD and the PSD corresponding to the mean in-cloud properties. These latter distributions are calculated doing the median or the mean of the observations considering only the in-cloud legs, *i.e.* using the data from legs 3 and 5 (legs with a red rectangle in Figure 2.8a). As explained in the Section 2.3, the legs 1 and 2 were done inside the precipitation layer and the leg 4 was done above the clouds according to the flight report.

Figures 2.18a-b show that the droplets have smaller sizes than the ice particles since their size ranges are around 2-40 μm and 80-2000 μm, respectively (we remind that smaller crystals were not measured due to instrument limitation, see Section 2.2.2). Moreover, the droplets are more numerous (by more than 4 orders of magnitude) than the ice particles. Except for the leg 4 (at $\approx$ 1000 m), this behaviour is quite the same for all the legs. The leg 4 reveals that only few droplets and quasi no ice particles are present at the top of the sampled low-level clouds (see Figure 2.8a). For the others legs, the differences between each of the DSDs or PSDs are small.

Regarding only the DSDs, the number of the smallest droplets (< 9 μm) is equivalent for all the legs except for the leg 1 (Figure 2.18a). The leg 1 shows that at an altitude of $\approx$ 60 m the number of the smallest droplets is more important than at higher altitudes whereas the number of larger droplets is less important. Indeed, the droplets with size larger than 10 μm are around one order of magnitude more numerous for legs 2, 3, and 5 compared to leg 1. The most observed drop sizes are different (but remains close) on each of these three legs: 19 μm for the leg 2 (*i.e.* at 220 m), 20 μm for the leg 3 (*i.e.* at 380 m), and 11 μm for the leg 5 (*i.e.* at 550 m). Considering the ice phase, the PSDs obtained for the legs 1, 2, and 3 are quite similar (Figure 2.18a); the ice particles with a diameter between 200 μm and 350 μm are nevertheless slightly less numerous for the leg 3 (*i.e.* at 380 m) than for the legs 1 and 2. The PSD obtained for the leg 5 is different than the three others since: the ice particles with diameters < 400 μm are less numerous, the ice particles with diameters between 400 μm and 1 mm are slightly

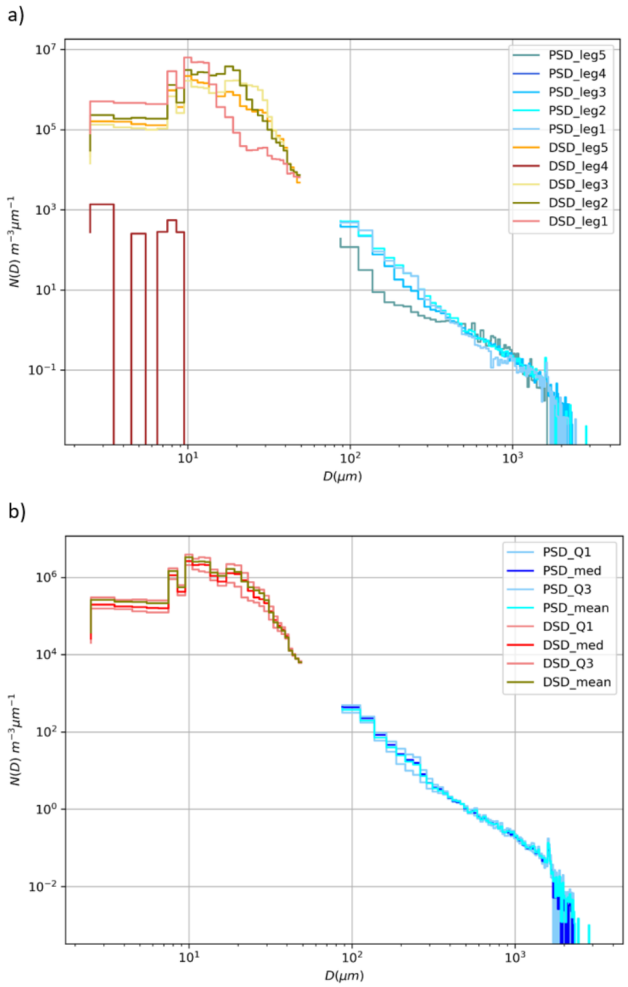

Figure 2.18: Mean PSDs and DSDs obtained (a) for each of the five legs (*i.e.* leg 1: 60 m, leg 2: 220 m, leg 3: 380 m, leg 5: 550 m, leg 4: 1000 m) of the SI case described in Figure 2.8a and (b) considering only the in-cloud legs (*i.e.* legs 3 and 5; legs with a red rectangle in Figure 2.8a). Both the mean and the median are shown to describe the properties of the in-cloud PSDs and DSDs. The Q1 and Q3 indicate the first and the third quartiles illustrating the small spread of the observations.

more numerous, and the maximum diameter observed at this altitude is around 1.5 mm. Indeed, even if they are few, the maximum size of the ice particles observed for the legs 1 and 2 are approximately 2.5 mm and 3 mm, respectively.

According to our analysis of the mean DSDs and PSDs for each leg of the flight, we can note that the microphysics properties of the liquid and ice hydrometeors along the leg 2 (which is supposed to be performed within the precipitation layer) are not so different than those obtained along the leg 3. This might be due to the fact that the leg 2 (*i.e.* leg at 220 m altitude) was performed at the vicinity of the cloud base. According to Figure 2.12, the LCL is at $\approx$ 200 m. Moreover, in the opposite, the microphysics properties for droplets and ice particles obtained along the leg 5 (at 550 m, which is close to the T-inversion shown in Figure 2.12) are quite different than those obtained for the other leg performed inside the clouds (*i.e.* the leg 3). The shorter period (only 2 min) of measurement for the leg 5 (see Figure 2.8a; see also Figures 2.19b-f and 2.20b-f) or the temporal gap ($\approx$ 15 min) between these both legs might explained this difference;

the properties of the low-level clouds could have changed between leg 3 and leg 5).

Thanks to the PSD and DSD measured for each leg of the flight, the temporal evolution of the concentration of droplets and ice particles (Figures 2.19b-f) can be calculated as well as the temporal evolution of the LWC and IWC (Figures 2.20b-f). Moreover, Figures 2.19a and 2.20a present, respectively, the mean and spread values for both concentrations and water contents for the ice and liquid phases providing thereby the vertical trends of all these microphysics parameters.

Figures 2.19b-f and 2.20b-f show that the concentrations as well as the contents of the liquid and ice phases along each leg are highly variable in the time. In order to distinguish the inside and outside cloud regions, thresholds on the IWC and LWC values are defined. Thus, we used the ranges defined in previous studies (Dupuy et al., 2018; Mioche et al., 2017) as IWC $\geq 5 \times 10^{-5}$ g m^{-3} and a LWC ≥ 0.01 g m^{-3}. Note that with this hypothesis the leg 2 would be performed inside clouds. However, considering the data from this leg in the calculation of the mean, the results do not change significantly.

Figure 2.19a confirms that the concentrations of both droplets and ice particles are negligible along the leg 4 (at $\approx$ 1000 m). Also, Figure 2.20a shows that the droplet concentration is higher than the ice particle concentration by approximately 3-4 orders of magnitude for all the other legs. Nevertheless, these concentrations are both quite constant along the profile below 600 m with an exception for N_{drop} at 60 m (leg 1). The maximum values observed for droplet and ice particle number concentration are 50.8 cm^{-3} and 4.5×10^{-2} cm^{-3} respectively, which are higher than the mean droplet concentration (20 ± 55 cm^{-3}) and the mean ice particle concentration ($(4.2 \pm 41) \times 10^{-4}$ cm^{-3}) found during the entire normal period (NP) of the ACLOUD campaign (see NP properties in Section 2.1).

Figure 2.20a indicates that the clouds sampled during the ACLOUD flight 19 mainly consisted of supercooled liquid water since the LWC is much higher than the IWC along the legs performed within the clouds. Note that according to the flight report only the legs 3 and 5 are performed inside clouds (see Figure 2.8a) whereas according to our thresholds the leg 2 was also performed inside clouds. Within the precipitation layer (below 100 m), the LWC is closer to the IWC. With the exception for the leg 5 (whose the tendencies for the DSD and PSD properties were also different than those of other in-cloud legs), the LWC and the IWC seem respectively slightly to increase and decrease with the increasing altitude. Note that the maximum LWC and IWC values observed for this SI case are 0.189 g m^{-3} and 0.0015 g m^{-3}, and these values are respectively higher and lower than the mean liquid and ice water contents found during NP (0.07 ± 0.08 g m^{-3} for the LWC and 0.05 ± 0.005 g m^{-3} for the IWC).

The combination of the different observations (see Figures 2.12-2.20) reveals the main thermodynamics and microphysics vertical properties of the low-level clouds observed over SI surface on the 17 June 2017. The cloud layer is in average present from $\approx$ 200 m to 600 m. Within the clouds, the temperature T decreases from -2°C to -5.5°C and rapidly increases just above the cloud top. The relative humidity RH inside the cloud is around 100% and declines to values around 85% above the cloud top. Thus, the low-level clouds are capped by a warmer and drier air which is common for the Arctic MPCs. Also, the droplet number concentration N_{drop} shows quasi constant values around 45 cm^{-3} and the LWC slightly increases with altitude inside the cloud layer. The ice particle concentration N_{ice} is close to a constant value ($\approx 3 \times 10^{-2}$ cm^{-3}) all along the profile

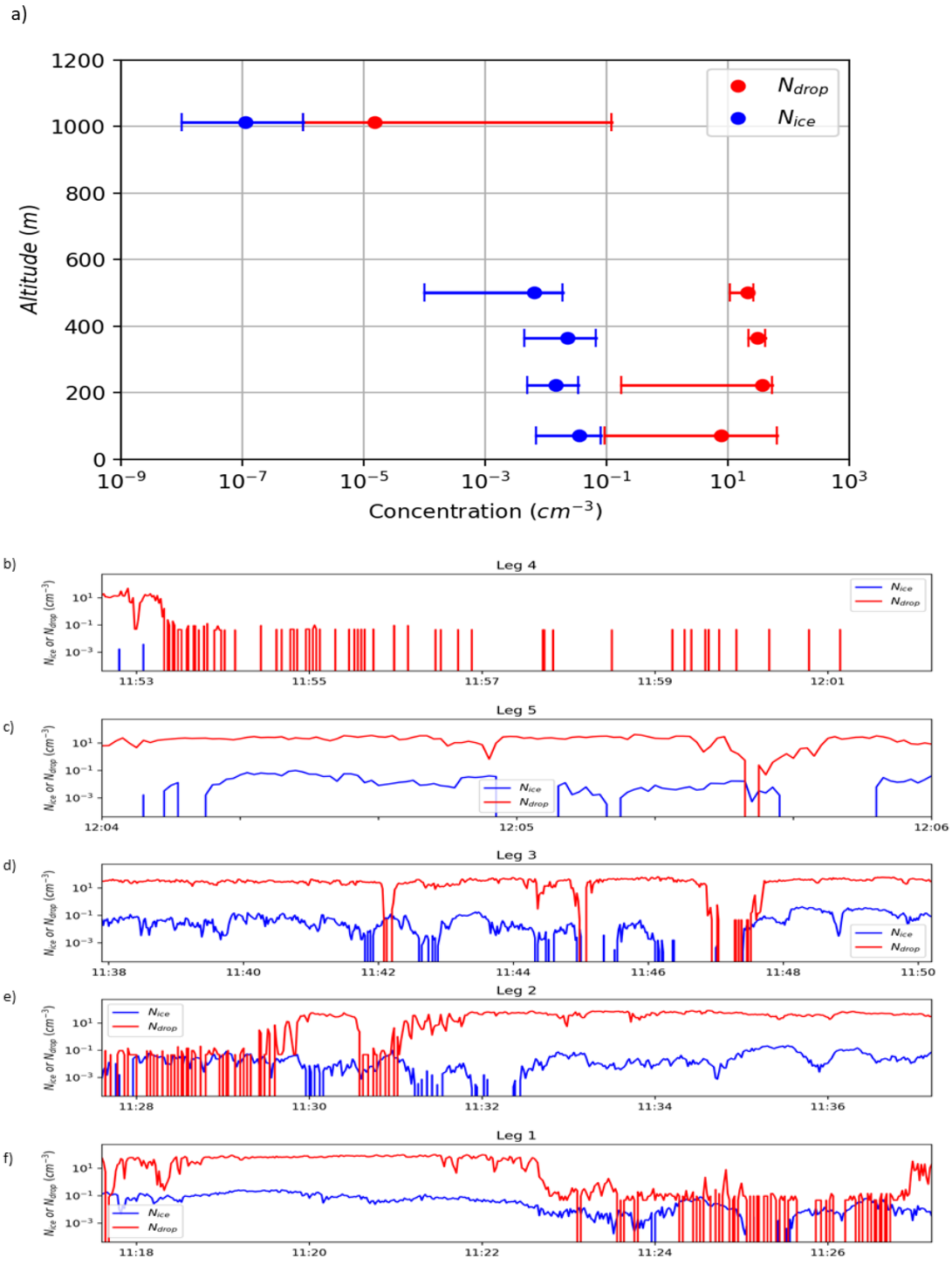

Figure 2.19: a) Vertical profile of the concentration of droplets (N_{drop}) and ice particles (N_{ice}) for the SI case from CPI and CDP measurements. Points correspond to the median of the observed data (for the different legs) and intervals indicate the first (Q1) and the third (Q3) quartiles. b-f) Temporal evolution of (N_{drop}) and ice particles (N_{ice}) for each leg (see Figure 2.8a for corresponding altitudes). Each parameter characterising the liquid or the ice phase are plotted in red or in blue, respectively.

inside the cloud layer. Moreover, the IWC seems to be slightly decreasing with altitude. However, the spread in the IWC values is important (see Q1 and Q3 values for each leg

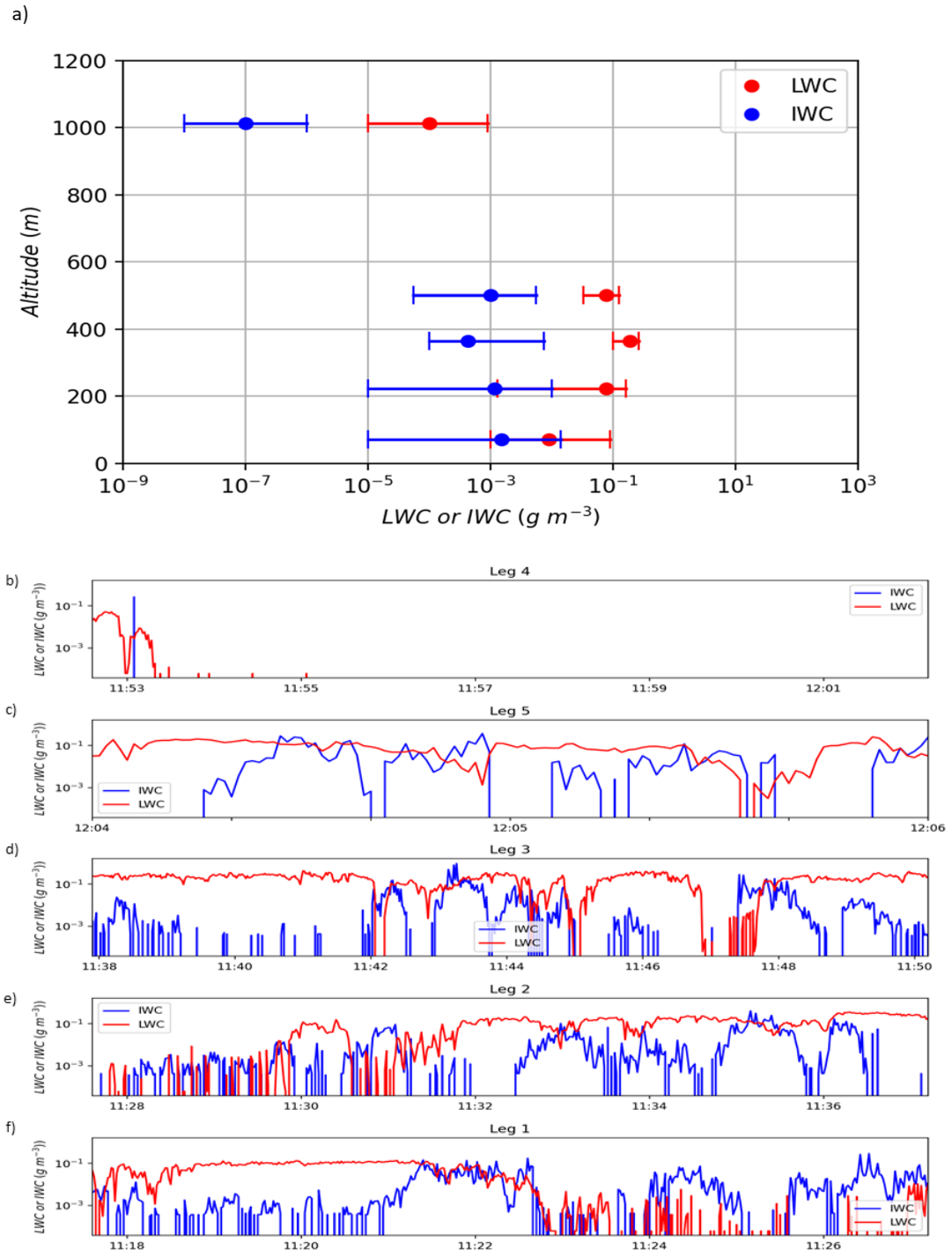

Figure 2.20: a) Vertical profile of the liquid (LWC) and ice water (IWC) contents for the SI case from CPI and CDP measurements. Points correspond to the median of the observed data (for the different legs) and intervals indicate the first (Q1) and the third (Q3) quartiles. b-f) Temporal evolution of (LWC) and ice particles (IWC) for each leg (see Figure 2.8a for corresponding altitudes). Each parameter characterising the liquid or the ice phase are plotted in red or in blue, respectively.

in Figure 2.20a) reflecting the extreme horizontal variability in the data. Both vertical tendencies for liquid (N_{drop} and LWC) and ice (N_{ice} and IWC) phases are typical for

MPCs generated by adiabatic lifting (Klingebiel et al., 2015; McFarquhar et al., 2011, 2007) with precipitating ice.

2.3.3 Open Ocean (OO) case study

This section presents the thermodynamics, radiative, and microphysics cloud properties observed for the open ocean (OO) case (see the green rectangles in Figure 2.7). The observations are presented in the same way than for the SI case in order to facilitate the comparison between the two case studies. Moreover, a synthetic comparison of the main features of the two cases will be available in the Section 2.4.

a) Thermodynamic and macrophysical properties

One of the dropsondes released during the ACLOUD flight 19 provides thermodynamical profile of the 17 June 2017 situation over open ocean surface. The exact position of this dropsonde is approximately at 78.3°N and 8.1°E; and the corresponding time is 14:25 UTC (see DS4 position in Figure 2.7a). Figure 2.21 presents the skew-T log-P diagram obtained with the DS4 measurements.

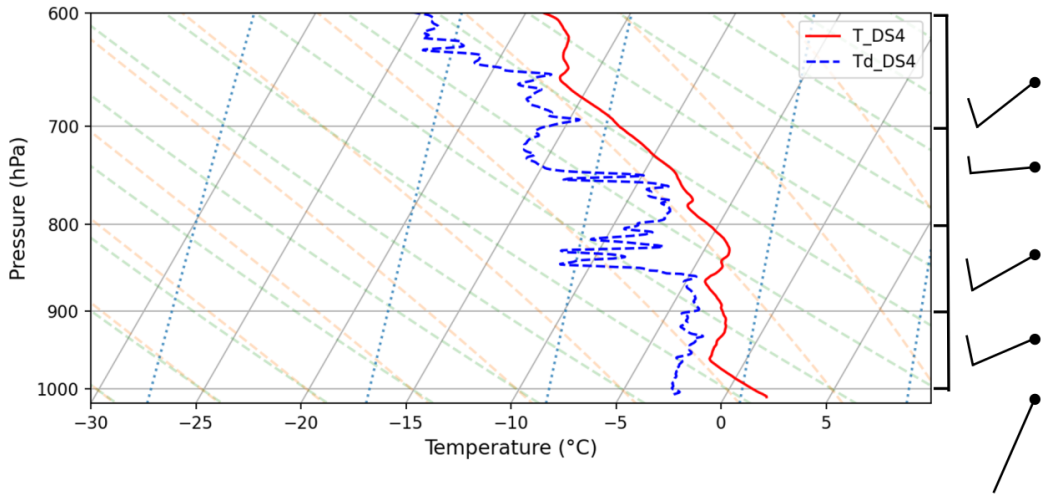

Figure 2.21: As in Figure 2.12 but for the DS4 dropsonde released over open ocean surface (OO) at 14:25 UTC.

Figure 2.21 shows that the temperature close to the surface is equal to 2.5°C which is higher than the surface temperature observed for the SI case. Then, the trend is quite similar to the SI profile. Indeed, the temperature decreases with the altitude up to the ≈ 960 hPa level (≈ 450 m) where there is a first temperature inversion. This T-inversion is present until approximately 920 hPa (≈ 800 m). At higher levels, the temperature decreases with the altitude except in the 860-825 hPa layer (*i.e.*, 1350-1700 m) where a second temperature inversion is observed. At ≈ 780 hPa (or 2150 m), a slightly thicker layer is present for the SI case (see the 725 hPa level in Figure 2.12) where isotherm conditions exist. Regarding the dew point temperature, it is equal to -2°C at the surface which is quite similar than for the SI case. Thus, the relative humidity is lower in the OO case (≈ 80%) than in the SI case (≈ 90%) at the surface. Then, the

mixing ratio is quasi constant up to 960 hPa (≈ 450 m) which means that the relative humidity increases with the altitude up to the 960 hPa level. The profile reveals humid conditions at higher altitudes with the exception of both 860-800 hPa and 750-700 hPa layers. The LCL is approximately at 940 hPa, *i.e.* at ≈ 500 m altitude. Due to the second temperature inversion at 860 hPa (*i.e.* at ≈ 1350 m altitude), we can assume that low-level thin clouds could be present over the OO surface. Moreover, according to the humid conditions observed at the highest altitudes of the DS4, especially around 780 hPa, a mid-level cloud layer could also be present. So, as in the SI case, two cloud layers could be present. However, according to the thermodynamics conditions (Figure 2.21), it seems that the bases of both cloud layers are slightly higher in the OO case in comparison with SI case.

Figure 2.22 presents the temporal evolution of the vertical profile of the radar reflectivity and the altitude of the cloud top for the OO case, derived from the lidar backscattering coefficient measurements.

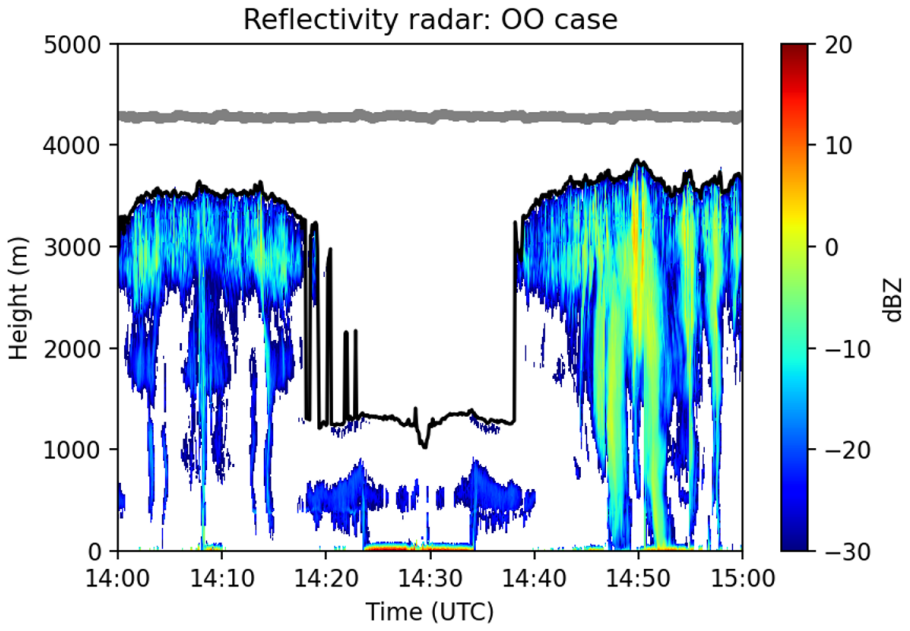

Figure 2.22: As in Figure 2.13 but for OO case. Round-trip of the Polar 5 aircraft is visible at 14:30 UTC.

As for the SI case, two types of clouds are observed: low-level clouds (300-1000 m) with small precipitation bands below, and mid-level clouds (2200-3500 m) with more intense precipitation (thick vertical bands of Z below the cloud base). Note that, using the AMALi Lidar system, the altitude of the cloud top is easier to determine than the altitude of the cloud base. Figure 2.22 also shows that, unlike in the SI case, the two layers of clouds are not concomitant in the OO case. Moreover, the round-trip done by the Polar 5 aircraft at 14:30 UTC permits to identify the temporal development of the mid-level clouds with, in particular, the intensification of the precipitation.

b) Air mass origin and aerosols properties

Using the CAT model (Baray et al., 2020), the air mass origin of both cloud layers can again be analysed (Figure 2.23) for this case. To do this, two sets of 72 hours

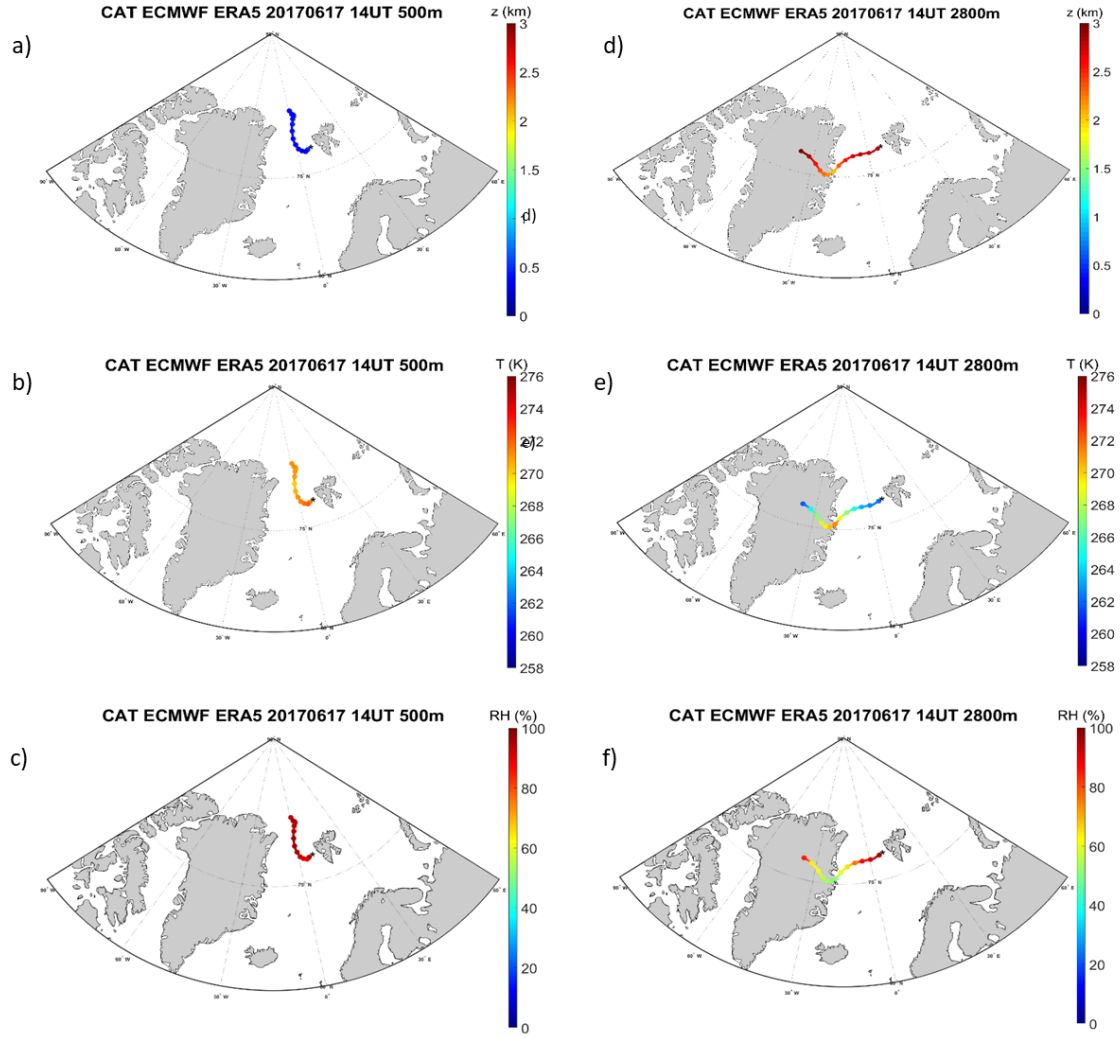

Figure 2.23: As in Figure 2.14 but for the two cloud layers of the OO case.

back-trajectories were performed using as start point the position of the Polar 5 aircraft at 14:00 UTC with an altitude of respectively 500 m or 2800 m to study the low-level clouds or the mid-level clouds.

As for the SI case, Figures 2.23a-c show that the air mass at the origin of the low-level clouds is from the North of the Svalbard. The altitude of this air mass is still constant (Figure 2.23a) and the temperature slightly decreases during the 42 first hours analysed (from 271 K to 269 K) and then increases (from 269 K to 273 K) during the 30 following hours (Figure 2.23d). These temperature variations can be explained by the uncommon local cool area identified at the North-West of the Svalbard on the 17 June 2017 (see ERA-5 synoptic conditions in Section 2.3.1). The air mass at the origin of the mid-level cloud layer is from the West of the Svalbard for the OO case (Figure 2.23d-f) while the air mass at the origin of the mid-level cloud layer for the SI case was from the

North-North-East of the Svalbard (see Section 2.3.2(a)). Figure 2.23d shows that the altitude of this air mass varies from 3 km to 2 km as it passes from Greenland to the Greenland Sea. The air mass temperature (Figure 2.23e) varies simultaneously with the altitude; colder temperatures at higher altitudes and vice versa. The air mass relative humidity also varies simultaneously with the altitude; more relative humidity at higher altitudes (where the temperatures are lower), and vice versa (Figure 2.23f).

The back-trajectories show that air masses at the origin of both cloud layers of the OO case are completely different. Thus, these air mass origins could impact the aerosol properties along the profile. Indeed, the northerly air mass within the boundary layer could be assumed clean whereas the westerly air mass within the free troposphere could be assumed polluted since hydrocarbon exploitation areas and mining activities are present on the east coast of Greenland. Moreover, in contrast to the SI case, sea salts could be locally emitted by the oceanic surface in the OO case. The aerosol measurements performed during ACLOUD from the Polar 6 aircraft can give few hints about the aerosol properties at the lowest levels of the atmosphere (Figure 2.24).

In this framework, Figure 2.24a shows the temporal evolution of the aerosol concentration $N_{AP,OO}$. We can see that $N_{AP,OO}$ is less variable in time than $N_{AP,SI}$. Note that there are missing data between 14:47 and 14:52 UTC due to instrumental malfunctions: the inlet heating broke two flights before and so the inlet was frozen from time to time. Moreover, the UHSAS broke during this ACLOUD flight 19. Thus, no CCN data ($N_{CCN,OO}$) are available for the OO case. According to Wendisch et al. (2019), the CCN concentrations were higher over open ocean surfaces (100 cm^{-3} in average) and Baudoux (2022) found that the median N_{CCN} is 28 cm^{-3} for all the normal period (NP period; see Figure 2.3) of the ACLOUD campaign. As for the SI case, $N_{AP,OO}$ concentrations were derived from the CPC (see Section 2.2). The $N_{AP,OO}$ median value is equal to 3×10^3 cm^{-3}, which is higher than the median value obtained for the whole campaign (240 cm^{-3}) (Wendisch et al., 2019). This quite polluted environment might be explained by the air mass origin previously studied and the oceanic surface from where aerosol particle emissions are more important than over sea ice surfaces. Using the same approach than for the SI case, the temporal evolution of the INP concentrations ($N_{INP,OO}$) can be calculated (Figure 2.24b). We can see that the $N_{INP,OO}$ is variable in time. The values for the $N_{INP,OO}$ remain low but are nevertheless higher than the $N_{INP,SI}$, especially after 14:52 UTC. The median $N_{INP,OO}$ is 8.55×10^{-3} L^{-1} which is, as for the SI case, lower than the mean N_{INP} concentration found in Wendisch et al. (2019) for that specific day. Nevertheless, as in Young et al. (2016), the median of our calculated INP concentrations over open ocean surface (OO case) are higher than over sea ice (SI case).

As already mentioned, the aerosol probes were not working well during our flight of interest and so the analyses presented for both the SI and the OO cases have to be cautiously considered. The observations performed on the Polarstern and presented in Wendisch et al. (2019), or a study using a larger data set (as the one performed by *e.g.* Baudoux (2022)) could be more appropriated.

Figure 2.24: As in Figure 2.15 but for the OO case and only for a) total aerosol particle number concentration ($N_{AP,OO}$), b) INP concentration ($N_{INP,OO}$) derived from the parameterisation of DeMott et al. (2010) and c) flight altitudes for Polar 6 aircraft.

c) Radiative properties

Using a similar method than for the SI case (see details in Section 2.3.2(c)), the observed upward, downward, and net fluxes of the solar (SW), terrestrial (LW) and total radiations for the OO case are analysed from Polar 5 at $\approx$ 4.5 km altitude. Figure 2.25a-c present the probability density functions (PDF) for each radiation type. We remind that, as for the SI case, the analysis is made taking into account the all sky conditions.

Figure 2.25a shows that $\approx$ 70% of the incoming solar energy is reflected (SW_d = 638 W m^{-2} whereas SW_u = 446 W m^{-2} in average) by the clouds and the ocean surface, note that the important contribution of the clouds due to the decrease of the surface albedo to 0.21 (see Figure 2.9) associated to the oceanic surface. Figure 2.25b shows that the amount of the down welling LW radiation is half of the LW radiation emitted from the ocean and the overlying clouds, resulting in LW_{net} equal to

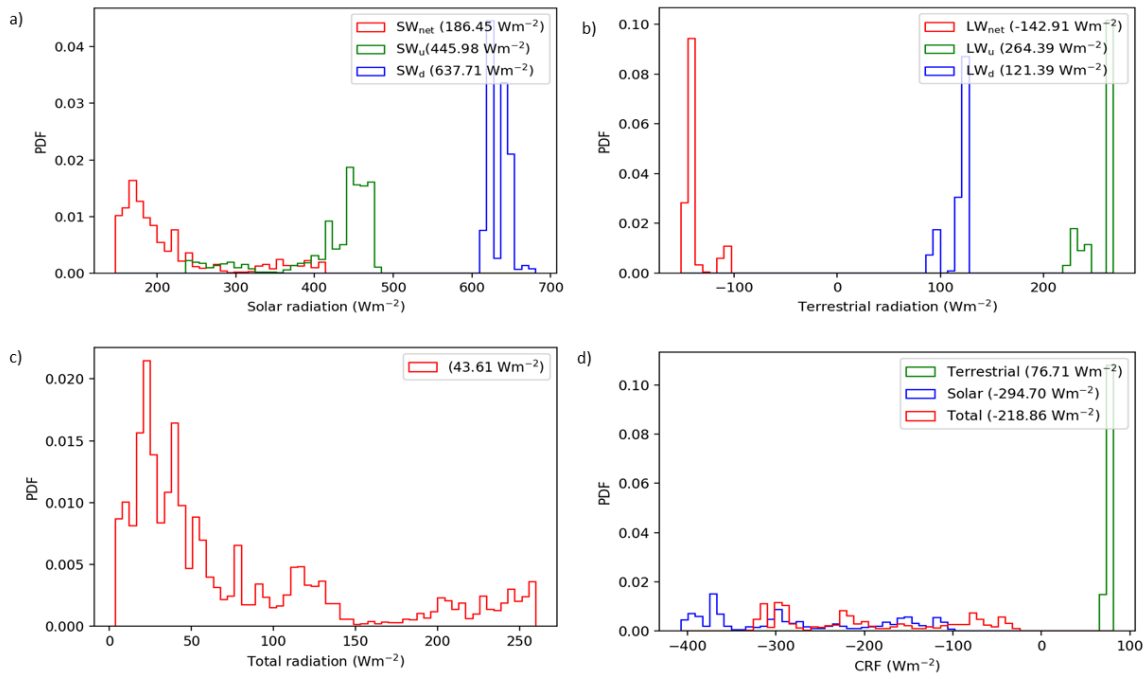

Figure 2.25: As in Figure 2.16 but for OO case.

-143 W m^{-2}. Note that LW_u median is higher than over SI, as the open ocean surface is warmer than the sea ice surface. As for the SI case, net surface irradiance is mainly dominated by its solar component, the median of the total radiation is positive (44 W m^{-2}, see Figure 2.25c). Figure 2.25d shows the CRF_{LW}, CRF_{SW} and total CRF for the OO case. The median values for the shortwave and longwave CRF contributions are CRF_{LW} = 77 W m^{-2} (warming effect) and CRF_{SW} = -295 W m^{-2} (cooling effect) respectively, whereas for the total CRF, the median is equal to -219 W m^{-2}. The total CRF showed in Figure 2.25d was calculated at $\approx$ 4.5 km altitude (height of Polar 5), the total CRF was also calculated at surface (not show here) and the results were found similar, showing that altitude do not have influence in CRF calculation. The total CRF is negative meaning there is an important cooling effect produced in the OO case, whereas over sea ice surface (*i.e.*, for the SI case) the total CRF is slightly positive (19 W m^{-2}; see Figure 2.16d) illustrating an opposite effect of the clouds according to the surface type.

Figure 2.26 presents the vertical profile (see flight legs in Figures 2.7b and 2.8b) of the sensible heat fluxes calculated for the OO case using the similar method than for the SI case.

For the OO case, the used convention is the same than for the SI case, *i.e.*, with negative flux when the atmosphere loses energy in favour of the cloud and positive if it is the opposite configuration. The fluxes with negative values suggest an advection of warm air from altitudes below the cloud layer. As the surface temperature increases with the transition from the sea ice to the open ocean, thus the sensible heat fluxes from the surface increase (compare Figure 2.17, for z = 100m). Within the cloud layer, the sensible fluxes are highly variable.

As in the SI case the profile of potential temperature (θ) is calculated over OO. The vertical variation of θ is even more negligible ($\approx$0.07 K), so we have also a strongly

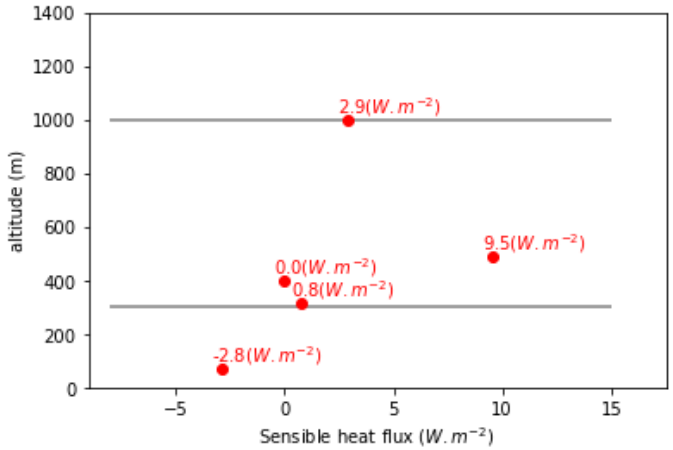

Figure 2.26: As in Figure 2.17 but for OO case.

coupled cloud-surface system for OO case.

d) Microphysical cloud properties

For the OO case, the Polar 6 aircraft flew over oceanic surfaces at altitudes lower than 1500 m (Figures 2.7a-b) and sampled the low-level clouds using the same strategy than for the SI case, *i.e.* with different legs (see Figure 2.8b). According to thresholds used on the LWC and IWC, the in-cloud observations were obtained along the legs 2, 3, and 4 (see red rectangles in Figure 2.8b) whereas the leg 1 was performed close to the surface within the precipitation layer.

Figures 2.27a-b shows the mean DSD and PSD obtained for each leg (Figure 2.27a) and averaged (median and mean) over legs 2, 3, and 4 (Figure 2.27b) in order to characterise the in-cloud properties.

As in the SI case, the droplets have smaller sizes and are more numerous than the ice particles whatever the considered leg (Figure 2.27a). The precipitation layer (leg 1) is composed of some droplets with size < 20 μm, a little less of ice particles within the 80-500 μm size range and even less ice particles on the 500-1000 μm size range (not visible on Figure 2.27a). At the top of the clouds (leg 5), there are numerous small droplets (≤ 10 μm) and an important concentration of large ones (≈ 30 μm) whereas the ice particles are not many and are quite small (< 250 μm). As studied in Klingebiel et al. (2015), the formation of the second size mode of the DSD for the leg 5 (Figure 2.27a) could be explained by the entrainment and the activation/condensation of fresh aerosol particles, or by the differential condensation processes occurring with cloud droplets engulfed in different eddies.

Along the in-cloud legs, the most frequent size of the observed droplets is different according to the altitude. Along the leg 2 (*i.e.* at 300 m), most droplets have a size of 15 μm and droplets < 10 μm are numerous whereas along the legs 3 and 4 (*i.e.* at 400 m and 500 m respectively), the droplets smaller than 10 μm are one order of magnitude less important and the most occurence size is close to 20 μm. This analysis reveals the behaviour quite homogeneous for the liquid phase inside the clouds (especially for legs 3 and 4) and an important difference with the lower part of the clouds (leg 2) which could

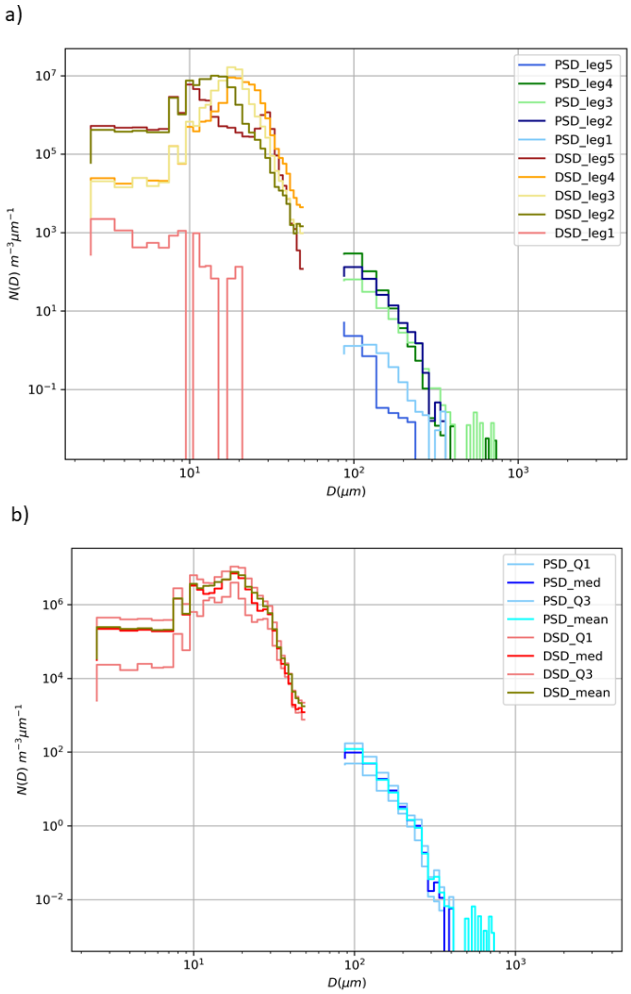

Figure 2.27: As in Figure 2.18 but for the OO case. Here, the five legs correspond to the following altitudes: leg 1: 60 m, leg 2: 300 m, leg 3: 400 m, leg 4: 500 m, and leg 5: 900 m.

be due to the different temperatures on the lower atmospheric layers. Thus, this explains the large variability (Q1-Q3 range) in the averaged in-cloud properties obtained for the liquid phase (Figure 2.27b). Figures 2.27a-b also show that the in-cloud properties for the ice phase are quite homogeneous vertically: a large number of ice particles between 100-300 μm and a small number of big ice particles between 500-800 μm.

In comparison with the SI case, the ice particles reach larger sizes and are more numerous within the low-level clouds in the SI case than in the OO case (see Figures 2.18b and 2.27b). The concentrations of droplets with sizes < 10 μm are quite similar in both cases but the larger droplets are slightly more numerous in the OO case. Moreover, we also have to note that the in-situ measurements made from the Polar 6 for the SI case were always performed within the low-level clouds (see Figure 2.13) whereas, for the OO case, it seems that they were performed either within the low-level clouds or within the precipitation associated to the mid-level clouds (see Figure 2.22).

Figures 2.28a and 2.29a present the mean and spread values for both concentrations and water contents for the ice and liquid phases respectively, calculated using measurements of each leg. Moreover, Figures 2.28b-f and 2.29b-f illustrate the important temporal variability of these microphysics parameters.

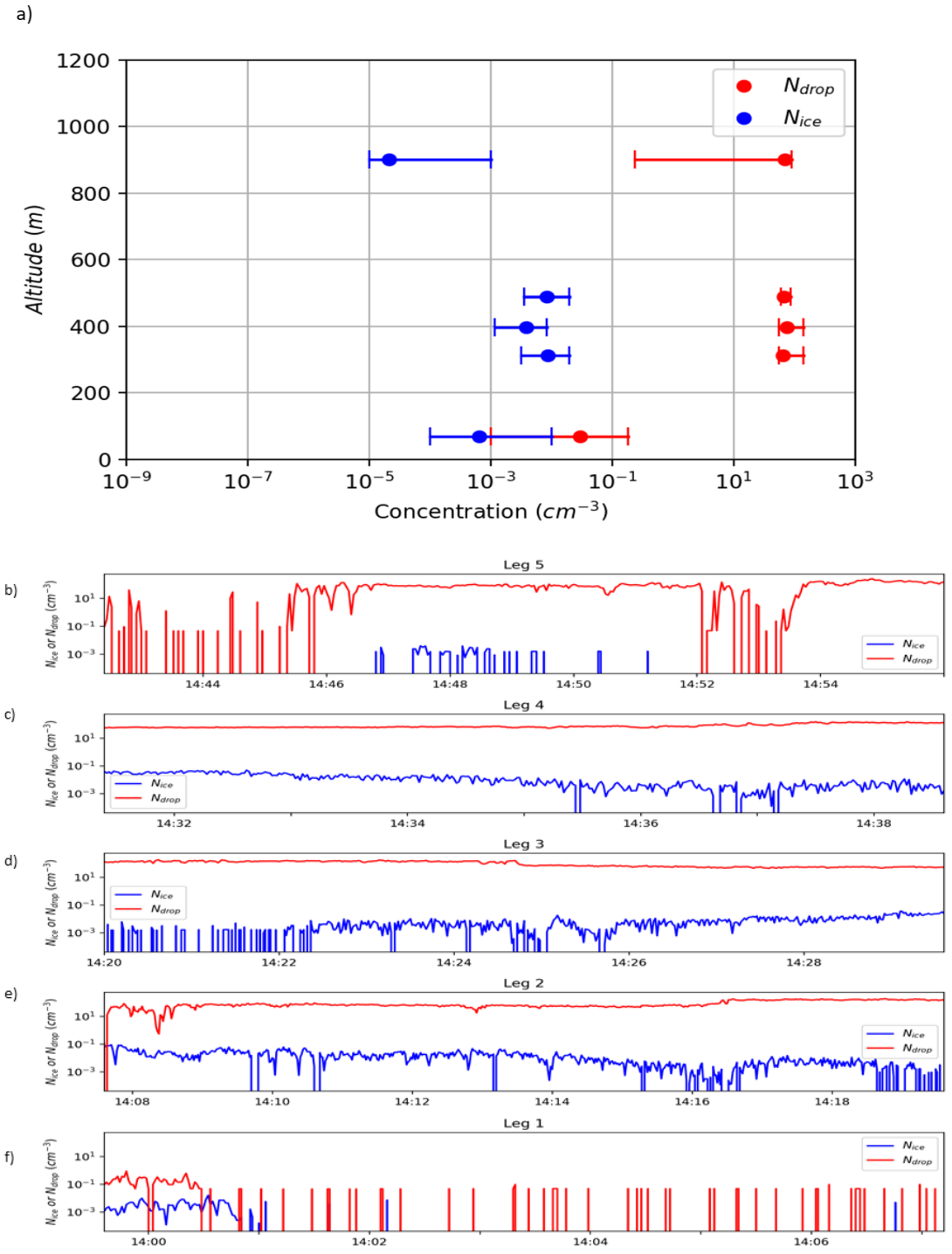

Figure 2.28: As in Figure 2.19 but for the OO case.

Figure 2.28a shows that the droplet concentrations are more important than the ice particle concentrations by approximately 4 orders of magnitude all along the profile (with an exception for the leg 1 where the N_{drops} is only 2 orders of magnitude greater than the N_{ice}). Figure 2.28a also confirms that the droplet concentrations are slightly more important in the OO case than in the SI case (within the clouds) whereas the ice particles concentrations are less important in the OO case (see Figure 2.19a for the SI concentrations). Moreover, as in the SI case, the concentrations of the droplets and

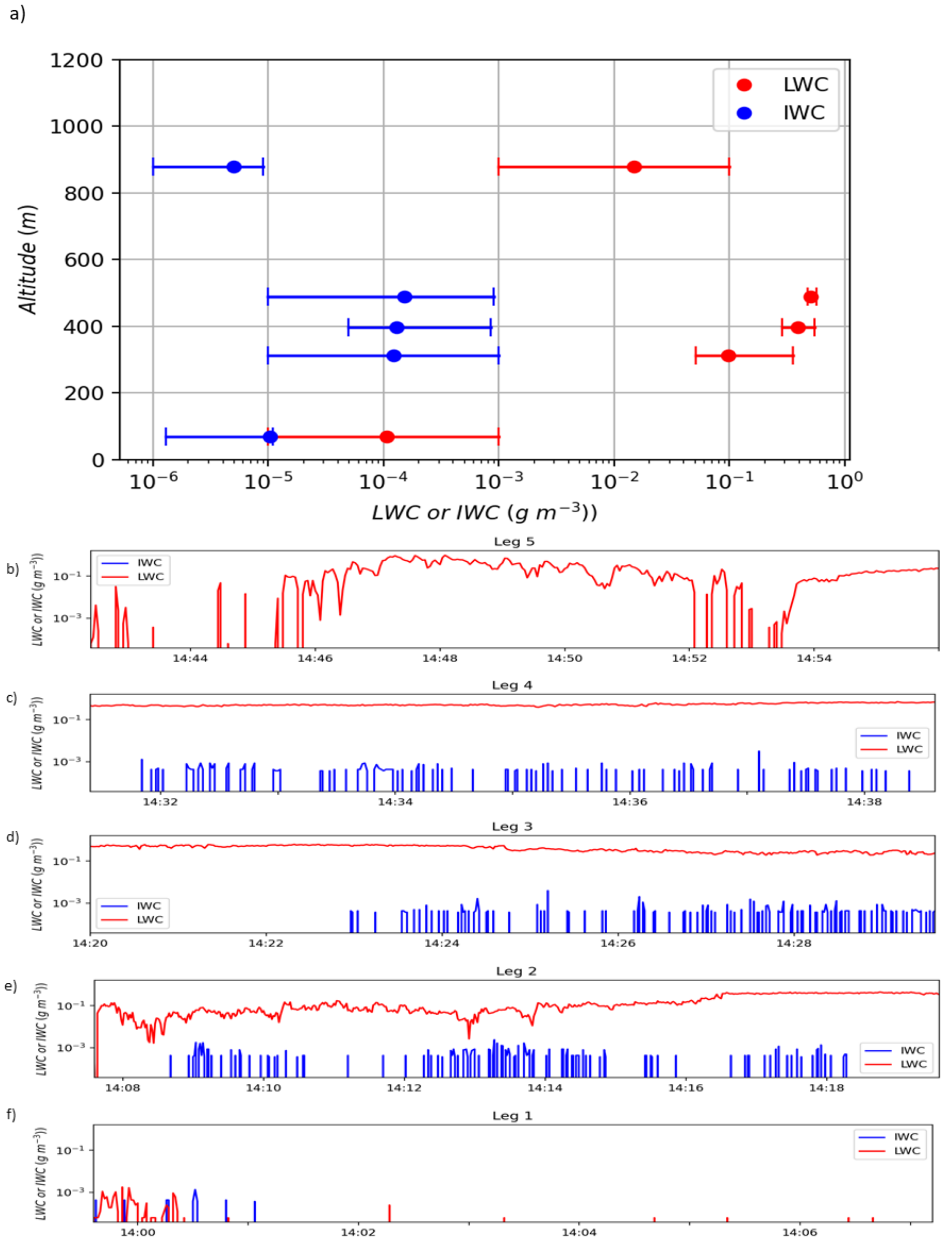

Figure 2.29: As in Figure 2.20 but for the OO case.

the ice particles are quasi constant along the profile within the cloud layer whereas below the clouds both concentrations sharply decrease to quite negligible values. Above the clouds (leg 5), the N_{drops} remains important whereas the N_{ice} becomes negligible. The maximum values observed for droplet and ice particle number concentrations are respectively: 75 cm^{-3} and 8.6 $\times$ 10^{-3} cm^{-3}, which are higher than the respective mean values found during all the ACLOUD (NP) normal period, these larger concentrations than those of the ACLOUD NP were also visible for the SI case.

Figure 2.29a shows that the LWC as well as the IWC within the precipitation layer are negligible whereas at the top of the cloud (leg 5) only the IWC is negligible, since the LWC reaches $\approx$ 1.5 $\times$ 10^{-2} g m^{-3}. Moreover, the LWC slightly increases whereas the IWC remains quite constant with the increasing altitude within the cloud layer. Note

that the maximum LWC and IWC values observed for the OO case are 0.51 g m^{-3} and 1.8 $\times$ 10^{-4}g m^{-3}. These values are respectively higher and close than the mean liquid and ice water contents found during the ACLOUD NP.

For the OO case, the main thermodynamics and microphysics vertical properties of the low-level clouds present over oceanic surfaces on the 17 June 2017 are provided using the association of the different observations shown in Figures 2.21-2.29. The low-level cloud layer is in average present from $\approx$ 300 m to 1000 m. Within the clouds, the temperature decreases and the relative humidity remains quasi constant. At the top of the cloud layer, the air becomes warmer and drier as it was observed for the SI case. Also, inside the cloud layer, the droplet number concentration N_{drops} shows quasi constant values around 75 cm^{-3} and the LWC slightly inscreases with the altitude. The ice particle concentration N_{ice} as well as the IWC are close to constant values ($N_{ice} \approx 8.6 \times 10^{-3}$ cm^{-3} and IWC $\approx 1.8 \times 10^{-4}$g m^{-3}). So, the upper part of the low-level clouds observed for the OO case is mainly composed of liquid phase and precipitating ice is present below the clouds (as it was the case for the SI situation). These microphysics features are common within MPCs in the Arctic region (see Wendisch et al., 2019, among others).

2.4 SI and OO observed cloud properties vs. previous Arctic expeditions

2.4.1 SI vs. OO

Table 2.1 summarises the main thermodynamics, radiative and microphysics properties of the MPC observed on the 17 June 2017. This table permits to identify the differences between clouds observed over sea ice surfaces (SI case) and over open ocean surfaces (OO case).

For both cases studied, the cloud base is almost the same while the cloud depth increased over the transition from sea ice to open ocean (see Figure 1.3), agreeing with observations of Young et al. (2016) and Palm et al. (2010). The surface temperature increased with transition from the frozen sea ice to the warm ocean, thus can induce an increasing sensible heat and latent heat fluxes from the surface. The MPC properties are characterised by increasing values of LWC with altitude, indeed in both cases the liquid phase is mainly present in the upper part of clouds. The maximum of LWC increased almost three-fold (from 0.19 to 0.51 g m^{-3}) over the transition from sea ice to open ocean, and this, in conjunction with a deeper cloud layer. The CRE over OO is negative (-218.86 W m^{-2}) meaning an important cooling effect, in contrast it is positive over SI (+19.36 W m^{-2}), showing an opposite effect. The clouds over OO with relatively high concentration (75 cm^{-3}) of large drops (20 μm) would likely reflect incoming SW radiation more efficiently than the SI clouds (-294.70 W m^{-2}).

One important change in cloud microphysics is the aerosol concentration, that is higher over OO (3000 cm^{-3}) than SI (13 cm^{-3}). This can be explained by the air mass origin and the oceanic surface. Observed ice number concentrations remain low over the transition, suggesting only primary ice formation is active (note that secondary ice

Parameters		Sea Ice	Open Ocean
Thermo-dynamics	Surface temperature (°C)	-2	2
	Surface potential temperature (°C)	-2.5	1.2
	LCL (hPa)	980	940
	Cloud base temperature (°C)	-1.2	0.4
	Cloud base potential temp. (°C)	-0.03	2.4
	Cloud top temperature (°C)	-4	-2.2
	Coupling	coupled	coupled
Aerosol particles	Median N_{AP} (cm^{-3})	13	3000
	Median N_{CCN} (cm^{-3})	9	No data
	Median N_{INP} (cm^{-3})	8.2×10^{-4}	8.5×10^{-3}
Cloud macrophysics	Cloud base (m)	200	300
	Cloud top (m)	600	1000
Radiation	Mean surface albedo	0.72	0.21
	CRF_{SW} (W m^{-2})	-39.51	-294.70
	CRF_{LW} (W m^{-2})	57.07	76.71
	CRF_{net} (W m^{-2})	19.36	-218.86
Cloud microphysics	Max. LWC (g m^{-3})	0.19	0.51
	Mean. LWC (g m^{-3})	0.11±0.06	0.33±0.21
	Max. IWC (g m^{-3})	0.0015	0.00018
	Mean. IWC (g m^{-3})	0.001±0.0005	0.00013 ±0.0001
	Max. N_{drops} (cm^{-3})	51	75
	Mean. N_{drops} (cm^{-3})	30±14	54±19
	Max. N_{ice} (cm^{-3})	0.045	0.0086
	Mean. N_{ice} (cm^{-3})	0.015±0.15	0.007±0.0041
	Mean. D_{drops} (μm)	10±0.0005	20±0.0001
	Max. D_{drops} (μm)	40	50
	Mean. $D_{crystals}$ (μm)	100	100
	Max. $D_{crystals}$ (μm)	3000	800

Table 2.1: Comparison between the main observed properties for both the SI and the OO cases. The mean values are given with ± one standard deviation.

formation is probably not possible due to the temperature ranges in both cases, > -4°C). The ice crystals reach larger sizes for the SI case (≈ 3000 μm) than OO case (≈ 800 μm), opposite to the results obtained by Young et al. (2016). Klein et al. (2009) and Morrison et al. (2009b) suggest that larger droplet sizes may be a common occurrence in ocean-based clouds, whilst small droplets are common in clouds over sea ice, regardless of season. This is in agreement with our study (≈ 50 μm and ≈ 40 μm, over OO and SI, respectively).

2.4.2 SI and OO vs. previous Arctic expeditions

The cloud properties from both the SI and the OO cases will now be compared to observations from previous Arctic expeditions. The first comparisons will be done to

observations performed during the ASTAR campaign, *i.e.* over the same region and at the same period (late spring) than ACLOUD. Then, in order to analyse the seasonality of the cloud properties, first we will compare the SI and OO properties to data collected earlier in spring (March-April) during the ACCACIA campaign, and second we will compare the study reported by Lloyd et al. (2015) during ACCACIA (early spring case/Svalbard) and ACACCIA (summer case/ Svalbard). In order to analyse the geographic impact on cloud properties, our SI and OO results will be compared to observations done during the ISDAC campaign which took place over the Beaufort Sea and the North of Alaska in early spring 2008. Details about the different campaigns are given in references cited in Tables 1.1 and 1.2. Finally, we will give a general conclusion about our observed clouds.

During the ASTAR campaign performed in the vicinity of Svalbard during May-June 2004 (late spring), high ice particle concentrations were observed (up to 0.05 cm^{-3}) over open ocean surfaces (for the case analysed in Gayet et al. (2009a)). The shattering of isolated drops during freezing and the ice splinter production during riming appear to be the most likely processes to explain the observations of high ice concentration (Gayet et al., 2009a). This does not agree with our data (0.0086 cm^{-3}) for the OO case. Note that the cloud top temperature is warmer (-4°C) than in the considered ASTAR cloud situation (-6°C), not enabling the secondary ice formation. However, our results are in agreement with mean values (0.003 cm^{-3}) found by Mioche et al. (2017), in the study of four airborne campaigns over Greenland Sea and the Svalbard region during spring.

To understand the impact of the seasonality in cloud properties, we compare our results obtained in a late spring period with the case study reported by Young et al. (2016) during the ACCACIA campaign, which was performed in early spring (March-April) around Svalbard. The cloud top temperatures over sea ice and open ocean surfaces (-18 °C and -23 °C, respectively) were much lower than our case studies (-4 °C and -2.2 °C, respectively). In our study, the concentration of cloud droplets were variable throughout the MPC layers in both cases, but mean N_{drop} increased from 30 ± 14 cm^{-3} over the sea ice to 54 ± 19 cm^{-3} over the open ocean. This increase was not observed in the case study reported by Young et al. (2016), where in contrary a reduction in the mean N_{drop} from 110 ± 36 cm^{-3} to 63 ± 30 cm^{-3} was observed. However low droplet concentrations over open ocean (63 ± 30 cm^{-3}) were measured for this ACCACIA case. These N_{drop} are similar with our observations over OO (54 ± 19 cm^{-3}), this suggests that such properties are common amongst over the open ocean surface. During the ACACCIA case reported by Young et al. (2016), the mean LWC observed over sea ice (0.1 ± 0.13 g m^{-3}) and open ocean surfaces (0.2 ± 0.12 g m^{-3}) are comparable to our mean LWC (0.11 ± 0.06 g m^{-3} and 0.33 ± 0.21 g m^{-3} for the SI and the OO case respectively). These results suggest that this is a common observation of clouds over sea ice and open ocean surfaces. Observed ice crystal number concentrations within the ocean cloud are similar to those measured over the sea ice (≈ 0.001 cm^{-3}) during ACCACIA case, however higher ice concentration were found during our study over SI and OO (0.045 and 0.0086 cm^{-3}, respectively). In addition, substantial microphysical differences were identified between the study reported by Lloyd et al. (2015) during ACCACIA (early spring case/Svalbard) and ACACCIA (summer case/ Svalbard). During the spring cases median N_{ice} (0.0005 cm^{-3}) were found to be lower by a factor of 5 than observations from the summer campaign (0.003 cm^{-3}) over sea ice and open ocean surfaces. Lloyd et al. (2015) reported that cloud layers in the summer spanned a warmer

temperature range (≈ 0 °C ≥ T > -10 °C) than in early spring (≈ -10 °C ≥ T > -20 °C) and enhancement of ice concentrations in these cases was expected to be due to secondary ice production through the Hallett-Mossop (H-M) process, emphasising that seasonality remains a crucial factor in the study of Arctic cloud microphysics.

The mean LWC observed over the sea ice during ISDAC and ACCACIA, are similar to the LWC (0.11 ± 0.06 g m^{-3}) of our SI case. This consistency suggests that there is no impact of aerosol sources related to geography, which can have a prominent influence on the liquid and ice phase of these clouds. Comparable results of the liquid phase were found between our study, and the MPC observations reported by other studies performed in diverse area of the Arctic(*e.g.* Verlinde et al. (2007), McFarquhar et al. (2011), Jackson et al. (2012) and Lloyd et al. (2015)) suggest that droplet number concentrations of ≈ 150 cm^{-3} or below are common amongst Arctic MPC in the transition season (spring-summer).

We can see that clouds observed during our case studies present a liquid phase which is in accordance with the clouds observed in Svalbard during spring 2016, but an ice phase which is lower than observed generally in this season, due to the warmer cloud temperatures found in our study. However, note that our ice particle concentrations are higher than those found during the ACLOUD normal period (NP), this can be explained by the higher mean temperatures reported (> 2 °C) during this period of the campaign in comparison with our case studies. Secondary ice formation has been found to play a great role in the late spring and summer cases studied by Gayet et al. (2009a) and Lloyd et al. (2015).

The observations of both the SI and the OO cases will be used to constrain the modelling tools. A comparative analysis given in the Chapter 4 between these ACLOUD observations and the simulation results obtained with the WRF model (Skamarock et al., 2008) will permit to study the ability of this commonly used mesoscale model (described in the Chapter 3) to reproduce the properties of the MPCs in the Arctic region (especially in the vicinity of the Svalbard archipelago), to better understand the physical processes responsible for the spatial distribution of the water and the ice phases within the MPCs, and to identify model weaknesses.

Chapter 3

Modelling tools

Previous Arctic expeditions and modelling studies demonstrated how the complex web of interactions between local and larger scale processes enable MPCs to persist for days or longer (Wendisch et al., 2019). While many processes involved in the MPCs formation are known, their interactions (*e.g.* with the moisture of the ABL or with environmental conditions (Pithan et al., 2018; Freud et al., 2017)) are not understood nor well represented by numerical models.

Several atmospheric models (process, regional, and global models) exist to bridge the spatiotemporal scales from local processes to global and long-term parameters. Models can assist in the interpretation of the local measurements, evaluate process parameterisations, quantify feedback mechanisms, and help to better determine the role of the MPCs in the Arctic amplification. The observations of the ACLOUD campaign, especially the data collected from the Polar 5 and the Polar 6 aircrafts on the 17 June 2017 for both the SI and the OO cases, will help to evaluate the predictive skills of the model used.

This Chapter is dedicated to the state-of-the-art of cloud modelling and the presentation of the modelling tools that are used for this thesis. First, a short overview of various cloud models at different scales is presented and then, a detailed description on the WRF model (Skamarock et al., 2008), and the different configurations that will be used during this thesis are provided.

3.1 Cloud modelling

3.1.1 Modelling scales

Different model approaches are used to simulate the formation and the evolution of clouds considering their temporal durations and their spatial extensions. Also, depending on the studied atmospheric processes, the model timestep is adapted: from seconds when the studies focus on the cloud formation to hours when the studies investigate the impacts of clouds on the climate. Figure 3.1 illustrates the main weather phenomena in Arctic classified according to their spatial and temporal scales (micro, meso, and synoptic scales); the model approach (process, regional or global) generally employed to

study each of these phenomena is also indicated. A hierarchy of models taking advantage of these different approaches is commonly used to study an atmospheric phenomenon, such as is envisaged in the $(AC)^3$ consortium in order to study the Arctic amplification (Wendisch et al., 2017). The process models, which focus on local-scale processes, are

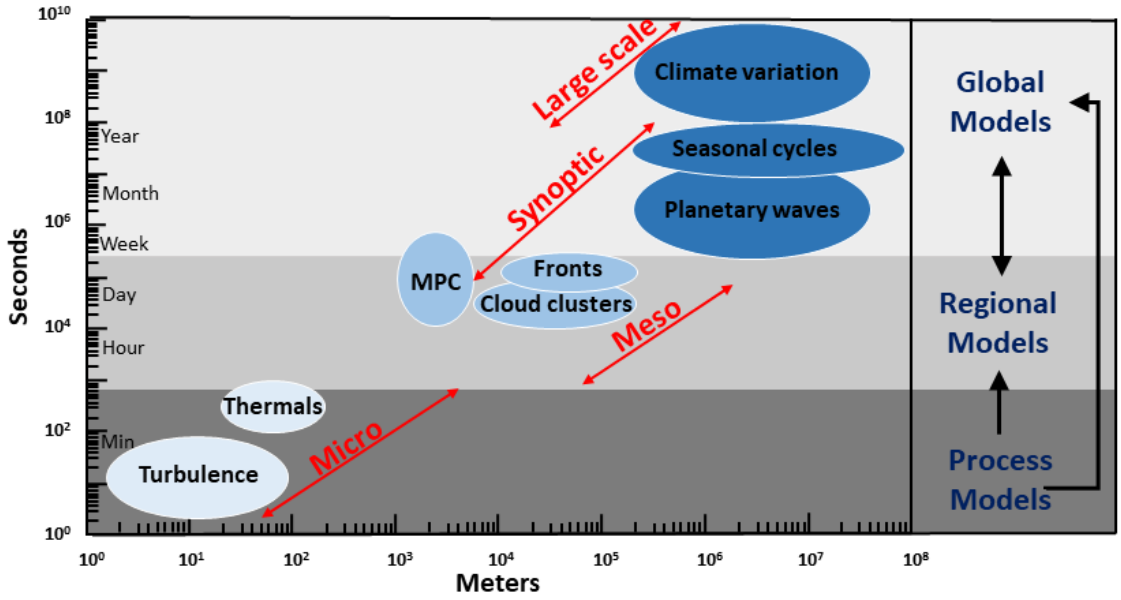

Figure 3.1: Hierarchy of models covering a wide range of spatial and temporal scales (micro, meso, and synoptic scales) to study the cloud properties. Figure adapted from Kagkara (2019).

oriented to help regional and global models to improve parameterisations (local modelling studies about Arctic clouds in Zhang et al., 2020, 2022). The regional models zoom in on specific areas providing results closer to the scale of the real-world observations about topography, land cover and soil types. These models have to force their boundaries at regular time intervals by the outputs of larger scale models. Sterzinger et al. (2022); Morrison et al. (2012); Klein et al. (2009) give examples of regional Arctic modelling studies. The global models provide the past, present and future evolutions of the climate over the Earth or over a wide part of the globe. Climate studies with a focus on the Arctic region can be found in Cesana et al. (2012); Sedlar et al. (2020). Due to the wider area and longer time, the global models are generally run at lower spatial and temporal resolutions than the regional models.

The choice of the used model depends directly on the scientific question being addressed (Held, 2005). Thus, when focusing on the processes involved in the formation of MPCs, clouds which can persist for several days to weeks, and on the evolution of their properties according to surface type, aerosol loading and thermodynamics (as studied in this thesis), modelling at the regional scale is required.

Numerical weather prediction (NWP) models, at the regional scale, can simulate the synoptic and mesoscale atmospheric motions. NWP models describe the evolution of wind, pressure, temperature, water vapour, clouds and precipitation in the atmosphere, as well as the exchange processes of the surface, and with the soil. There are many mesoscale NWP models such as the French Meso-NH (*Mesoscale Non-Hydrostatic*; Lac et al. (2018)) and the operational AROME (*Applications of Research to Operations at MEsoscale*; Seity et al. (2011)) models, the British MetUM (*Met Office Unified Model*;

Grosvenor et al. (2017)), and the American RAMS (*Colorado State University's Regional Atmospheric Modeling System*; Cotton et al. (2003)) and WRF (Skamarock et al., 2008)) models, which are applied on regional scales.

The WRF model is the regional model used during this thesis and it will be described in details in the Section 3.2 as well as the numerical configurations used for the simulations presented in Chapter 4.

3.1.2 Basic principles of the atmospheric models

All the atmospheric models start the integration from an initial state of the atmosphere, which is documented by operational meteorological observations coupled with an assimilation procedure, or through data from other models with lower resolution, such as the models for weather forecast.

Then, the dynamics solver, which is the element of the models where the basic primitive equations governing the dynamics of the atmospheric fluid are integrated numerically (implying a discretisation of these equations in time and space), gives the evolution of the atmospheric fundamental variables (wind, pressure, temperature, and water content in the air). By definition, the evolution of the atmospheric fluid is described with the principle of conservation of the momentum (Newton's law; Equation 3.1), the mass (equation of continuity; Equation 3.2), and the energy (first law of thermodynamics; Equation 3.3), as well as the equation of state of the ideal gases (Equation 3.4), whose the formulations in a Cartesian system are given by:

$$\frac{d\vec{v}}{dt} = -2\vec{\Omega} \wedge \vec{v} - \frac{1}{\rho}\vec{\nabla}p + \vec{g} + \vec{F} \tag{3.1}$$

$$\frac{1}{\rho}\frac{d\rho}{dt} + \vec{\nabla} \cdot \vec{v} = 0 \tag{3.2}$$

$$c_p \frac{dT}{dt} = Q + \frac{1}{\rho}\frac{dp}{dt} \tag{3.3}$$

$$p = \rho R T \tag{3.4}$$

with $\vec{\Omega}$ the Earth's rotation rate, $\vec{g}$ the gravity, $\vec{F}$ the internal fluid friction forces (viscosity), c_p the heat capacity at constant pressure p, Q the diabatic energy transfers and R the ideal gas constant.

There are several possible approximations (hydrostatism, compressibility, etc.) of these basic primitive equations used in order to represent the evolution of the atmospheric fluid. Moreover, additional modules are coupled to the dynamics solver to parameterise other physical properties such as radiation, surface fluxes, turbulence, and microphysics. Thus, the representation of the atmosphere dynamics coupled with physics parametrisation can be quite different for a variety of numerical regional models (Cotton et al., 2003; Skamarock et al., 2008; Seity et al., 2011; Grosvenor et al., 2017; Lac et al., 2018).

3.1.3 Representations of the cloud microphysics

The key process, which impacts simulation results for the cloud properties (formation, development and dissipation), is the representation of the microphysics properties, such as the exchanges between the different phases of water, *i.e.* liquid and ice phases as well as water vapour. Thus, the microphysics is a fundamental part of cloud modelling and a critical factor in NWP models.

The cloud microphysics can have different representations depending on the scientific objectives and the computational time: *bulk* or *bin*. The one or more moments (*bulk*) microphysics modules where the hydrometeors' distributions and the microphysics processes are parameterised using, *e.g.*, an exponential or a gamma function to represent the hydrometeors' distributions (see Figure 3.2b). The *bin* microphysics modules where the hydrometeors' distributions do not follow a predetermined mathematical function, but are discretised on size (or mass) grids (Figure 3.2a) and the processes are represented using a more detailed approach than in the *bulk* modules (Khain et al., 2015). This latter approach requires a significant number of variables and therefore a considerable computational time making impossible to use this representation in operational numerical forecast models.

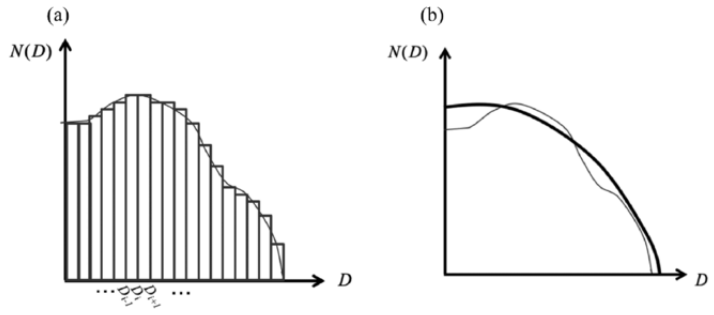

Figure 3.2: Diagram illustrating the (a) *bin*, and the (b) parameterised representation for the size distribution of the hydrometeors $N(D)$. Figure from Planche (2021).

Previous studies were performed in order to compare results provided by several regional models using different assumptions for the dynamics and the microphysics (as in Klein et al., 2009; Morrison et al., 2011, among others). For example, Arteaga et al. (2020) showed how these assumptions impact the simulation results for the properties of clouds and the subsequent precipitation of an intense precipitating event observed over the South-East of France (over the Cévennes-Vivarais mountains) during the HYMEX campaign (Ducrocq et al., 2014). In this study, the simulation results provided by the WRF model using a 2-moment bulk microphysics (Skamarock et al., 2008; Thompson et al., 2008; Morrison et al., 2009a) and the DESCAM model using a detailed (bin) microphysics were compared to the available observations. The results from DESCAM (DEtailed SCAvenging Model; Flossmann and Wobrock (2010); Planche et al. (2010, 2014)) were comparable to the observations for the precipitation field at the surface. On the contrary, the simulation results from WRF reproduced neither the intensity nor the distribution of the observed precipitation. Indeed, it seems that the diabatic effects induced by the microphysics were too important impacting the low-level dynamics properties, and so the cloud initiation in the WRF model.

3.2 Description of the WRF model

The WRF model is a numerical weather prediction (NWP) model designed for both atmospheric research and operational applications (Skamarock et al., 2008). Since the 2000s, the development of the WRF model has been a collaborative effort from the National Centre for Atmospheric Research (NCAR), the National Oceanic and Atmospheric Administration (NOAA), and the Federal Aviation Administration (FAA), among others. WRF is maintained and supported as a community model to facilitate wide use. Thanks to a very active international user community, the model is updated every 6 months.

WRF is suitable for a broad span of applications across scales ranging from meters to thousands of kilometres, and a whole range of physics and dynamics options permits to use the WRF model for diverse atmospheric and meteorological applications including, *e.g.* real-time NWP, forecast research, and idealised simulations (*e.g.* LES and 2D configurations) (Wang et al., 2017).

The principal components of the WRF model are the two possible dynamics solvers (the Advanced Research WRF (ARW) and the Non-hydrostatic Mesoscale Model (NMM) solvers), and the physics modules (microphysics, cumulus, surface, planetary boundary layer, and radiation; see interactions in Figure 3.3) that interface with the dynamics solver.

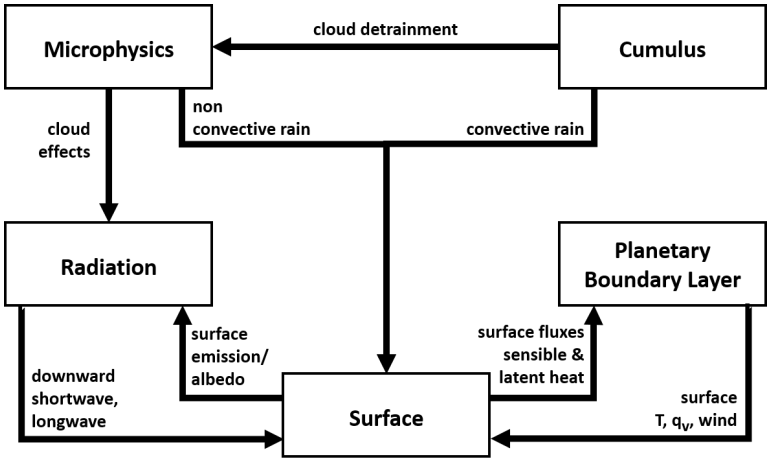

Figure 3.3: Schematic of physics modules and their interactions in the WRF model. Figure adapted from Dudhia (2014).

Skamarock et al. (2008) give details about all the modules and options available in the WRF model. Hereafter, a focus will be done on the WRF version 3.8.1 (with the ARW dynamics solver) which is the configuration used during this thesis, and on the modules and options which are used and tested in the Chapter 4.

3.2.1 Dynamics main properties

The ARW dynamics solver integrates the *fully compressible*, and *non-hydrostatic* Euler equations. The equations are given in flux-form using variables with conservative

properties (Skamarock et al., 2008). Moreover, the equations are formulated using a *terrain-following mass vertical coordinate* (Laprise, 1992). These assumptions are described below:

Fully compressible: Most of the atmospheric phenomena can be assumed as Boussinesq flows for which density perturbations are ignored, except where they appear in terms multiplied by the acceleration due to the gravity g (*i.e.* in buoyancy terms). This approximation that permits to simplify the continuity equation (Equation 3.2) is nonetheless not used in the WRF model. Thereby, considering a fully compressible dynamics, the atmospheric air parcel enables a quick and elastically response to all pressure disturbances. Consequently, the acoustic waves can be solutions of the equations integrated by the model leading to probable numerical instabilities even though acoustic waves do not have a notable influence on the meteorological processes. To avoid the presence of acoustic waves, WRF uses a time-split numerical method during the integration of the dynamics equations (Skamarock and Klemp, 1992) while other models such as Meso-NH (Lac et al., 2018) or Clark-Hall (Clark, 1977; Clark et al., 1996) use an anelastic assumption.

Non-hydrostatic: Mesoscale models, such as WRF, Clark-Hall, and Meso-NH, are used to study the development of fine-scale meteorological systems (*i.e.* convective systems) with intense vertical accelerations. These intense convective motions imply that the hydrostatic approximation according to which the vertical acceleration is assumed to be negligible, is not applicable in such numerical models. However, note that the hydrostatic approximation is justified in large-scale modelling and allows a considerable reduction in computational time (Spiga, 2008).

Vertical coordinate: Several vertical coordinates can be used in mesoscale models: the altitude z (orthogonal coordinate), the terrain-following altitude z' (non-orthogonal coordinate) (Clark, 1977; Gal-Chen and Somerville, 1975; Clark and Farley, 1984), and the pressure p (Eliassen, 1949). The WRF model uses a vertical pressure coordinate called η following the topography which is defined by the Equation 3.5:

$$\eta = \frac{p_h - p_{h,t}}{p_{h,s} - p_{h,t}} \tag{3.5}$$

where p_h represents the hydrostatic pressure at the level considered, $p_{h,s}$ the hydrostatic pressure at the surface, and $p_{h,t}$ the hydrostatic pressure at the top of the model. The coordinate η therefore varies between the value 1 on the surface of the model, up to 0 at the top, as shown in Figure 3.4a. This vertical coordinate is proposed by Laprise (1992) and permits to better take into account the topography of the terrain, thanks to higher density of levels towards the surface.

Considering these assumptions, the flux-form Euler equations describing the atmospheric fluid extended to their "moist" versions can be given as a function of $\mu_d(x, y)$ which represents the mass of the dry air in the column (x, y). The main variables are defined as:

$$\vec{V} = \mu_d \vec{v} = (u^\star, v^\star, w^\star)\,, \qquad \Theta = \mu_d \theta \tag{3.6}$$

where $\vec{v} = (u, v, w)$ is the wind and θ the potential temperature.

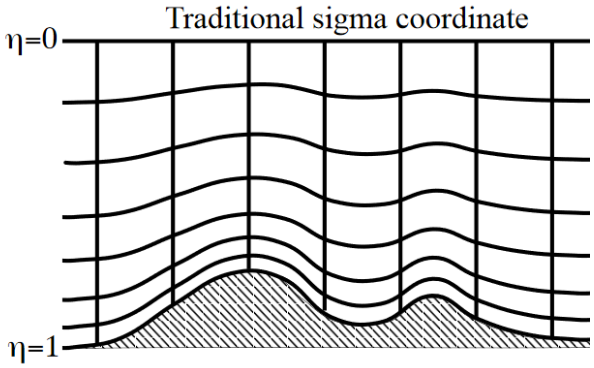

Figure 3.4: Schematic of the traditional vertical coordinate used in WRF Version 3. Figure from Skamarock et al. (2019).

With these definitions, the equations can be written (more details in Skamarock et al. (2008)) as follow:

$$\frac{\partial u^\star}{\partial t} = -(\nabla \cdot \vec{V} u) - \mu_d \alpha \frac{\partial p}{\partial x} - \left(\frac{\alpha}{\alpha_d}\right) \frac{\partial p}{\partial \eta} \frac{\partial \phi}{\partial x} + F_{u^\star} \tag{3.7}$$

$$\frac{\partial v^\star}{\partial t} = -(\nabla \cdot \vec{V} v) - \mu_d \alpha \frac{\partial p}{\partial y} - \left(\frac{\alpha}{\alpha_d}\right) \frac{\partial p}{\partial \eta} \frac{\partial \phi}{\partial y} + F_{v^\star} \tag{3.8}$$

$$\frac{\partial w^\star}{\partial t} = -(\nabla \cdot \vec{V} w) + g \left[\left(\frac{\alpha}{\alpha_d}\right) \frac{\partial p}{\partial \eta} - \mu_d\right] + F_{w^\star} \tag{3.9}$$

$$\frac{\partial \theta^\star}{\partial t} = -(\nabla \cdot \vec{V} \theta) + F_{\theta^\star} \tag{3.10}$$

$$\frac{\partial \mu_d}{\partial t} = -(\nabla \cdot \vec{V}) \tag{3.11}$$

$$\frac{\partial \phi}{\partial t} = -\left[(\nabla \cdot \vec{V} \phi) - gW\right] - \mu_d^{-1} \tag{3.12}$$

$$\frac{\partial Q_m}{\partial t} = -(\nabla \cdot \vec{V} q_m) + F_{Q_m} \tag{3.13}$$

where α_d and α are respectively the inverse density of the dry air ($\alpha_d = 1/\rho_d$) and the inverse density of the full parcel ($\alpha = \alpha_d \left(1 + \sum_n q_n\right)$, with q_n the mixing ratios (mass per mass of dry air) for water vapour and other species: cloud, rain, ice, snow...). $F_{u^\star}$, $F_{v^\star}$, $F_{w^\star}$, and $F_{\theta^\star}$ represent the forcing terms resulting from model physics, turbulent mixing, spherical projections, and earth's rotation.

Also, the following diagnostic relations give the dry inverse density and the full pressure (vapour plus dry air):

$$\frac{\partial \phi}{\partial \eta} = -\alpha \mu_d \tag{3.14}$$

$$p = p_0 \left(\frac{R_d \theta \left(1 + \left(R_v / R_d\right) q_v\right)}{p_0 \alpha_d}\right)^\gamma \tag{3.15}$$

with $\gamma = c_p/c_v = 1.4$ the ratio of heat capacities for dry air, R_d and R_v the gas constants for dry and moist air, and p_0 the reference pressure (assumed equal to 1000 hPa).

Equations 3.7 - 3.13 shows that the dynamics, the thermodynamics and the microphysics properties are tied in a cloudy environment.

3.2.2 Physics parameterisations

This section presents the physics modules used during this thesis according to the different categories illustrated in Figure 3.3. Note that no cumulus module is presented hereafter because no cumulus parameterisation is used in the simulations described in Chapter 4. Indeed, the cumulus module is helpful for simulations using coarse grid sizes (*e.g.*, greater than 10 km) because the sub-grid scale convective eddies cannot be resolved by the model (Skamarock et al., 2008). This is not the case in our simulations because the used grid sizes do not exceed 9 km and the formation of deep convection do not take place.

a) Surface properties

The surface properties are described thanks to both the surface layer module and the land-surface module. The surface layer module calculates the friction velocities and the exchange coefficients that enable the estimation of the surface heat and moisture fluxes by the land-surface module and the surface stress in the planetary boundary layer (PBL) module. The surface module provides the stability-dependent information about the surface layer for the land-surface and the PBL modules. Regarding the land-surface module, it used the atmospheric properties from the surface layer module, the radiative forcing from the radiation module, and the precipitation forcing from the microphysics module. No horizontal interactions are assumed in the land-surface module implying that it can be considered as a 1-D module for each grid-point.

For our simulations, we choose to use the surface layer module described in Janjić (2002), which is based on similarity theory (Monin and Obukhov, 1954), combined with the Noah land-surface module (Chen and Dudhia, 2001). This surface layer module explicitly parameterises the viscous sub-layer over the water surfaces. These modules are similar to those used in the polar version of WRF, as described *e.g.* in Hines et al. (2011).

b) Radiation

The radiation module allow to calculate the atmospheric temperature tendencies by means of the radiative flux divergence. In addition it also provides the LW and SW radiation for the surface heat budget. LW radiation includes thermal radiation absorbed and emitted by gases and surfaces. Upward LW (LW_u) radiative flux from the ground is determined by the surface emissivity which depends on the land-surface type and the ground temperature. SW radiation corresponds to the solar spectrum; the physical processes include the absorption, the reflection, and the scattering in the atmosphere and at the earth surfaces. The upward SW (SW_u) flux from the ground corresponds to the reflection due to the surface albedo (α). Within the atmosphere, the radiation mainly responds to cloud and water vapour distributions. Moreover, the radiation module is a one-dimensional module meaning that each column is treated independently and the fluxes correspond to those in infinite horizontally uniform planes with cloud fractions at each layer.

The atmospheric radiation module used in our simulations is the Rapid Radiative

Transfer Model for GCMs (RRTMG, Iacono et al. (2008); Iacono (2011)) which is a state-of-the-art widely used radiative module that has been implemented in many national and international dynamical model for weather (*e.g.* the Korean Integrated Model (KIM), the Chinese Global/Regional Assimilation and Prediction System (GRAPES), and the French Non-hydrostatic Meso-scale atmospheric model (Meso-NH)) and climate (*e.g.* the NCAR Community Atmosphere Model (CAM5), the ECMWF Integrated Forecast System (IFS), and the Laboratoire de Météorologie Dynamique (LMD) LMDZ climate model) applications. This module is based on the single-column correlated k-distribution reference module (RRTM, Mlawer et al. (1997)) and includes the Monte-Carlo Independent Column Approximation (McICA) technique (Barker et al., 2007; Pincus et al., 2003) for representing sub-grid cloud variability.

c) Planetary boundary layer (PBL)

The PBL module is responsible for vertical sub-grid scale fluxes due to eddy transports in the lower atmospheric column. The surface fluxes are provided by the surface layer and land-surface modules (see Section 3.2.2(a)). The PBL module calculates the flux profiles within the well-mixed boundary layer and the stable layer, and thus also contributes to the atmospheric tendencies of the temperature, the moisture, and the horizontal momentum in the entire atmospheric column. The module is one-dimensional, and assumes that there is a clear scale separation between sub-grid eddies and resolved eddies.

As explained in the Chapter 1, the properties of the Arctic MPCs can be impacted by the features of the boundary layer. Thus, the sensitivity of the MPCs' properties to the PBL representation is estimated and shown in the Chapter 4. Both PBL modules used in our simulations are the Mellor-Yamada-Janjic (MYJ) PBL module (Janjić, 1990, 1996, 2002) and the Mellor-Yamada-Nakanishi-Niino Level 3 (MYNN3) module (Nakanishi and Niino, 2006, 2009). The choice of the PBL parameterisations used for our simulations described in Chapter 4 is based upon the previous studies performed over polar regions (e.g., in Wilson et al., 2011; Tastula et al., 2012; Xue et al., 2022, among others).

The MYJ PBL module is a 1.5-order local closure module based on a prognostic equation for the turbulent kinetic energy (TKE). In this module, nonlocal transport associated with large eddies is considered by adding a counter gradient term in the heat and momentum transport equations. The module also includes a TKE diffusion outside the mixed layer, which combined with the counter gradient transport, improving the representation of the entrainment at the top of the PBL. The PBL height is designated as the height at which the TKE becomes lower than a TKE threshold equal to 0.2 $m^2\ s^{-2}$ (Njuki et al., 2022). The MYNN3 module, which is a modified version of the MYJ module, uses results from large eddy simulations (LES) to derive the expressions of stability and mixing length (whereas these expressions are derived from observations in the MYJ module). This modification makes the MYNN3 module suitable for applications over a wider range of static stability regimes (Cohen et al., 2015).

d) Microphysics

The microphysics modules include water vapour, (liquid- and ice-) cloud, and (liquid- and ice-) precipitation processes as described in Figure 3.5.

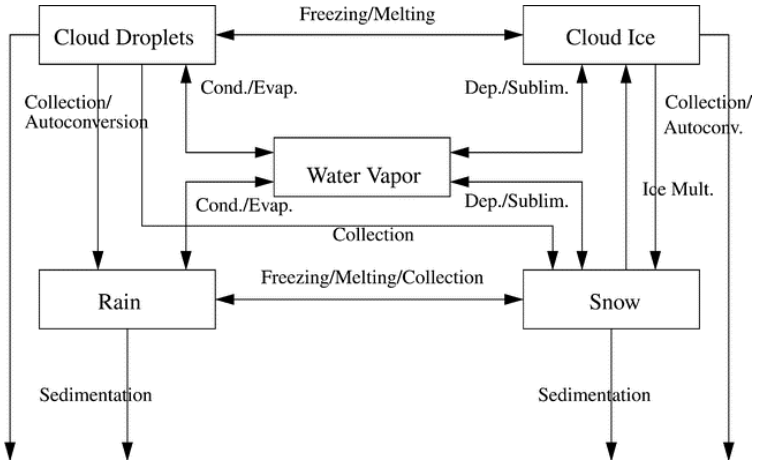

Figure 3.5: Interaction processes between the different categories of water in, *e.g.*, the microphysics module described in Morrison et al. (2005). Figure from Morrison et al. (2005).

In the version 3.8.1 of WRF, there are many microphysics modules available which are more or less sophisticated. In order to estimate how the properties of the Arctic MPCs can be impacted by the microphysics representation, we performed sensitivity studies (presented in the Chapter 4) using the two most widely used microphysics modules for Arctic cloud studies (as in Hines et al., 2011; Bromwich et al., 2009; Girard and Sokhandan Asl, 2014; Fu et al., 2019, among others), *i.e.* the Morrison et al. 2-moment scheme (Morrison et al., 2005; Morrison and Pinto, 2005; Morrison et al., 2009a) and the Milbrandt-Yau Double-Moment scheme (Milbrandt and Yau, 2005a,b).

The Morrison et al. 2-moment scheme is a bulk microphysics scheme with prognostic variables that include number (N) and mass mixing ratios (q) of cloud ice ($|_i$), rain ($|_r$), snow ($|_s$), and graupel ($|_g$) / hail ($|_h$), and the mixing ratios of cloud droplets ($|_c$) and water vapour ($|_v$) (10 variables in total). The prediction of two-moments (*i.e.* both number and mass mixing ratio) allows for a more robust treatment of the particle size distributions, which are essential in the calculations of the microphysical process rates and the cloud/precipitation evolutions. The particle size distributions for all hydrometeor categories are treated using gamma functions, $N(D) = N_0 D^{\mu} e^{-\lambda D}$, with the hydrometeor diameters D, and the associated intercept N_0, shape μ, and slope λ parameters. Both N_0 and λ are derived from the predicted mixing ratio q and number N of each hydrometeor species using the Equations 3.16 and 3.17 (whereas μ has a constant value):

$$\lambda = \left[\frac{cN\Gamma(\mu + d + 1)}{q\Gamma(\mu + 1)} \right]^{1/d} \tag{3.16}$$

$$N_0 = \frac{N\lambda^{\mu+1}}{\Gamma(\mu + 1)} \tag{3.17}$$

where Γ is the Euler gamma function and the parameters c and d are given by the assumed power-law mass-diameter relationship ($m(D) = cD^d$) of the hydrometeors for

each species (this mathematical relationship was also used to deduce the IWC from the airborne observations; see Section 2.2.2). For the precipitation species as well as the cloud ice $\mu = 0$ (*i.e.* giving exponential functions or Marshall-Palmer distributions). For the cloud droplets, μ is a function of the predicted droplet number concentration following the observations of Martin et al. (1994).

The Milbrandt-Yau Double-Moment scheme is a fully double-moment scheme that carries graupel and hail as separate species. It therefore has 12 prognostic variables in addition to the water vapour mass mixing ratio. As in the Morrison et al. 2-moment scheme, the particle size distributions are described using the three-parameter gamma distribution function treating N_0 and λ as prognostic parameters (with mass-diameter relationship) and holding μ constant, for each hydrometeor categories. Table 3.1 summarises the main assumptions of both the Morrison and the Milbrandt-Yau 2-moment schemes for the hydrometeor representations.

	Morrison scheme	**Milbrandt-Yau scheme**
Mass variables	q_x for $x \in \{v, c, r, i, s, g\}$	q_x for $x \in \{v, c, r, i, s, g, h\}$
Number variables	N_x for $x \in \{r, i, s, g\}$	N_x for $x \in \{c, r, i, s, g, h\}$
m-D coefficients	$c_x = \frac{\pi}{6}\rho_x$ & $d_x = 3$ for $x \in \{c, r, s, g, i\}$	$c_x = \frac{\pi}{6}\rho_x$ & $d_x = 3$ for $x \in \{c, r, s, g, h\}$ & $c_i = 440$ kg m^{-3}
Shape parameter	$\mu_x = 0$ for $x \in \{r, i, s, g\}$ $\mu_c = fct(N_c, T, p)$	$\mu_x = 0$ for $x \in \{r, s, g, i, h\}$ & $\mu_c = 3$
References	Morrison et al. (2005) Morrison and Pinto (2005) Morrison et al. (2009b)	Milbrandt and Yau (2005a) Milbrandt and Yau (2005b) Milbrandt and Yau (2006)

Table 3.1: Main characteristics of the both microphysics schemes used in this thesis in order to represent the different hydrometeor species. The definitions of the variables are given in the Section 3.2.2(d) and the subscripts $|_{(v,c,r,i,g,h)}$ correspond respectively to the water vapour, cloud droplet, rain drop, ice, graupel, and hail species. ρ_x corresponds to the density assumed for each species.

In the Morrison et al. 2-moment scheme (Morrison et al., 2009b), various options exist in order to represent a number of microphysics processes and the choices have to be done considering the studied cases. For example, when this scheme is used in WRF-Chem simulations, the droplet concentration can be predicted (Zhang et al., 2021) but in the WRF simulations, as performed during this thesis, a constant droplet concentration is set. The default value is 250 cm^{-3} but it has been adjusted in our simulations (see Chapter 4) according to the CCN concentrations observed over sea ice and open ocean surfaces during the ACLOUD campaign (see Chapter 2). The ice phase is formed via both the instantaneous freezing of droplets at temperatures lower than -40°C and the heterogeneous ice nucleation mechanisms which are active at warmer temperatures. Indeed, the Morrison et al. 2-moment scheme uses three parameterisations, which are all tied to the atmospheric temperature (T), to represent the different heterogeneous ice nucleation mechanisms: the deposition and/or the condensation freezing (active below -8°C) is parameterised according to Cooper (1986), and the contact and the immersion freezing (both active below -4°C) follow the works of Meyers et al. (1992) and Bigg (1953) respectively. Moreover, the ice particles can also be produced by secondary ice processes (SIPs), which results from, *e.g.*, the interactions of already-formed ice particles

with other ice particles or with supercooled droplets (as described in Field et al., 2017; Korolev and Leisner, 2020). In the Morrison et al. 2-moment scheme, the only SIP that has been implemented in the version 3.8.1 of WRF is the rime-splintering process (Hallett and Mossop, 1974; Mossop and Hallett, 1974; Mossop, 1976, 1985a,c,b), also known as the Hallett-Mossop process, which refers to the production of ice splinters after collisions of supercooled droplets with ice particles. This process is active only in a limited temperature range, between -3°C and -8°C, and requires the presence of supercooled liquid droplets. In addition to the T-condition, the Hallett-Mossop process is activated in the Morrison et al. 2-moment scheme when both the snow and cloud liquid (or rain) mass mixing ratios are greater than 0.1 g kg^{-1} and 0.5 g kg^{-1} (or 0.1 g kg^{-1}) respectively (corresponding to the same thresholds defined in Rutledge and Hobbs (1984)). Then, the number of the splinters is based on the mass of the rimed water assuming a diameter size of 10 μm.

In the Milbrandt-Yau Double-Moment scheme, three heterogeneous ice nucleation mechanisms are represented: the deposition freezing, the condensation freezing, and the contact freezing. The deposition and the condensation freezing are based on the parameterisation given by either Meyers et al. (1992) or Cooper (1986). Regardless of the parameterisation used, these two mechanisms are both activated at warmer temperatures (at T below than -5°C) in the Milbrandt-Yau Double-Moment scheme than in the Morrison et al. 2-moment scheme. The third mechanism considered in the Milbrandt-Yau Double-Moment scheme, which is the contact freezing, is represented according to Young (1974) and is activated at T below than -2°C. Regarding the cloud nucleation process, the droplet number concentration (activated aerosols) is calculated as a function of the vertical wind speed (w), the temperature (T), and the pressure (p) based on relations/methods developed by Cohard et al. (1998) and Cohard and Pinty (2000).

e) Physics interactions

Even if the physics parameterisations are categorised in different modules, many interactions (as illustrated in Figure 3.3) exist between these modules via the model variables (*i.e.* variables such as the potential temperature θ or the wind components u, v, w; see Equations 3.7-3.10) and their tendencies, and via the surface fluxes.

At each model timestep, the surface module, which interacts with all other modules (see Figure 3.3), updates the land variables but does not provide tendencies for the atmospheric variables; on the contrary, the microphysics module updates the atmospheric variables. The radiation and the PBL modules calculate the variable tendencies and the sum of them contributes to the forcing for the dynamics. Note that the radiation and the PBL modules can be called at their own frequency, which can be different than the model timestep. If they are called with lower frequencies, the tendencies calculated by each of these two modules are kept constant until the next call. Consequently, the WRF simulations normally use a less frequent call for the radiation module (it is called every 9 min in our simulations) because they are quite expensive. Even if a less frequent call is also possible for the surface and the PBL modules, they are called at every timestep in most simulations. Unlike for the other physics modules, there is no option in the dynamics solver to call the microphysics module at lower frequencies than the model timestep because of its important saturation adjustment function that interacts with the dynamics, especially in situations with resolved convection (*i.e.* with high resolution).

Thus, due to the different physics interactions, the radiation module is called first because of the required radiative fluxes in the land-surface module, which also requires rainfall from the microphysics module, but that is from the previous timestep since the microphysics module is considered at the end of the model timestep. The PBL module is necessarily after the land-surface module because it requires the heat and the moisture fluxes.

3.3 Model and simulation setup

The WRF model is composed by several systems (as illustrated in Figure 3.6): the WRF Pre-processing system (WPS), the dynamics ARW solver (described in Section 3.2), and the Post-processing tools. Note that the WPS is an essential system for the model initialisation and is directly influenced by the external data sources (*e.g.* the terrestrial and meteorological data) used for the simulations. All these systems will be presented in the following paragraphs, with emphasis on the configurations/properties used in the simulations described in the Chapter 4.

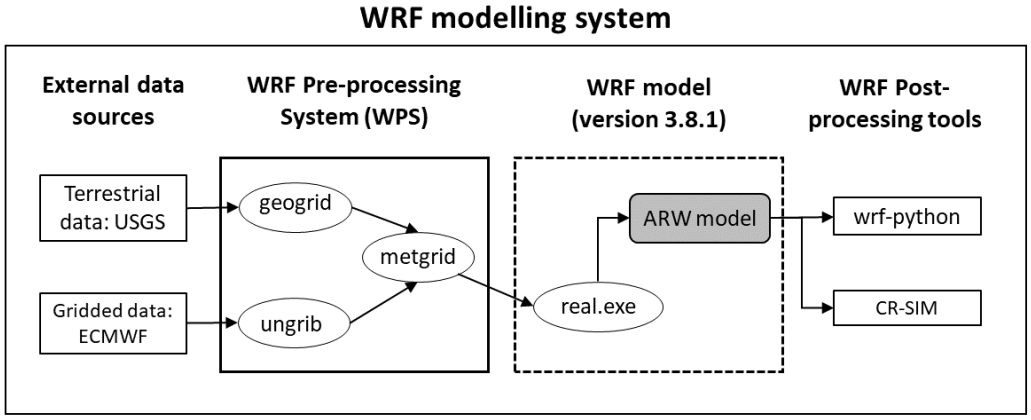

Figure 3.6: Diagram illustrating the flowchart for the version 3.8.1 of the WRF modelling system used in this thesis. Figure adapted from Wang et al. (2017).

3.3.1 WRF Pre-processing System (WPS) and external data sources

The WRF pre-processing system (WPS), which is consisted of three independent steps, is used to define the simulation domains, interpolate the terrestrial data to the simulation domains, and "ungrib" and interpolate the meteorological data from another regional or global model to the simulation domains.

The WPS first step is to configure the simulation domains and interpolate the terrestrial datasets (which correspond to the soil categories, land-use category, terrain height, annual mean deep soil temperature, monthly vegetation fraction, monthly albedo, maximum snow albedo, and slope category) to the model grids (using the *geogrid* program). For our simulations, the model domain is set to 120 × 120 points with a 9 km horizontal resolution. This domain (d01), with a polar stereographic projection in order to give a better representation of the Arctic domain, is centred close to Ny-Ålesund (Svalbard) at 78.5°N in latitude and 10°E in longitude. Two other domains (d02 and d03) are nested into the area of interest considering exchanges in both ways between the wider domain and the nested narrower domain (*i.e.,* a two-way nesting configuration is used). Indeed, previous studies found that two-way nesting produced better results (as in Harris and Durran, 2010) than one-way nesting (*i.e.,* exchanges only from the widest domain to the nested domain). The innermost domain (d03), which uses the finest resolution in our simulations (1 km), covers either the ACLOUD flight 19 path over the sea ice surface or over the open-ocean surface (see flight path in Figure 2.7). The horizontal domain configuration used for both SI and OO cases (described in the Chapter 2) is presented in the Table 3.2 (and illustrated in the Chapter 4). The terrestrial data applied over these domains are provided by the USGS (United States Geological Survey; Anderson et al. (1976)) which consider 16 soil-type categories and 24 land-use-type categories (listed in Wang et al. (2017)). In our simulations, the data with the highest resolution are chosen for each terrestrial field (2 m and 10 m).

Domain ID	Number of points horizontally	Horizontal resolution	Number of points vertically
d01	120 × 120	9 km	105
d02	274 × 232	3 km	105
d03	487 × 430	1 km	105

Table 3.2: WRF domain configuration for both SI and OO cases (which are described in the Chapter 2).

The WPS second step involves reading the GRIB external data (*i.e.* the time-varying meteorological fields from another regional or global model) and writing them to an intermediate (simpler) format (using the *ungrib* program). The last step of the WPS is, through the *metgrid* program, to horizontally interpolate the intermediate-format meteorological data onto the already defined simulation domains. The meteorological data used in order to initialise our simulations are extracted from ERA-5, which is the fifth generation ECMWF reanalysis data for the global climate and weather modelling (Hersbach et al., 2018b). The atmospheric thermodynamics (*e.g.* air temperature (T), specific humidity (SH), and geopotential height (gp)) and dynamics (wind U- and V-components) fields used in this thesis are given every 6 h across a specified number of pressure levels, and with a spatial resolution of 0.25° × 0.25° in latitude and longitude.

3.3.2 WRF processing system with the ARW dynamics solver

As illustrated in Figure 3.6, the WRF processing system is composed of two successive steps. Indeed, the fields generated by the WPS are used by the WRF *real.exe* preprocessor for vertical interpolation to the WRF model levels. In this step, the model

setup is specified using the same horizontal domain configuration as in the WPS and defining the properties of the vertical grid for all the domains. In order to resolve the low-level MPCs, 105 non-equidistant vertical levels were defined in all our domains (see Table 3.2 and Figure 3.7).

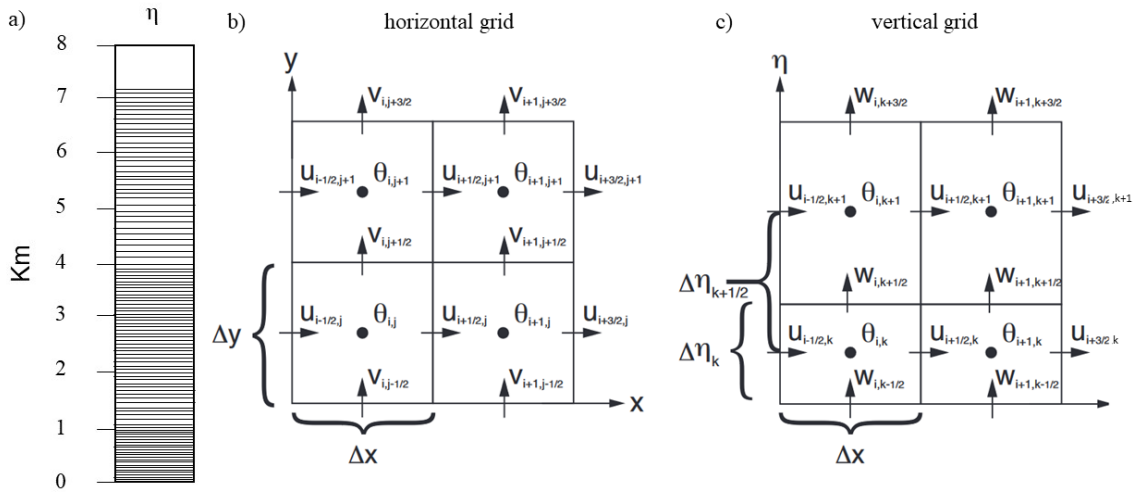

Figure 3.7: Diagrams illustrating (a) the η levels used in our simulations for all the domains, (b) the WRF horizontal and (c) vertical grids (with the wind U-, V-, and W- components and the potential (θ) temperature). Figure adapted from Wang et al. (2017).

After *real.exe* completion, the numerical integration is executed using the ARW (Advanced Research WRF) dynamics solver which performs time and space integrations of the atmospheric properties discretizing the equations (certain are given in the Section 3.2.1) on the specified horizontal and vertical grids and computing approximate solutions. The ARW dynamics solver uses a time-split integration scheme, low-frequency modes are integrated using a third order Runge-Kutta (RK3) time integration scheme, while the high-frequency acoustic modes are integrated over smaller time steps to maintain numerical stability (Skamarock and Klemp, 1992). Regarding the spatial grids, an Arakawa C-type grid is used where dynamics variables such as the wind components are resolved at the junction between the grid cells (*i.e.* staggered variables), while the other variables such as the potential temperature are resolved at the centre of each of them (*i.e.* unstaggered variables) (see Figures 3.7b-c). More details about the ARW numerical approaches are given in Wang et al. (2017).

3.3.3 Post-processing tools

At the end of the simulations, the WRF outputs NetCDF files are not directly ready to compare with ACLOUD observations because *e.g.* the outputs are given according to a vertical coordinate that is not physically useful or the needed variables are not available in these outputs and should be computed with the help of others variables and/or the assumptions of the used physics modules. Thus, in order to analyse the WRF outputs, many post-processing tools are available.

The WRF-python v.1.3.2 package (Ladwig, 2017), created by the NCAR (National Center for Atmospheric Research, Boulder, CO) and available on the following website:

http://wrf-python.rtfd.org, provides a collection of 30 diagnostic calculations, several interpolation routines, and utilities to help with plotting the outputs from the WRF model. So, I used part of these routines in order to calculate variables needed to make comparisons with ACLOUD observations and to interpolate the WRF outputs onto the altitudes of the Polar 5 and Polar 6 flights. When the comparative analyses between the ACLOUD data and the WRF results required options which are not available in the WRF-python package I developed adapted Python routines.

Moreover, in order to do the WRF-MiRAC (see Section 2.2.1) comparisons, I run the Cloud-resolving model Radar SIMulator (CR-SIM; Oue et al. (2020)). The CR-SIM uses outputs from high-resolution cloud-resolving models such as WRF to emulate multi-wavelength, zenith-pointing, and scanning radar observables and multi-sensor (radar and lidar) products. It allows direct comparisons between the results of our WRF simulations to the remote-sensing MiRAC product (*i.e.* the reflectivity at 94 GHz) using a forward-modelling framework consistent with the assumptions used in the microphysics module. Indeed, this simulator is adapted to compute radar and lidar observables by integrated scattering properties over the discrete PSDs, using a constant bin size for each hydrometeor species, based on the used microphysics module. The environmental variables such as the pressure, the temperature, the dry air density, and the height above the sea level are obtained from WRF outputs. The single-scattering properties are calculated using the T-matrix method (Mishchenko, 2000) and look-up tables (Ryzhkov et al., 2011). The CR-SIM is licensed under the General Public Licence (GNU) and both the software and the user guide are online (Tatarevic et al., 2019). Figure 3.8 shows an example of reflectivity fields produced by CR-SIM for either each hydrometeor species considered in the used microphysics scheme or for the whole species of hydrometeors. Thus, it allows to understand the contributions of each hydrometeor species to the radar reflectivity field.

The WRF model, with these assumptions and configurations, will be used in the following chapter to study the sensitivity of the MPCs observed during the ACLOUD campaign over various types of surfaces (sea-ice and open-ocean) to thermodynamics, microphysics and boundary layer properties.

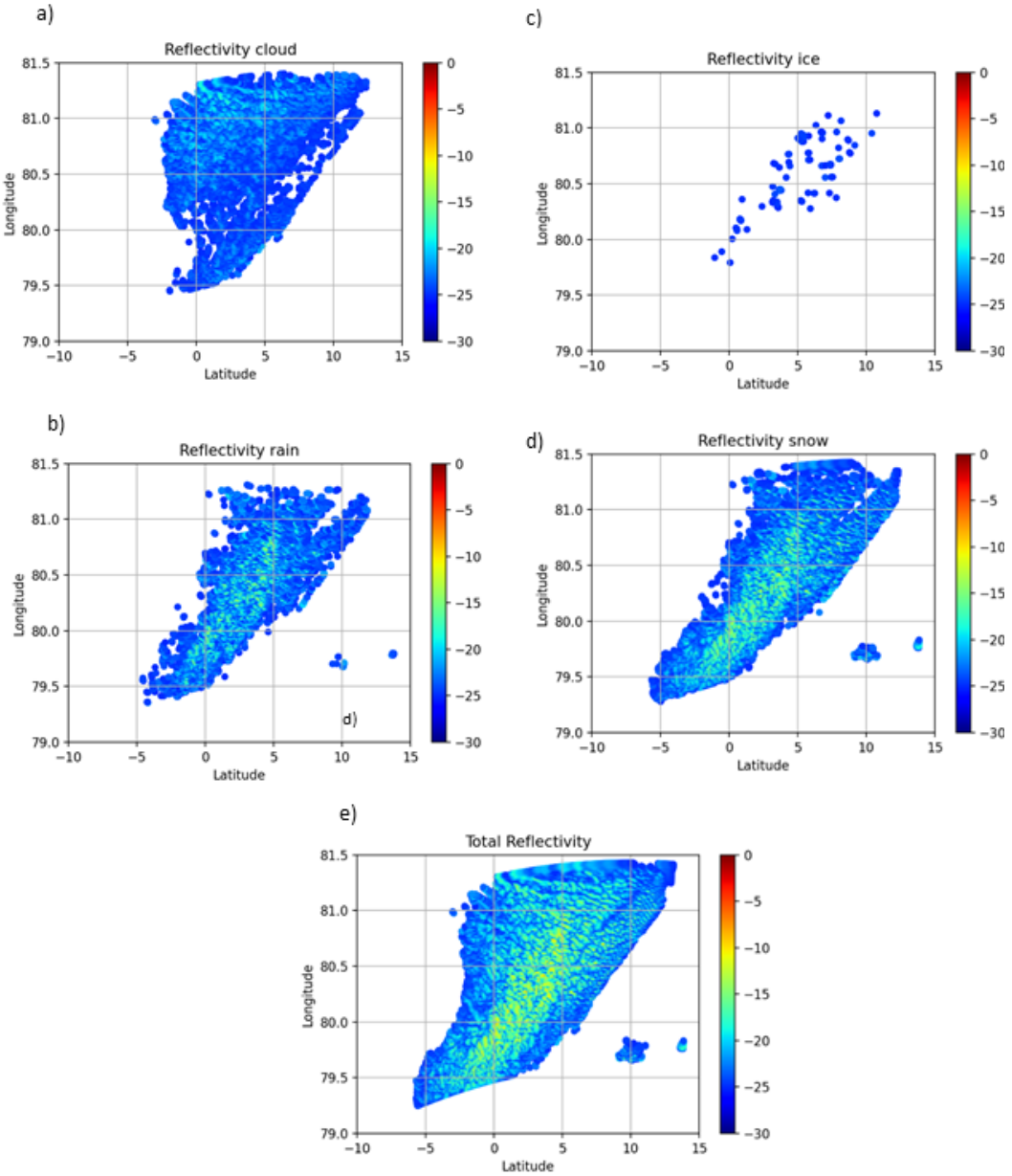

Figure 3.8: Illustration of the CR-SIM outputs. Horizontal cross section at 300 m altitude of the 94 GHz radar reflectivity field (in dBZ) for each hydrometeor species: (a) cloud, (b) rain, (c) ice, (d) snow, and (e) for all the hydrometeors.

Chapter 4

Modelled MPCs under different environmental conditions

In the previous chapters, the prevailing synoptic conditions and the temporal and spatial evolution of the two mixed-phase cloud systems observed during the flight 19 of the ACLOUD campaign over different surface types (*i.e.,* over sea ice (SI) or open ocean (OO)) have been discussed, as well as the characteristics of the WRF model.

The present chapter is dedicated to the simulation of these two ACLOUD cases with the WRF model. The analysis of the simulation results takes place in order to confirm the model's ability to represent such Arctic clouds and provide information on the occurring processes for these two MPC cases according to their different environmental (or thermodynamics) conditions and surface properties. Also, sensitivity studies of cloud microphysics to CCN concentration have been performed in order to assess the impact of air pollution on the MPCs' properties for both cases.

The results presented in this chapter correspond to a scientific article currently submitted for peer-review. This chapter/paper is organised as follows: first, an intercomparison between the available observations is presented in order to specify the environmental conditions and the microphysics properties of the two different cases; then, the baseline simulations obtained with WRF for both SI and OO cases are described illustrating the role of the initial set-up for the thermodynamics as well as the considered physics parameterisations; and lastly, sensitivity studies focussing on the impact of the CCN concentration on the distribution of the cloud condensed (liquid and ice) phases are described.

Arctic mixed-phase clouds simulated by the WRF model: Comparisons with ACLOUD radar and in-situ airborne observations and sensitivity of microphysics properties

Diana Arteaga[(1)], Céline Planche[(1,2,*)], Frédéric Tridon[(3,1)], Régis Dupuy[(1)], Antoine Baudoux[(1)], Sandra Banson[(1)], Jean-Luc Baray [(1)], Guillaume Mioche[(1)], Wolfram Wobrock[(1)] and Olivier Jourdan[(1,*)]

[(1)] Université Clermont Auvergne (UCA), CNRS-INSU, Laboratoire de Météorologie Physique (LaMP), OPGC, F-63000 Clermont-Ferrand, France.

[(2)] Institut Universitaire de France (IUF).

[(3)] DIATI, Politecnico di Torino, Turin, Italy.

Corresponding authors [(*)]: celine.planche@uca.fr & olivier.jourdan@uca.fr

Highlights

- Mixed phase cloud microphysical properties vary with the underlying surface
- Better cloud representativeness when using finer vertical grid for initiation data
- Cloud vertical properties impacted by boundary layer and microphysics schemes
- The modelled ice crystal number and mass concentrations are underestimated
- Increasing the droplets concentrations leads to an increase in both cloud phases

Abstract

The microphysics of two mixed-phase cloud systems (MPCs), one over sea ice, another over open ocean, was investigated using in-situ probes and cloud radar on-board aircrafts during the ACLOUD field campaign, west of Svalbard on 17 June 2017. Observations were compared to WRF simulations using different model configurations. This comparison reveals discrepancies in the vertical profile of the ice crystals concentrations for both MPCs due to slightly higher temperatures in WRF than observed, affecting the ice formation. Sensitivity analyses address the impact of assumptions used for the microphysics (MP) and the boundary layer (BL) schemes on the simulated vertical properties of the MPCs. The role of the vertical resolution of the large scale data used for model initialisation was also investigated. Results show that the model performance improves for large scale initialisation with more numerous levels close to the surface. Moreover, modifying the BL or MP scheme influences the altitudes of the cloud top and base, and the liquid and ice water amounts. This study also highlights how an increase in the CCN (cloud condensation nuclei) and droplet concentrations can impact the vertical profiles of the liquid and ice water amounts.

Keywords: Arctic cloud microphysics, WRF modelling, CCN, surface properties.

1. Introduction

This section has been deleted to avoid repeating the elements of context and the current scientific questions already presented in the Chapter "Introduction" of this thesis manuscript.

2. ACLOUD observations

The ACLOUD (Arctic CLoud Observations Using airborne measurements during polar Day) field study was conducted within the framework of the ”Arctic Amplification: climate relevant atmospheric and surface processes, and feedback mechanisms” $(AC)^3$ project (Wendisch et al., 2017, 2019). The ACLOUD campaign took place between 23 May and 26 June 2017 in the North-West of the Svalbard archipelago (covering 76-81°N and 10-28°E). This region is known to be influenced by different air mass types (e.g., intrusions of warm air from the South or cold air from the Arctic Ocean) and by long range transport of aerosols and pollutants from the mid-latitudes (Knudsen et al., 2018; Wendisch et al., 2023). It is located between the Greenland Sea and the Arctic Ocean and characterised by transitioning zone between sea ice and open ocean in spring (Young et al., 2016). As shown in Knudsen et al. (2018), various synoptic conditions impacted the region during the ACLOUD campaign. Three key periods were identified: a cold period (CP; 23-29 May), a warm period (WP; 30 May-12 June) and a normal period (NP; 13-26 June). The associated changes of the synoptic conditions lead to sudden variations in the atmospheric thermodynamics properties and cloud structures (Ruiz-Donoso et al., 2020; Wendisch et al., 2023).

2.1. ACLOUD flight 19

Flight 19 performed on the 17 June 2017 lasted more than 5 hours and permitted to sample two different cloud structures over either sea ice or open ocean surfaces corresponding to, respectively, the SI and the OO cases studied hereafter. Figure 1a shows the collocated flight tracks of both aircraft on the 17 June 2017. Note that there is approximately a 7 minutes gap between the two aircrafts for both cases (Polar 5 is ahead of Polar 6). Polar 5 always flew at higher altitudes than the Polar 6 (Figure 1b) permitting to observe the overall thermodynamic and microphysical structure of the cloud using dropsondes and remote sensing measurements. On the contrary, Polar 6 flew at lower altitudes, i.e., inside the low-level mixed-phase clouds (MPCs), using a staircase strategy in order to analyse the profile of cloud microphysics properties (ice and droplet concentrations) thanks to the on-board in-situ probes.

The different instruments available on the Polar 5 and Polar 6 during the flight 19 performed on the 17 June 2017 and the associated atmospheric parameters are:

1. *Vertically pointing MIRAC 94 GHz cloud radar (Polar 5)* (Küchler et al., 2017) provides the radar reflectivity Z_e (in $mm^6\ m^{-3}$) and then the reflectivity factor $Z = 10\ log_{10}Z_e$ (in dBZ) with an uncertainty of 0.5 dBZ (Mech et al., 2019). The data set is available via Kliesch and Mech (2019);
2. *Airborne Mobile Aerosol Lidar (AMALI) system (Polar 5)* (Stachlewska et al., 2010) informs on the cloud top height. The processed data of MiRAC and AMALi were merged and published in a combined data set: Kliesch and Mech (2019) and Neuber et al. (2019), respectively;
3. *Dropsondes (Polar 5)* which were operated by AVAPS (Advanced Vertical Atmospheric Profiling System; Ikonen et al. (2010)) provide vertical profiles of air temperature, humidity, pressure, and horizontal wind vector between the typical flight altitude of 3-4 km and the surface with a vertical resolution of 5 m (Ehrlich et al., 2019b);
4. *Cloud droplet probe (CDP) (Polar 6)* gives the droplet number size distribution (DSD) over the size range from 2 µm to 50 µm (with a 1-2 µm bin width) (Ehrlich et al., 2009) permitting to derive microphysics quantities such as the liquid water content (LWC) and the concentration of droplets (N_{drop});
5. *Cloud imaging probe (CIP) (Polar 6)* gives the size and the shape of cloud particles (Baumgardner et al., 2011) with a nominal size ranges of 25 to 1550 µm with a 25 µm resolution hereafter called the particle size distributions (PSD). Non-spherical ice

crystals were separated from liquid droplets based on their circularity parameter (circularity larger than 1.25 and image area larger than 16 pixels) following the approach developed by Crosier et al. (2011). Only these non-spherical particle images were used for the computation of the ice phase properties. In the analysis of the particle concentration only the sizes >75 µm were considered with an uncertainty of 50% (Baumgardner et al., 2017). The ice water content (IWC) is then derived considering the maximum dimension (D_{max}) for the non-spherical crystals as the diameter (D) (see Leroy et al. (2016) for details) and an adapted power law mass-diameter (m-D) relationship, such as the relation of Brown and Francis (1995) which is widely used in the literature for mixed-phase clouds (e.g., Crosier et al. (2011), and Lloyd et al. (2015)). DSD and PSD data are published in Dupuy et al. (2019);

6. *Aerosol particle number (Polar 6)* is observed by a condensation particle counter (CPC TSI-3010) providing the total number concentration of particles in the diameter range 10 nm to 3 µm (Mertes et al., 1995). The number of cloud condensation nuclei (CCN) are determined from measurements with a counterflow virtual impactor (CVI) (Twohy et al., 2003; Ehrlich et al., 2019a). In order to determine the concentration of ice-nucleating particles (INP), we used the parameterisation of DeMott et al. (2010) which relates the INP concentration (in L^{-1}) to the air temperature T and the number concentration of the aerosol particles with diameters larger than 0.5 µm (in cm^{-3}).

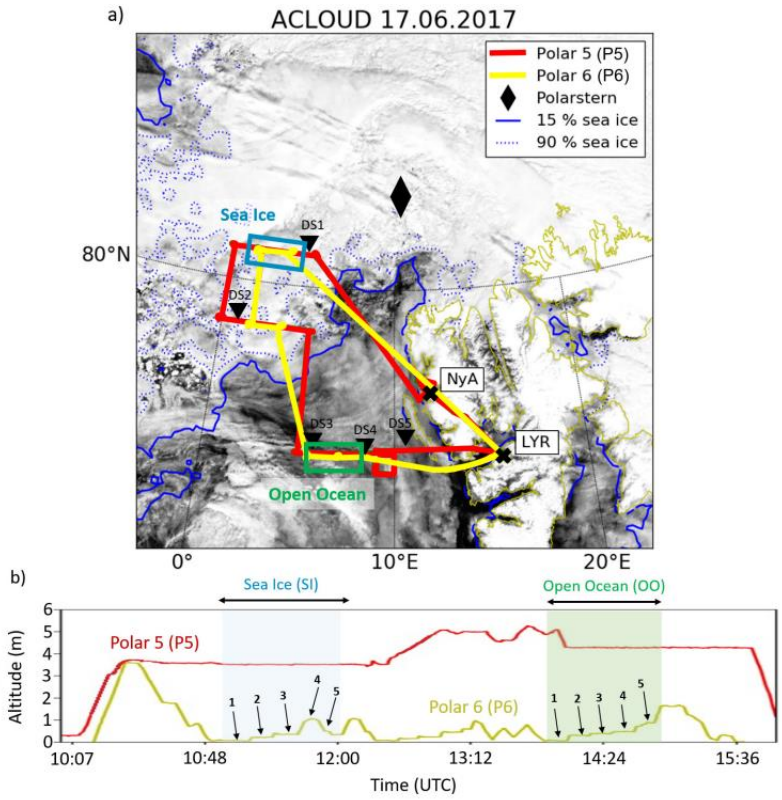

Figure 1. Flight paths (a) and altitudes (b) for both the Polar 5 (P5, in red) and the Polar 6 (P6, in yellow) aircrafts done on the 17 June 2017 (*i.e.*, the ACLOUD flight 19). Note that Polar 5 performed three horizontal paths at several constant altitudes. The solid and dotted blue lines indicate the 15% and the 90% sea ice concentration (derived from the AMSR2 measurements; Ludwig et al. (2019)). The white shading represents the cloud cover (visible image from MODIS). Locations where the dropsondes (DS) were released are marked by black triangles. Blue and green rectangles on both panels present the domain analyses for, respectively, the sea ice (SI) and the open ocean (OO) case studies. The small numbers on panel b) indicate the legs (*i.e.*, periods when the aircraft flew at constant altitude) performed by the P6 aircraft. The distance between the SI and OO domains is approximately 245 km.

This instrumental setting permits to characterise the structures of two cloud systems present on the 17 June 2017 over sea ice at 12:00 UTC (noon local time) and over open ocean at 14:00 UTC (afternoon local time), respectively called SI and OO cases hereafter (see locations in Figure 1).

2.2. Overview of the two case studies

In this section, the vertical structure of temperature and humidity, aerosol properties, and cloud microphysics features observed for both situations are analysed in order to give the main cloud characteristics of the two SI and OO cases.

2.2.1. Synoptic and thermodynamic conditions

The synoptic conditions are given by the operational reanalysis data of the ERA-5 from the European Centre for Medium-Range Weather Forecasts (ECMWF) (Copernicus Climate Change Service (C3S), 2017) which provides data on a 0.25° x 0.25° horizontal grid. Figures 2a-c show the 750 hPa geopotential height, relative humidity with respect to liquid water (*RH*) and temperature (*T*) as well as the surface pressure fields on the 17 June 2017 at 12:00 UTC.

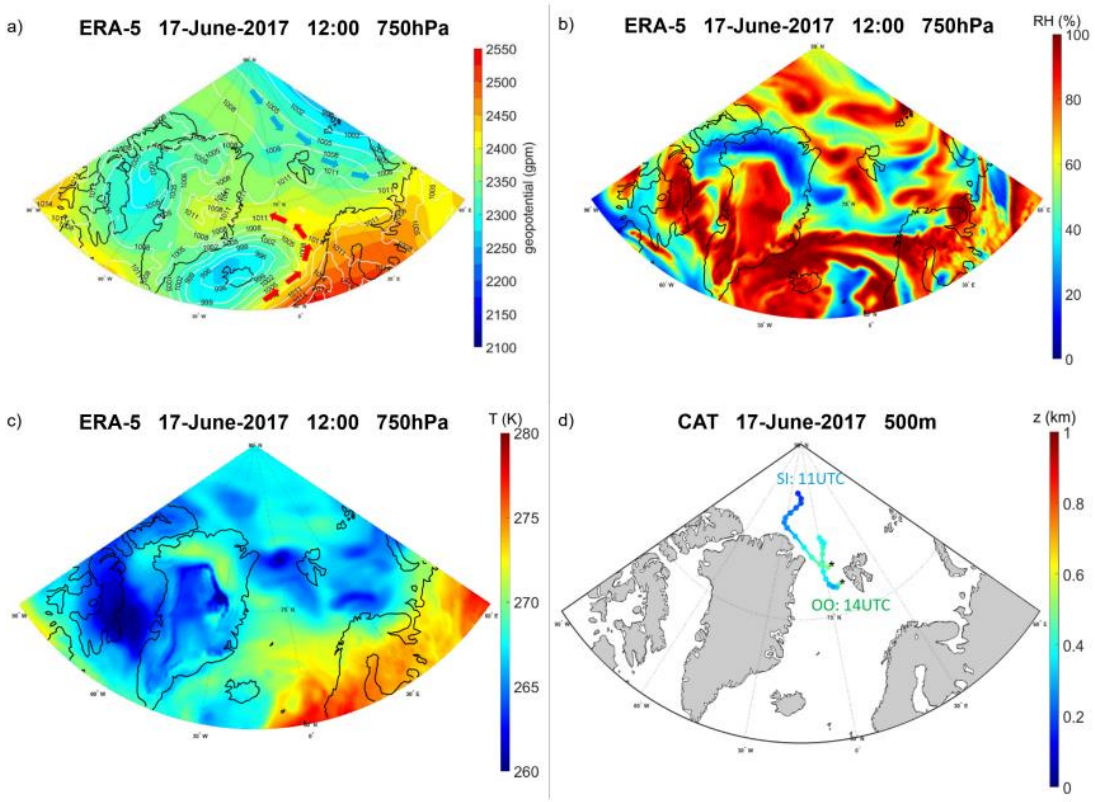

Figure 2. Synoptic maps of the ERA-5 reanalyse product provided by ECMWF on 17 June 2017 at 12:00 UTC for (a) the sea level pressure (in hPa; white contours) and the 750 hPa geopotential heights (in meters; colour scale), (b) the relative humidity (RH) (in %), and (c) the air temperature *T* (in K). Blue and red arrows on panel (a) represent the two air masses towards the Svalbard archipelago. Panel (d) illustrates the 72 hours mean mass back-trajectories calculated from the positions represented by the black stars. These start points correspond to the P6 aircraft position in longitude and in latitude at 11:00 UTC and 14:00 UTC respectively, and at an altitude of ≈ 500 m (corresponding to the SI and the OO cases).

Figure 2a shows that three low (L) pressure systems were present around the ACLOUD region at approximately 2.5 km height: the first one centred over Iceland, the second one over the Baffin Sea west of Greenland, and the third one at the North-East of the Svalbard archipelago. In addition, a weak high (H) pressure system was located over Northern Europe. These

synoptic conditions induced two main air masses around the Svalbard archipelago: a cold polar air mass coming from the North Pole (blue arrows) and a temperate air mass from the North Atlantic Ocean via the Norwegian Sea (red arrows). Note that the latter air mass is regularly observed in this region bringing moisture and heat from mid-latitudes to higher latitudes (Sorteberg and Walsh, 2008; Tjernström and Graverson, 2009; Woods et al., 2013; Dufour et al., 2016; Yu et al., 2019, among others). These two air masses caused important variations in the temperature and relative humidity fields in the vicinity of the ACLOUD region (Figures 2b-c). The *RH* is in average equal to 87% over the ACLOUD flight 19 area with several saturation spots. *RH* decreases sharply to about 40% or 50% at the South or the North of the ACLOUD area. We can note that temperature increases by 7°C and humidity drops to 52% at the North of the Svalbard archipelago. In the opposite, a cooler air spot present at the West of the Svalbard archipelago is associated increasing *RH*. These thermodynamics conditions induce weather changes which can promote cloud formation and persistence (as in Savre et al., 2014).

The vertical thermodynamics properties for our both case studies can be illustrated by the observations of the dropsondes (DS) released from the Polar 5 aircraft. Two of these dropsondes are specifically used to describe *T* and *RH* profiles of both case studies: DS1 which was released over sea ice surface at 11:20 UTC and DS4 which was launched over the ocean at 14:25 UTC (see for both positions Figure 1a). Figure 3 presents the skew-T log-P diagram obtained from the DS1 and DS4 measurements.

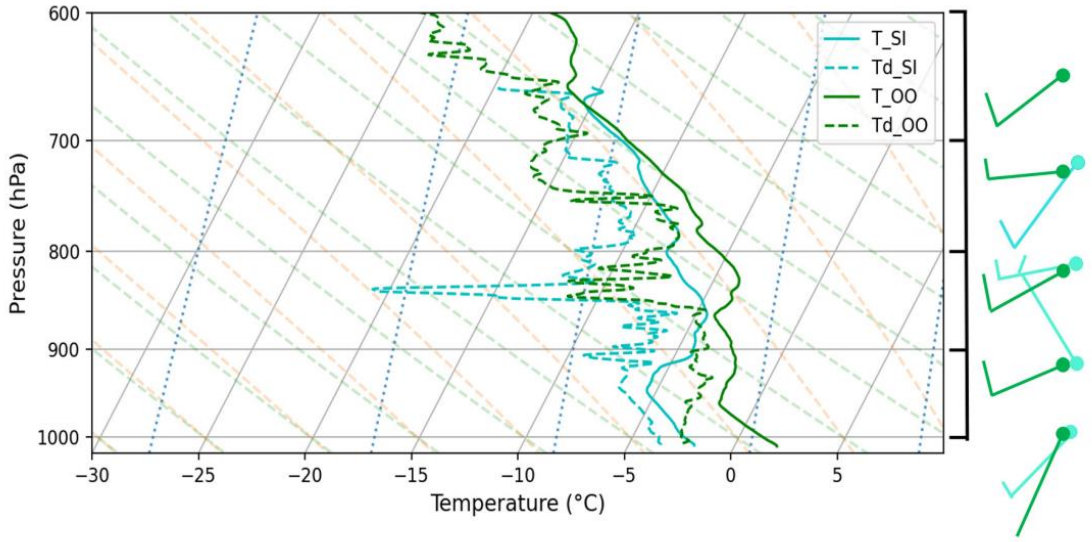

Figure 3. Skew-T Log-P diagram with the vertical profiles of the air temperature *T* (solid lines) and the dew point temperature T_d (dashed lines) measured from the dropsondes DS1 and DS4. These dropsondes are released at 11:20 UTC (DS1) over sea ice surface (SI: in light blue) and at 14:25 UTC (DS4) over open ocean surface (OO: in green). The positions of DS1 and DS4 are represented in Figure 1a. The barbs show the vertical properties of the horizontal wind speed and direction for both situations.

Figure 3 shows that the surface temperature is equal to -2°C for the SI case whereas it reaches +2°C for the OO case. At 950 hPa (around 500 m), a temperature inversion occurs in both cases reaching up to 860 hPa for SI and up to 920 hPa for OO. An elevated inversion layer can also be detected for OO reaching from 860 hPa to 820 hPa. Figure 3 shows that the Lifting Condensation Level (LCL) can be estimated at approximately 980 hPa (around 200 m altitude) for SI whereas it is slightly higher for OO (at 940 hPa, i.e. around 500 m altitude). Next to the temperature inversions located at approx. 950 hPa, low-level thin clouds occurred in both SI and OO cases, which is confirmed by the radar reflectivity measurements shown in Section

2.2.3. Moreover, according to the elevated relative humidity (*RH* = 95%) observed in DS1 and DS4 measurements, a second cloud layer was present at higher altitudes (around 2500 m altitude) for both OO and SI cases (see also Section 2.2.3). However, as for the low-level clouds, the base of these mid-level clouds is slightly higher in the OO case in comparison with the SI case.

2.2.2 Air masses origin and aerosol properties

Arctic cloud properties are strongly linked to the air mass origin and thus to the aerosol properties (Gultepe et al., 2000; Gultepe and Isaac, 2002). The air mass origin for both cases are studied using the 3D kinematic trajectory CAT model (Computing Advection-interpolation of atmospheric parameters and Trajectory tool; Baray et al. (2020)) in a backward mode. CAT is initialised with the wind fields from the ERA-5 reanalysis data (Hersbach et al., 2018a,b) provided by the ECMWF organisation and generated using the Copernicus Climate Change Service information. The back-trajectories are calculated over 72 hours using this dynamical tool over a topography matrix with a horizontal grid resolution of ≈ 10 km, and wind field data with a spatial resolution of 0.25° in latitude and longitude, provided every 3 hours. The number of vertical levels was set to 20 between 1000 hPa and 300 hPa. The initial spatial and temporal coordinates (represented by the black stars in Figure 2d) were defined accordingly to the position of the Polar 6 aircraft at 11:00 UTC and 14:00 UTC for the SI and the OO case, respectively and at an altitude of 500 m (which corresponds to in-cloud conditions for both cases according to Figure 3). Figure 2d shows that the air mass origin of both cases came from the North of the Svalbard, staying over sea ice surfaces, and remained in the atmospheric boundary layer (i.e., below 500 m altitude). Note that in the free atmosphere, the air mass towards the Svalbard archipelago is coming from the North-East for the SI case whereas it is coming from the West for the OO case (Arteaga, 2023).

The CPC instrument deployed on the Polar 6 aircraft is used to measure the aerosol concentrations. For the SI case, the median value of the aerosol concentration ($N_{AP,SI}$) is equal to 13 ± 63 cm^{-3} whereas for the OO case $N_{AP,OO}$ is equal to 3000 ± 365cm^{-3}. This significant difference in N_{AP} could be explained by the varying environmental surface conditions. The high value over open ocean can be due to local sea salt emissions, and by the pollution (note that contrasted N_{AP} values according to surface properties are also discussed in Wendisch et al. (2019, 2023)). Regarding the CCN concentration, the median value measured for the SI case ($N_{CCN,SI}$) is 9 cm^{-3} which is quite low but comparable with observations performed at the North of the Svalbard archipelago (Tjernström et al., 2014; Leck and Svensson, 2015). Observations of the CCN concentration for the OO case ($N_{CCN,OO}$) are not available because of the malfunction of the dedicated instrument during the ACLOUD flight 19. Wendisch et al. (2019) found that the CCN concentration over open ocean surfaces ($N_{CCN,OO}$) is in average equal to 100 cm^{-3} during all the ACLOUD period and Baudoux (2022) estimated that $N_{CCN,OO}$ is in average equal to 28 cm^{-3} when focusing only on measurements done from 13 to 26 June 2017 under synoptic conditions similar to the OO case. The temporal evolution of the INP concentrations can be determined using aerosol observations and the parameterisation of DeMott et al. (2010). Using this method, the median values estimated for $N_{INP,SI}$ and $N_{INP,OO}$ are respectively equal to 8.19 x 10^{-4} L^{-1} and 8.5 x 10^{-3} L^{-1}. We can note that our estimated INP concentrations over open ocean (OO case) are higher than over sea ice surfaces (SI case) which is similar than in previous studies performed over the same region (Young et al., 2016).

2.2.3 Cloud microphysics properties

This section focuses on the observations done by the MIRAC 94 GHz cloud radar (Polar 5) and the on-board cloud probes (Polar 6) deployed during ACLOUD to characterise the in-cloud properties.

Figure 4 shows the temporal evolution of the vertical profiles of the radar reflectivity (*Z*) obtained with MIRAC (Küchler et al., 2017; Mech et al., 2019) for both cases. For the SI case, two types of clouds are present: low-level clouds (200-600 m) with precipitating ice and droplets close to the cloud top and mid-level clouds (1500-3500 m) with vertical bands of Z which could be associated to precipitating ice crystals (Figure 4a). For the OO case (Figure 4b), two types of clouds are also observed but with cloud bases at higher altitudes than for the SI case: low-level clouds (300-1000 m) with small precipitation bands below and mid-level clouds (2200-3500 m) with stronger precipitation (thick vertical bands of *Z* below the cloud base). Both radar reflectivity fields are consistent with our analysis of the skew-T log-P diagram given in Section 2.2.1. Figure 4b also shows that, unlike in the SI case, the two cloud layers are not concomitant in the OO case. Moreover, the round-trip done by the Polar 5 aircraft permits to identify the temporal development of the mid-level clouds with, in particular, the intensification of the precipitation (especially for the OO case).

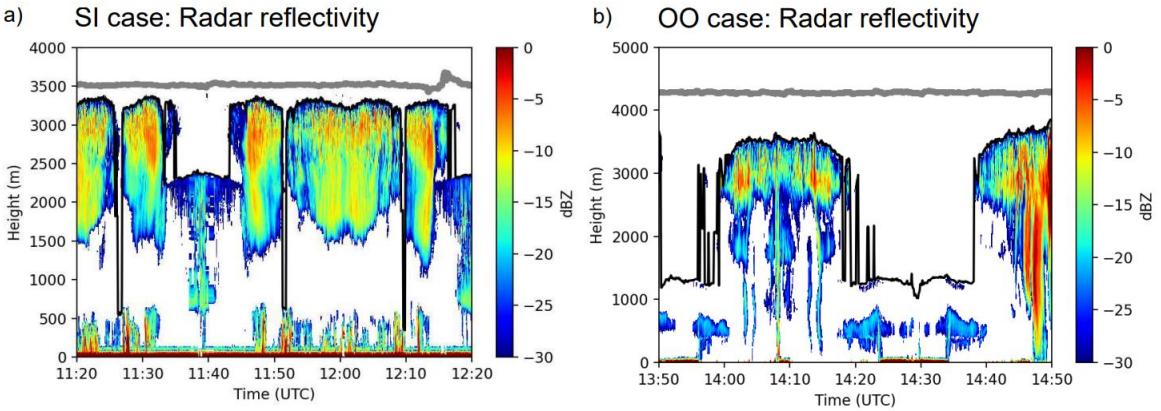

Figure 4. Temporal evolution of the profile of the radar reflectivity obtained with the 94 GHz MIRAC cloud radar system deployed on-board the Polar 5 (P5) aircraft for (a) the SI case and (b) the OO case. The grey thick solid lines represent the P5 flight altitude. The black thin solid lines describe the altitude of the cloud top determined by the AMALi lidar system. Note that the Polar 5 aircraft turned back several times over the SI (at 11:40 UTC and 12:00 UTC) and OO (at 14:10 UTC and 14:30 UTC) domains.

Polar 6 in situ measurements were performed at altitudes below 1 km, according to the Figure 1b. Thus, the microphysics probes only sampled the low-level clouds and the precipitation from mid-level clouds in both cases. Figures 5a-b show the mean cloud droplet size distributions (DSD) and ice particle size distributions (PSD) derived from CDP and CIP data for each leg performed by the Polar 6 (Figure 1b) for the SI and OO cases. Ehrlich et al. (2009) have shown that the ice-PSDs remain quite similar whatever hypothesis was made to calculate the particles diameter (i.e., the maximum diameter D_{max} (Leroy et al., 2016), the equivalent diameter D_{eq} (McFarquhar and Heymsfield, 1996), or the circumpolar diameter D_{cc} (Brown and Francis, 1995)). We consider in this study the maximum diameter D_{max} of the ice particles to compute the PSDs (see in Section 2.1).

Figure 5 shows the PSDs obtained for the different flight legs. For the SI case the PSDs extends to larger sizes than for the OO. For the SI case (Figure 5a), leg 4 reveals that only few droplets and no ice particles are present at an altitude of 1000 m. Figure 5a also shows that the mean PSD obtained for the leg 5 is slightly different than for the three others legs: ice particles with diameters < 400 µm are less numerous. The shorter period (only 2 min) of measurement for the leg 5 (see Figure 1b) or the temporal gap (≈ 15 min) between this leg with all the other legs might explained this difference for the SI case (the properties of the sampled mixed-phase clouds could have evolved). Regarding the OO case, Figure 5b shows that, even if the DSDs' shapes are quite similar than for the SI case, the droplets are slightly

more numerous (OO: 75 cm^{-3}; SI: 51 cm^{-3}) and have larger sizes (OO: 50 µm; SI: 40 µm). The higher aerosol (or CCN) concentrations observed for the OO case (see Section 2.2.2) could have impacted the droplet microphysics properties. Figure 5b also shows that the ice particles remain smaller and less numerous in the OO case than in the SI case.

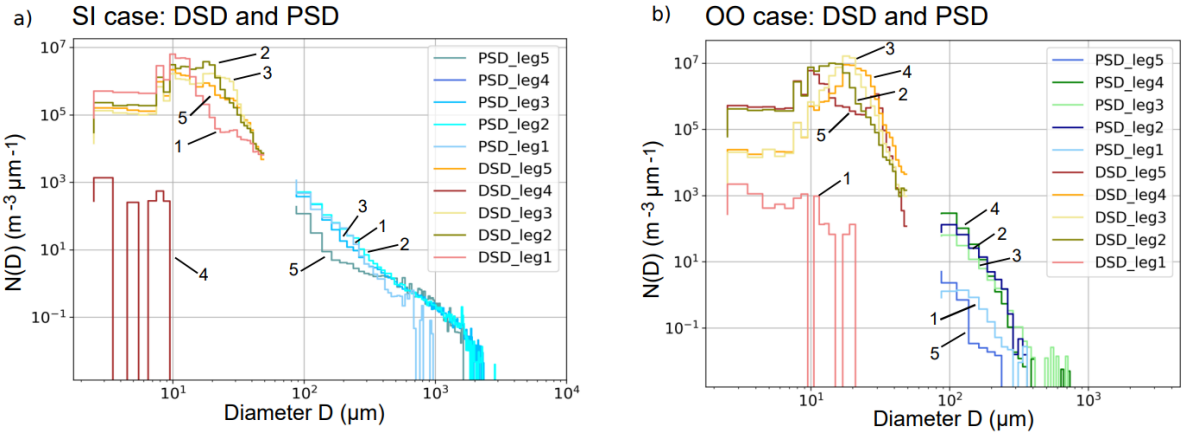

Figure 5. Median (calculated with ≈ 350 individual spectre for each leg) droplet size distributions (DSDs) and ice particle size distributions (PSDs) calculated for the five different legs of the Polar 6 (P6) aircraft (described in Figure 1b) for (a) the SI case (*i.e.*, leg 1: 60 m, leg 2: 220 m, leg 3: 380 m, leg 5: 550 m, and leg 4: 1000 m) and (b) the OO case (*i.e.*, leg 1: 60 m, leg 2: 300 m, leg 3: 400 m, leg 4: 500 m, and leg 5: 900 m).

2.2.3.1 Cloud radar vs. in-situ probe observations

The instruments deployed on board the Polar 5 and Polar 6 have the advantage of probing the same clouds with different techniques, i.e., remote sensing and in-situ measurements. Using these two experimental approaches allows us to compare observations from the in-situ microphysics probes with profiles of the MIRAC cloud radar. In order to compare co-localised radar reflectivity data with Polar 6 in-situ measurements, we selected the suitable data taking into account both the spatial and temporal position for each legs of the SI and OO cases. Only the periods with in-cloud legs are considered for this study, i.e., legs 1-3 for the SI case and the legs 1-4 for the OO case. Data from the leg 5 of the SI case are not considered because this leg is too short (≈ 2 min) to correctly define co-localised data.

Figure 6 presents the probability density functions (PDF) of the reflectivities measured by the MIRAC radar (Polar 5) and those calculated from observed PSDs and DSDs on board Polar 6, with the help of a cloud reflectivity model. We applied the electromagnetic-microphysical model SSRGA (Self-Similar Rayleigh-Gans Approximation). In order to study the impact of the ice particles size and shape, two different mass-diameter relations $m(D) = aD^b$ relations were used, which consider different hypothesis regarding the degree of riming of the ice aggregates (see more details in Tridon et al., 2019a). The first relation which was developed by Brown and Francis (1995) assumes unrimed aggregates ($m(D) = 0.012D^{1.9}$; called hereafter BF95) whereas the second one which was developed more recently by Leinonen and Szyrmer (2015) assumes slightly rimed aggregates ($m(D) = 0.033D^{1.94}$; called hereafter LS15). In both cases D_{max} was used (as indicated in Section 2.1). This latter relation has been derived from a model for ice aggregation and riming described in Leinonen and Szyrmer (2015) in which rimed aggregates are obtained by subsequent aggregation of ice crystals and riming in supercooled liquid clouds (the LS15 relation used hereafter corresponds to the SSRGA-LS15-B0.2 configuration in the nomenclature given in Tridon et al. (2019a) associated to the fitting method of Ori et al. (2021)).

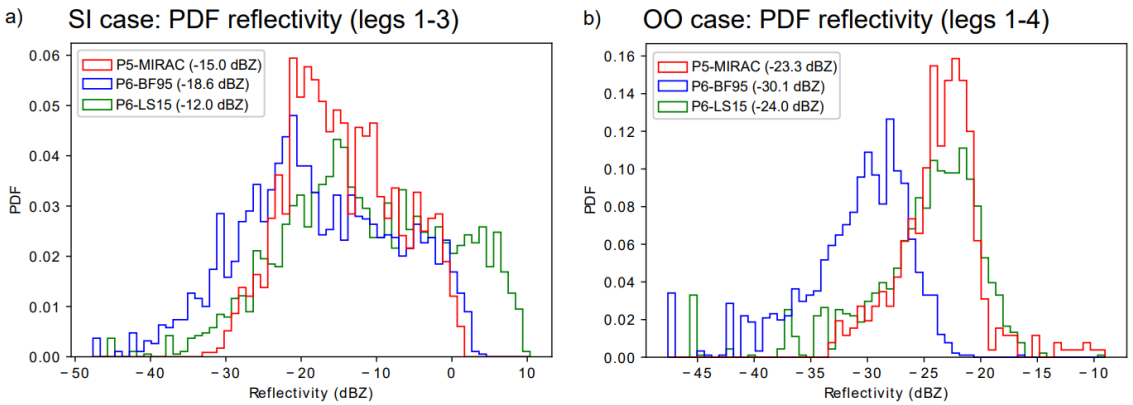

Figure 6. Probability density function (PDF) of the reflectivities measured by the MIRAC cloud radar (deployed on-board the P5) and calculated from in-situ measurements (deployed on-board the P6) for (a) the SI case and (b) the OO case. The SSRGA electromagnetic-microphysical approach and two different mass-diameter relations: Brown and Francis (1995) (BF95) or Leinonen and Szyrmer (2015) (LS15), to consider different hypothesis regarding the degree of riming of the ice aggregates, are applied to the in-situ PSD data. Values in the legend indicate the median of the respective parameters.

For the OO case, Figure 6b clearly shows that the reflectivities calculated from in-situ measurements considering slightly rimed aggregates (P6-LS15) become more comparable to the reflectivities measured by the MIRAC radar (P5-MIRAC) than the ones considering unrimed aggregates (P6-BF95). For the SI case, this trend is not clear. This comparative analyse suggests the presence of slightly rimed aggregates in both cases but with a degree of riming less important in the SI case than in the OO case (also found in Järvinen et al. (2023)). In order to confirm that the riming process occurs in both situations, we analyse the CIP images of ice crystals with sizes larger than 500 µm (i.e., the minimum size for a reasonable analysis) for the different in-cloud legs. Figure 7a shows the presence of slightly rimed aggregates for each in-cloud leg of the SI situation. However, for the OO situation, the small occurrence of ice crystals with sizes larger than 500 µm (see Figure 5b) do not allow us to obtain a representative sample of slightly rimed aggregates (Figure 7b). Nevertheless, the sampled aggregates seem to have more rounded shapes in the OO case, allowing us to assume that the riming process is probably more efficient in that case compared to the SI case.

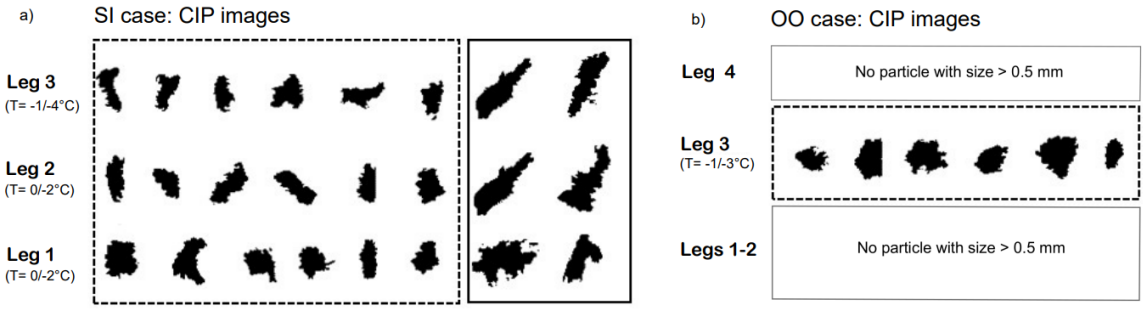

Figure 7. Examples of CIP images illustrating the presence of slightly rimed aggregates in the different legs. For the OO case, only images for leg 3 are represented due to the small occurrence of ice crystals with sizes larger than 500 µm (see Figure 5b) which is the minimum size for a reasonable analysis of the CIP images. The images enclosed in the dashed and solid black rectangles correspond to aggregates in size ranges 0.5-1 mm and >1 mm, respectively. Temperature ranges (in °C) for each leg are also indicated.

2.2.3.2 Vertical profiles of the MPCs' properties

From the numerous DSDs and PSDs measured along the different legs of the flight, we know the concentrations of droplets (N_{drop}) and ice crystals (N_{ice}) and we can deduce liquid water (LWC) and ice water (IWC) contents for both SI and OO cases (Arteaga, 2023). The mean and the spread values of both concentrations (Figures 8a-b) and water and ice contents (Figures 8c-d) along the different flight legs (Figure 1b) allow estimating the vertical profiles of the cloud properties for the SI and the OO cases. Moreover, in order to well identify the in-cloud regions, we consider critical thresholds on both the liquid water ($LWC_c \geq 0.01$ g m^{-3}) and ice water contents ($IWC_c \geq 5 \times 10^{-5}$ g m^{-3}) as applied in Mioche et al. (2017) and Dupuy et al. (2018). Note that the calculated IWC varies according to the used mass-diameter relationship.

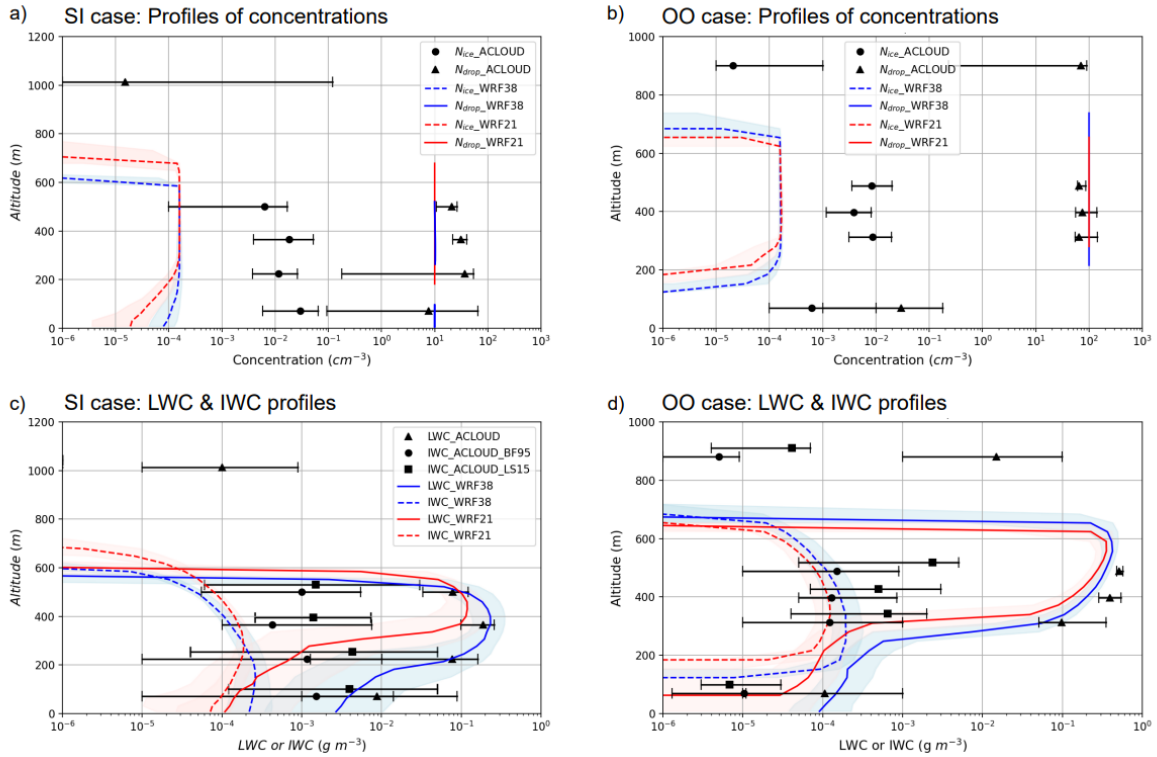

Figure 8. Median vertical profiles of the droplet (N_{drop}) and ice particle (N_{ice}) concentrations (a-b), and of the liquid (LWC) and ice (IWC) water contents (c-d) for the SI case (a,c) and the OO case (b,d) obtained from in-situ ACLOUD observations (black circles and squares). For the observations, the IWC are calculated using either the BF95 (circles) or the LS15 (squares) mass-diameter relationship. Note that all results obtained using LS15 are plotted with a vertical shift (+30 m) to make the figure easier to read. Symbols correspond to the median values obtained for the different legs and the intervals indicate the first (Q1) and the third (Q3) quartiles. Median profiles (solid lines) and Q1-Q3 spread (coloured shadings) obtained for WRF21 (red) and WRF38 (blue) simulations are also represented. Note that the y-axes are different for both cases.

For the SI case, data collected along leg 4 (at ≈ 1000 m) do not characterise in-cloud properties because the mean LWC and IWC values are respectively lower than the LWC_c and IWC_c thresholds (Figure 8c). At this altitude, the mean N_{drop} and N_{ice} (< 10^{-6} cm^{-3}) are both negligible (Figure 8a). At ≈ 60 m (leg 1), we can note that the mean LWC is lower than the LWC_c threshold but both the mean N_{drop} and N_{ice} cannot be neglected (see also Figure 5a). Thus, we assume that the Polar 6 aircraft flew in the precipitation layer (fight report) and close to the cloud base. Within the cloud layer, the N_{drop} is 3 orders of magnitude higher than the N_{ice}, and both concentrations remain quite constant along the profile at around 35 drops per cm^3 and 0.015 crystals per cm^3. Moreover, while the LWC remains quite constant, the IWC slightly decreases

with the increasing altitude (regardless the mass-diameter relation used in the calculations of the IWC).

Figure 8d shows that, according to the LWC_c and IWC_c thresholds, only the legs 2-4 (in the altitude range from 200 to 800 m) are performed inside the clouds for the OO case. Figure 5b has shown that the precipitation (at 60 m: leg1) is composed of few ice crystals. Moreover, we can note that the IWC calculated at 900 m (leg 5) increases for the LS15 relation (IWC ≈ IWC_c for leg 5 with the LS15 relation), implying that the large number of small drops in this level may effect riming of ice crystals. Within the cloud layer, the supercooled liquid water phase is more dominating in the OO case than in the SI case since the LWC is more important while the IWC remains comparable (Figures 8c-d). Moreover, the mean vertical trends are different: the LWC increases with the increasing altitude (up to 0.51 g m^{-3}) in the OO, whereas the IWC remains quite constant for both *m-D* relationships.

The two cloud systems observed either over sea ice or over open ocean formed under quite warm arctic conditions since the temperatures measured inside clouds are between 0°C and -5°C for the SI case and between 0°C and -3°C for the OO case (see Figure 7). The supercooled liquid water dominates the MPCs of both cases (Figures 8c-d). Ice formation took place by the heterogeneous nucleation process. The stronger concentration of N_{ice} for the SI case confirms the role of the decreasing temperature for heterogeneous nucleation. However, as the temperature in the cloud layer for the SI case ranges mainly between -5°C to -6°C (Figure 3), we can suppose that also the Hallett-Mossop process contributes to the ice crystal number concentration (Korolev and Leisner, 2020).

3. Numerical simulations of both MPC cases

3.1. Model description and strategy of analysis

Simulations of the two MPCs observed over sea ice (SI case) and open ocean (OO case) were done using the non-hydrostatic and compressible Advanced Research version of the Weather Research and Forecasting (WRF) model version 3.8.1 (Skamarock et al., 2008) which uses a terrain-following mass vertical coordinate. Physics processes are parameterised and categorised in different schemes in order to describe microphysics, surface, boundary layer, and radiation properties. For this study, the simulations for both SI and OO cases use the following set of parameterisations: the shortwave and longwave radiations follow the RRTMG (Rapid Radiative Transfer Model for GCMs) scheme based on Iacono et al. (2008) and Iacono (2011); the surface properties are described by the surface layer scheme of Janjic (2002) (based on the Eta similarity theory (Monin and Obukhov, 1954)) combined with the Noah land-use module (Chen and Dudhia, 2001); the boundary layer follows the Mellor-Yamada-Janjic (MYJ) scheme (Janjic, 2002), and the scheme of Morrison et al. (2009) is used to describe the cloud microphysics (initialising the CCN concentration for both cases according to the observations: $N_{CCN,SI}$ ≈ 10 cm^{-3} and $N_{CCN,OO}$ ≈ 100 cm^{-3}). This set of parameterisations is identical to that used in the WRF-Polar version developed by the Ohio State University (Hines et al., 2011). However, in our study, the modifications done to the Noah land-surface model and the sea ice treatment (Hines and Bromwich, 2008; Bromwich et al., 2009) are not considered. Indeed, there are particularly important for long-term simulations where the sea ice surface and the snow cover are evolving which is not the case for our cases that last less than one day. However, in order to better represent the surface properties, we adjust the surface albedo for sea ice (α_{SI} ≈ 0.79) and ocean (α_{OO} ≈ 0.21) surfaces according to the mean surface radiative properties observed during ACLOUD on the 17 June 2017 (Stapf et al., 2019a,b, 2020).

A two-way nested configuration is used with three domains at increasing grid spacing: 9, 3, and 1 km. In the horizontal, the numbers of grid points are, from the outermost to the innermost domain, 120 x 120, 274 x 232, and 487 x 430. The two wider domains are centred on the Ny-Ålesund station (NyA in Figure 1a) whereas the innermost domain is centred on the flight position either at 11:00 UTC or at 14:00 UTC in order to respectively study the SI or OO cases (stars in Figure 2d). For the three domains, the vertical grid consists of 105 non-equidistant levels (with a model lid at 350 hPa) in order to have more levels at the altitudes of the MPCs (mean vertical grid spacing equal to 30-35 m within the first kilometre). The outermost domain is initialised at 00:00 UTC 17 June 2017 and forced every 6 hours with the ERA-5 reanalysis data (Hersbach et al., 2018a) from the European Centre for Medium-Range Weather Forecasts (ECMWF). These data provide the fields of air temperature, specific humidity, geopotential, and wind components with a spatial resolution of 0.25° x 0.25° in latitude and longitude for a specified number of pressure levels. Two different simulations using either 21 or 38 pressure levels (6 or 9 of them are present in the pressure range 1000-800 hPa, respectively) are performed in order to study the role of the model initiation. The three additional pressure levels in the lowest layer of the atmosphere correspond to the 975 hPa, 875 hPa and 825 hPa levels. The model settings described above provide the baseline simulations, which will be referred to as WRF21 or WRF38 for 21 or 38 pressure levels used in the ERA-5 reanalysis data for the two MPC cases. The simulations performed for this study are summarised in Table 1.

Table 1. Description of all the modelling experiments done in this study using the ECMWF ERA-5 reanalysis data for WRF initialisation: with either 21 or 38 pressure levels; and with two different parameterisations to describe the (BL) boundary layer (the MYJ or MYNN3 scheme) and the (MP) microphysics (the Morrison et al. (MORR) or the Milbrandt-Yau (MIYA) 2-moment scheme). Additional sensitivity studies are performed varying the initial CCN concentration [*n*]. Note that in WRF38* baseline simulations, [*n*] is equal to 10 cm^{-3} for the SI case whereas it is equal to 100 cm^{-3} for the OO case.

Name	Description
WRF21	Using 21 ERA-5 levels, and with MYJ & MORR physics schemes
WRF38	Using 38 ERA-5 levels, and with MYJ & MORR physics schemes
WRF-BL	As in WRF38, but with MYNN3 boundary layer scheme
WRF-MP	As in WRF38, but with MIYA microphysics scheme
WRF-[*n*]CCN	As in WRF38*, but with CCN concentration equal to [*n*] cm^{-3}

The instrumentation deployed on-board the Polar 5 and the Polar 6 aircrafts can be used to quantitatively compare the simulated thermodynamics and microphysics properties of the MPCs. The vertical profiles of the thermodynamics conditions obtained from the dropsondes (Figure 3) and the cloud microphysics properties from the MIRAC cloud radar (Figure 4) as well as the in-situ probes (Figures 5-6) are relevant in this context. Comparisons of model results with profiling observations are challenging because a model cannot be expected to reproduce the exact system evolution in space and time. In addition, the representativeness of the observed profile (DS1 or DS4 dropsonde), the time-height (MIRAC cloud radar), or time-level (in-situ data leg) is unknown. Therefore, as in Tridon et al. (2019b) and Planche et al. (2019), we statistically compare the different observations to a large number of model columns or level-points over the whole simulated cloud for both cases. Thus, two parallelepipedic volumes with a base of 300 x 140 km^2 and a vertical extension of 1-1.2 km are defined within the innermost domain. Each of them encompasses the trajectory of the P6 aircraft for both cases, as represented on the Figure 1a.

In order to evaluate the sensitivity of modelled MPCs properties to the representation of the physics processes, additional simulations are performed using different parameterisations for the boundary layer (BL) and the microphysics (MP). For these simulations, we choose BL and MP schemes which are commonly used for Arctic cloud studies (such as in Bromwich et al.

(2009); Hines et al. (2011); Xue et al. (2022), among others). Thus, we replaces the MYJ scheme by the Mellor-Yamada-Nakanishi-Niino Level 3 (MYNN3) boundary layer scheme (Nakanishi and Niino, 2006, 2009) and the Morrison scheme by the Milbrandt-Yau (MIYA) microphysics scheme (Milbrandt and Yau, 2005a,b). MYNN3 is a modified version of the MYJ scheme which uses results from large eddy simulations to derive the expressions of stability and mixing length instead of observations. In both 2-moments MP schemes, the prognostic variables include number (N) and mass mixing ratio (q) for all different hydrometeor species (such as rain drop, ice, and snow). The particle size distribution for each hydrometeor species (x) is described by a gamma function: $N_x(D) = N_{0,x}D^{\mu x}\, e^{-\lambda x D}$, where D is the diameter, and $N_{0,x}$, μ_x and λ_x are the intercept, the shape and the slope parameters. For each hydrometeor species, $N_{0,x}$ and λ_x are calculated according to Equations 1 and 2 (while μ_x is fixed):

$$\lambda_x = \left[\frac{a_x N_x \Gamma(\mu_x+b_x+1)}{q_x \Gamma(\mu_x+1)}\right]^{1/b_x} \quad \text{(Equation 1)}$$

$$N_{0,x} = \frac{N_x \lambda^{\mu x+1}}{\Gamma(\mu_x+1)} \quad \text{(Equation 2)}$$

Γ is the Euler gamma function, the parameters a_x and b_x are given by the assumed power-law mass-diameter relationship ($m(D) = a_x D^{b_x}$) for each hydrometeors species. Table 2 summarises the main assumptions of both MP schemes for hydrometeors' representations. Note that most of the hydrometeor size distributions follow an exponential function since μ_x is equal to 0. Most of the microphysics processes are based on similar approaches in both MP schemes. A difference however consists for the heterogeneous ice nucleation mechanisms which start at different temperatures: the deposition/condensation and the contact/immersion freezing mechanisms are active at T < -8°C and T < -4°C in the Morrison scheme whereas they are respectively active at T < -5°C and T < - 2°C in the Milbrandt scheme.

Table 2. Main characteristics of both microphysics schemes used in this study to described the different hydrometeor species (x). The definition of the q, N, a, b, and μ variables are given in the text and *v, c, r, i, g, h* correspond to the water vapour, cloud droplet, rain drop, ice, graupel, and hail species, respectively. ρ_x corresponds to the density for each species. Note that μ_c follows Martin et al. (1994) in MORR scheme.

	Morrison scheme (MORR)	**Milbrandt-Yau scheme (MIYA)**
Mass variables	q_x for $x \in \{v, c, r, i, s, g\}$	q_x for $x \in \{v, c, r, i, s, g, h\}$
Number variables	N_x for $x \in \{r, i, s, g\}$	N_x for $x \in \{c, r, i, s, g, h\}$
***m-D* coefficients**	$a_x = \frac{\pi}{6}\rho_x$ & $b_x = 3$ for $x \in \{c, r, i, s, g\}$	$a_x = \frac{\pi}{6}\rho_x$ & $b_x = 3$ for $x \in \{c, r, s, g, h\}$ & a_i = 440 kg m^{-3}
Shape parameter	$\mu_x = 0$ for $x \in \{r, i, s, g\}$ $\mu_c = fct(N_c, T, p)$	$\mu_x = 0$ for $x \in \{r, i, s, g, h\}$ & $\mu_c = 3$

3.2. WRF baseline simulations

In Figure 8, results from WRF21 and WRF38 simulations for both SI and OO cases are already included. In WRF experiments, the microphysics properties are determined by selecting a sample of points within the parallelepipedic volume matching with the P6 flight path (leading typically to more than 200 points in total). Temporally, we consider all the model outputs every 5 min between 11:00 and 12:00 UTC for the SI case and between 14:00 and 15:00 UTC for the OO case. Moreover, from the WRF experiments, the LWC is calculated using the mass mixing ratios of both cloud (q_c) and rain (q_r) species while the IWC is calculated using the mass mixing ratios of both ice (q_i) and snow (q_s) species (the other ice species in MORR are empty for the two studied MPC cases). Regarding the concentration profiles, the sum of N_c and N_r is used to determine N_{drop} while the sum of N_i and N_s is used for N_{ice}. Note that N_c, which is not a prognostic variable in the Morrison scheme, is fixed according to the N_{CCN} values used to

initialise both cases (Section 3.1). Consequently, N_{drop} profiles in Figures 8a-b depict a constant value of 10 cm^{-3} for SI and 100 cm^{-3} for OO in both WRF21 and WRF38 simulations.

The median LWC profiles in WRF38 do better compare with observations than in WRF21 for both SI and OO cases (Figures 8c-d). However, neither the vertical evolution nor the amount of the IWC are well reproduced in both WRF21 and WRF38 experiments for the SI case. WRF38 better hits the observed IWC, especially in the first 200 m, for the OO case. The simulated median IWC profile in WRF38 is closer to the observed IWC, which was calculated by means of the BF95 *m-D* relationship (Figure 8d). This, however, is in contradiction to our results of Section 2.2.3 where we found that radar reflectivity is better reproduced when the LF15 *m-D* relationship for rimed particles is used. Despite this, the simulated median IWC profile in WRF38 is within the spread interval of the observations. Figure 8d shows that the simulated OO cloud top is not well reproduced in WRF38 and WRF21 since the LWC and IWC sharply decrease at 650 m altitude while the observations suggest a cloud top at ≈ 900 m (leg 5). N_{drop} profiles (Figures 8a-b) reflect the CCN number concentrations initially chosen for SI and OO cases. The selected number of 100 CCN cm^{-3} overestimates the N_{drop} observations for the OO case by 20-30%. For the SI case, 10 CCN cm^{-3} underestimates the observations for N_{drop} by a factor of 2-4. N_{ice} is underestimated in WRF21 as well as in WRF38. This underestimation is around one order of magnitude for the OO case whereas it reaches approximately two orders of magnitude for the SI case.

This disagreement will further be investigated by exploiting the dropsonde data at the altitudes where the MPCs formed. Figures 9a-b compare the mean vertical evolution of the thermodynamics properties simulated in WRF21 and WRF38 with the profile of the observed air temperature T and dew point temperature T_d. Simulated profiles of T and T_d are obtained averaging the 20 x 20 model columns centred on the position in latitude and longitude of each dropsonde (Figure 1) for a one-hour period for the time of the dropsonde releases, *i.e.,* from 10:30 UTC to 11:30 UTC for the SI case and from 13:30 UTC to 14:30 UTC for the OO case.

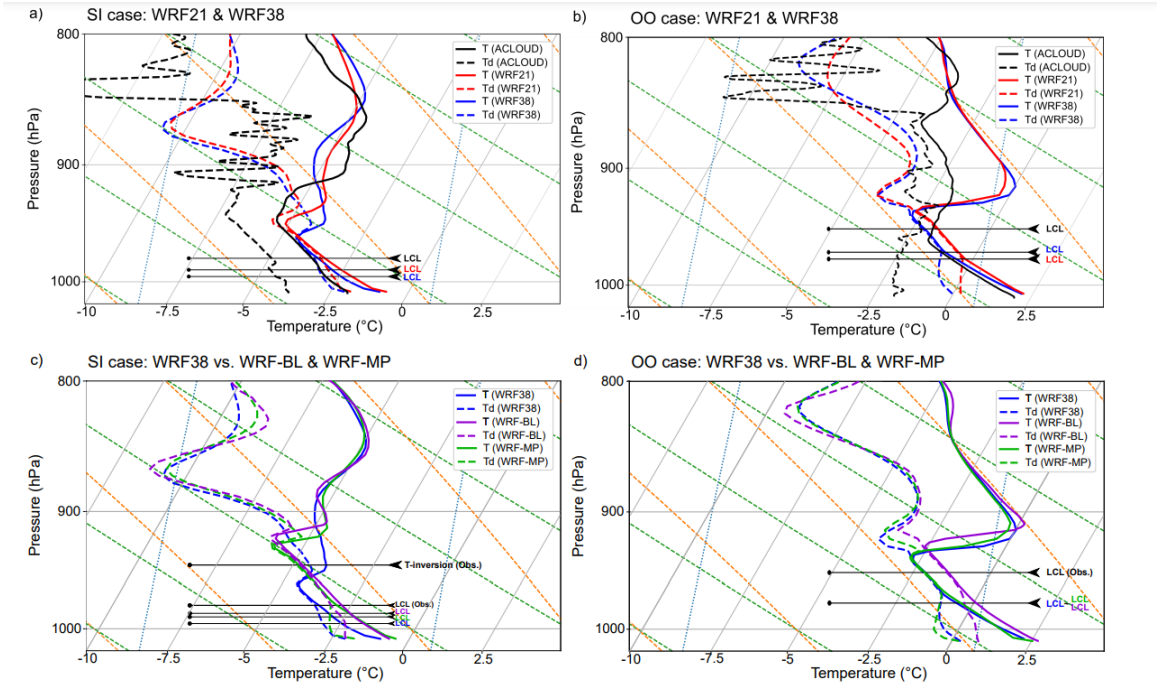

Figure 9. Mean vertical profiles of the air temperature T (solid lines) and the dew point temperature T_d (dashed lines) obtained in WRF38 (blue), in WRF21 (red) and from observations (black) for (a) the SI case and (b) the OO case. Results from the WRF sensitivity studies, WRF-BL (purple) and WRF-MP (green), presented in Section 3.3 for (c) the SI case and (d) the OO case are also illustrated.

According to Figure 9a, the LCL obtained in both WRF21 and WRF38 are comparable to the observations for the SI case. However, even if the vertical evolution of T_d is similar to the observations up to 950 hPa, it is overestimated by ≈ 1.5-2°C while the T is overestimated by ≈ 1-1.5°C close to the surface in both simulations. These warmer conditions could explain the weak simulated IWCs. As the vertical variations of the potential temperature (θ) between surface and cloud base are below 0.5°C, observations and simulations reveal a coupled cloud-surface situation as proposed by Gierens et al. (2020) and Griesche et al. (2021). Also, the T-inversion that is present at a slightly higher altitude in WRF21 than in WRF38 justifies the difference in the altitude of the cloud top visible in Figure 8c for the SI case. The altitude of the T-inversion in the observations (located just above the isotherm layer) suggests a cloud top at higher altitudes than in both experiments, *i.e.,* between the flight legs 5 and 4 (see Figure 1b). For the OO case, the vertical profile of T is well reproduced close to the surface by both WRF experiments while modelled T_d is overestimated by ≈ 2°C (Figure 9b). The LCL is therefore lower in the simulations than in the observations. As for the SI case, the adiabatic conditions indicate the presence of surface-coupled clouds. At higher altitudes, T_d is better estimated by the simulations but the T-inversion is more marked and T is overestimated by ≈ 2°C in the pressure range from 925-850 hPa. These differences in the vertical evolution of T impact the altitude of the cloud top as well as the amount of the liquid and ice water contents (Figure 8d). Based on our analyses presented in Figures 8 and 9, the WRF38 experiment will be considered hereafter as our reference experiment.

Additional comparisons between observations and baseline simulations (*i.e.,* WRF38) are performed on the vertical properties of the MPCs for both cases using a statistical approach. Figure 10 shows the altitude-dependent probability density functions (a-PDF) of reflectivities measured by the MIRAC 94 GHz cloud radar (deployed on P5).

In order to focus on the MPCs properties, we excluded MIRAC data from 11:35 to 11:45 UTC in our analysis to avoid the precipitation of the mid-level clouds for the SI case (see Figure 4a). Similarly, we selected only MIRAC data from 14:15 to 14:45 UTC to avoid the rainy periods of the mid-level clouds for the OO case (see Figure 4b). PDFs of radar reflectivities calculated from in situ probe measurements (along in-cloud legs done by the P6 aircraft, Figure 6) are also shown in Figure 10. From the WRF experiments, the 94 GHz radar reflectivities are calculated with the Cloud-resolving model Radar SIMulator (CR-SIM, Oue et al. (2020)). It is a forward-modelling post-processing tool that emulates various remote sensing products in accordance with assumptions used in the microphysics scheme, *i.e.,* the Morrison scheme for both WRF38 baseline experiments (Table 2). The WRF data are selected with the same method used for the LWC and IWC analyses detailed for Figure 8.

Figures 10a-b show different vertical evolutions of the median a-PDF reflectivities of the MIRAC observations for both cases. For the SI case, it increases from -22 dBZ to -12 dBZ towards the ground whereas, for the OO case, it reaches a maximum of -20 dBZ at an altitude of 800 m and then slightly decreases to -25 dBZ at the cloud base. These vertical trends are consistent with in-situ measurements which have shown that hydrometeors are larger in the SI case (Figure 5). In WRF38, the vertical evolution of the median a-PDF of the modelled reflectivities is comparable to the observations for both cases (Figures 10c-d). However, the reflectivities fields are more homogeneous in the model than in the MIRAC observations (see Q1-Q3 spread). Also, Figure 10d confirms that MPCs simulated for the OO case are less high than observed (due to the position of the T-inversion; Figure 9b).

Figure 10 has shown that radar reflectivities modelled in WRF38 are in accordance with cloud radar MIRAC observations for both cases. This agreement is mainly due to the fact that the simulated ice particle spectra underestimate the observed particle number but give a wider

spectrum with larger particles, which contribute essentially to the reflectivity. Table 2 shows that the modelled ice PSDs are prescribed according to exponential distributions (μ = 0) in MORR whereas the observed PSDs are rather defined according to gamma distributions (see Figure 5).

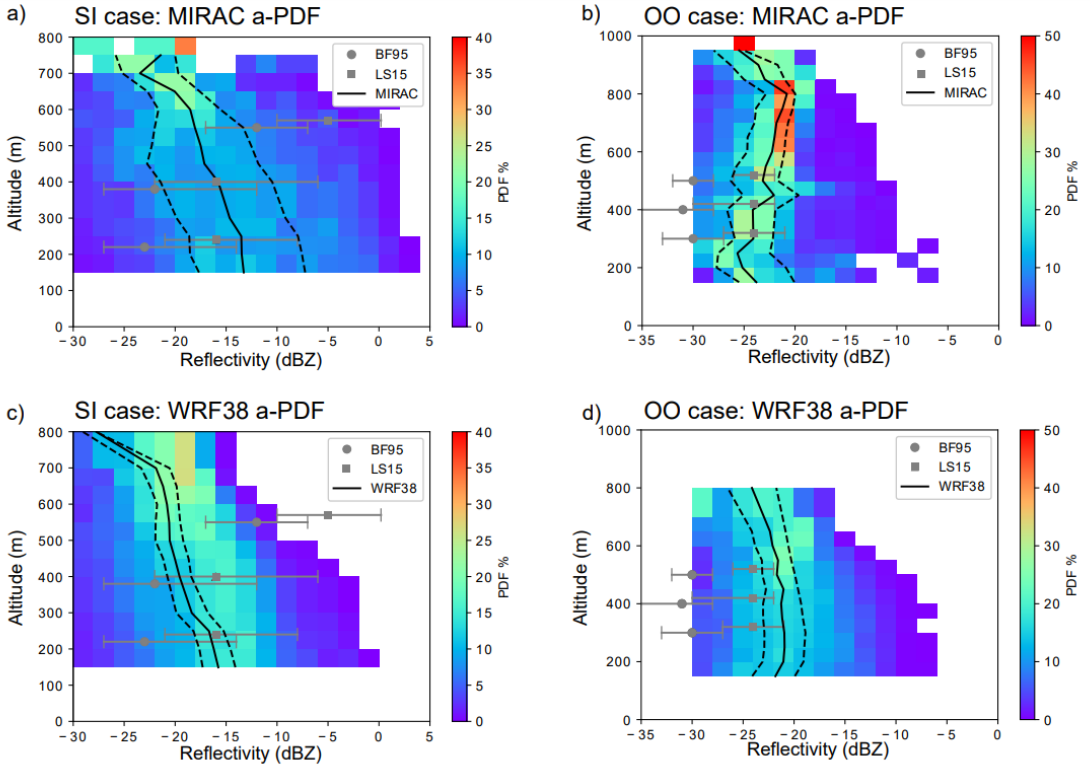

Figure 10. Altitude-dependent probability density function (a-PDFs) of the reflectivities, resolved in bins of 2 dBZ, from the MIRAC radar system (a-b) and obtained applying the CR-SIM module to the WRF38 simulations (c-d) for the SI case (a,c) and for OO case (b,d). The a-PDFs are obtained calculating the PDF for each retrieved level. Solid black lines represent the median whereas dashed black lines represent the first (Q1) and the third (Q3) quartiles. Median (grey symbols) and Q1-Q3 spread of the PDF of the reflectivities calculated from in-situ measurements using BF95 (circles) or LS15 (squares) are also illustrated. Note that all the results obtained using LS15 are plotted with a vertical shift (+30 m) to make the figure easier to read.

3.3 Impact of the boundary layer (BL) and microphysics (MP) parameterisations

The WRF38 baseline experiment provides reasonable results compare to the observations with some discrepancies as the underestimation of the ice phase and the altitude of the cloud top. To evaluate how these MPC parameters can be impacted by the physics parameterisations used in our modelling set-up, we performed sensitivity studies using other representations for the boundary layer (BL) and the microphysics (MP), as described in Section 3.1. These alterations with respect to WRF38 set-up are summarised in Table 1. Figure 11 represents the median vertical profiles of the LWC and IWC obtained in WRF-BL and WRF-MP for both cases.

LWC and IWC simulated with WRF-BL are similar to the values found in WRF38 but both liquid and ice water phases extend on thicker layers and are present at higher altitudes. For the SI case, the cloud liquid water phase is vertically shifted by approximately +200 m and the cloud ice reaches up to 800 m altitude (Figure 11). Figures 11b,d show that the impacts are opposite for the OO case since IWC is vertically shifted by approximately +200 m whereas the liquid water phase extends over 500 m, *i.e.,* 100 m more than in WRF38. The modifications of the vertical profiles of the condensed water for the two cases can be induced by changes in surface

sensible (F_{sen}) and latent (F_{lat}) fluxes and in the thermodynamics structure within the boundary layer. Indeed, the mean F_{lat} increases by around 20% in WRF-BL for both cases, while a significant reduction in the mean F_{sen} of -25% only occurs for the SI case. Table 3 summarises the mean F_{sen} and F_{lat} obtained for each WRF-BL experiments. With Figure 9, we can see that the air temperature at the surface is 1°C higher in WRF-BL than in WRF38 for the SI case. The lower atmospheric layer is more humid up to 910 hPa where a more marked *T*-inversion is present, *i.e.,* at higher altitude than in WRF38 as well as in the observations (see Figure 9c). For the OO case, the *T*-inversion is also located at a slightly higher altitude (≈ 10-20 hPa) than in WRF38 (Figure 9d). Below this point, *T* and T_d have a similar vertical gradient even if they are stronger than in WRF38.

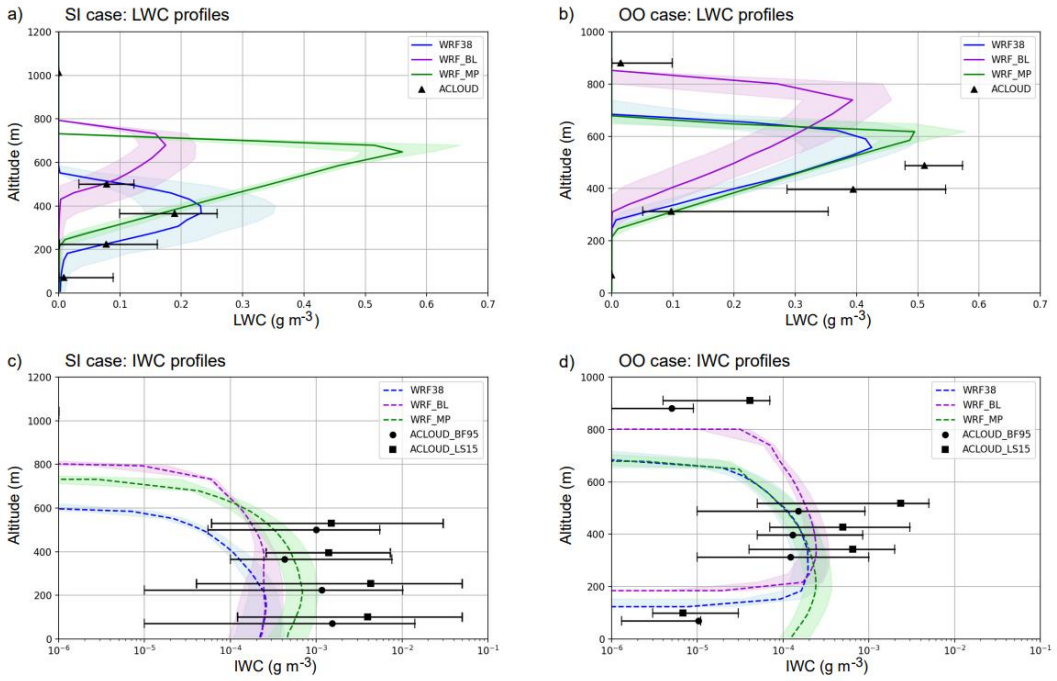

Figure 11. Median (solid or dashed lines) vertical profiles of the LWC (a-b) and IWC (c-d) for the SI case (a,c) and the OO case (b,d) simulated in WRF38 (blue), WRF-BL (purple), and WRF-MP (green) experiments. Coloured shadings represents the Q1-Q3 spread. Observations are indicated by black symbols (compare Figure 8).

Figure 11 also represents the vertical profiles of the LWC and IWC obtained in WRF-MP for both cases (see Table 1). In that WRF microphysics experiment, not only the quantities for LWC and IWC change but also their vertical profiles. For the SI case, the ice phase is more important than in WRF38 by a factor of 2 and extends up to 750 m altitude (≈ 150 m higher than in WRF38) and becomes more comparable to the observations (see Figure 11c). The liquid phase simulated in WRF-MP also extends up to 750 m and reaches a maximum of 0.56 g m^{-3} at 650 m altitude, *i.e.,* an amount which is two times higher than in WRF38 or in the observations (Figure 11a). So, with the MIYA microphysics scheme (used in the WRF-MP experiment), both LWC and IWC become more important than in WRF38 for the SI case. This is due to changes in the temperature and humidity profile: the *T*-inversion is located at higher altitude (as in WRF-BL) and also the lowest levels of the atmosphere are more humid and warmer (0.5-1°C) in WRF-MP compared to the WRF38 experiment and the observations (Figures 9a,c). The liquid water fraction (LWF) estimated for WRF38 is higher (≈ 90%) than WRF-BL (≈ 70%) in the lowest layers for SI case. For the OO case, the changes in the vertical profile of the LWC and the IWC are minimal in WRF-MP compared to WRF38 (Figures 11b,d) since only the ice phase appears more important in the lowest atmosphere and the maximum

of the liquid phase increases around 20% at the cloud top. At this altitude of 925 hPa, more water vapour is available according to the thermodynamics conditions (see Figure 9d) while they are similar to WRF38 conditions at lower altitudes. For the OO case the vertical distribution of water is almost the same in both cases.

Table 3. Mean surface sensible (F_{sen}) and latent (F_{lat}) fluxes simulated in WRF38 and WRF-BL for both SI and OO cases. The numbers in brackets indicate the respective relative differences between WRF-BL and WRF38.

	SI case		**OO case**	
	WRF38	**WRF-BL**	**WRF38**	**WRF-BL**
F_{sen} (W m^{-2})	4.94	3.67 (-25.7%)	21.81	21.44 (-1.70%)
F_{lat} (W m^{-2})	3.38	4.10 (+21.3%)	26.03	31.10 (+19.5%)

The MIYA microphysics scheme (used in the WRF-MP experiment, see Table 1) implies more ice, especially in the SI case. This is mainly related to the different temperature thresholds used in MORR and MIYA microphysics schemes in order to activate the heterogeneous ice nucleation mechanisms. Indeed, all of the ice formation mechanisms parameterised in MIYA are activated at warmer temperatures than in MORR (see Section 3.1). Thus, these assumptions can have an important impact on the SI simulations where in-cloud temperatures are flirting with the threshold values.

4. Sensitivity to CCN concentration

An additional sensitivity study is performed using the WRF38 baseline simulations for the SI and the OO cases (defined in Section 3.2) in order to investigate the effects of the CCN concentration (N_{CCN}) on MPCs' microphysics properties. In that context, several WRF experiments are done (see Table 1) where the cloud droplet concentration (N_c) is set equal to CCN concentrations ([n]) as observed in various Arctic or marine environmental conditions (*e.g.* Planche et al. (2017); Wendisch et al. (2019); Baudoux (2022)). Figure 12 shows the median vertical profiles of LWC and IWC for the different scenarios.

For the SI case, an increase by a factor of three in the CCN concentration (from 10 cm^{-3} in WRF-10CCN to 30 cm^{-3} in WRF-30CCN) impacts the LWC as well as the IWC (Figures 12a,c). Indeed, the LWC increases by a factor of 2 while the IWC increases from 1.5 x 10^{-4} g m^{-3} to 5.1 x 10^{-4} g m^{-3}. Also, the vertical distribution of the liquid water phase is modified since it extends over 600 m (*i.e.,* 100 m more than in WRF38) (Figure 12a). Consequently, with an increasing CCN perturbation, the liquid water phase becomes more important and extends over deeper layer. Stronger changes in the CCN concentration modify the thermodynamics properties close to the surface and induce modifications in the MPC development. Indeed, in all WRF experiments with $N_{CCN} \geq 100$ cm^{-3} the T-inversion evolves vertically since it is located around 150 m higher than in WRF38 (not shown). Note that an increase of 2.5 times in the CCN concentration from 100 cm^{-3} to 250 cm^{-3} only induces a slight increase (+5%) in liquid phase and almost no effect on the ice phase (see WRF-100CCN and WRF-250CCN in Figures 12a,c). Thus, no linear relationship between CCN and LWC/IWC exists in all WRF experiments with $N_{CCN} \geq 100$ cm^{-3} ; the boundary layer conditions seems "to be saturated" for a perturbation of 100 CCN cm^{-3} for the SI case.

For the OO case, with an increase in the CCN concentration by a factor of three (from 10 to 30 cm^{-3}), the liquid phase increases by a factor of 2.5 and extends over deeper layer while the ice phase increases by a factor of 10 (Figures 12b,d). These changes in the IWC are more important than in the SI case for an identical variation in the initial CCN concentration. Increasing the CCN concentration to 100 cm^{-3}, the LWC continue to increase and the cloud top becomes higher. Note that in all sensitivity tests with CCN concentrations higher than ≥ 250 cm^{-3}, the total water content remains similar. As in the SI case, there is a critical CCN

concentration from which the boundary layer seems “to be saturated” for the OO case. Moreover, the thermodynamics properties are quite similar in all experiments, except in that WRF-10CCN, where the *T*-inversion does not evolve vertically by remains at an altitude of 300 m.

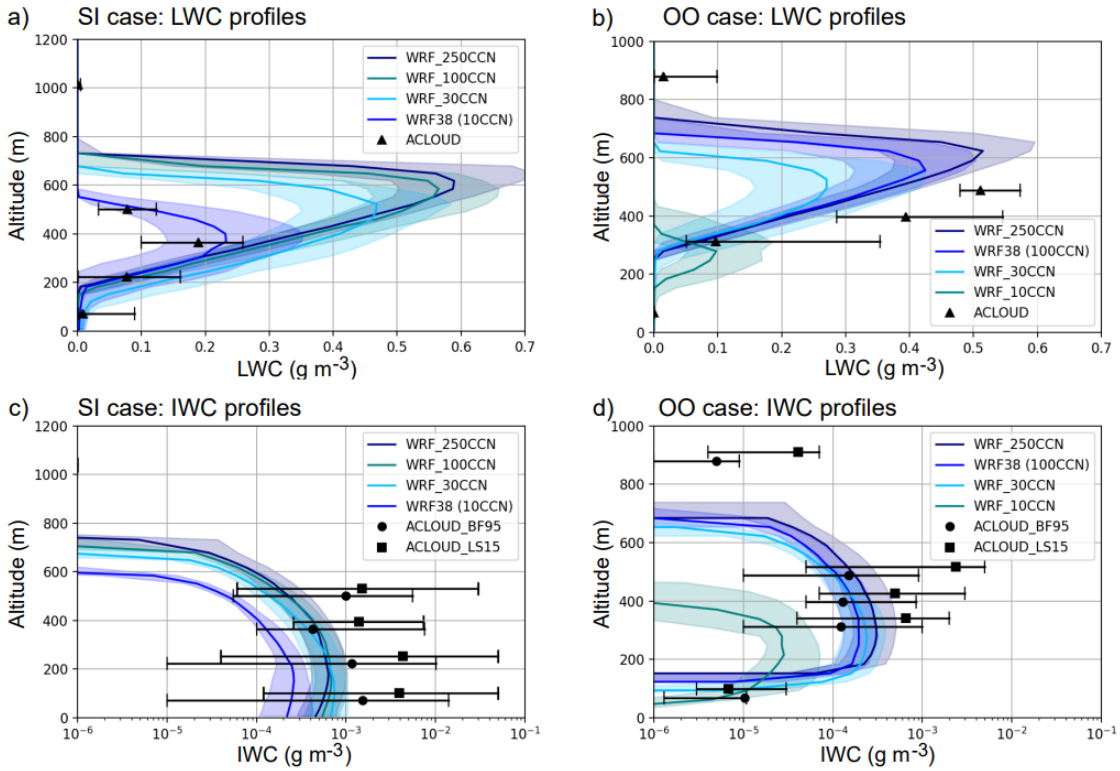

Figure 12. As in Figure 11, but for the different WRF-[*n*]CCN experiments where [*n*] = 10 cm^{-3}, 30 cm^{-3}, 100 cm^{-3}, and 250 cm^{-3}. Note that in the WRF38 baseline experiments described in Section 3.2, [*n*] = 10 cm^{-3} for the SI case and [*n*] = 100 cm^{-3} for the OO case.

Sensitivity of cloud microphysics properties to CCN concentration is more important for the SI case than for the OO case. As in *e.g.* Eirund et al. (2019), a rising CCN concentration successively increases LWC and IWC. However, at a critical concentration, the LWC and IWC no longer increase for both SI and OO cases. Moreover, the higher the CCN concentration is, the deeper the cloud is.

5. Discussion

During the ACLOUD campaign 2017 two shallow cloud layers (<700 m) were probed, one over Sea Ice surface (SI) at temperatures around -5°C, another over the Open Ocean (OO) under slightly warmer conditions around -2°C. LIDAR and RADAR observations indicate that the cloud field over Sea Ice typically ranged from the surface up to 500 m while clouds over Open Ocean were more elevated with a cloud base close to 200 m and a cloud top around 900 m (Figure 4). In situ measurements show that LWC reaches 0.4 g m^{-3} at 400 m over Open Ocean while a maximum of 0.2 g m^{-3} is obtained in cloud layers over Sea Ice at the same altitude level. LWC still increases in the OO case up to 0.5 g m^{-3} at 500 m (Figure 8d) while LWC in the SI case at these levels strongly decreases indicating the top of the cloud. We presume that strong entrainment with sub-saturated air from altitudes above cloud top reduced the LWC in the SI case. In addition, in the SI case, the vertical structure of the temperature measured by the dropsonde DS1 (Figure 3) reflects a wet adiabatic profile indicating a well-mixed structure over the entire cloud layer. In contrast to that, the observed temperature profile (DS4) in the

lower 400 m of the OO case is dry-adiabatic, justifying the observed LWC of 0.4 g m^{-3} for adiabatic ascent between 200 and 400 m.

Airborne measurements indicate that the aerosol particle concentrations differed significantly between both situations, suggesting that the CCN concentration over Sea Ice (with 10 cm^{-3}) represent a cleaner environment than clouds encountered in the Open Ocean case (with 100 cm^{-3}). This strong discrepancy could not be confirmed by measurements of the droplet number, which typically counted 30 droplets/cm^3 in the SI case, and only 70 droplets/cm^3 in the OO case. The number of ice crystals was not correlated with the differences in aerosol concentration: while 20 crystals per litre were counted in the SI case, only 5 crystals per litre were detected in clouds over Open Ocean. We can speculate that the lower temperatures in the SI clouds intensified ice particle formation due to more efficient heterogeneous nucleation. The colder temperatures of the SI case also probably favoured the formation and the growth of larger crystals up to 2 mm, while ice particles sizes remained below 0.5 mm in the OO case (Figure 5). The presence of large ice crystals is confirmed by observations of the cloud radar reflectivity *Z* at 94 GHz. While *Z* remains below -20 dBZ in the cloud layers over open ocean, it is higher, ranging from -20 to 0 dBZ in the SI case.

After an integration time of 12 to 14 h, simulations with the WRF model reasonably reproduced the low arctic cloud layers observed on 17 June 2017 over Sea Ice and Open Ocean. Model results for cloud layer depth, prevailing LWC and drop number are quite comparable with the observations, however, IWC and crystal number are significantly underestimated. Furthermore the model could not represent the mid-level cloud layer, which was observed by remote sensing instruments between 1500 and 3500 m in both cases (Figure 4).

In a first step the role of the vertical resolution of the large-scale data, which provide initial and boundary conditions for the model, was tested. Simulations with 21 vertical levels were compared with those using 38 levels. The low-level cloud layer formed produced in both configurations. However, with additional levels next to the surface, clouds could form at lower altitudes causing a slight increase of LWC in the 400 m level, thus in better agreement with the observations. Model results for ice crystal number concentration N_{ice} and IWC are only marginally affected by the change of the vertical resolution. Most striking is the comparison between simulation and observations of N_{ice}. Modelled ice crystal numbers are 100 times smaller than observed numbers in the SI case and 50 times smaller than observations in the OO case (Figure 8). Observational results for the IWC are uncertain as this quantity depends significantly on the *m-D* relationship applied to the particle number distributions and representing the degree of riming of the ice particles (Figures 8 and 10). The resulting IWC range in the SI case typically from 1 to 5 mg m^{-3} and from 0.1 to 1 mg m^{-3} in the OO case. The maximum IWC found by the model remained in both cases below 0.2 mg m^{-3}. We can see from these results that the formation of ice crystals and the resulting IWC are significantly underestimated by the microphysics of the model. To a certain extent, the underestimation of the modelled IWC can also be attributed to the warmer air, simulated in the first 500 m for all modelled cases. This underestimation is more pronounced in the SI case, where the simulated temperature in the lower 300 m was up to 1.5 °C higher than the observed one.

Significant changes in the vertical structure of the simulated boundary and cloud layer occurred, after replacing the MYJ boundary layer scheme by the model of Nakanishi and Niino (2009) (MYNN3). The use of the MYNN3 scheme caused a significant vertical shift of the cloud layer in both cases (see WRF-BL in Figure 11). Cloud top for the SI case extends from 450 to 750 m and for the OO case from 400 to 800 m. All microphysical properties remained quite similar in the cloud layer as in previous simulations using the MYJ scheme (WRF38 in Figure 11). The lifting of the cloud top is accompanied by the lifting of the temperature inversion (Figures 9c and d). Below the inversion, the cloud evolution produced a wet adiabatic lapse

rate, and the temperature increased from the surface up to cloud top compared to the MYJ results. This warming in the boundary layer can be attributed to the increase in surface latent heat flux (Table 3), which increased in both cases by 20% for simulations with the MYNN3 scheme. We can speculate that this modified evolution in the boundary layer is due to the different parameterisation of turbulence used in MYNN3 scheme.

Heterogeneous ice nucleation is the dominant microphysical process for crystal formation in the temperature range slightly below 0°C. All simulation results discussed until here concerned the Morrison scheme, wherein heterogeneous nucleation is triggered for temperatures below -4°C. The consequence of a shift to warmer temperatures for the cloud layer were studied by the microphysics scheme MIYA wherein heterogeneous nucleation begins at -2°C. For the simulation with MIYA microphysics (see WRF-MP in Figure 11) over Open Ocean no remarkable modifications occurred in the profiles of LWC and IWC. This is confirmed by the boundary layer structure (Figure 9d), which is almost identical with the profiles of WRF38 for the Morrison scheme (MORR). This result is not surprising as the temperatures in the simulated OO case remain largely above -2°C. Under colder conditions, as those of the Sea Ice case, the magnitude of LWC, IWC as well as the cloud layer depth increased significantly. Due to the amplified release of latent heat by water vapour condensation, temperatures in the cloud became almost 1°C warmer and cloud top increased by 200 m. As the increase of LWC in the MIYA scheme dominates the results in the SI case, it becomes obvious that also other cloud parameterisations than heterogeneous ice nucleation influence these model results. Thus, simulations with the MIYA microphysics do not provide unambiguous information on the role of the temperature threshold for heterogeneous ice nucleation.

The microphysics scheme of Morrison is initialised with a fixed CCN value, which corresponds to the number of cloud droplets that is kept constant along the simulation. Variations of the CCN number (Figure 12) show that an increasing CCN concentration leads to more LWC and clouds become deeper. The same result can be detected for the vertical profiles of IWC, even though the trend is less pronounced. This unexpected behaviour of LWC with changing cloud drop number is basically due to the fact that the total drop number determines, consecutively to LWC, the shape (μ_c; Table 2) of the gamma size distribution (Martin et al., 1994). For a given LWC of 0.2 g m^{-3} and droplet numbers of 10, 30, 50, 100 or 200 per cm^3 (typical values encountered in our Sea Ice case), the resulting gamma distribution corresponds to an effective radius of 15.72, 10.89, 9.22, 7.45 or 6.17 µm, respectively (Figure 13a). Thus, the lower the number concentrations the more spread the modelled droplet spectrum. The most important consequence of this is that fall speed and auto-conversion rate both increase and enhance the precipitation formation when low droplet concentrations are simulated (as in Khairoutdinov and Kogan (2000); Planche et al. (2015), among others). In this example, for spectra with 10 drops per cm^3 the corresponding mass-weighted fall speed of the droplets is almost 10 times higher and the auto-conversion rate is 200 times stronger than for a spectra with 200 drops per cm^3 (Figure 13b). Thus, the increase of LWC and cloud depth encountered in the simulations for increasing CCN numbers could be attributed to the overestimation of precipitation caused by the use of a prescribed gamma function.

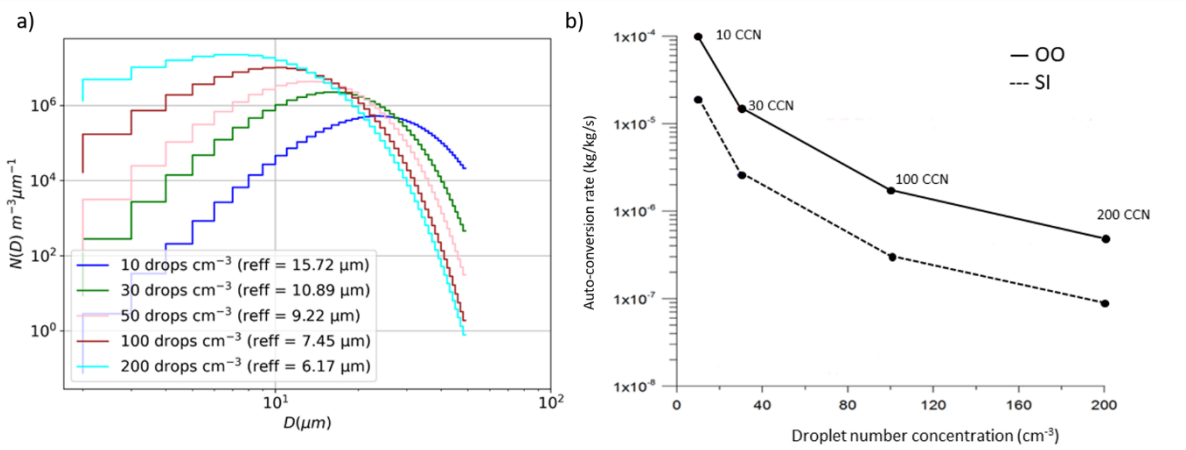

Figure 13. Impacts of the initial droplet number concentration on (a) the drop size distribution (DSD) and the effective radius, and then on (b) the auto-conversion rate using the MORR microphysics scheme. Panels (a) is obtained for a given LWC of 0.2 g m^{-3} (typical value encountered in our Sea Ice case). Panel (b) are obtained considering a LWC equal to 0.2 g m^{-3} for the SI case and 0.4 g m^{-3} for the OO case.

6. Conclusions and outlook

The main objective of this work was to evaluate the performance of the WRF model to reproduce arctic MPCs formed over different surfaces, i.e. over sea ice and over open ocean. To do this, we compared the modelling results with a large number of observations (in-situ and remote sensing) performed during the ACLOUD flight 19 where two MPC systems were observed over sea ice and open ocean. Both MPCs evolved in a quite warm environment (between 0 and -4°C) are characterised by a dominating liquid phase. Also the impact of particle pollution on the cloud parameters was investigated varying the CCN/droplets number concentration.

For both cases, the WRF model underestimates the observed ice crystals concentrations and the associated IWC using the microphysics schemes MORR or MIYA. Temperatures in WRF simulations are slightly higher than the observed ones, effecting that ice formation via the heterogeneous ice nucleation process becomes quite unimportant. However, simulated radar reflectivity reasonably compares with observations because the predefined exponential function for the ice particle distribution describes wider spectra with larger particles than observed (which are essential to the reflectivity).

Changing the number of levels in the vertical profiles of the ERA-5 data used to initialise the simulations affects both the altitude of the MPC layer and the LWC while modifying the boundary layer scheme (MYJ or MYNN3) essentially impacts the altitudes of the cloud top and base. Thus, WRF better reproduces the two arctic MPCs studied in this work when the level ERA-5 level are more numerous close to the surface and with the MYJ scheme.

Increasing the CCN/droplets concentration induces deeper clouds and more LWC. Also the ice amount increases but remains significantly smaller than the liquid amount. Actually, due to the gamma function used to represent the drop size distributions, the effective droplet radius becomes smaller impacting strongly the efficiency of the warm rain processes (i.e., lower auto-conversion rate). This impacts the altitude of the *T*-inversion inducing deeper cloudy conditions where ice can also be formed.

In the future, it is planned to simulate our two MPC systems with a 3D mesoscale model using the DESCAM bin microphysics scheme (DEtailed SCAvenging Model; Flossmann and

Wobrock, 2010; Planche et al., 2014) where the size distributions for drops and ice crystals are not predefined and the supersaturation is explicitly computing for each time step (i.e., no saturation adjustment assumption is used). Then, more extensive studies are possible to quantify the role of the aerosol particles with respect to the liquid and the ice phase of the different MPCs.

Data availability

The datasets analysed for this study can be found in the PANGAEA (Data Publisher for Earth and Environmental Science) database: https://www.pangaea.de/?t=Atmosphere.
All the datasets are listed in the references section.

Author contributions

D.A. performed the simulations, data analysis and wrote the manuscript. SB installed the WRF model and the CR-SIM module on the national calculators. R.D., A.B., G.M., F.T. and O.J. contributed to the analyses of the in-situ aircraft data. C.P. and W.W. contributed to the analyses of the WRF simulations and comparisons between observations and simulation results. J.-L.B. contributed to the analyses using the CAT model. F.T. contributed to the analyses of the radar observations. C.P., O.J. and W.W. supervised D.A. All the authors contributed to the writing/reading of the manuscript.

Funding

The lead author was funded by a doctoral fellowship from the Ecole Doctorale des Sciences Fondamentales (EDSF) of the University Clermont Auvergne (UCA). This work is a contribution to the ACME and $(MPC)^2$ projects, supported by the Agence Nationale de la Recherche under the Grants ANR-21-CE-01-0003 and ANR-22-CE01-0009, respectively. The model calculations have been done on the French computer GENCI facilities of the Institut du Développement des ressources en Informatique Scientifique (IDRIS) CNRS at Orsay, the Centre Informatique National de l'Enseignement Supérieur (CINES) at Montpellier, the Très Grand Centre de Calcul (TGCC) at the CEA, under the project 05056 and the Centre Régional de Ressources Informatiques (CRRI) UCA at Clermont-Ferrand.

Conflict of interest

The authors declare no conflict of interest.

Acknowledgements

The authors acknowledge all the person involved in the ACLOUD campaign for collecting and supplying the data used in this study, especially to André Ehrlich who was the coordinator of the campaign. D.A. would also like to acknowledge Mario Mech and Johannes Stapf for the details they provided about the remote sensing and radiative data which are available via the PANGAEA database. S.B. would like to thank the members of the CR-SIM team for their help in installing this module.

References

Arteaga, D., 2023. Étude des nuages arctiques en phase mixte observés en juin 2017 lors de la campagne ACLOUD à l'aide du modèle atmosphérique WRF. Ph.D. Thesis, Université Clermont Auvergne, Clermont-Ferrand, France.

Baray, J.-L., Deguillaume, L., Colomb, A., Sellegri, K., Freney, E., Rose, C., et al., 2020. Cézeaux- Aulnat-Opme-Puy De Dôme: A multi-site for the long-term survey of the tropospheric composition and climate change. Atmos. Meas. Tech. 13, 3413–3445. https://doi.org/10.5194/amt-13-3413-2020.

Baudoux, A., 2022. Impact des conditions environnementales sur les propriétés microphysiques des nuages en Arctique. Master's thesis, Université Clermont Auvergne, Clermont Ferrand, France.

Baumgardner, D., Brenguier, J., Bucholtz, A., Coe, H., DeMott, P., Garrett, T., et al., 2011. Airborne instruments to measure atmospheric aerosol particles, clouds and radiation: A cook's tour of mature and emerging technology. Atmos. Res. 102, 10–29. https://doi.org/10.1016/j.atmosres.2011.06.021.

Baumgardner, D., Jonsson, H., Dawson, W., O'Connor, D., and Newton, R., 2017. The cloud, aerosol and precipitation spectrometer: a new instrument for cloud investigations. Atmos. Res. 59, 251–264. https://doi.org/10.1016/S0169-8095(01)00119-3.

Bromwich, D. H., Hines, K. M., and Bai, L.-S., 2009. Development and testing of Polar Weather Research and Forecasting model: 2. Arctic Ocean. J. Geophys. Res.-Atmos. 114, D08122. https://doi.org/10.1029/2008JD010300.

Brown, P. R. A. and Francis, P. N., 1995. Improved measurements of the ice water content in cirrus using a total-water probe. J. Atmos. Ocean. Tech. 12, 410–414. https://doi.org/10.1175/1520-0426(1995)0122.0.CO;2.

Chen, F. and Dudhia, J., 2001. Coupling an Advanced Land Surface-Hydrology Model with the Penn State-NCAR MM5 Modeling System. Part I: Model Implementation and Sensitivity. Mon. Wea. Rev. 129, 569–585. https://doi.org/10.1175/1520-0493(2001)129(0569:CAALSH)2.0.CO;2.

Copernicus Climate Change Service (C3S), 2017. ERA5: Fifth Generation of ECMWF Atmospheric Reanalyses of the Global Climate (Copernicus Climate Change Service Climate Data Store (CDS)).

Crosier, J., Bower, K. N., Choularton, T. W., Westbrook, C. D., Connolly, P. J., Cui, Z. Q., et al., 2011. Observations of ice multiplication in a weakly convective cell embedded in supercooled mid-level stratus. Atmos. Chem. Phys. 11, 257–273. https://doi.org/10.5194/acp-11-257-2011.

DeMott, P., Prenni, A., Liu, X., Kreidenweis, S., Petters, M., Twohy, C., et al., 2010. Predicting global atmospheric ice nuclei distributions and their impacts on climate. Proc. Natl. Acad. Sci. 107, 11217–11222. https://doi.org/10.1073/pnas.0910818107.

Dufour, A., Zolina, O., and Gulev, S. K., 2016. Atmospheric Moisture Transport to the Arctic: Assessment of Reanalyses and Analysis of Transport Components. J. Climate. 29, 5061–5081. https://doi.org/10.1175/JCLI-D-15-0559.1.

Dupuy, R., Jourdan, O., Mioche, G., Ehrlich, A., Waitz, F., Gourbeyre, C., et al., 2018. Cloud microphysical properties of summertime Arctic stratocumulus during the ACLOUD campaign: Comparison with previous results in the European Arctic. In 15th Conference on Cloud Physics (Vancouver, Canada), http://hal.archives–ouvertes.fr/hal–01932907.

[Dataset] Dupuy, R., Jourdan, O., Mioche, G., Gourbeyre, C., Leroy, D., and Schwarzenböck, A., 2019. CDP, CIP and PIP: In-situ arctic cloud microphysical properties observed during ACLOUD-AC3 campaign in June 2017. https://doi.org/10.1594/PANGAEA.899074.

Ehrlich, A., Wendisch, M., Bierwirth, E., Gayet, J.-F., Mioche, G., Lampert, A., et al., 2009. Evidence of ice crystals at cloud top of Arctic boundary-layer mixed-phase clouds derived from airborne remote sensing. Atmos. Chem. Phys. 9, 9401–9416. https://doi.org/10.5194/acp-9-9401-2009.

Ehrlich, A., Wendisch, M., Lüpkes, C., Buschmann, M., Bozem, H., Chechin, D., et al., 2019a. A comprehensive in situ and remote sensing data set from the Arctic CLoud Observations Using airborne measurements during polar Day (ACLOUD) campaign. Earth System Science Data. 11, 1853–1881. https://doi.org/10.5194/essd-11-1853-2019.

[Dataset] Ehrlich, A., Wendisch, M., Lüpkes, C., Buschmann, M., Bozem, H., Chechin, D., et al., 2019b. Collection of data sources for the Arctic CLoud Observations Using airborne measurements during polar Day (ACLOUD) campaign, North-West of Svalbard between 23 May - 26 June 2017. https://doi.org/10.1594/PANGAEA.902603.

Eirund, G., Possner, A., and Lohmann, U., 2019. Response of Arctic mixed-phase clouds to aerosol perturbations under different surface forcings. Atmos. Chem. Phys. 19, 9847–9864. https://doi.org/10.5194/acp-19-9847-2019.

Flossmann, A. I., and Wobrock, W., 2010. A review of our understanding of the aerosol-cloud interaction from the perspective of a bin resolved cloud scale modelling. Atmos. Res. 97(4), 2010, 478–497. https://doi.org/10.1016/j.atmosres.2010.05.008.

Gierens, R., Kneifel, S., Shupe, M. D., Ebell, K., Maturilli, M., and Löhnert, U., 2020. Low-level mixed-phase clouds in a complex Arctic environment. Atmos. Chem. Phys. 20, 3459–3481. https://doi.org/10.5194/acp-20-3459-2020.

Griesche, H. J., Ohneiser, K., Seifert, P., Radenz, M., Engelmann, R., and Ansmann, A., 2021. Contrasting ice formation in Arctic clouds: surface-coupled vs. surface-decoupled clouds. Atmos. Chem. Phys. 21, 10357–10374. https://doi.org/10.5194/acp-21-10357-2021.

Gultepe, I., Isaac, G., Hudak, D., Nissen, R., and Strapp, J. W., 2000. Dynamical and Microphysical Characteristics of Arctic Clouds during BASE. J. Climate. 13, 1225–1254. https://doi.org/10.1175/1520-0442(2000) 0132.0.CO;2.

Gultepe, I. and Isaac, G. A., 2002. Effects of air mass origin on Arctic cloud microphysical parameters for April 1998 during FIRE.ACE. J. Geophys. Res.-Atmos. 107(C10). https://doi.org/10.1029/2000JC000440.

Hersbach, H., Bell, B., Berrisford, P., Biavati, G., Horányi, A., Muñoz Sabater, J., et al., 2018a. ERA5 hourly data on single levels from 1959 to present (Copernicus Climate Change Service (C3S) Climate Data Store (CDS)). https://doi.org/10.24381/cds.adbb2d47.

Hersbach, H., Bell, B., Berrisford, P., Biavati, G., Horányi, A., Muñoz Sabater, J., et al., 2018b. ERA5 hourly data on single levels from 1959 to present (Copernicus Climate Change Service (C3S) Climate Data Store (CDS)). https://doi.org/10.24381/cds.bd0915c6.

Hines, K. M. and Bromwich, D. H., 2008. Development and testing of Polar WRF. Part I: Greenland Ice Sheet meteorology. Mon. Wea. Rev. 136, 1971–1989. https://doi.org/10.1175/2007MWR2112.1.

Hines, K. M., Bromwich, D. H., Bai, L.-S., Barlage, M., and Slater, A. G., 2011. Development and Testing of Polar WRF. Part III: Arctic Land. J. Climate. 24, 26–48. https://doi.org/10.1175/2010JCLI3460.1.

Iacono, M., Delamere, J., Mlawer, E. J., Shephard, M., Clough, S., and Collins, W. D., 2008. Radiative forcing by long-lived greenhouse gases: Calculations with the AER radiative transfer models. J. Geophys. Res.-Atmos. 113, D13103. https://doi.org/10.1029/2008JD009944.

Iacono, M. J., 2011. Application of Improved Radiation Modeling to General Circulation Models (Atmospheric and Environmental Research, Inc.), Final Technical Report Edn.

Ikonen, I., Demetriades, N. W. S., and Holle, R., 2010. Vaisala dropsondes: History, status, and applications. In 29th Conference on Hurricanes and Tropical Meteorology (SPONSOR, Tucson, Ariz.), 1–4.

Janjic, Z., 2002. Nonsingular Implementation of the Mellor-Yamada Level 2.5 Scheme in the NCEP Meso Model. NCEP Office Note 437, 61.

Järvinen, E., Nehlert, F., Xu, G., Waitz, F., Mioche, G., Dupuy, R., et al., 2023. Investigating the vertical extent and short-wave radiative effects of the ice phase in Arctic summertime low-level clouds. Atmos. Chem. Phys. 23, 7611–7633. https://doi.org/10.5194/acp-23-7611-2023.

Khairoutdinov, M., and Y. Kogan, 2000. A New Cloud Physics Parameterization in a Large-Eddy Simulation Model of Marine Stratocumulus. Mon. Wea. Rev. 128, 229–243. https://doi.org/10.1175/1520-0493(2000)128<0229:ANCPPI>2.0.CO;2.

[Dataset] Kliesch, L.-L. and Mech, M., 2019. Airborne radar reflectivity and brightness temperature measurements with POLAR 5 during ACLOUD in May and June 2017. https://doi.org/10.1594/PANGAEA.899565.

Knudsen, E. M., Heinold, B., Dahlke, S., Bozem, H., Crewell, S., Gorodetskaya, I. V., et al., 2018. Meteorological conditions during the ACLOUD/PASCAL field campaign near Svalbard in early summer 2017. Atmos. Chem. Phys. 18, 17995–18022. https://doi.org/10.5194/acp-18-17995-2018.

Korolev, A. and Leisner, T., 2020. Review of experimental studies of secondary ice production. Atmos. Chem. Phys. 20, 11767–11797. https://doi.org/10.5194/acp-20-11767-2020.

Küchler, N., Kneifel, S., Löhnert, U., Kollias, P., Czekala, H., and Rose, T., 2017. A W-band radar-radiometer system for accurate and continuous monitoring of clouds and precipitation. J. Atmos. Ocean. Tech. 34, 2375–2392. https://doi.org/10.1175/JTECHD-17-0019.1.

Leck, C. and Svensson, E., 2015. Importance of aerosol composition and mixing state for cloud droplet activation over the Arctic pack ice in summer. Atmos. Chem. Phys. 15, 2545–2568. https://doi.org/10.5194/acp-15-2545-2015.

Leinonen, J. and Szyrmer, W., 2015. Radar signatures of snowflake riming: A modeling study. Earth and Space Science 2, 346–358. https://doi.org/10.1002/2015EA000102.

Leroy, D., Fontaine, E., Schwarzenboeck, A., and Strapp, J. W., 2016. Ice Crystal Sizes in High Ice Water Content Clouds. Part I: On the Computation of Median Mass Diameter from In Situ Measurements. J. Atmos. Ocean. Tech. 33, 2461–2476. https://doi.org/10.1175/JTECH-D-15-0151.1.

Lloyd, G., Choularton, T. W., Bower, K. N., Crosier, J., Jones, H., Dorsey, J. R., et al., 2015. Observations and comparisons of cloud microphysical properties in spring and summertime Arctic stratocumulus clouds during the ACCACIA campaign. Atmos. Chem. Phys. 15, 3719–3737. https://doi.org/10.5194/acp-15-3719-2015.

Ludwig, V., Spreen, G., Haas, C., Istomina, L., Kauker, F., and Murashkin, D., 2019. The 2018 North Greenland polynya observed by a newly introduced merged optical and passive microwave sea-ice concentration dataset. The Cryosphere. 13, 2051–2073. https://doi.org/10.5194/tc-13-2051-2019.

Martin, G. M., Johnson, D. W., and Spice, A., 1994. The Measurement and Parameterization of Effective Radius of Droplets in Warm Stratocumulus Clouds. J. Atmos. Sci. 51, 1823–1842. https://doi.org/10.1175/1520-0469(1994)051<1823:TMAPOE>2.0.CO;2.

McFarquhar, G. M. and Heymsfield, A. J., 1996. Microphysical characteristics of three anvils sampled during the Central Equatorial Pacific Experiment. J. Atmos. Sci. 53, 2401–2423. https://doi.org/10.1175/1520-0469(1996)053,2401:MCOTAS.2.0.CO;2.

Mech, M., Kliesch, L.-L., Anhäuser, A., Rose, T., Kollias, P., and Crewell, S., 2019. Microwave Radar/radiometer for Arctic Clouds (MiRAC): first insights from the ACLOUD campaign. Atmos. Meas. Tech. 12, 5019–5037. https://doi.org/10.5194/amt-12-5019-2019.

Mertes, S., Schröder, F., and Wiedensohler, A., 1995. The particle detection efficiency curve of the Tsi-3010 CPC as a function of the temperature difference between saturator and condenser. Aerosol. Sci. Technol. 23, 257–261. https://doi.org/10.1080/02786829508965310.

Milbrandt, J. A. and Yau, M. K., 2005a. A multi-moment bulk microphysics parametrization. Part I: Analysis of the role of the spectral shape parameter. J. Atmos. Sci. 62, 3051–3064. https://doi.org/10.1175/JAS3534. 1.

Milbrandt, J. A. and Yau, M. K., 2005b. A multi-moment bulk microphysics parametrization. Part II: A proposed three-moment closure and scheme description. J. Atmos. Sci. 62, 3065–3081. https://doi.org/10.1175/JAS3535.1.

Mioche, G., Jourdan, O., Delanoë, J., Gourbeyre, C., Febvre, G., Dupuy, R., et al., 2017. Vertical distribution of microphysical properties of Arctic springtime low-level mixed-phase clouds over the Greenland and Norwegian seas. Atmos. Chem. Phys. 17, 12845–12869. https://doi.org/10.5194/acp-17-12845-2017.

Monin, A. S. and Obukhov, A. M., 1954. Basic laws of turbulent mixing in the surface layer of the atmosphere. Contrib. Geophys. Inst. Acad. Sci. USSR 151, 163–187.

Morrison, H., Thompson, G., and Tatarskii, V., 2009. Impact of Cloud Microphysics on the Development of Trailing Stratiform Precipitation in a Simulated Squall Line: Comparison of One and Two-Moment Schemes. Mon. Wea. Rev. 137, 991–1007. https://doi.org/10.1175/2008MWR2556.1.

Nakanishi, M. and Niino, H., 2006. An Improved Mellor-Yamada Level 3 Model: Its Numerical Stability and Application to a Regional Prediction of Advection Fog. Boundary-Layer Meteorology. 119, 397–407. https://doi.org/10.1007/s10546-005-9030-8.

Nakanishi, M. and Niino, H., 2009. Development of an improved turbulence closure model for the atmospheric boundary layer. J. Meteorol. Soc. Japan. Ser. II. 87, 895–912. https://doi.org/10.2151/jmsj.87.895.

[Dataset] Neuber, R., Schmidt, L. V., Ritter, C., and Mech, M., 2019. Cloud top altitudes observed with airborne lidar during the ACLOUD campaign. https://doi.org/10.1594/PANGAEA.899962.

Ori, D., von Terzi, L., Karrer, M., and Kneifel, S., 2021. SnowScatt 1.0: consistent model of microphysical and scattering properties of rimed and unrimed snowflakes based on the self-similar Rayleigh-Gans approximation. Geosci. Model Dev. 14, 1511–1531. https://doi.org/10.5194/gmd-14-1511-2021.

Oue, M., Tatarevic, A., Kollias, P., Wang, D., Yu, K., and Vogelmann, A. M., 2020. The Cloud-resolving model Radar SIMulator (CR-SIM) Version 3.3: description and applications of a virtual observatory. Geosci. Model Dev. 13, 1975–1998. https://doi.org/10.5194/gmd-13-1975-2020.

Planche, C., Mann, G. W., Carslaw, K. S., Dalvi, M., Marsham, J. H., and Field, P. R., 2017. Spatial and temporal CCN variations in convection-permitting aerosol microphysics simulations in an idealized marine tropical domain. Atmos. Chem. Phys. 17, 3371–3384. https://doi.org/10.5194/acp-17-3371-2017.

Planche, C., Marsham, J., Field, P., Carslaw, K., Hill, A., Mann, G., and Shipway, B. 2015. Precipitation sensitivity to autoconversion rate in a Numerical Weather Prediction Model. Q. J. R. Meteorol. Soc. 141, 2032-2044. DOI: 10.1002/qj.2497

Planche, C., Tridon, F., Banson, S., Thompson, G., Monier, M., Battaglia, A., et al., 2019. On the Realism of the Rain Microphysics Representation of a Squall Line in the WRF Model. Part II: Sensitivity Studies on the Rain Drop Size Distributions. Mon. Wea. Rev. 147, 2811–2825. https://doi.org/10.1175/MWR-D-18-0019.1.

Planche, C., Wobrock, W., and Flossmann, A. 2014. The continuous melting process in a cloud scale model using a bin microphysics scheme. Q. J. R. Meteorol. Soc. 140, 1986–1996. https:// doi.org/10.1002/qj.2265

Ruiz-Donoso, E., Ehrlich, A., Schäfer, M., Jäkel, E., Schemann, V., Crewell, S., et al., 2020. Small-scale structure of thermodynamic phase in Arctic mixed-phase clouds observed by airborne remote sensing during a cold air outbreak and a warm air advection event. Atmos. Chem. Phys. 20, 5487–5511. https://doi.org/10.5194/acp-20-5487-2020.

Savre, J., Ekman, A. M. L., Svensson, G., and Tjernström, M., 2014. Large-eddy simulations of an Arctic mixed-phase stratiform cloud observed during ISDAC: sensitivity to moisture aloft, surface fluxes and large-scale forcing. Quart. J. Roy. Meteorol. Soc. 141, 1177–1190. https://doi.org/10.1002/qj.2425.

Skamarock, W. C., Klemp, J. B., Dudhia, J., Gill, D. O., Baker, D. M., Duda, M. G., et al., 2008. A Description of the Advanced Research WRF Version 3 (NCAR/TN-475+STR Technical Note, 125 pp.).

Sorteberg, A. and Walsh, J. E., 2008. Seasonal cyclone variability at 70°N and its impact on moisture transport into the Arctic. Tellus A. 60, 570–586. https://doi.org/10.1111/j.1600-0870.2007.00314.x.

Stachlewska, I. S., Neuber, R., Lampert, A., Ritter, C., and Wehrle, G., 2010. AMALi-the Airborne Mobile Aerosol Lidar for Arctic research. Atmos. Chem. Phys. 10, 2947–2963. https://doi.org/10.5194/acp-10-2947-2010.

Stapf, J., Ehrlich, A., Jäkel, E., Lüpkes, C., and Wendisch, M., 2020. Reassessment of shortwave surface cloud radiative forcing in the Arctic: consideration of surface-albedo-cloud interactions. Atmos. Chem. Phys. 20, 9895–9914. https://doi.org/10.5194/acp-20-9895-2020.

[Dataset] Stapf, J., Ehrlich, A., Jäkel, E., and Wendisch, M., 2019a. Aircraft measurements of broadband irradiance during the ACLOUD campaign in 2017. https://doi.org/10.1594/PANGAEA.900442.

[Dataset] Stapf, J., Ehrlich, A., Jäkel, E., and Wendisch, M., 2019b. Cloud radiative forcing, LWP and cloud-free albedo derived from airborne broadband irradiance observations during the ACLOUD campaign. https://doi.org/10.1594/PANGAEA.909289.

Tjernström, M., Leck, C., Birch, C. E., Bottenheim, J. W., Brooks, B. J., Brooks, I. M., et al., 2014. The Arctic Summer Cloud Ocean Study (ASCOS): overview and experimental design. Atmos. Chem. Phys. 14, 2823–2869. https://doi.org/10.5194/acp-14-2823-2014.

Tjernström, M. and Graverson, R., 2009. The vertical structure of the lower Arctic troposphere analyzed from observations and the ERA-40 reanalysis. Q. J. R. Meteorol. Soc. 135, 431–443. https://doi.org/10.1002/qj.380.

Tridon, F., Battaglia, A., Chase, R. J., Turk, F. J., Leinonen, J., Kneifel, S., et al., 2019a. The microphysics of stratiform precipitation during OLYMPEX: Compatibility between triple-frequency radar and airborne in situ observations. J. Geophys. Res. - Atmos. 124, 8764–8792. https://doi.org/10.1029/2018JD029858.

Tridon, F., Planche, C., Mroz, K., Banson, S., Battaglia, A., Van Baelen, J., et al., 2019b. On the Realism of the Rain Microphysics Representation of a Squall Line in the WRF Model. Part I: Evaluation with Multifrequency Cloud Radar Doppler Spectra Observations. Mon. Wea. Rev. 147, 2787–2810. https://doi.org/10.1175/MWR-D-18-0018.1.

Twohy, C., Strapp, J., and Wendisch, M., 2003. Performance of a Counterflow Virtual Impactor in the NASA Icing Research Tunnel. J. Atmos. Ocean. Technol. 20, 781–790. https://doi.org/10.1175/1520-0426(2003) 020⟨0781:POACVI⟩2.0.CO.

Wendisch, M., Brückner, M., Burrows, J. P., Crewell, S., Dethloff, K., Ebell, K., et al., 2017. ArctiC Amplification: Climate Relevant Atmospheric and SurfaCe Processes, and Feedback Mechanisms $(AC)^3$. Eos, Trans. Amer. Geophys. Union. 98. https://doi.org/10.1029/2017EO064803.

Wendisch, M., Brückner, M., Crewell, S., Ehrlich, A., Notholt, J., Lüpkes, C., et al., 2023. Atmospheric and Surface Processes, and Feedback Mechanisms Determining Arctic Amplification: A Review of First Results and Prospects of the $(AC)^3$ Project. Bull. Amer. Meteorol. Soc. 104, E208–E242. https://doi.org/10.1175/BAMS-D-21-0218.1.

Wendisch, M., Macke, A., Ehrlich, A., Lüpkes, C., Mech, M., Chechin, D., et al., 2019. The Arctic Cloud Puzzle: Using ACLOUD/PASCAL Multiplatform Observations to Unravel the Role of Clouds and Aerosol Particles in Arctic Amplification. Bull. Amer. Meteorol. Soc. 100, 841–871. https://doi.org/10.1175/BAMS-D-18-0072.1.

Woods, C., Caballero, R., and Svensson, G., 2013. Large-scale circulation associated with moisture intrusions into the Arctic during winter. Geophys. Res. Lett. 40, 4717–4721. https://doi.org/10.1002/grl.50912.

Xue, J., Xiao, Z., Bromwich, D. H., and Bai, L., 2022. Polar WRF V4.1.1 simulation and evaluation for the Antarctic and Southern Ocean. Front. Earth Sci. 16, 1005–1024. https://doi.org/10.1007/s11707-022-0971-8.

Young, G., Jones, H. M., Choularton, T. W., Crosier, J., Bower, K. N., Gallagher, M. W., et al., 2016. Observed microphysical changes in Arctic mixed-phase clouds when transitioning from sea ice to open ocean. Atmos. Chem. Phys. 16, 13945–13967. https://doi.org/10.5194/acp-16-13945-2016.

Yu, L., Yang, Q., Zhou, M., Zeng, X., Lenschow, D. H., Wang, X., et al., 2019. The Intraseasonal and Interannual Variability of Arctic Temperature and Specific Humidity Inversions. Atmosphere. 10(4). https://doi.org/10.3390/atmos10040214.

Conclusions and perspectives

Conclusions

In this thesis, we have used the WRF model to reproduce low level (MPCs) observed on 17 June 2017 over the northern Fram Strait between Greenland and Svalbard, during the ACLOUD campaign. Two case studies were selected to study the impact of the surface on the overlying cloud layer. Two low cloud fields were encountered, one over ice (SI) and another over open ocean (OO). MIRAC cloud radar, dropsondes and in-situ microphysics probes deployed on-board the Polar 5 and Polar 6 aircrafts were compared with results of the WRF model. We have shown how the microphysical properties of mixed-phase clouds can significantly change over sea ice and over the ocean.

The surface properties have a significant impact on MPCs properties. Our study supports previous results obtained during the ACCACIA, AFLUX and MOSAIC-ACA campaigns (Young et al., 2016, 2017; Moser et al., 2023). Near surface temperature increased significantly by 4°C from sea ice to ocean. Enhanced surface fluxes, vertical motion, and turbulent activity imply a more efficient mixing in the boundary layer over ocean than over the sea ice. This increased vertical moisture flux likely promotes the formation of more cloud droplets and increases the probability of efficient collision-coalescence. Consequently the cloud layer became deeper, with higher LWC. As the boundary layer over sea ice is generally less humid, cloud droplet and ice crystal formation and growth are limited compared to the cloud formation over open ocean.

The predominant change in cloud microphysics was in the liquid phase. The supercooled liquid water phase is generally more dominating in the OO case that in the SI case, in accordance with several previous studies performed in the Arctic (Mioche et al., 2017; Gierens et al., 2020; Järvinen et al., 2023, among others). LWC is more important while the IWC remains comparable between the SI and OO case. Due to the contrasted liquid-ice partitioning in both cases, the cloud droplets-ice crystals interaction processes can be different. Indeed, a comparative analysis between in-situ microphysics probes and the MIRAC cloud radar suggests the presence of slightly rimed aggregates in both cases but with a degree of riming less important in the SI case than in the OO case. This comparative study also illustrates the necessity to consider adaptive mass-diameter relationships according to the degree of riming in the calculations of the radar reflectivity or the IWC from in-situ measurements. Moreover, the ice number concentrations were low but they remained higher than the INP concentrations (estimated from the aerosol concentration observations) and they decrease over the transition from SI to OO. This suggests that ice phase over surfaces with sea ice can be formed by the heterogeneous nucleation process and possibly by secondary ice processes. In example, the Hallett-

Mossop process, which occurs in a temperature range between -8°C and -3°C, could be more or less active according to the case. Moreover, the ice crystals sizes observed were typically found to be larger over sea ice (max. 2 mm) than over the open ocean (max. 0.5 mm).

The instrumentation deployed on-board the Polar 5 and the Polar 6 aircrafts was used to quantitatively compare the simulated thermodynamics and microphysics properties of the MPCs with results of the WRF model. Two different simulations using either 21 (WRF21) or 38 (WRF38) pressure levels in the initial ERA5 reanalysis data (in WRF38; three pressure levels were added for the lowest layers at 975 hPa, 875 hPa, and 825 hPa) are performed in order to understand the role of the model initialisation. The WRF38 baseline experiment provided reasonable results compared to the observations in both cases SI and OO, with some discrepancies: underestimation of the ice phase (especially for the SI case where the temperatures close to the surface remain 2°C higher than observed) and underestimation of the altitude of the cloud top (mainly over OO). The ice underestimation was mainly attributed to differences in thermodynamical properties, notably the higher temperatures between 300-500 m. Simulated ice number concentrations were low and remained low over ocean, suggesting only primary ice formation was active. The secondary ice production is not possible because simulated temperatures are quite warm, which can explain the underestimation of ice compared to the observations. The ice crystals observed and simulated were typically found to be larger over sea ice than over the open ocean.

To evaluate the sensitivity of modelled MPCs properties to the representation of the physics processes, modelling experiments were performed using different parameterisations for the boundary layer (BL) and the microphysics (MP). Two boundary layer (BL) schemes were tested: MYJ: Mellor-Yamada-Janjic (Janjić, 2002) and MYNN3: Mellor-Yamada-Nakanishi Niino (Nakanishi and Niino, 2006, 2009). Both schemes are based on the use of TKE, but differ in the way mixing lengths scales are formulated. Simulated clouds in the WRF-BL experiment (using MYNN3) have similar LWC and IWC as in the WRF38 experiment (using MYJ) in both cases SI and OO, but both liquid and ice water phases extend on thicker layers and are present at higher altitudes. The trends obtained in the vertical distribution of the condensed water phases for both cases can be induced by variations in surface sensible (F_{sen}) and latent (F_{lat}) fluxes and in thermodynamics features within the boundary layer. With this sensitivity study, the MYJ boundary layer scheme (used in WRF38) seems to be more appropriate to represent conditions of the lower atmosphere in the Arctic, because simulation results for the vertical evolutions of the temperature and relative humidity as well as the condensed water phases are in better agreement with the observations (as *e.g.,* in Matejka et al. (2021) and Loyer (2022)).

The microphysical representation was tested, using two double-moment schemes: Morrison (used in the WRF38 experiment) (Morrison et al., 2009a) and Milbrandt and Yau (MIYA, used in the WRF-MP experiment) (Milbrandt and Yau, 2005a,b). The main difference between both schemes is the ice representation. The MIYA scheme applies the same prognostic variables as the Morrison scheme. However, the three ice formation mechanisms (deposition, contact and immersion freezings) considered in MIYA are activated at warmer temperatures ($\approx$ 2-3°C higher) than in Morrison. In the WRF-MP experiment, not only the quantities for LWC and IWC change but also their vertical profiles. For the SI case, both condensed water phases become more important than in

WRF38. This is due to variations in the thermodynamics properties: the T-inversion is located at a higher altitude (as in WRF-BL) and is also more pronounced. Also the highest levels of the atmosphere are more humid and cooler in WRF-MP compared to the WRF38 experiment, which allows to activate the heterogeneous ice nucleation mechanisms and promotes the increase of IWC. For the OO case, no significant change in the vertical profile of the LWC and the IWC are obtained in WRF-MP compared with WRF38.

The robustness of the response of the model results to different aerosol (with CCN ability) concentrations was investigated by several scenarios: 10, 30, 100 and 250 CCN cm^{-3} over SI and OO. The CCN concentrations were chosen to match the observed N_{CCN} over the sea ice (10 cm^{-3}) and over open sea (100 cm^{-3}), and with other different CCN concentrations observed in various marine environmental conditions. The microphysical structure of MPCs is particularly more sensitive to CCN concentration over SI than over OO, as Eirund et al. (2019) has previously shown. Over OO the changes in the LWC and IWC are less important than over SI case for an identical variation in the initial CCN concentration. The increasing CCN concentration over SI and OO, induced an increase on LWC and IWC and also enhanced cloud vertical extension. This could be a result of the latent heat release during cloud droplet formation which feeds back onto the updraft velocities (Eirund et al., 2019). Also, the cloud deepening leads to an increase in IWC because at higher altitudes, the heterogeneous ice nucleation process becomes more active. Studies have previously shown that the microphysical structure of MPCs is particularly sensitive to the modelled ice crystal concentration (Young et al., 2016; Eirund et al., 2019). For high CCN concentrations (higher than 100 cm^{-3} for the SI case and higher than 250 cm^{-3} for the OO case), the response in the vertical profiles of the LWC and IWC is small as if the boundary layer becomes saturated for these critical CCN concentrations.

Perspectives

Arctic low-level mixed-phase clouds were quite well reproduced by the WRF atmospheric model. Nevertheless, discrepancies were found in the simulated properties of the ice phase compared to observations, such as the underestimations of the IWC and the ice crystal concentrations. Moreover, the model had difficulties to reproduce the ice particle size distributions. Thus, this suggests that the ice phase processes such as the ice formation can still be improved in this model. Indeed, the accurate knowledge of the ice crystal concentration is of primary importance to correctly parameterise the initiation and evolution of the ice phase in models. It could reduce the significant uncertainties in the modelling of the liquid-ice partitioning within MPCs, and so better understand their roles in the Arctic amplification.

In the WRF model, the different parameterisations used to describe the heterogeneous ice nucleation processes are dependent on the temperature (Bigg, 1953; Cooper, 1986; Meyers et al., 1992) but all of them were developed within colder temperature ranges than those encountered in both ACLOUD cases studied in this thesis. Additional tests were done in this work using other parameterisations such as those of Young et al. (2017), Mioche et al. (2017), and DeMott et al. (2010) but no reasonable results were found because the application range of these relationships are estab-

lished for significantly lower temperatures. In the future, it could be interesting to simulate colder cases formed under cold air outbreak conditions observed during recent campaigns, *e.g.,* AFLUX (spring 2019) or RALI-THINICE (summer 2022). Moreover, in the framework of the (MPC)^2 (*Microphysical Process Characterization of Mixed Phase Clouds in the European Arctic*) project recently funded by the ANR program (https://anr.fr/Projet-ANR-22-CE01-0009), cloud data from several key cases observed during different campaigns performed in the Arctic region will be analysed in order to develop new heterogeneous ice nucleation parameterisations that can be more adapted to warm conditions encountered in both ACLOUD cases. Then, they could be implemented in the WRF model to evaluate the new ability of the model to better reproduce both MPCs.

The observations used in this study to compare with the WRF simulation results suffer from few limitations. Firstly, the INP concentrations were estimated using the (DeMott et al., 2010) parameterisation and the observation of the aerosol concentrations. Also, the microphysics properties are solely based on the CIP probe which has strong limitation for the liquid-ice phase discrimination and only samples crystals larger than about 100 μm. The Small Ice Detector mark 3 (SID-3) which can give information on the smaller crystals could have been associated to better estimate the ice concentrations. Thus, the differences found in the ice concentrations between observations and simulations could even be larger. In the future, it can be of interest to focus on MPC situations for which all these observations are available.

Moreover, it could be interesting to simulate both ACLOUD cases studied in this thesis with another atmospheric model such as DESCAM which uses a detailed (bin) microphysics module (Flossmann and Wobrock, 2010; Planche et al., 2010, 2014; Kagkara et al., 2020; Arteaga et al., 2020). This model simulates the number distribution functions for aerosol particles, droplets/raindrops and ice/snow. Unlike in the WRF model, none predefined hydrometeor distributions are used in DESCAM which could facilitate the comparisons with observed DSDs and ice PSDs. Also, DESCAM is explicitly computing supersaturation for each time step (*i.e.,* no saturation adjustment assumption is used) and the heterogeneous ice nucleation process is dependent on the supersaturation (Meyers et al., 1992). Thus, the ability of ice formation is quite different compared to that in the WRF model. Currently, in the framework of the ACME (*Aerosol-Cloud interactions in contrasted Marine Environments*) project recently funded by the ANR program (https://anr.fr/Projet-ANR-21-CE01-0003), the different secondary ice mechanisms: such as the Hallett-Mossop rime-splintering, the breakup of large freezing droplets, and the ice breakup associated to ice-ice collisions (more details in Lauber et al. (2020) and Korolev and Leisner (2020)) are implemented to the DESCAM module in order to better estimate the ice concentrations in MPCs. Then, sensitivity studies could be performed using DESCAM in order to study the impact of thermodynamics and aerosol loadings on our both cases focussing on the simulated ice concentrations in order to compare with WRF results where only the Hallett-Mossop rime-splintering process is considered.

Since the low-level MPCs are generally coupled to the surface, the representation of the boundary layer properties is important to accurately simulate the lifecyle of these clouds. Simulations performed using both WRF and DESCAM could investigate the impact of this representation (parameterised vs. explicit).

Appendix A

Extended abstract in French

A.1 Introduction

Différents processus physiques associés aux conditions de surface et thermodynamiques ainsi qu'aux concentrations en particules d'aérosol influencent la formation et la persistance des nuages en phase mixte (MPCs pour "mixed-phase clouds") présents en Arctique. Ces nuages qui ont un rôle important dans le phénomène du réchauffement climatique accéléré en Arctique (appelé phénomène d'Amplication arctique) sont encore mal compris à cause de leurs différentes rétroactions. Dans le cadre de la campagne internationale ACLOUD (*Arctic CLoud Observations Using airborne measurements during polar Day*) qui s'est déroulée au Svalbard au printemps 2017, deux systèmes nuageux ayant des caractéristiques contrastées ont été échantillonnés le 17 juin 2017 avec le radar nuage MIRAC (94 GHz), des dropsondes et des mesures de sondes microphysiques insitu, instruments qui étaient déployés à bord des avions de recherche Polar 5 et Polar 6.

Ce travail de thèse montre comment les observations ACLOUD peuvent être utilisées pour évaluer la représentation des propriétés des MPCs dans le modèle WRF (*Weather Research and Forecasting model*) et étudie également comment les propriétés des MPCs sont impactées par différentes conditions de thermodynamiques atmosphériques, de surface et de concentration des aerosols.

A.2 Observations ACLOUD

La campagne ACLOUD a été menée dans le cadre du projet "*Arctic Amplification: climate relevant atmospheric and surface processes, and feedback mechanisms*" $(AC)^3$ (Wendisch et al., 2017, 2019). La campagne ACLOUD s'est déroulée entre le 23 mai et le 26 juin 2017 dans le Nord-Ouest de l'archipel du Svalbard (couvrant la zone 76-81°N et 10-28°E). Cette région est connue pour être influencée par différents types de masses d'air (par ex., des intrusions d'air chaud en provenance du Sud ou d'air froid en provenance de l'Océan Arctique) et par le transport sur de longues distances de particules d'aérosol et de polluants en provenance des latitudes moyennes (Knudsen et al., 2018; Wendisch et al., 2022). De plus, cette région est située entre la mer du Groenland et l'océan Arctique et se caractérise par une zone de transition entre la glace

de mer et l'océan au printemps (Young et al., 2016). Comme le montrent Knudsen et al. (2018), diverses conditions synoptiques ont affecté la région pendant la campagne ACLOUD. Trois périodes clés ont été définies : une période froide (CP pour "cold period"; 23-29 mai), une période chaude (WP pour "warm period"; 30 mai-12 juin) et une période normale (NP pour "normal period"; 13-26 juin). Ces différentes situations synoptiques entraînent des variations soudaines dans les propriétés thermodynamiques de l'atmosphère et la structure des nuages (Ruiz-Donoso et al., 2020; Wendisch et al., 2022).

A.2.1 Vol 19 du 17 juin 2017

Pendant la campagne ACLOUD, des observations colocalisées ont été réalisées et de nombreux paramètres atmosphériques ont été mesurés par des instruments installés sur les avions Polar 5 (P5) et Polar 6 (P6) de l'Institut allemand Alfred Wegener (AWI) (Wesche et al., 2016). A bord de l'avion Polar 5, le radar nuage MIRAC (94 GHz) et un lidar ont été embarqués, mais aussi des dropsondes, tandis que l'avion Polar 6 a principalement été équipé d'instruments in-situ utilisés pour caractériser, par exemple, les particules d'aérosol, les gouttelettes d'eau surfondue et les cristaux de glace au sein des nuages.

Le vol 19 effectué le 17 juin 2017 a duré plus de 5 heures et a permis d'échantillonner deux structures nuageuses différentes au-dessus de la glace de mer (à 11:00 UTC) ou au-dessus de l'océan (à 14:00 UTC), correspondant respectivement aux cas SI (pour "Sea Ice") et OO (pour "Open Ocean") étudiés ci-après. L'avion Polar 5 a toujours volé à des altitudes plus élevées que l'avion Polar 6, ce qui a permis de mesurer les caractéristiques verticales de la thermodynamique de l'atmosphère et de la microphysique des nuages à l'aide des dropsondes et des mesures de télédétection (radar et lidar). En ce qui concerne l'avion Polar 6, il a volé à des altitudes plus basses, c'est-à-dire à l'intérieur des stratocumulus arctiques en phase mixte, en utilisant une stratégie de paliers afin d'obtenir le profil vertical des propriétés microphysiques des différents nuages échantillonés (par ex., les profils des concentrations en cristaux de glace ou en gouttelettes).

A.2.2 Conditions synoptiques et de pollution des deux cas d'étude

Les conditions synoptiques peuvent être obtenues à partir des données de réanalyse ERA-5 fournies par le Centre Européen pour les Prévisions Météorologiques à Moyen Terme (CEPMMT) (Copernicus Climate Change Service (C3S)) sur une grille horizontale de 0,25° × 0,25° et pour différents niveaux de pression. La journée du 17 juin 2017 est marquée par trois systèmes de basses pressions (ou dépressions) présents autour de la région survolée lors de la campagne ACLOUD : le premier est centré sur l'Islande, le second sur la mer de Baffin à l'Ouest du Groenland, et le troisième au Nord-Est de l'archipel du Svalbard. En outre, un système de hautes pressions (ou anticyclone) peu intense était localisé sur le Nord de l'Europe. Ces conditions synoptiques ont induit deux courants de masses d'air autour du Svalbard : une masse d'air froid en provenance du pôle Nord et une masse d'air tempéré en provenance de l'océan Atlantique Nord via la mer de Norvège. A noter que cette dernière masse d'air est régulièrement observée

sur cette région apportant ainsi de l'humidité et de la chaleur des moyennes latitudes vers les latitudes plus élevées (Sorteberg and Walsh, 2008; Tjernström and Graverson, 2009; Woods et al., 2013; Dufour et al., 2016; Yu et al., 2019, entre autres). Ces deux masses d'air ont provoqué d'importantes variations dans les champs de température (T) et d'humidité relative (RH) au voisinage de la région de la campagne ACLOUD.

Les propriétés des nuages arctiques sont étroitement liées à l'origine de la masse d'air et donc aux propriétés des aérosols (Gultepe et al., 2000; Gultepe and Isaac, 2002). L'origine de la masse d'air pour chacun des MPCs étudiés est analysée à l'aide du modèle CAT (Computing Advection-interpolation of atmospheric parameters and Trajectory tool) avec des rétro-trajectoires (Baray et al., 2020). Les rétro-trajectoires sont calculées sur 72 heures en utilisant une topographie ayant une résolution horizontale d'environ 10 km^2 et avec des champs de vent fournis par les données de réanalyses ERA-5 (Hersbach et al., 2018a,b) toutes les 3 heures et avec une résolution spatiale de 0,25° en latitude et longitude. Pour les deux MPCs étudiés, les masses d'air à leur origine viennent du Nord-Est du Svalbard. Par conséquent, ces deux masses d'air ne sont donc pas passées au-dessus de zones anthropiques et les concentrations en particules d'aérosol mesurées ne sont pas caractéristiques d'environnements pollués. En effet, pour le cas SI, la valeur médiane observée pour la concentration en aérosols est égale à 13 ± 63 cm^{-3} et, pour le cas OO, elle est égale à 3000 ± 365cm^{-3}. La différence dans ces valeurs médianes peut être expliquée par les propriétés de surface ; les sels marins peuvent plus facilement être émis localement par l'océan dans le cas OO.

A.2.3 Propriétés microphysiques des nuages

Les deux systèmes de MPCs étudiés se sont formés soit au-dessus de la banquise, soit au-dessus de l'océan, ce qui permet d'étudier l'effet des changements de surface sur les propriétés nuageuses. Les observations révèlent une situation de couplage "nuage-surface" pour les deux cas puisque les variations verticales de la température potentielle entre la surface et la base des différents MPCs sont inférieures à 0,5°C. Les MPCs observés au-dessus de l'océan (cas OO) se sont formés dans des conditions plus chaudes que ceux observés au-dessus de la banquise (cas SI). De plus, pour le système nuageux OO, sa base est située à plus haute altitude, son contenu en eau liquide surfondue (LWC) est plus important et son contenu en eau glacée (IWC) est plus faible que pour le système nuageux SI. Les distributions en taille des cristaux de glace (ou PSD pour "particle size distributions") obtenues pour les différents paliers effectués par l'avion P6 s'étendent à des tailles plus importantes pour le cas SI que pour le cas OO. De plus, pour le cas OO, même si les formes des distributions en taille des gouttes (ou DSD pour "drop size distributions") sont assez similaires à celles du cas SI, les gouttelettes sont légèrement plus nombreuses (OO : 75 cm^{-3} ; SI : 51 cm^{-3}) et ont des tailles plus élevées (OO : 50 μm ; SI : 40 μm).

Les instruments déployés à bord des avions Polar 5 et Polar 6 ont l'avantage de mesurer les mêmes zones des nuages avec des techniques différentes, à savoir la télédétection et les mesures des sondes in-situ. Les réflectivités mesurées par le radar nuage MIRAC (Polar 5) ont été comparées avec les réflectivités calculées à partir des PSD et DSD observées (Polar 6). Pour ces dernières, nous avons utilisé un modèle électromagnétique-microphysique type SSRGA (Self-Similar de Rayleigh-Gans) et afin

d'étudier l'impact de la taille et de la forme des particules de glace, deux relations masse-diamètre (m-D) différentes ont été utilisées, chacune considérant différents degrés de givrage pour les particules de glace (voir plus de détails dans Tridon et al. (2019)). La première relation qui a été développée par Brown and Francis (1995) suppose des agrégats non givrés (relation appelée 'BF95' par la suite) tandis que la seconde, développée plus récemment par Leinonen and Szyrmer (2015) suppose des agrégats légèrement givrés (relation appelée 'LS15' par la suite). Pour le cas OO, les réflectivités calculées à partir des mesures des sondes in-situ en considérant des agrégats légèrement givrés (P6-LS15) deviennent plus comparables aux réflectivités mesurées par le radar MIRAC (P5-MIRAC) que celles qui considèrent des agrégats non givrés (P6-BF95). Pour le cas SI, cette tendance n'est pas aussi claire. Cette analyse comparative suggère la présence d'agrégats légèrement givrés dans les deux cas, mais avec un degré de givrage moins important dans le cas SI que dans le cas OO. Ceci est cohérent au vu des études, par exemples, de Mioche et al. (2017); Gierens et al. (2020); Järvinen et al. (2023) qui ont montré que la teneur en eau liquide surfondue (essentielle dans le processus de givrage) est plus élevée dans les MPCs observés au-dessus de l'océan que dans ceux observés au-dessus de la banquise.

A.3 Simulations numériques des deux cas d'étude

A.3.1 Description du modèle et stratégie d'analyse

Les simulations des deux MPCs observés au-dessus de la banquise (cas SI) et de l'océan (cas OO) ont été effectuées en utilisant la version 3.8.1 du modèle WRF (Skamarock et al., 2008). Les processus physiques sont paramétrés et catégorisés dans différents schémas afin de décrire les propriétés de la microphysique, de la surface, de la couche limite et du rayonnement.

Pour cette étude, les simulations des cas SI et OO utilisent l'ensemble des paramétrisations suivantes: les rayonnements solaire et terrestre suivent le schéma RRTMG (Rapid Radiative Transfer Model for GCMs) ; les propriétés de surface sont décrites par le schéma de la couche de surface de Janjić (2002) combiné au schéma de surface Noah (Chen and Dudhia, 2001) ; la couche limite est décrite par le schéma de Mellor-Yamada-Janjic (MYJ) ; et le schéma de Morrison et al. (2009b) est utilisé pour représenter la microphysique des nuages. A noter que l'initialisation de la concentration en CCN (N_{CCN}) est définie en fonction des observations ACLOUD pour les deux cas : c'est-à-dire 10 cm^{-3} pour le cas SI et 100 cm^{-3} pour le cas OO. Cet ensemble de paramétrisations est proche de celui utilisé dans la version WRF-Polar développée par l'Ohio State University (Hines et al., 2011). De plus, afin de mieux représenter les propriétés de la surface, nous avons ajusté l'albédo de surface pour la banquise (0,79) et les surfaces océaniques (0,21) en fonction des propriétés radiatives moyennes de surface observées pendant ACLOUD le 17 juin 2017 (Stapf et al., 2019a,b, 2020).

Une configuration de trois domaines imbriqués (two way) a été utilisée pour chacun des cas d'étude afin de zoomer sur les zones d'intérêt avec une résolution horizontale de plus en plus fine : 9 km pour le domaine le plus large (avec 120 × 120 points de grille), 3 km pour le domaine intermédiaire (avec 274 × 232 points de grille) et 1 km pour le

domaine le plus petit (avec 487 × 430 points de grille). Les deux domaines les plus larges sont centrés sur la station de Ny-Alesund (Svalbard), tandis que le domaine le plus imbriqué est centré sur la position de l'avion P6 à 11:00 UTC ou à 14:00 UTC afin d'étudier respectivement les cas SI ou OO. Pour les trois domaines, la grille verticale est composée de 105 niveaux non équidistants afin de mieux représenter les altitudes où se situent des MPC (espacement moyen de la grille verticale égal à 30-35 m dans le premier kilomètre). Les simulations sont initialisées à 00:00 UTC le 17 juin 2017 et forcées toutes les 6 heures à l'aide des données de réanalyse ERA-5 (Hersbach et al., 2018a). Ces données fournissent des champs de température, d'humidité spécifique, du géopotentiel et des différentes composantes du vent sur une grille ayant une résolution spatiale de 0,25° × 0,25° en latitude et longitude pour un nombre spécifié de niveaux de pression. Deux simulations différentes ont été réalisées utilisant soit 21 ou 38 niveaux de pression (c'est-à-dire avec 6 ou 9 d'entre eux présents dans la gamme de pression 1000-800 hPa, respectivement) afin de comprendre le rôle des conditions atmosphériques initiales dans les capacités du modèle WRF à reproduire les propriétés des MPCs observés. A noter que les trois niveaux de pression ajoutés dans la couche la plus basse de l'atmosphère correspondent aux niveaux de 975 hPa, 875 hPa et 825 hPa. Les paramètres du modèle décrits dans cette section fournissent le set-up des simulations dites 'de base' pour les deux cas de MPCs, qui seront appelées par la suite 'WRF21' ou 'WRF38' pour faire référence aux 21 ou 38 niveaux de pression utilisés dans les données ERA-5 dans l'initialisation du modèle WRF.

A.3.2 Simulations 'de base' obtenues avec le modèle WRF

Afin de définir les simulations 'de base', nous avons sélectionné un échantillon représentatif de points dans les sorties du modèle WRF afin de réaliser des comparaisons robustes avec les observations des dropsondes, du radar nuage MIRAC ou des sondes microphysiques in-situ. Pour cela, nous avons défini un volume autour de la trajectoire des dropsondes ou de celle du Polar 6, où nous avons effectué des a-PDF (Altitude-dependent PDF) pour comparer avec les observations du radar. Au niveau temporel, nous avons considéré toutes les sorties du modèle (qui sont toutes les 5 min) entre 11:00 et 12:00 UTC pour le cas SI et entre 14:00 et 15:00 UTC pour le cas OO.

Au niveau thermodynamique, pour le cas SI, la température T est plus élevé d'environ 1-1,5°C près de la surface dans les simulations WRF21 et WRF38 alors que la température du point de rosée T_d est similaire aux observations jusqu'à 950 hPa et est surestimée de 1,5-2°C par la suite. Pour le cas OO, le profil de T est bien reproduit près de la surface à la fois dans WRF21 et WRF38 alors que T_d est surestimée de 2°C. Ainsi, le niveau de condensation par élévation (LCL pour "Lifting Condensation Level") simulé pour le cas SI est comparable aux observations alors que, pour le cas OO, il est à une altitude plus faible dans les simulations WRF. De plus, les inversions de T observées pour chacun des cas sont soit moins marquées soit à une altitude différente dans les simulations, impactant ainsi l'altitude du sommet des nuages (surtout pour le cas OO où le LWC et l'IWC diminuent fortement à 650 m d'altitude alors que les observations suggèrent un sommet du MPC à 900 m). Néanmoins, pour chacun des cas, les simulations WRF reproduisent le couplage "surface-nuage" observé par les dropsondes.

Au niveau microphysique, les profils médians des LWC simulés dans WRF38 sont

plus proches des observations que ceux simulés dans WRF21, et ceci pour les deux cas d'étude SI et OO. De plus, les concentrations simulées en gouttelettes d'eau surfondue sont proches des observations à la fois dans WRF21 et WRF38 ; ceci est principalement dû à notre initialisation de N_{CCN} (ou de N_c puisque le schéma de Morrison et al. (2009b) est à un moment pour l'eau nuageuse). Il faut toutefois noter que l'évolution verticale de N_{drops} dans le cas SI n'est pas très bien reproduite dans WRF aux altitudes du MPC. En ce qui concerne la phase glacée des MPCs étudiés, ni l'évolution verticale du IWC ni sa quantité sont bien reproduites dans WRF21 et WRF38 pour le cas SI. Pour le cas OO, WRF38 reproduit mieux les propriétés observées du IWC, en particulier dans les premiers 200 m. Néanmoins, ce profil médian du IWC simulé dans WRF38 est plus proche de celui déduit des observations en supposant des aggrégats non givrés (c'est-à-dire en utilisant la loi masse-diamètre BF95 pour calculer l'IWC à partir des sondes microphysiques in-situ). Ceci est en contradiction avec nos résultats présentés dans la Section A.2.3 où nous avions constaté que les réflectivités radar étaient plus en adéquation avec celles mesurées par le radar MIRAC lorsque la relation masse-diamètre LS15 était utilisée. Malgré cela, le profil IWC médian simulé dans le WRF38 reste dans l'intervalle de variabilité (qui est relativement important) des observations. De plus, pour les deux cas, les concentrations en cristaux de glace (N_{ice}) sont sous-estimées dans WRF21 ainsi que dans WRF38. Cette sous-estimation est environ d'un ordre de grandeur pour le cas OO alors qu'elle atteint environ deux ordres de grandeur pour le cas SI.

D'après nos comparaisons entre observations et simulations pour à la fois le cas SI et le cas OO, nous avons défini les expériences 'de base' WRF38 comme nos expériences de référence. Nous avons donc comparé les a-PDF des réflectivités radar simulées dans WRF38 aux observations du radar nuage pour chacun des cas d'étude. Ces comparaisons montrent que les réflectivités radars simulées (et calculées à l'aide du modèle CR-SIM (Oue et al., 2020)) sont proches de celles mesurées par le radar nuage. Cette adéquation est principalement due aux hypothèses utilisées dans le schéma microphysique pour représenter les distributions en taille des hydrométéores qui paramétrise ces distributions selon une approche exponentielle qui induit plus de gros hydrométéores dans les simulations.

A.3.3 Etudes de sensibilité

La simulation de référence WRF38 fournit des résultats raisonnables par rapport aux observations avec toutefois une certaine sous-estimation de la phase glace et de l'altitude du sommet des nuages. Pour évaluer comment ces paramètres des MPCs peuvent être impactés par les paramétrisations physiques utilisées, des études de sensibilité ont été réalisées pour estimer l'impact des schémas numériques utilisés pour décrire la couche limite (BL pour "boundary layer") et la microphysique (MP) sur les propriétés nuageuses et ont révélé que la base et l'épaisseur des nuages dépendent fortement du schéma BL choisi, tandis que l'IWC et le LWC dépendent fortement du schéma MP choisi, mais avec des variabilités différentes selon les deux cas.

Des études de sensibilité supplémentaires ont été réalisées afin d'étudier l'impact des aérosols sur les systèmes SI et OO et montrent que la réponse des LWC et IWC au nombre de CCN n'est pas linéaire. Il existe une concentration critique en CCN

(différente selon les deux cas) au-delà de laquelle la couche limite atmosphérique semble être saturée impactant peu les systèmes nuageux. Aussi, dans des conditions propres, le développement du cas OO est différent car la thermodynamique de la BL a été modifiée.

Appendix B

List of abbreviations

AP : aerosol particle
ABL : atmospheric boundary layer
$ACLOUD$: Arctic CLoud Observations Using airborne measurements during polar Day
AEC : atmospheric energy convergence
AWI : German Alfred Wegener Institute
$AVAPS$: Advanced Vertical Atmospheric Profiling System
$AMALi$: Airborne Mobile Aerosol Lidar
CCN : cloud condensation nuclei
CRF : cloud radiative forcing
CDP : cloud droplet probe
CIP : cloud imaging probe
CPC : condensation particle counter
CVI : counterflow virtual impactor
CDR : cloud droplet residuals
CP : cold period
CAT : Computing Advection-interpolation of atmospheric parameters and Trajectory tool
$CPRs$: cloud particle residues
DS : drop sonde
DSD : droplet number size distribution
$ERA5$: European Re-Analysis
$ECMWF$: European Centre for Medium-Range Weather Forecasts
F_{sh} : sensible heat fluxes at the surface
F_{lh} : latent heat fluxes at the surface
GCM : global climate model
HC : heat conduction
IWC : ice water content
INP : ice nucleating particles
LWC : liquid water content
LW : longwave
LCL : lifting condensation level
MPC : mixed phase cloud
M : energy flux of the ice melting
$MCAO$: marine cold air outbreak

N_{ice} : ice number concentrations
N_{drop} : droplets number concentration
NP : normal period
NM : nautical miles
NWP : numerical weather prediction
OO : open ocean
OEC : oceanic energy convergence
PSD : particle size distribution
$PASCAL$: Physical feedbacks of Arctic planetary boundary level Sea ice, Cloud and AerosoL
PDF : probability density functions
RH : relative humidity
SW : shortwave
SI : sea ice
TOA : top of atmosphere
TKE : turbulent kinetic energy
$UHSAS$: ultra-high sensitivity aerosol spectrometer
WBF : Wegener-Bergeron-Findeisen mechanism
WP : warm period
WRF : Weather Research and Forecasting

Bibliography

Abbatt, J. P. D., W. R. Leaitch, A. A. Aliabadi, A. K. Bertram, J.-P. Blanchet, A. Boivin-Rioux, H. Bozem, J. Burkart, R. Y. W. Chang, J. Charette, J. P. Chaubey, R. J. Christensen, A. Cirisan, D. B. Collins, B. Croft, J. Dionne, G. J. Evans, C. G. Fletcher, M. Galí, R. Ghahremaninezhad, E. Girard, W. Gong, M. Gosselin, M. Gourdal, S. J. Hanna, H. Hayashida, A. B. Herber, S. Hesaraki, P. Hoor, L. Huang, R. Hussherr, V. E. Irish, S. A. Keita, J. K. Kodros, F. Köllner, F. Kolonjari, D. Kunkel, L. A. Ladino, K. Law, M. Levasseur, Q. Libois, J. Liggio, M. Lizotte, K. M. Macdonald, R. Mahmood, R. V. Martin, R. H. Mason, L. A. Miller, A. Moravek, E. Mortenson, E. L. Mungall, J. G. Murphy, M. Namazi, A.-L. Norman, N. T. O'Neill, J. R. Pierce, L. M. Russell, J. Schneider, H. Schulz, S. Sharma, M. Si, R. M. Staebler, N. S. Steiner, J. L. Thomas, K. von Salzen, J. J. B. Wentzell, M. D. Willis, G. R. Wentworth, J.-W. Xu, and J. D. Yakobi-Hancock, 2019: Overview paper: New insights into aerosol and climate in the Arctic. *Atmos. Chem. Phys.*, **19 (4)**, 2527–2560, doi:10.5194/acp-19-2527-2019.

Abe, M., T. Nozawa, T. Ogura, and K. Takata, 2016: Effect of retreating sea ice on Arctic cloud cover in simulated recent global warming. *Atmospheric Chemistry and Physics*, **16 (22)**, 14 343–14 356.

ACIA, 2005: *Arctic Climate Impact Assessment*. ACIA Overview report. Cambridge University Press, 1020 pp.

AMAP, 1998: *AMAP Assessment Report: Arctic Pollution Issues*. Arctic Monitoring and Assessment Programme (AMAP), Oslo, Norway, 859 pp.

AMAP, 2021: *Arctic climate change update 2021: Key trends and impacts. Summary for policy-makers*. Arctic Monitoring and Assessment Programme (AMAP), Tromsø, Norway, 16 pp.

Anderson, J. R., E. E. Hardy, J. T. Roach, and R. E. Witmer, 1976: *A land use and land cover classification system for use with remote sensor data*. Professional Paper 964 ed., USGS Numbered Series, 28 pp., doi:10.3133/pp964.

Arteaga, D., C. Planche, C. Kagkara, W. Wobrock, S. Banson, F. Tridon, and A. I. Flossmann, 2020: Evaluation of two cloud-resolving models using bin or bulk microphysics representation for the HyMeX-IOP7a Heavy Precipitation Event. *Atmosphere*, **11**, doi: 10.3390/atmos11111177.

Baray, J.-L., L. Deguillaume, A. Colomb, K. Sellegri, E. Freney, C. Rose, J. Van Baelen, J.-M. Pichon, D. Picard, P. Fréville, L. Bouvier, M. Ribeiro, P. Amato, S. Banson, A. Bianco, A. Borbon, L. Bourcier, Y. Bras, M. Brigante, P. Cacault, A. Chauvigné, T. Charbouillot, N. Chaumerliac, A.-M. Delort, M. Delmotte, R. Dupuy, A. Farah, G. Febvre, A. Flossmann, C. Gourbeyre, C. Hervier, M. Hervo, N. Huret, M. Joly, V. Kazan, M. Lopez, G. Mailhot, A. Marinoni, O. Masson, N. Montoux, M. Parazols, F. Peyrin, Y. Pointin, M. Ramonet,

M. Rocco, M. Sancelme, S. Sauvage, M. Schmidt, E. Tison, M. Vaïtilingom, P. Villani, M. Wang, C. Yver-Kwok, and P. Laj, 2020: Cézeaux-Aulnat-Opme-Puy De Dôme: a multi-site for the long-term survey of the tropospheric composition and climate change. *Atmos. Meas. Tech.*, **13 (6)**, 3413–3445, doi:10.5194/amt-13-3413-2020.

Barker, H., J. Cole, J.-J. Morcrette, R. Pincus, and P. Raisanen, 2007: Monte Carlo Independent Column Approximation (McICA): Up and running in North America and Europe. *Talk presented at the 17th Atmospheric Radiation Measurement (ARM) Science Team Meeting, Monterey, CA, March 26-30.*

Barrie, L., J. Bottenheim, R. Schnell, R. Crutzen, and R. Rasmussen, 1988: Ozone destruction and photochemical reactions at polar sunrise in the lower Arctic atmosphere. *Nature.*, **334**, 1875–1883, doi:10.1038/334138a0.

Battisti, D. S., C. M. Bitz, and R. E. Moritz, 1997: Do General Circulation Models Underestimate the Natural Variability in the Arctic Climate? *Journal of Climate*, **10**, 1909–1920.

Baudoux, A., 2022: Impact des conditions environnementales sur les propriétés microphysiques des nuages en Arctique. Master Report, Ecole de l'OPGC, Université Clermont Auvergne, Clermont Ferrand, 40 pp.

Baumgardner, D., J. Brenguier, A. Bucholtz, H. Coe, P. DeMott, T. Garrett, J. Gayet, M. Hermann, A. Heymsfield, A. Korolev, M. Krämer, A. Petzold, W. Strapp, P. Pilewskie, J. Taylor, C. Twohy, M. Wendisch, W. Bachalo, and P. Chuang, 2011: Airborne instruments to measure atmospheric aerosol particles, clouds and radiation: A cook's tour of mature and emerging technology. *Atmos. Res.*, **102 (1)**, 10–29, doi:10.1016/j.atmosres.2011.06.021.

Beck, L. J., N. Sarnela, H. Junninen, C. J. M. Hoppe, O. Garmash, F. Bianchi, M. Riva, C. Rose, O. Peräkylä, D. Wimmer, O. Kausiala, T. Jokinen, L. Ahonen, J. Mikkilä, J. Hakala, X. He, J. Kontkanen, K. K. E. Wolf, D. Cappelletti, M. Mazzola, R. Traversi, C. Petroselli, A. P. Viola, V. Vitale, R. Lange, A. Massling, J. K. Njgaard, R. Krejci, L. Karlsson, P. Zieger, S. Jang, K. Lee, V. Vakkari, J. Lampilahti, R. C. Thakur, K. Leino, J. Kangasluoma, E. Duplissy, E. Siivola, M. Marbouti, Y. J. Tham, A. Saiz-Lopez, T. Petäjä, M. Ehn, D. R. Worsnop, H. Skov, M. Kulmala, V. Kerminen, and M. Sipilä, 2021: Differing Mechanisms of New Particle Formation at Two Arctic Sites. *Geophysical Research Letters*, **12 (15)**, 6775–6798.

Beesley, J. A., 2000: Estimating the effect of clouds on the arctic surface energy budge. *J. Geophys. Res. - Atmos.*, **105 (D8)**, 10–103, doi:10.1029/2000JD900043.

Bergeron, T., 1935: On the physics of clouds and precipitation. *Int. Union Geod. Geophys.*, 156–178.

Bierwirth, E., A. Ehrlich, M. Wendisch, J.-F. Gayet, C. Gourbeyre, R. Dupuy, A. Herber, R. Neuber, and A. Lampert, 2013: Optical thickness and effective radius of Arctic boundary-layer clouds retrieved from airborne nadir and imaging spectrometry. *Atmos. Meas. Tech.*, **6**, 1189–1200, doi:10.5194/amt-6-1189-2013.

Bigg, E. K., 1953: The supercooling of water. *Proc. Phys. Soc. B*, **66**, 688–694, doi:10.1088/0370-1301/66/8/309.

Bintanja, R., R. Graversen, and W. Hazeleger, 2011: Arctic winter warming amplified by the thermal inversion and consequent low infrared cooling to space. *Nat. Geosci*, **4**, 758–761, doi:10.1038/ngeo1285.

Bintanja, R., E. C. van der Linden, and W. Hazeleger, 2012: Boundary layer stability and Arctic climate change: a feedback study using EC-Earth. *Climate Dynamics*, **39 (11)**, 2659–2673, doi:10.1007/s00382-011-1272-1.

Bintanja, R., K. Van-der Wiel, E. Van-der Linden, J. Reusen, L. Bogerd, F. Krikken, and F. Selten, 2020: Strong future increases in Arctic precipitation variability linked to poleward moisture transport. *Science Advances*, **6**, doi:10.1126/sciadv.aax6869.

Bridgman, H., R. Schnell, J. Kahl, G. Herbert, and E. Joranger, 1989: A major haze event near Point Barrow, Alaska: analysis of probable source regions and transport pathways. *Atmos. Environ.*, **23**, 2537–2549, doi:10.1016/0004-6981(89)90265-5.

Bromwich, D. H., K. M. Hines, and L.-S. Bai, 2009: Development and testing of Polar Weather Research and Forecasting model: 2. Arctic Ocean. *J. Geophys. Res. - Atmos.*, **114 (D8)**, doi:10.1029/2008JD010300.

Brown, P. R. A. and P. N. Francis, 1995: Improved measurements of the ice water content in cirrus using a total-water probe. *J. Atmos. Ocean. Technol.*, **12**, 410–414, doi:10.1175/1520-0426(1995)0122.0.CO;2.

Browse, J., K. S. Carslaw, S. R. Arnold, K. Pringle, and O. Boucher, 2012: The scavenging processes controlling the seasonal cycle in Arctic sulphate and black carbon aerosol. *Atmospheric Chemistry and Physics*, **12 (15)**, 6775–6798.

Cai, Y., D. Montague, W. Mooiweer, and T. Deshler, 2008: Performance characteristics of the ultra high sensitivity aerosol spectrometer for particles between 55 and 800 nm: Laboratory and field studies. *J. Aerosol Sci.*, **39**, 759–769, doi:10.1016/j.jaerosci.2008.04.007.

Cantrell, W. and A. Heymsfield, 2005: Production of Ice in Tropospheric Clouds: A Review. *Bull. Amer. Meteorol. Soc.*, **86**, 795–808, doi:10.1175/BAMS-86-6-795.

Cesana, G., J. E. Kay, H. Chepfer, J. M. English, and G. de Boer, 2012: Ubiquitous low-level liquid-containing Arctic clouds: New observations and climate model constraints from CALIPSO-GOCCP. *Geophys. Res. Lett.*, **39 (20)**, L20 804, doi:10.1029/2012GL053385.

Chang, R. Y., C. Leck, M. Graus, M. Müller, J. Paatero, J. F. Burkhart, A. Stohl, L. H. Orr, K. Hayden, S. M. Li, A. Hansel, M. Tjernström, W. R. Leaitch, and J. P. D. Abbatt, 2011: Aerosol composition and sources in the central arctic ocean during ascos. *Atmospheric Chemistry and Physics*, **11**, 10 619–10 636.

Chapman, W. L. and J. E. Walsh, 2007: Simulations of arctic temperature and pressure by global coupledmodels. *J. Climate*, **20**, 609–632, doi:10.1175/JCLI4026.1.

Chen, F. and J. Dudhia, 2001: Coupling an advanced land-surface/hydrology model with the Penn State / NCAR MM5 modeling system. Part I: Model description and implementation. *Mon. Wea. Rev.*, **129**, 569–585, doi:10.1175/1520-0493(2001)129<0569:CAALSH>2.0.CO;2.

Chernokulsky, A. and I. I. Mokhov, 2012: Climatology of total cloudiness in the arctic: An intercomparison of observations and reanalyses. *Advances in Meteorology*, 1–15, doi:10.1155/2012/542093.

Choi, Y.-S., C.-H. Ho, C.-E. Park, T. Storelvmo, and I. Tan, 2014: Influence of cloud phase composition on climate feedbacks. *J. Geophys. Res. Atmos.*, **119**, 3687–3700, doi:10.1002/2013JD020582.

Christensen, M. W., K. Suzuki, B. Zambri, and G. Stephens, 2014: Ship track observations of a reduced shortwave aerosol indirect effect in mixed-phase clouds. *Geophys. Res. Lett.*, **41**, 6970–6977, doi:10.1002/2014GL061320.

Claremar, B., F. Obleitner, C. Reijmer, V. Pohjola, A. Waxegard, F. Karner, and A. Rutgersson, 2012: Applying a mesoscale atmospheric model to svalbard glaciers. *Adv. Meteor.*, **2012 (321649)**, doi:10.1155/2012/321649.

Clark, T. L., 1977: A small scale dynamic model using terrain following coordinate transformation. *J. Comput. Phys.*, **24**, 186–215, doi:10.1016/0021-9991(77)90057-2.

Clark, T. L. and R. D. Farley, 1984: Severe downslope windstorm calculations in two and three spatial dimensions using anelastic interactive grid nesting: a possible mechanism for gustiness. *J. Atmos. Sci.*, **41**, 329–350, doi:10.1175/1520-0469(1984)041<0329:SDWCIT>2.0.CO;2.

Clark, T. L., W. D. Hall, and J. L. Coen, 1996: *Source code documentation for the Clark-Hall cloud scale model, code version G3CH01.* NCAR/TN-426+STR, NCAR Technical note, NCAR, Boulder, CO, USA, doi:10.5065/D67W694V.

Cohard, J.-M. and J.-P. Pinty, 2000: A comprehensive two-moment warm microphysical bulk scheme. I: Description and tests. *Quart. J. Roy. Meteorol. Soc.*, **126 (566)**, 1815–1842, doi:10.1002/qj.49712656613.

Cohard, J.-M., J.-P. Pinty, and C. Bedos, 1998: Extending Twomey's analytical estimate of nucleated cloud droplet concentrations from CCN spectra. *J. Atmos. Sci.*, **55**, 3348–3357, doi:10.1175/1520-0469(1998)055<3348:ETSAEO>2.0.CO;2.

Cohen, A. E., S. M. Cavallo, M. C. Coniglio, and H. E. Brooks, 2015: A Review of Planetary Boundary Layer Parameterization Schemes and Their Sensitivity in Simulating Southeastern U.S. Cold Season Severe Weather Environments. *Weather and Forecasting*, **30 (3)**, 591–612, doi:10.1175/WAF-D-14-00105.1.

Cohen, J., X. Zhang, J. Francis, T. Jung, R. Kwok, J. Overland, T. Ballinger, R. Blackport, U. Bhatt, H. Chen, D. Coumou, S. Feldstein, D. Handorf, M. Hell, G. Henderson, M. Ionita, M. Kretschmer, F. Laliberte, S. Lee, H. Linderholm, W. Maslowski, I. Rigor, C. Routson, J. Screen, T. Semmler, D. Singh, D. Smith, J. Stroeve, P. Taylor, T. Vihma, M. Wang, S. Wang, Y. Wu, M. Wendisch, and J. Yoon, 2018: Arctic change and possible influence on mid-latitude climate and weather: A US CLIVAR White Paper. *US CLIVAR Rep.*, doi:10.5065/D6TH8KGW.

Cooper, W. A., 1986: Ice Initiation in Natural Clouds. *Meteorol. Monogr.*, **21**, 29–32, doi:10.1175/0065-9401-21.43.29.

Copernicus Climate Change Service (C3S), 2017: ERA5: Fifth Generation of ECMWF Atmospheric Reanalyses of the Global Climate. *Copernicus Climate Change Service Climate Data Store (CDS)*, URL https://cds.climate.copernicus.eu/cdsapp#!/home.

Costa, A., J. Meyer, A. Afchine, A. Luebke, G. Günther, J. R. Dorsey, M. W. Gallagher, A. Ehrlich, M. Wendisch, D. Baumgardner, H. Wex, and M. Krämer, 2017: Classification of Arctic, midlatitude and tropical clouds in the mixed-phase temperature regime. *Atmos. Chem. Phys.*, **17**, 12 219–12 238, doi:10.5194/acp-17-12219-2017.

Cotton, W., R. Pielke Sr., R. Walko, G. E. Liston, C. J. Tremback, H. Jiang, R. L. McAnelly, J. Y. Harrington, M. E. Nicholls, G. G. Carrio, and J. P. McFadden, 2003: RAMS 2001: Current status and future directions. *Meteorology and Atmospheric Physics*, **82**, 5–29, doi: 10.1007/s00703-001-0584-9.

Crosier, J., K. N. Bower, T. W. Choularton, C. D. Westbrook, P. J. Connolly, Z. Q. Cui, I. P. Crawford, G. L. Capes, H. Coe, J. R. Dorsey, P. I. Williams, A. J. Illingworth, M. W. Gallagher, and A. M. Blyth, 2011: Observations of ice multiplication in a weakly convective cell embedded in supercooled mid-level stratus. *Atmos. Chem. Phys.*, **11 (1)**, 257–273, doi:10.5194/acp-11-257-2011.

Curry, J. A., 1986: Interactions among Turbulence, Radiation and Microphysics in Arctic Stratus Clouds. *J. Atmos. Sci.*, **43**, 90–106, doi:10.1175/1520-0469(1986)043<0090: IATRAM>2.0.CO;2.

Curry, J. A., 1995: Interactions among aerosols, clouds, and climate of the Arctic Ocean. *Sci. Tot. Environ.*, **160**, 777–791, doi:10.1016/0048-9697(95)04411-S.

Curry, J. A., W. B. Rossow, D. Randall, and J. L. Schramm, 1996: Overview of Arctic Cloud and Radiation Characteristics. *J. Climate.*, **9 (8)**, 1731–1764, doi:10.1175/1520-0442(1996) 009<1731:OOACAR>2.0.CO;2.

Dall'Osto, M., D. C. Beddows, P. Tunved, R. Krejci, J. Ström, H. C. Hansson, Y. J. Yoon, K. T. Park, S. Becagli, R. Udisti, T. Onasch, C. D. Ódowd, R. Simó, and R. M. Harrison, 2017: Arctic sea ice melt leads to atmospheric new particle formation. *Scientific Reports*, **7 (1)**, 1–10.

Davy, R. and S. Outten, 2020: The Arctic Surface Climate in CMIP6: Status and Developments since CMIP5. *J. Climate.*, **33 (18)**, 8047–8068, doi:10.1175/JCLI-D-19-0990.1.

De Boer, G., E. Eloranta, and M. D. Shupe, 2009: Arctic Mixed-Phase Stratiform Cloud Properties from Multiple Years of Surface-Based Measurements at Two High-Latitude Locations. *J. Atmos. Sci.*, **66**, 2874–2887, doi:10.1175/2009JAS3029.1.

de Boer, G., H. Morrison, M. D. Shupe, and R. Hildner, 2011: Evidence of liquid dependent ice nucleation in high-latitude stratiform clouds from surface remote sensors. *Geophys. Res. Lett.*, **38 (1)**, doi:10.1029/2010GL046016.

de Boer, G., M. D. Shupe, P. M. Caldwell, S. E. Bauer, O. Persson, J. S. Boyle, M. Kelley, S. A. Klein, and M. Tjernström, 2014: Near-surface meteorology during the Arctic Summer Cloud Ocean Study (ASCOS): evaluation of reanalyses and global climate models. *Atmos. Chem. Phys.*, **14 (1)**, 427–445, doi:10.5194/acp-14-427-2014.

Dee, D. P., S. M. Uppala, A. J. Simmons, P. Berrisford, P. Poli, S. Kobayashi, U. Andrae, M. A. Balmaseda, G. Balsamo, P. Bauer, P. Bechtold, A. C. M. Beljaars, L. van de Berg, J. Bidlot, N. Bormann, C. Delsol, R. Dragani, M. Fuentes, A. J. Geer, L. Haimberger, S. B. Healy, H. Hersbach, E. V. Hólm, L. Isaksen, P. Kållberg, M. Köhler, M. Matricardi, A. P. McNally, B. M. Monge-Sanz, J.-J. Morcrette, B.-K. Park, C. Peubey, P. de Rosnay, C. Tavolato, J.-N. Thépaut, and F. Vitart, 2011: The ERA-Interim reanalysis: configuration and performance of the data assimilation system. *Quart. J. Roy. Meteorol. Soc.*, **137**, 553–597, doi:10.1002/qj.828.

Delanoë, J., A. Protat, O. Jourdan, J. Pelon, M. Papazzoni, R. Dupuy, J. F. Gayet, and C. Jouan, 2013: Comparison of Airborne In Situ, Airborne Radar-Lidar, and Spaceborne Radar-Lidar Retrievals of Polar Ice Cloud Properties Sampled during the POLARCAT Campaign. *J. Atmos. Ocean. Technol.*, **30**, 57–73, doi:10.1175/JTECH-D-11-00200.1.

DeMott, P., A. Prenni, X. Liu, S. Kreidenweis, M. Petters, C. Twohy, M. Richardson, T. Eidhammer, and D. Rogers, 2010: Predicting global atmospheric ice nuclei distributions and their impacts on climate. *Proc. Natl. Acad. Sci.*, **107**, 11 217–11 222, doi: 10.1073/pnas.0910818107.

Deser, C., R. Tomas, M. Alexander, and D. Lawrence, 2010: The seasonal atmospheric response to projected Arctic sea ice loss in the late twenty-first century. *J. Climate.*, **23**, 333–351, doi:10.1175/2009JCLI3053.1.

Ducrocq, V., I. Braud, S. Davolio, R. Ferretti, C. Flamant, A. Jansa, N. Kalthoff, E. Richard, I. Taupier-Letage, P.-A. Ayral, S. Belamari, A. Berne, M. Borga, B. Boudevillain, O. Bock, J.-L. Boichard, M.-N. Bouin, O. Bousquet, C. Bouvier, J. Chiggiato, D. Cimini, U. Corsmeier, L. Coppola, P. Cocquerez, E. Defer, J. Delanoë, P. Di Girolamo, A. Doerenbecher, P. Drobinski, Y. Dufournet, N. Fourrié, J. J. Gourley, L. Labatut, D. Lambert, J. Le Coz, F. S. Marzano, G. Molinié, A. Montani, G. Nord, M. Nuret, K. Ramage, W. Rison, O. Roussot, F. Said, A. Schwarzenboeck, P. Testor, J. Van Baelen, B. Vincendon, M. Aran, and J. Tamayo, 2014: HyMeX-SOP1: The Field Campaign Dedicated to Heavy Precipitation and Flash Flooding in the Northwestern Mediterranean. *Bull. Amer. Meteorol. Soc.*, **95**, 1083–1100, doi:10.1175/BAMS-D-12-00244.1.

Dudhia, J., 2014: A history of mesoscale model development. *Asia-Pac. J. Atmos. Sci.*, **50**, 121–131, doi:10.1007/s13143-014-0031-8.

Dufour, A., O. Zolina, and S. K. Gulev, 2016: Atmospheric Moisture Transport to the Arctic: Assessment of Reanalyses and Analysis of Transport Components. *J. Climate.*, **29 (14)**, 5061–5081, doi:10.1175/JCLI-D-15-0559.1.

Dupuy, R., O. Jourdan, G. Mioche, C. Gourbeyre, D. Leroy, and A. Schwarzenböck, 2019: CDP, CIP and PIP: In-situ arctic cloud microphysical properties observed during ACLOUD-AC3 campaign in June 2017. *PANGAEA*, doi:10.1594/PANGAEA.899074.

Dupuy, R., O. Jourdan, G. Mioche, A. Ehrlich, F. Waitz, C. Gourbeyre, E. Jarvinen, M. Schnaiter, and A. Schwarzenboeck, 2018: *Cloud microphysical properties of summertime Arctic stratocumulus guring the ACLOUD campaign: Comparison with previous results in the European Arctic.* Conference on Cloud Physics, Vancouver Canada.

Eastman, R. and S. G. Warren, 2010: Interannual variations of Arctic cloud types in relation to sea ice. *J. Climate*, **23**, 4216–4232, doi:10.1175/2010JCLI3492.1.

Ebell, K., T. Nomokonova, M. Maturilli, and C. Ritter, 2020: Radiative Effect of Clouds at Ny-Ålesund, Svalbard, as Inferred from Ground-Based Remote Sensing Observations. *J. Appl. Meteorol. and Climatol.*, **59 (11)**, 3–22, doi:10.1175/JAMC-D-19-0080.1.

Ehrlich, A., M. Wendisch, E. Bierwirth, J.-F. Gayet, G. Mioche, A. Lampert, and B. Mayer, 2009: Evidence of ice crystals at cloud top of Arctic boundary-layer mixed-phase clouds derived from airborne remote sensing. *Atmos. Chem. Phys.*, **9**, 9401–9416, doi:10.5194/acp-9-9401-2009.

Ehrlich, A., M. Wendisch, C. Lüpkes, M. Buschmann, H. Bozem, D. Chechin, H.-C. Clemen, R. Dupuy, O. Eppers, J. Hartmann, A. Herber, E. Jäkel, E. Järvinen, O. Jourdan, U. Kästner, L.-L. Kliesch, F. Köllner, M. Mech, S. Mertes, R. Neuber, E. Ruiz-Donoso, M. Schnaiter, J. Schneider, J. Stapf, and M. Zanatta, 2019a: A comprehensive in situ and remote sensing data set from the Arctic CLoud Observations Using airborne measurements during polar Day (ACLOUD) campaign. *Earth System Science Data*, **11 (4)**, 1853–1881, doi: 10.5194/essd-11-1853-2019.

Ehrlich, A., M. Wendisch, C. Lüpkes, M. Buschmann, H. Bozem, D. Chechin, H.-C. Clemen, R. Dupuy, O. Eppers, J. Hartmann, A. Herber, E. Jäkel, E. Järvinen, O. Jourdan, U. Kästner, L.-L. Kliesch, F. Köllner, M. Mech, S. Mertes, R. Neuber, E. Ruiz-Donoso, M. Schnaiter, J. Schneider, J. Stapf, and M. Zanatta, 2019b: Collection of data sources for the Arctic CLoud Observations Using airborne measurements during polar Day (ACLOUD) campaign, North-West of Svalbard between 23 May - 26 June 2017. *PANGAEA*, doi: 10.1594/PANGAEA.902603.

Eirund, G., A. Possner, and U. Lohmann, 2019: Response of Arctic mixed-phase clouds to aerosol perturbations under different surface forcings. *Atmos. Chem. Phys.*, **19**, 9847–9864, doi:10.5194/acp-19-9847-2019.

Eliassen, A., 1949: The Quasi-static Equations of Motion with Pressure as Independent Variable. *Geofys. Publ.*, **17**, 3–44.

English, J. M., J. E. Kay, A. Gettelman, X. Liu, Y. Wang, Y. Zhang, and H. Chepfer, 2014: Contributions of clouds, surface albedos, and mixed-phase ice nucleation schemes to Arctic radiation biases in CAM5. *J. Climate*, **27**, 5174–5197, doi:10.1175/JCLI-D-13-00608.1.

ESOTC, 2020: European State of the Climate 2020. *Copernicus Climate Change Service (C3S)/ECMWF*, doi:10.24381/43nj-sb24, URL https://climate.copernicus.eu/esotc/2020.

Fan, I., M. Ovtchinnikov, J. Comstock, S. McFarlane, and A. Khain, 2009: Ice formation in Arctic mixed-phase clouds: Insights from a 3-D cloud-resolving model with size-resolved aerosol and cloud microphysics. *J. Geophys. Res. - Atmos.*, **114**, doi:10.1029/2008JD010782.

Field, P. R., A. J. Heymsfield, and A. R. Bansemer, 2006: Shattering and particle interarrival times measured by optical array probes in ice clouds. *J. Atmos. Ocean. Technol.*, **23**, 1357–1371, doi:10.1175/JTECH1922.1.

Field, P. R., R. P. Lawson, P. R. A. Brown, G. Lloyd, C. Westbrook, D. Moisseev, A. Miltenberger, A. Nenes, A. Blyth, T. Choularton, P. Connolly, J. Buehl, J. Crosier, Z. Cui, C. Dearden, P. DeMott, A. Flossmann, A. Heymsfield, Y. Huang, H. Kalesse, Z. A. Kanji, A. Korolev, A. Kirchgaessner, S. Lasher-Trapp, T. Leisner, G. McFarquhar, V. Phillips, J. Stith, and S. Sullivan, 2017: Secondary Ice Production: Current State of the Science and Recommendations for the Future. *Meteorol. Monogr.*, **58**, 7.1–7.20, doi: 10.1175/AMSMONOGRAPHS-D-16-0014.1.

Findeisen, W., 1938: Kolloid-meteorologische vorgange bei neiderschlags-bildung. *Meteorol Z*, **55**, 121–133.

Fletcher, J., S. Mason, and C. Jakob, 2016: The Climatology, Meteorology, and Boundary Layer Structure of Marine Cold Air Outbreaks in Both Hemispheres. *J. Climate.*, **29**, 1999–2014, doi:10.1175/JCLI-D-15-0268.1.

Flossmann, A. I. and W. Wobrock, 2010: A review of our understanding of the aerosol-cloud interaction from the perspective of a bin resolved cloud scale modelling. *Atmos. Res.*, **97 (4)**, 478–497, doi:10.1016/j.atmosres.2010.05.008.

Foken, T., M. Aubinet, and R. Leuning, 2012: The eddy-covarianced method. *Eddy Covariance: A Practical Guide to Measurement and Data Analysis*, 1–19, doi:10.1007/978-94-007-2351-1_1.

Forbes, R. M. and M. Ahlgrimm, 2014: On the representation of high-latitude boundary layer mixed-phase cloud in the ECMWF global model. *Mon. Wea. Rev.*, **142**, 3425–3445, doi:10.1175/MWR-D-13-00325.1.

Francis, J. A. and E. Hunter, 2007: Changes in the fabric of the Arctic's greenhouse blanket. *Environ. Res. Lett.*, **2**, 045 011, doi:10.1088/1748-9326/2/4/045011.

Freud, E., R. Krejci, P. Tunved, R. Leaitch, Q. T. Nguyen, A. Massling, H. Skov, and L. Barrie, 2017: Pan-Arctic aerosol number size distributions: seasonality and transport patterns. *Atmos. Chem. Phys.*, **17 (13)**, 8101–8128, doi:10.5194/acp-17-8101-2017.

Frey, M. M., S. J. Norris, I. M. Brooks, P. S. Anderson, K. Nishimura, X. Yang, A. E. Jones, M. G. Mastromonaco, D. H. Jones, and E. Wolff, 2020: First direct observation of sea salt aerosol production from blowing snow above sea ice. *Atmos. Chem. Phys.*, **20 (4)**, 2549–2578.

Fridlind, A. M., A. S. Ackerman, G. McFarquhar, G. Zhang, M. R. Poellot, P. J. DeMott, A. J. Prenni, and A. J. Heymsfield, 2007: Ice properties of single-layer stratocumulus during the Mixed-Phase Arctic Cloud Experiment: 2. Model results. *J. Geophys. Res. - Atmos.*, **112 (D24)**, doi:10.1029/2007JD008646.

Fu, S., X. Deng, M. D. Shupe, and H. Xue, 2019: A modelling study of the continuous ice formation in an autumnal Arctic mixed-phase cloud case. *Atmos. Res.*, **228**, 77–85, doi:10.1016/j.atmosres.2019.05.021.

Gal-Chen, T. and R. C. J. Somerville, 1975: On the use of a coordinate transformation for the solution of the Navier-Stokes equations. *J. Comput. Phys.*, **17**, 209–228, doi:10.1016/0021-9991(75)90037-6.

Garrett, T. and C. Zhao, 2006: Increased Arctic cloud longwave emissivity associated with pollution from mid-latitudes. *Nature.*, **440**, 787–789, doi:10.1038/nature04636.

Garrett, T. J., M. M. Maestas, S. K. Krueger, and C. T. Schmidt, 2009: Acceleration by aerosol of a radiative-thermodynamic cloud feedback influencing Arctic surface warming. *Geophys. Res. Lett.*, **36**, doi:10.1029/2009GL040195.

Gayet, J., G. Mioche, A. Dörnbrack, A. Ehrlich, A. Lampert, and M. Wendisch, 2009a: Microphysical and optical properties of Arctic mixed-phase clouds. The 9 April 2007 case study. *Atmos. Chem. Phys.*, **9**, 6581–6595, doi:10.5194/acp-9-6581-2009.

Gayet, J., R. Treffeisen, A. Helbig, J. Bareiss, A. Matsuki, A. Herber, and A. Schwarzenboeck, 2009b: On the onset of the ice phase in boundary layer Arctic clouds. *J. Geophys. Res. - Atmos.*, **114**, doi:10.1029/2008JD011348.

Gayet, J.-F., I. S. Stachlewska, O. Jourdan, V. Shcherbakov, A. Schwarzenboeck, and R. Neuber, 2007: Microphysical and optical properties of precipitating drizzle and ice particles obtained from alternated lidar and in situ measurements. *Annales Geophysicae*, **25**, 1487–1497, doi:10.5194/angeo-25-1487-2007.

Gettelman, A., X. Liu, S. J. Ghan, H. Morrison, S. Park, A. J. Conley, S. A. Klein, J. Boyle, D. L. Mitchell, and J.-L. F. Li, 2010: Global simulations of ice nucleation and ice supersaturation with an improved cloud scheme in the Community Atmosphere Model. *J. Geophys. Res.*, **115 (D18216)**, doi:10.1029/2009JD013797.

Gierens, R., S. Kneifel, M. D. Shupe, K. Ebell, M. Maturilli, and U. Löhnert, 2020: Low-level mixed-phase clouds in a complex Arctic environment. *Atmos. Chem. Phys.*, **20**, 3459–3481, doi:10.5194/acp-20-3459-2020.

Gilgen, A., W. T. K. Huang, L. Ickes, D. Neubauer, and U. Lohmann, 2018: How important are future marine and shipping aerosol emissions in a warming Arctic summer and autumn? *Atmos. Chem. Phys.*, **18**, 10 521–10 555, doi:10.5194/acp-18-10521-2018.

Girard, E. and N. Sokhandan Asl, 2014: Relative importance of acid coating on ice nuclei in the deposition and contact modes for wintertime Arctic clouds and radiation. *Meteorol. Atmos. Phys.*, **123**, 81–92, doi:10.1007/s00703-013-0298-9.

Gourdal, M., O. Crabeck, M. Lizotte, V. Galindo, M. Gosselin, M. Babin, M. Scarratt, and M. Levasseur, 2019: Upward transport of bottom-ice dimethyl sulfide during advanced melting of Arctic first-year sea ice. *Elementa: Science of the Anthropocene*, **7**.

Grachev, A. A., F. C. W., P. P. O. G., A. E. L., and G. P. S., 2005: Stable boundary-layer scaling regimes: The SHEBA data. *Bound.-Layer Meteor.*, **116**, 201–235.

Graversen, R. G., T. Mauritsen, M. Tjernstrom, E. Kallen, and G. Svensson, 2007: Vertical structure of recent Arctic warming. *Nature.*, **541**, 53–56, doi:10.1038/nature06502.

Graversen, R. G. and M. Wang, 2009: Polar amplification in a coupled model with locked albedo. *Climate Dynamics*, **33**, 629–643, doi:10.1007/s00382-009-0535-6.

Griesche, H. J., K. Ohneiser, P. Seifert, M. Radenz, R. Engelmann, and A. Ansmann, 2021: Contrasting ice formation in Arctic clouds: surface-coupled vs. surface-decoupled clouds. *Atmos. Chem. Phys.*, **21 (13)**, 10 357–10 374, doi:10.5194/acp-21-10357-2021.

Grobner, J., I. Reda, S. Wacker, S. Nyeki, K. Behrens, and J. Gorman, 2014: A new absolute reference for atmospheric longwave irradiance measurements with traceability to SI units. *J. Geophys. Res*, **119**, 7083–7090, doi:10.1002/2014JD021630.

Grosvenor, D. P., P. R. Field, A. A. Hill, and B. J. Shipway, 2017: The relative importance of macrophysical and cloud albedo changes for aerosol-induced radiative effects in closed-cell stratocumulus: insight from the modelling of a case study. *Atmos. Chem. Phys.*, **17 (8)**, 5155–5183, doi:10.5194/acp-17-5155-2017.

Gultepe, I., G. Isaac, D. Hudak, R. Nissen, and J. W. Strapp, 2000: Dynamical and Microphysical Characteristics of Arctic Clouds during BASE. *J. Climate.*, **13**, 1225–1254, doi:10.1175/1520-0442(2000)0132.0.CO;2.

Gultepe, I. and G. A. Isaac, 2002: Effects of air mass origin on Arctic cloud microphysical parameters for April 1998 during FIRE.ACE. *J. Geophys. Res. - Atmos.*, **107 (D21)**, doi:10.1029/2000JC000440.

Hall, A., 2004: The role of surface albedo feedback in climate. *J. Climate.*, **17**, 1550–1568, doi:10.1175/1520-0442(2004)017<1550:TROSAF>2.0.CO;2.

Hallett, J. and S. C. Mossop, 1974: Production of secondary ice crystals during the riming process. *Nature.*, **249**, 26–28, doi:10.1038/249026a0.

Harrington, J. Y., T. Reisin, W. R. Cotton, and S. M. Kreidenweis, 1999: Cloud resolving simulations of Arctic stratus. *Atmos. Res.*, **51**, 45–75, doi:10.1016/S0169-8095(98)00098-2.

Harris, L. M. and D. R. Durran, 2010: An Idealized Comparison of One-Way and Two-Way Grid Nesting. *Mon. Wea. Rev.*, **138 (6)**, 2174–2187, doi:10.1175/2010MWR3080.1.

Held, I. M., 2005: The Gap between Simulation and Understanding in Climate Modeling. *Bull. Amer. Meteorol. Soc.*, **86 (11)**, 1609–1614, doi:10.1175/BAMS-86-11-1609.

Herber, A., 2019: Meteorological observations during POLAR 5 campaign PAMARCMIP 2018. *PANGAEA*, doi:10.1594/PANGAEA.898788.

Herber, A., A. Ehrlich, C. Lupkes, M. Wendisch, and M. Mech, 2020: Master tracks in different resolutions during POLAR 5 campaign P5.223.MOSAiC.ACA.2020. *PANGAEA*, doi:10.1594/PANGAEA.924603.

Hersbach, H., B. Bell, P. Berrisford, G. Biavati, A. Horányi, J. Muñoz Sabater, J. Nicolas, C. Peubey, R. Radu, I. Rozum, D. Schepers, A. Simmons, C. Soci, D. Dee, and J.-N. Thépaut, 2018a: ERA5 hourly data on single levels from 1959 to present. *Copernicus Climate Change Service (C3S) Climate Data Store (CDS)*, doi:10.24381/cds.adbb2d47.

Hersbach, H., B. Bell, P. Berrisford, G. Biavati, A. Horányi, J. Muñoz Sabater, J. Nicolas, C. Peubey, R. Radu, I. Rozum, D. Schepers, A. Simmons, C. Soci, D. Dee, and J.-N. Thépaut, 2018b: ERA5 hourly data on single levels from 1959 to present. *Copernicus Climate Change Service (C3S) Climate Data Store (CDS)*, doi:10.24381/cds.bd0915c6.

Hersbach, H., P. de Rosnay, B. Bell, D. Schepers, A. Simmons, C. Soci, S. Abdalla, M. Alonso-Balmaseda, G. Balsamo, P. Bechtold, P. Berrisford, J.-R. Bidlot, E. de Boisséson, M. Bonavita, P. Browne, R. Buizza, P. Dahlgren, D. Dee, R. Dragani, M. Diamantakis, J. Flemming, R. Forbes, A. J. Geer, T. Haiden, E. Hólm, L. Haimberger, R. Hogan, A. Horányi, M. Janiskova, P. Laloyaux, P. Lopez, J. Munoz-Sabater, C. Peubey, R. Radu, D. Richardson, J.-N. Thépaut, F. Vitart, X. Yang, E. Zsótér, and H. Zuo, 2018c: Operational global reanalysis: progress, future directions and synergies with NWP. *ERA Report Series, ECMWF*, doi:10.21957/tkic6g3wm.

Heymsfield, A. J., M. Krämer, A. Luebke, P. Brown, D. J. Cziczo, C. Franklin, P. Lawson, U. Lohmann, G. McFarquhar, Z. Ulanowski, and K. Van Tricht, 2017: Cirrus Clouds. *Meteorol. Monogr.*, **58**, 2.1–2.26, doi:10.1175/AMSMONOGRAPHS-D-16-0010.1.

Hines, K. M., D. H. Bromwich, L.-S. Bai, M. Barlage, and A. G. Slater, 2011: Development and Testing of Polar WRF. Part III: Arctic Land. *J. Climate.*, **24**, 26–48, doi:10.1175/2010JCLI3460.1.

Hirdman, D., H. Sodemann, S. Eckhardt, J. F. Burkhart, A. Jefferson, T. Mefford, P. K. Quinn, S. Sharma, J. Ström, and A. Stohl, 2010: Source identification of short-lived air pollutants in the Arctic using statistical analysis of measurement data and particle dispersion model output. *Atmospheric Chemistry and Physics*, **10 (2)**, 669–693.

Hobbs, P. V., T. J. Garrett, R. J. Ferek, S. R. Strader, D. A. Hegg, G. M. Frick, W. A. Hoppel, R. F. Gasparovic, L. M. Russell, D. W. Johnson, C. O'Dowd, P. A. Durkee, K. E. Nielsen, and G. Innis, 2000: Emissions from Ships with respect to Their Effects on Clouds. *J. Atmos. Sci.*, **57**, 2570–2590, doi:10.1175/1520-0469(2000)057<2570:EFSWRT>2.0.CO;2,.

Hopkins, T., 1991: The GIN Sea - A synthesis of its physical oceanography and literature review 1972-1985. *Earth-Science Reviews.*, **30**, 175–318, doi:10.1016/0012-8252(91)90001-V.

Huang, K., J. S. Fu, V. Y. Prikhodko, J. M. Storey, A. Romanov, E. L. Hodson, J. Cresko, I. Morozova, Y. Ignatieva, and J. Cabaniss, 2015: Russian anthropogenic black carbon: Emission reconstruction and Arctic black carbon simulation. *Journal of Geophysical Research: Atmospheres*, **120 (21)**, 306–333.

Iacono, M. J., 2011: *Application of Improved Radiation Modeling to General Circulation Models.* Final Technical Report ed., Atmospheric and Environmental Research, Inc., 39 pp.

Iacono, M. J., J. S. Delamere, E. J. Mlawer, M. W. Shephard, S. A. Clough, and W. D. Collins, 2008: Radiative forcing by long-lived greenhouse gases: Calculations with the AER radiative transfer models. *J. Geophys. Res. - Atmos.*, **113**, D13 103, doi:10.1029/2008JD009944.

Igel, A. L., A. M. Ekman, C. Leck, M. Tjernström, J. Savre, and J. Sedlar, 2017: The free troposphere as a potential source of arctic boundary layer aerosol particles. *Geophys. Res. Lett*, **44**, 7053–7060, doi:10.1002/2017GL073808.

Ikonen, I., N. W. S. Demetriades, and R. Holle, 2010: Vaisala dropsondes: History, status, and applications. *29th Conference on Hurricanes and Tropical Meteorology*, SPONSOR, Tucson, Ariz.

Intrieri, J. M., M. D. Shupe, T. Uttal, and B. J. McCarty, 2002a: An annual cycle of Arctic cloud characteristics observed by radar and lidar at SHEBA. *J. Geophys. Res. - Ocean*, **107 (C10)**, doi:10.1029/2000JC000439.

Intrieri, J. M., M. D. Shupe, T. Uttal, and B. J. McCarty, 2002b: An annual cycle of Arctic cloud characteristics observed by radar and lidar at SHEBA. *J. Geophys. Res. - Ocean*, **107 (C10)**, doi:10.1029/2000JC000423.

IPCC, 2013: *Climate Change 2013: The Physical Science Basis. Contribution of Working Group I to the Fifth Assessment Report of the Intergovernmental Panel on Climate Change.* [Stocker, T.F., D. Qin, G.-K. Plattner, M. Tignor, S.K. Allen, J. Boschung, A. Nauels, Y. Xia, V. Bex and P.M. Midgley (eds.)]. Cambridge University Press, Cambridge, United Kingdom and New York, NY, USA.

IPCC, 2018: *Summary for Policymakers.* In: Global Warming of 1.5°C. An IPCC Special Report on the impacts of global warming of 1.5°C above pre-industrial levels and related global greenhouse gas emission pathways, in the context of strengthening the global response to the threat of climate change, sustainable development, and efforts to eradicate poverty [Masson-Delmotte, V., P. Zhai, H.-O. Pörtner, D. Roberts, J. Skea, P.R. Shukla, A. Pirani, W. Moufouma-Okia, C. Péan, R. Pidcock, S. Connors, J.B.R. Matthews, Y. Chen, X. Zhou, M.I. Gomis, E. Lonnoy, T. Maycock, M. Tignor, and T. Waterfield (eds.)]. Cambridge University Press, Cambridge, UK and New York, NY, USA, doi:10.1017/9781009157940.001.

Jackson, R. C., G. M. McFarquhar, A. V. Korolev, M. E. Earle, P. S. K. Liu, R. P. Lawson, S. Brooks, M. Wolde, A. Laskin, and M. Freer, 2012: The dependence of ice microphysics on aerosol concentration in arctic mixed-phase stratus clouds during ISDAC and M-PACE. *J. Geophys. Res. - Atmos.*, **117**, doi:10.1029/2012JD017668.

Jacob, D. J., J. H. Crawford, H. Maring, A. D. Clarke, J. E. Dibb, L. K. Emmons, R. A. Ferrare, C. A. Hostetler, P. B. Russell, H. B. Singh, A. M. Thompson, G. E. Shaw, E. McCauley, J. R. Pederson, and J. A. Fisher, 2010: The Arctic Research of the Composition of the Troposphere from Aircraft and Satellites (ARCTAS) mission: design, execution, and first results. *Atmos. Chem. Phys.*, **10 (11)**, 5191–5212, doi:10.5194/acp-10-5191-2010.

Janjić, Z. I., 1990: The Step-Mountain Coordinate: Physical Package. *Mon. Wea. Rev.*, **118 (7)**, 1429–1443, doi:10.1175/1520-0493(1990)118<1429:TSMCPP>2.0.CO;2.

Janjić, Z. I., 1996: The surface layer in the NCEP Eta Model. *Eleventh Conference on Numerical Weather Prediction, Norfolk, VA, 19-23 August; Amer. Meteor. Soc., Boston, MA, 354-355.*

Janjić, Z. I., 2002: *Nonsingular implementation of the Mellor-Yamada Level 2.5 scheme in the NCEP Meso model.* NCEP Office Note, No. 437, 61 pp.

Järvinen, E., F. Nehlert, G. Xu, F. Waitz, G. Mioche, R. Dupuy, O. Jourdan, and M. Schnaiter, 2023: Vertical distribution of ice optical and microphysical properties in Arctic low-level mixed-phase clouds during ACLOUD. *Atmos. Chem. Phys. Discuss.*, **2023**, 1–30, doi:10.5194/acp-2022-855.

Jeffries, M. O., J. E. Overland, and D. K. Perovich, 2013: The Arctic shifts to a new normal. *Phys. Today*, **66**, 35–40, doi:10.1063/PT.3.2147.

Jourdan, O., 2022: Rôle de la glace atmosphérique sur le cycle de vie des nuages et leurs propriétés microphysiques et optiques : contribution des observations in situ. *HDR, Université Clermont Auvergne, Clermont Ferrand, France*, 281.

Jourdan, O., G. Mioche, T. J. Garrett, A. Schwarzenböck, J. Vidot, Y. Xie, V. Shcherbakov, P. Yang, and J.-F. Gayet, 2010: Coupling of the microphysical and optical properties of an Arctic nimbostratus cloud during the ASTAR 2004 experiment: Implications for light-scattering modeling. *J. Geophys. Res. - Atmos.*, **115**, doi:10.1029/2010JD014016.

Kagkara, C., 2019: Modélisation microphysique détaillée de l'épisode de précipitation intense IOP7a observé lors de l'expérience HYMEX: Etude de l'impact de la pollution. Ph.D. thesis, Université Clermont Auvergne, Clermont Ferrand, 185 pp.

Kagkara, C., W. Wobrock, C. Planche, and A. I. Flossmann, 2020: The sensitivity of intense rainfall to aerosol particle loading: a comparison of bin-resolved microphysics modelling with observations of heavy precipitation from HyMeX IOP7a. *Natural Hazards and Earth System Sciences*, **20 (5)**, 1469–1483, doi:10.5194/nhess-20-1469-2020.

Küchler, N., S. Kneifel, U. Löhnert, P. Kollias, H. Czekala, and T. Rose, 2017: A W-band radar-radiometer system for accurate and continuous monitoring of clouds and precipitation. *J. Atmos. Ocean. Technol.*, **34**, 2375–2392, doi:10.1175/JTECHD-17-0019.1.

Khain, A. P., K. D. Beheng, A. Heymsfield, A. Korolev, S. O. Krichak, Z. Levin, M. Pinsky, V. Phillips, T. Prabhakaran, A. Teller, S. C. van den Heever, and J.-I. Yano, 2015: Representation of microphysical processes in cloud-resolving models: Spectral (bin) microphysics versus bulk parameterization. *Reviews of Geophysics*, **53 (2)**, 247–322, doi:10.1002/2014RG000468.

Khon, V. C., I. I. Mokhov, M. Latif, V. A. Semenov, and W. Park, 2010: Perspectives of Northern Sea Route and Northwest Passage in the twenty-first century. *Climatic Change*, **100**, 757–768, doi:10.1007/s10584-009-9683-2.

Kilpelainen, T., V. T., and O. H., 2012a: Modelling of spatial variability and topographic effects over Arctic fjords in Svalbard. *Tellus*, **63A**, 223–237, doi:10.1111/j.1600-0870.2010.00481.x.

Kilpelainen, T., T. Vihma, M. Manninen, A. Sjoblom, E. Jakobson, T. Palo, and M. Maturillif, 2012b: Modelling the vertical structure of the atmospheric boundary layer over Arctic fjords in Svalbard. *Q. J. R. Meteorol. Soc.*, doi:10.1002/qj.1914.

Klein, S. A., R. B. McCoy, H. Morrison, A. S. Ackerman, A. Avramov, G. d. Boer, M. Chen, J. N. S. Cole, A. D. Del Genio, M. Falk, M. J. Foster, A. Fridlind, J.-C. Golaz, T. Hashino, J. Y. Harrington, C. Hoose, M. F. Khairoutdinov, V. E. Larson, X. Liu, Y. Luo, G. M. McFarquhar, S. Menon, R. A. J. Neggers, S. Park, M. R. Poellot, J. M. Schmidt, I. Sednev, B. J. Shipway, M. D. Shupe, D. A. Spangenberg, Y. C. Sud, D. D. Turner, D. E. Veron, K. v. Salzen, G. K. Walker, Z. Wang, A. B. Wolf, S. Xie, K.-M. Xu, F. Yang, and G. Zhang, 2009: Intercomparison of model simulations of mixed-phase clouds observed during the ARM Mixed-Phase Arctic Cloud Experiment. I: single-layer cloud. *Quart. J. Roy. Meteorol. Soc.*, **135 (641)**, 979–1002, doi:10.1002/qj.416.

Kliesch, L.-L. and M. Mech, 2019: Airborne radar reflectivity and brightness temperature measurements with POLAR 5 during ACLOUD in May and June 2017. *PANGAEA*, doi:10.1594/PANGAEA.899565.

Klingebiel, M., A. de Lozar, S. Molleker, R. Weigel, A. Roth, L. Schmidt, J. Meyer, A. Ehrlich, R. Neuber, M. Wendisch, and S. Borrmann, 2015: Arctic low-level boundary layer clouds: in situ measurements and simulations of mono- and bimodal supercooled droplet size distributions at the top layer of liquid phase clouds. *Atmos. Chem. Phys.*, **15 (2)**, 617–631, doi:10.5194/acp-15-617-2015.

Knollenberg, R. G., 1976: Three new instruments for cloud physics measurements. *in: Preprints Int. Conf. Cloud Physics, Boulder, Amer. Meteor. Soc*, 545–561.

Knudsen, E. M., B. Heinold, S. Dahlke, H. Bozem, S. Crewell, I. V. Gorodetskaya, G. Heygster, D. Kunkel, M. Maturilli, M. Mech, C. Viceto, A. Rinke, H. Schmithüsen, A. Ehrlich, A. Macke, C. Lüpkes, and M. Wendisch, 2018: Meteorological conditions during the ACLOUD/PASCAL field campaign near Svalbard in early summer 2017. *Atmos. Chem. Phys.*, **18 (24)**, 17 995–18 022, doi:10.5194/acp-18-17995-2018.

Kobayashi, S., Y. Ota, and Y. Harada, 2015: The JRA-55 Reanalysis: General Specifications and Basic Characteristics. *Journal of the Meteorological Society of Japan*, **93 (1)**, 5–48, doi:10.2151/jmsj.2015-001.

Kolstad, E. W., 2017: Higher ocean wind speeds during marine cold air outbreaks. *Quart. J. Roy. Meteorol. Soc.*, **143 (706)**, 2084–2092, doi:10.1002/qj.3068.

Kolstad, E. W., T. J. Bracegirdle, and I. A. Seierstad, 2009: Marine cold-air outbreaks in the North Atlantic: temporal distribution and associations with large-scale atmospheric circulation. *Climate Dynamics*, **33**, 187–197, doi:10.1007/s00382-008-0431-5.

Komurcu, M., T. Storelvmo, I. Tan, U. Lohmann, Y. Yun, J. Penner, Y. Wang, X. Liu, and T. Takemura, 2014: Intercomparison of the cloud water phase among global climate models. *J. Geophys. Res. - Atmos.*, **119**, 3372–3400, doi:10.1002/2013JD021119.

Korolev, A. and T. Leisner, 2020: Review of experimental studies of secondary ice production. *Atmos. Chem. Phys.*, **20**, 11 767–11 797, doi:10.5194/acp-20-11767-2020.

Korolev, A., G. McFarquhar, P. R. Field, C. Franklin, P. Lawson, Z. Wang, E. Williams, S. J. Abel, D. Axisa, S. Borrmann, J. Crosier, J. Fugal, M. Krämer, U. Lohmann, O. Schlenczek, M. Schnaiter, and M. Wendisch, 2017: Mixed-Phase Clouds: Progress and Challenges. *Meteorol. Monogr.*, **58**, 5.1–5.50, doi:10.1175/AMSMONOGRAPHS-D-17-0001.1.

Korolev, A. V., 2007: Limitations of the Wegener-Bergeron-Findeisen Mechanism in the Evolution of Mixed-Phase Clouds. *J. Atmos. Sci.*, **64**, 3372–3375, doi:0.1175/JAS4035.1.

Korolev, A. V. and G. A. Isaac, 2003: Phase transformation of mixedphase clouds. *Quart. J. Roy. Meteorol. Soc.*, **129**, 19–38, doi:10.1256/qj.01.203.

Korolev, A. V., G. A. Isaac, S. G. Cober, J. Strapp, and J. Hallett, 2003: Microphysical characterization of mixed-phase clouds. *Quart. J. Roy. Meteorol. Soc.*, **129**, 39–65, doi:10.1256/qj.01.204.

Lac, C., J.-P. Chaboureau, V. Masson, J.-P. Pinty, P. Tulet, J. Escobar, M. Leriche, C. Barthe, B. Aouizerats, C. Augros, P. Aumond, F. Auguste, P. Bechtold, S. Berthet, S. Bielli, F. Bosseur, O. Caumont, J.-M. Cohard, J. Colin, F. Couvreux, J. Cuxart, G. Delautier, T. Dauhut, V. Ducrocq, J.-B. Filippi, D. Gazen, O. Geoffroy, F. Gheusi, R. Honnert, J.-P. Lafore, C. Lebeaupin Brossier, Q. Libois, T. Lunet, C. Mari, T. Maric, P. Mascart, M. Mogé, G. Molinié, O. Nuissier, F. Pantillon, P. Peyrillé, J. Pergaud, E. Perraud, J. Pianezze, J.-L. Redelsperger, D. Ricard, E. Richard, S. Riette, Q. Rodier, R. Schoetter, L. Seyfried, J. Stein, K. Suhre, M. Taufour, O. Thouron, S. Turner, A. Verrelle, B. Vié, F. Visentin, V. Vionnet, and P. Wautelet, 2018: Overview of the Meso-NH model version 5.4 and its applications. *Geosci. Model Dev.*, **11 (5)**, 1929–1969, doi:10.5194/gmd-11-1929-2018.

Lacour, A., H. Chepfer, M. D. Shupe, N. B. Miller, V. Noel, J. Kay, D. D. Turner, and R. Guzman, 2017: Greenland Clouds Observed in CALIPSO-GOCCP: Comparison with Ground-Based Summit Observations. *J. Climate.*, **30**, 6065–6083, doi:10.1175/JCLI-D-16-0552.1.

Ladwig, W., 2017: *wrf-python (Version 1.3.2) [Software].* Boulder, Colorado: ed., UCAR/NCAR, doi:10.5065/D6W094P1.

Lance, S., C. A. Brock, D. Rogers, and J. A. Gordon, 2010: Water droplet calibration of the Cloud Droplet Probe (CDP) and in-flight performance in liquid, ice and mixed-phase clouds during ARCPAC. *Atmos. Meas. Tech.*, **3 (6)**, 1683–1706, doi:10.5194/amt-3-1683-2010.

Lance, S., M. D. Shupe, G. Feingold, C. A. Brock, J. Cozic, J. S. Holloway, R. H. Moore, A. Nenes, J. P. Schwarz, J. R. Spackman, K. D. Froyd, D. M. Murphy, J. Brioude, O. R. Cooper, A. Stohl, and J. F. Burkhart, 2011: Cloud condensation nuclei as a modulator of ice processes in Arctic mixed-phase clouds. *Atmos. Chem. Phys.*, **11 (15)**, 8003–8015, doi:10.5194/acp-11-8003-2011.

Laprise, R., 1992: The Euler equations of motion with hydrostatic pressure as an independent variable. *Mon. Wea. Rev.*, **120**, 197–207, doi:10.1175/1520-0493(1992)120<0197:TEEOMW>2.0.CO;2.

Lauber, A., A. Kiselev, T. Pander, P. Handmann, and T. Leisner, 2020: Secondary Ice Formation during Freezing of Levitated Droplets. *J. Atmos. Sci.*, **75**, 2815–2826, doi:10.1175/JAS-D-18-0052.1.

Lawson, R. P., 2011: Effects of ice particles shattering on the 2D-S probe. *Atmos. Meas. Tech.*, **4**, 1361–1381, doi:10.5194/amt-4-1361-2011.

Leck, C. and C. Persson, 1996: Seasonal and short-term variability in dimethyl sulfide, sulfur dioxide and biogenic sulfur and sea salt aerosol particles in the arctic marine boundary layer during summer and autumn. *Tellus B: Chemical and Physical Meteorology*, **48 (2)**, 272–299.

Leck, C. and E. Svensson, 2015: Importance of aerosol composition and mixing state for cloud droplet activation over the Arctic pack ice in summer. *Atmos. Chem. Phys.*, **15 (5)**, 2545–2568, doi:10.5194/acp-15-2545-2015.

Leinonen, J. and W. Szyrmer, 2015: Radar signatures of snowflake riming: A modeling study. *Earth and Space Science*, **2 (8)**, 346–358, doi:10.1002/2015EA000102.

Lenaerts, J. T. M., K. Van-Tricht, S. Lhermitte, and T. L'Ecuyer, 2017: Polar clouds and radiation in satellite observations, reanalyses, and climate models. *Geophys. Res. Lett.*, **44**, doi:10.1002/2016GL072242.

Leroy, D., E. Fontaine, A. Schwarzenboeck, and J. W. Strapp, 2016: Ice Crystal Sizes in High Ice Water Content Clouds. Part I: On the Computation of Median Mass Diameter from In Situ Measurements. *J. Atmos. Ocean. Technol.*, **33**, 2461–2476, doi:10.1175/JTECH-D-15-0151.1.

Lesins, G., T. J. Duck, and J. R. Drummond, 2012: Surface Energy Balance Framework for Arctic Amplification of Climate Change. *J. Climate.*, **25**, 8277–8288, doi:10.1175/JCLI-D-11-00711.1.

Lim, K.-S. S. and S.-Y. Hong, 2010: Development of an effective double-moment cloud microphysics schemewith prognostic cloud condensation nuclei (CCN) for weather and climatemodels. *Mon. Wea. Rev.*, **138**, 1587–1612, doi:10.1175/2009MWR2968.1.

Linell, K. and J. C. F. Tedrow, 1981: *Soil and permafrost surveys in the Arctic*. Clarendon Press, Oxford, 279 pp.

Liu, Y., J. R. Key, Z. Liu, X. Wang, and S. J. Vavrus, 2012: A cloudier Arctic expected with diminishing sea ice. *Geophys. Res. Lett.*, **39 (5)**, doi:10.1029/2012GL051251.

Liu, Y., M. Shupe, Z. Wang, and G. Mace, 2017: Cloud vertical distribution from combined surface and space radar-lidar observations at two Arctic atmospheric observatories. *Atmospheric Chemistry and Physics*, **17 (9)**, 5973–5989, doi:10.1038/nature04449.

Lloyd, G., T. W. Choularton, K. N. Bower, J. Crosier, H. Jones, J. R. Dorsey, M. W. Gallagher, P. Connolly, A. C. R. Kirchgaessner, and T. Lachlan-Cope, 2015: Observations and comparisons of cloud microphysical properties in spring and summertime Arctic stratocumulus clouds during the ACCACIA campaign. *Atmos. Chem. Phys.*, **15**, 3719–3737, doi:10.5194/acp-15-3719-2015.

Loewe, K., A. M. L. Ekman, M. Paukert, J. Sedlar, M. Tjernström, and C. Hoose, 2017: Modelling micro- and macrophysical contributors to the dissipation of an Arctic mixed-phase cloud during the Arctic Summer Cloud Ocean Study (ASCOS). *Atmos. Chem. Phys.*, **17**, 6693–6704, doi:10.5194/acp-17-6693-2017.

Loyer, L., 2022: Étude de processus-cl?s de la couche limite nuageuse en Arctique. Ph.D. thesis, Université de Sorbone, France, 195 pp.

Lu, J. and M. Cai, 2009: Quantifying contributions to polar warming amplification in an idealized coupled general circulation model. *Climate Dynamics*, **34**, 669–687, doi:10.1007/s00382-009-0673-x(2009).

Lubin, D. and A. M. Vogelmann, 2006: A climatologically significant aerosol longwave indirect effect in the Arctic. *Nature*, **439**, 453–456, doi:10.1038/nature04449.

Ludwig, V., G. Spreen, C. Haas, L. Istomina, F. Kauker, and D. Murashkin, 2019: The 2018 North Greenland polynya observed by a newly introduced merged optical and passive microwave sea-ice concentration dataset. *The Cryosphere*, **13 (7)**, 2051–2073, doi:10.5194/tc-13-2051-2019.

Luo, Y., K.-M. Xu, H. Morrison, G. M. McFarquhar, Z. Wang, and G. Zhang, 2008: Multilayer arctic mixed-phase clouds simulated by a cloud-resolving model: Comparison with ARM observations and sensitivity experiments. *J. Geophys. Res. - Atmos.*, **113 (D12)**, doi:10.1029/2007JD009563.

Lüpkes, C., A. Ehrlich, M. Wendisch, S. Crewell, and M. Mech, 2019: Master tracks in different resolutions during POLAR 5 campaign AFLUX 2019. *PANGAEA*, doi:10.1594/PANGAEA.902876.

Lüpkes, C., T. Vihma, G. Birnbaum, S. Dierer, T. Garbrecht, V. M. Gryanik, M. Gryschka, J. Hartmann, G. Heinemann, L. Kaleschke, S. Raasch, H. Savijärvi, K. H. Schlünzen, and U. Wacker, 2011: Mesoscale Modelling of the Arctic Atmospheric Boundary Layer and Its Interaction with Sea Ice. *In: Lemke, P., Jacobi, HW. (eds) Arctic Climate Change. Atmospheric and Oceanographic Sciences Library, vol 43. Springer, Dordrecht*, 279–324, doi:10.1007/978-94-007-2027-5_7.

Macke, A. and H. Flores, 2018: The Expeditions PS106/1 and 2 of the Research Vessel POLARSTERN to the Arctic Ocean in 2017. *Reports on Polar and Marine Research, Alfred-Wegener-Institut, Helmholtz-Zentrum für Polar- und Meeresforschung*, Bremerhaven, Germany, 1–171, doi:10.2312/BzPM_0719_2018.

Mahrt, L., O. S., and S. J., 1998: Nocturnal Boundary-Layer Regimes. *Boundary-Layer Meteorology*, **88**, 255–278, doi:10.1023/A:1001171313493.

Maillard, J., F. Ravetta, J. Raut, V. Mariage, and J. Pelon, 2021: Characterisation and surface radiative impact of Arctic low clouds from the IAOOS field experiment. *Atmospheric Chemistry and Physics*, **21 (5)**, 4079–4101.

Makiranta, E., T. Vihma, A. Sjöblom, and E.-M. Tastula, 2011: Observations and modelling of the atmospheric boundary layer over sea ice in a Svalbard fjord. *Boundary-Layer Meteorol.*, **140**, 105–123, doi:10.1007/s10546-011-9609-1.

Martin, G. M., D. W. Johnson, and A. Spice, 1994: The Measurement and Parameterization of Effective Radius of Droplets in Warm Stratocumulus Clouds. *J. Atmos. Sci.*, **51 (13)**, 1823–1842, doi:10.1175/1520-0469(1994)051<1823:TMAPOE>2.0.CO;2.

Martin, M., R. Y.-W. Chang, B. Sierau, S. Sjogren, E. Swietlicki, J. P. D. Abbatt, C. Leck, and U. Lohmann, 2011: Cloud condensation nuclei closure study on summer arctic aerosol. *Atmos. Chem. Phys.*, **11 (22)**, 11 335–11 350, doi:10.5194/acp-11-11335-2011.

Matejka, M., K. Láska, K. Jeklová, and J. Hosek, 2021: High-Resolution Numerical Modelling of Near-Surface Atmospheric Fields in the Complex Terrain of James Ross Island, Antarctic Peninsula. *Atmosphere*, **12 (3)**, doi:10.3390/atmos12030360.

Mauritsen, T., J. Sedlar, M. Tjernström, C. Leck, M. Martin, M. Shupe, S. Sjogren, B. Sierau, P. O. G. Persson, I. M. Brooks, and E. Swietlicki, 2011: An Arctic CCN-limited cloud-aerosol regime. *Atmos. Chem. Phys.*, **11 (1)**, 165–173, doi:10.5194/acp-11-165-2011.

Mayer, M., S. Tietsche, L. Haimberger, T. Tsubouchi, J. Mayer, and H. Zuo, 2019: An Improved Estimate of the Coupled Arctic Energy Budget. *J. Climate.*, **32 (22)**, 7915–7934, doi:10.1175/JCLI-D-19-0233.1.

McFarquhar, G. M. and A. J. Heymsfield, 1996: Microphysical characteristics of three anvils sampled during the Central Equatorial Pacific Experiment. *J. Atmos. Sci.*, **53**, 2401–2423, doi:10.1175/1520-0469(1996)053,2401:MCOTAS.2.0.CO;2.

McFarquhar, G. M., G. Zhang, M. R. Poellot, G. L. Kok, R. McCoy, T. Tooman, A. Fridlind, and A. J. Heymsfield, 2007: Ice properties of single-layer stratocumulus during the Mixed-Phase Arctic Cloud Experiment: 1. Observations. *J. Geophys. Res. - Atmos.*, **112 (D24)**, doi:10.1029/2007JD008633.

McFarquhar, G. M., S. Ghan, J. Verlinde, A. Korolev, J. W. Strapp, B. Schmid, J. M. Tomlinson, M. Wolde, S. D. Brooks, D. Cziczo, M. K. Dubey, J. Fan, C. Flynn, I. Gultepe, J. Hubbe, M. K. Gilles, A. Laskin, P. Lawson, W. R. Leaitch, P. Liu, X. Liu, D. Lubin, C. Mazzoleni, A.-M. Macdonald, R. C. Moffet, H. Morrison, M. Ovchinnikov, M. D. Shupe, D. D. Turner, S. Xie, A. Zelenyuk, K. Bae, M. Freer, and A. Glen, 2011: Indirect and Semi-direct Aerosol Campaign: The Impact of Arctic Aerosols on Clouds. *Bull. Amer. Meteorol. Soc.*, **92 (2)**, 183–201, doi:10.1175/2010BAMS2935.1.

Mech, M., L.-L. Kliesch, A. Anhäuser, T. Rose, P. Kollias, and S. Crewell, 2019: Microwave Radar/radiometer for Arctic Clouds (MiRAC): first insights from the ACLOUD campaign. *Atmos. Meas. Tech.*, **12 (9)**, 5019–5037, doi:10.5194/amt-12-5019-2019.

Mech, M., A. Ehrlich, A. Herber, C. Lüpkes, M. Wendisch, S. Becker, Y. Boose, D. Chechin, S. Crewell, R. Dupuy, C. Gourbeyre, J. Hartmann, E. Jäkel, O. Jourdan, L.-L. Kliesch, M. Klingebiel, B. Kulla, G. Mioche, M. Moser, E. Ruiz-Donoso, M. Schäfer, J. Stapf, and C. Voigt, 2022: MOSAiC-ACA and AFLUX : Arctic campaigns characterizing the exit area of MOSAiC. *Nature Scientific Data*, doi:SDATA-22-00964.

Mellat, A., M. Bailey, H. Mustonen, K. Marttila, H. Klein, E. Gribanov, K. Bret-Harte, M. Chupakov, A. Divine, D. Else, and I. Filippov, 2021: Hydroclimatic controls on the isotopic traits of pan-Arctic summer rainfall events. *Frontiers in Earth Sciences*, **9 (367)**, doi:10.3389/feart.2021.651731.

Mertes, S., K. Lehmann, A. Nowak, A. Massling, and A. Wiedensohler, 2005: Link between aerosol hygroscopic growth and droplet activation observed for hill-capped clouds at connected flow conditions during FEBUKO. *Atmos. Environ.*, **39**, 4247–4256, doi:10.1016/j.atmosenv.2005.02.010.

Mertes, S., F. Schröder, and A. Wiedensohler, 1995: The Particle detection Efficiency Curve of the Tsi-3010 CPC As A Function of the Temperature Difference Between Saturator and Condenser. *Aerosol. Sci. Technol.*, **23**, 257–261, doi:10.1080/02786829508965310.

Meyers, M. P., P. J. Demott, and W. R. Cotton, 1992: New primary ice nucleation parameterizations in an explicit cloud model. *J. Appl. Meteorol.*, **31**, 708–721, doi:10.1175/1520-0450(1992)031<0708:NPINPI>2.0.CO;2.

Middlemas, E., J. Kay, B. Medeiros, and E. Maroon, 2020: Quantifying the influences of cloud radiative feedbacks on Arctic surface warming using cloud locking in an Earth system model. *Geophysical Research Letters*, **47**, doi:10.1029/2020GL089207.

Milbrandt, J. A. and M. K. Yau, 2005a: A multimoment bulk microphysics parametrization. Part I: Analysis of the role of the spectral shape parameter. *J. Atmos. Sci.*, **62**, 3051–3064, doi:10.1175/JAS3534.1.

Milbrandt, J. A. and M. K. Yau, 2005b: A multimoment bulk microphysics parametrization. Part II: A proposed three-moment closure and scheme description. *J. Atmos. Sci.*, **62**, 3065–3081, doi:10.1175/JAS3535.1.

Milbrandt, J. A. and M. K. Yau, 2006: A Multimoment Bulk Microphysics Parameterization. Part IV: Sensitivity Experiments. *J. Atmos. Sci.*, **63**, 3137–3159, doi:10.1175/JAS3817.1.

Mioche, G. and O. Jourdan, 2018: Chapter 6 - Spaceborne Remote Sensing and Airborne In Situ Observations of Arctic Mixed-Phase Clouds. Mixed-Phase Clouds. *C. Andronache, Ed., Elsevier*, 121–150.

Mioche, G., O. Jourdan, M. Ceccaldi, and J. Delanoë, 2015: Variability of mixed-phase clouds in the Arctic with a focus on the Svalbard region: a study based on spaceborne active remote sensing. *Atmos. Chem. Phys.*, **15 (5)**, 2445–2461, doi:10.5194/acp-15-2445-2015.

Mioche, G., O. Jourdan, J. Delanoë, C. Gourbeyre, G. Febvre, R. Dupuy, M. Monier, F. Szczap, A. Schwarzenboeck, and J. Gayet, 2017: Vertical distribution of microphysical properties of Arctic springtime low-level mixedphase clouds over the Greenland and Norwegian seas. *Atmos. Chem. Phys.*, **17 (20)**, 12 845–12 869, doi:10.5194/acp-17-12845-2017.

Mishchenko, M. I., 2000: Calculation of the amplitude matrix for a nonspherical particle in a fixed orientation. *Appl. Opt.*, **39**, 1026–1031, doi:10.1364/AO.39.001026.

Mlawer, E. J., S. J. Taubman, P. D. Brown, M. J. Iacono, and S. A. Clough, 1997: Radiative transfer for inhomogeneous atmospheres: RRTM, a validated correlated-k model for the longwave. *J. Geophys. Res. - Atmos.*, **102 (D14)**, 16 663–16 682, doi:10.1029/97JD00237.

Monin, A. S. and A. M. Obukhov, 1954: Basic laws of turbulent mixing in the surface layer of the atmosphere. *Contrib. Geophys. Inst. Acad. Sci. USSR*, **151**, 163–187.

Morrison, A. L., J. E. Kay, W. R. Frey, H. Chepfer, and R. Guzman, 2019: Cloud Response to Arctic Sea Ice Loss and Implications for Future Feedback in the CESM1 Climate Model. *Journal of Geophysical Research : Atmospheres*, **124 (2)**, 1003–1020.

Morrison, H., J. A. Curry, and V. I. Khvorostyanov, 2005: A New Double-Moment Microphysics Parameterization for Application in Cloud and Climate Models. Part I: Description. *J. Atmos. Sci.*, **62 (6)**, 1665–1677, doi:10.1175/JAS3446.1.

Morrison, H., G. de Boer, G. Feingold, J. Harrington, M. D. Shupe, and K. Sulia, 2012: Resilience of persistent Arctic mixed-phase clouds. *Nat. Geosci*, **5**, 11–17, doi:10.1038/ngeo1332.

Morrison, H. and A. Gettelman, 2008: A new two-moment bulk stratiform cloud microphysics scheme in the Community Atmosphere Model, version 3 (CAM3). Part I: Description and numerical tests. *J. Climate*, **21**, 3642–3659, doi:10.1175/2008JCLI2105.1.

Morrison, H. and J. Pinto, 2005: Mesoscale Modeling of Springtime Arctic Mixed-Phase Stratiform Clouds Using a New Two-Moment Bulk Microphysics Scheme. *J. Atmos. Sci.*, **62**, 3683–3704, doi:10.1175/JAS3564.1.

Morrison, H., G. Thompson, and V. Tatarskii, 2009a: Impact of Cloud Microphysics on the Development of Trailing Stratiform Precipitation in a Simulated Squall Line: Comparison of One- and Two-Moment Schemes. *Mon. Wea. Rev.*, **137 (3)**, 991–1007, doi:10.1175/2008MWR2556.1.

Morrison, H., R. B. McCoy, S. A. Klein, S. Xie, Y. Luo, A. Avramov, M. Chen, J. N. Cole, M. Falk, M. J. Foster, A. D. Del-Genio, J. Y. Harrington, C. Hoose, M. F. Khairoutdinov, V. E. Larson, X. Liu, G. M. McFarquhar, M. R. Poellot, K. von Salzen, B. J. Shipway, M. D. Shupe, Y. C. Sud, D. D. Turner, D. E. Veron, G. K. Walker, Z. Wang, A. B. Wolf, K. M. Xu, F. Yang, and G. Zhang, 2009b: Intercomparison of model simulations of mixed-phase clouds observed during the ARM Mixed-Phase Arctic Cloud Experiment. II: Multilayer cloud. *Quart. J. Roy. Meteorol. Soc.*, **135**, 1003–1019, doi:10.1002/qj.415.

Morrison, H., P. Zuidema, A. S. Ackerman, A. Avramov, G. de Boer, J. Fan, A. M. Fridlind, T. Hashino, J. Y. Harrington, Y. Luo, M. Ovchinnikov, and B. Shipway, 2011: Intercomparison of cloud model simulations of Arctic mixed-phase boundary layer clouds observed during SHEBA/FIRE-ACE. *J. Adv. in Modeling Earth Syst.*, **3 (2)**, doi:10.1029/2011MS000066.

Moser, M., C. Voigt, T. Jurkat-Witschas, V. Hahn, G. Mioche, O. Jourdan, R. Dupuy, C. Gourbeyre, A. Schwarzenboeck, J. Lucke, Y. Boose, M. Mech, S. Borrmann, A. Ehrlich, A. Herber, C. Lüpkes, and M. Wendisch, 2023: Microphysical and thermodynamic phase analyses of Arctic low-level clouds measured above the sea ice and the open ocean in spring and summer. . *Atmos. Chem. Phys. Discuss.*, 1–27, doi:10.5194/acp-2023-44.

Mossop, S. C., 1976: Production of secondary ice particles during the growth of graupel by riming. *Quart. J. Roy. Meteorol. Soc.*, **102**, 45–57, doi:10.1002/qj.49710243104.

Mossop, S. C., 1985a: Microphysical properties of supercooled cumulus clouds in which an ice particle multiplication process operated. *Quart. J. Roy. Meteorol. Soc.*, **111**, 183–198, doi:10.1002/qj.49711146708.

Mossop, S. C., 1985b: Secondary ice particle production during rime growth: The effect of drop size distribution and rimer velocity. *Quart. J. Roy. Meteorol. Soc.*, **111**, 1113–1124, doi:10.1002/qj.49711147012.

Mossop, S. C., 1985c: The Origin and Concentration of Ice Crystals in Clouds. *Bull. Amer. Meteorol. Soc.*, **66**, 264–198, doi:10.1175/1520-0477(1985)066<0264:TOACOI>2.0.CO;2.

Mossop, S. C. and J. Hallett, 1974: Ice crystal concentration in cumulus clouds: Influence of the drop spectrum. *Science.*, **186**, 632–634, doi:10.1126/science.186.4164.632.

Nakanishi, M. and H. Niino, 2006: An Improved Mellor-Yamada Level 3 Model: Its Numerical Stability and Application to a Regional Prediction of Advection Fog. *Boundary-Layer Meteorology*, **119**, 397–407, doi:10.1007/s10546-005-9030-8.

Nakanishi, M. and H. Niino, 2009: Development of an Improved Turbulence Closure Model for the Atmospheric Boundary Layer. *Journal of the Meteorological Society of Japan. Ser. II*, **87 (5)**, 895–912, doi:10.2151/jmsj.87.895.

Neuber, R., L. V. Schmidt, C. Ritter, and M. Mech, 2019: Cloud top altitudes observed with airborne lidar during the ACLOUD campaign. *PANGAEA*, doi:10.1594/PANGAEA.899962.

Njuki, S. M., C. M. Mannaerts, and Z. Su, 2022: Influence of Planetary Boundary Layer (PBL) Parameterizations in the Weather Research and Forecasting (WRF) Model on the Retrieval of Surface Meteorological Variables over the Kenyan Highlands. *Atmosphere*, **13 (2)**, doi:10.3390/atmos13020169.

Nomokonova, T., K. Ebell, U. Löhnert, M. Maturilli, C. Ritter, and E. O'Connor, 2019: Statistics on clouds and their relation to thermodynamic conditions at Ny-Ålesund using ground-based sensor synergy. *Atmospheric Chemistry and Physics*, **19 (6)**, 4105–4126.

Ogren, J., J. Heintzenberg, and R. Charlson, 1985: In situ sampling of clouds with a droplet to aerosol converter. *Geophys. Res. Lett.*, **12**, 121–124, doi:10.1029/GL012i003p00121.

Ohata, S., M. Koike, A. Yoshida, N. Moteki, K. Adachi, N. Oshima, H. Matsui, O. Eppers, H. Bozem, M. Zanatta, and A. B. Herber, 2021: Arctic black carbon during PAMARCMiP 2018 and previous aircraft experiments in spring. *Atmos. Chem. Phys.*, **21 (20)**, 15 861–15 881, doi:10.5194/acp-21-15861-2021.

Oue, M., A. Tatarevic, P. Kollias, D. Wang, K. Yu, and A. M. Vogelmann, 2020: The Cloud-resolving model Radar SIMulator (CR-SIM) Version 3.3: description and applications of a virtual observatory. *Geosci. Model Dev.*, **13**, 1975–1998, doi:10.5194/gmd-13-1975-2020.

Ovchinnikov, M., A. Korolev, and J. Fan, 2011: Effects of ice number concentration on dynamics of a shallow mixed-phase stratiform cloud. *J. Geophys. Res. - Atmos.*, **116**, 223–248, doi:10.1029/2011JD015888.

Overland, J., E. Dunlea, J. Box, R. Corell, M. Forsius, V. Kattsov, M. Olsen, J. Pawlak, L. Reiersen, and M. Wang, 2019: The urgency of Arctic change. *Science Direct*, **21**, 6–13, doi:10.1016/j.polar.2018.11.008.

Overland, J. E., 1985: Atmospheric boundary layer structure and drag coefficients over sea ice. *J. Geophys. Res. - Ocean*, **90**, 9029–9049, doi:10.1029/JC090iC05p09029.

Palm, S. P., S. T. Strey, J. Spinhirne, and T. Markus, 2010: Influence of Arctic sea ice extent on polar cloud fraction and vertical structure and implications for regional climate. *J. Geophys. Res. - Atmos.*, **115 (D21)**, doi:10.1029/2010JD013900.

Papritz, L., S. Pfahl, H. Sodemann, and H. Wernli, 2015: A Climatology of Cold Air Outbreaks and Their Impact on Air-Sea Heat Fluxes in the High-Latitude South Pacific. *J. Climate.*, **28**, 342–364, doi:10.1175/JCLI-D-14-00482.1.

Park, S., C. Bretherton, and P. Rasch, 2014: Integrating cloud processes in the Community Atmosphere Model, version 5. *J. Climate*, **27**, 6821–6856, doi:10.1175/JCLI-D-14-00087.1.

Parkinson, C., J. Comiso, H. Zwally, D. Cavalieri, P. Gloersen, and W. Campbell, 1987: *Arctic Sea ice, 1973-1976: Satellite passive-microwave observations.* NASA Technical Reports Server, Washington D.C., 296 pp.

Persson, P. O. G., 2002: Measurements near the Atmospheric Surface Flux Group tower at SHEBA : Near-surface conditions and surface energy budget. *Journal of Geophysical Research : Oceans*, **107 (C10)**.

Persson, P. O. G., 2010: *Summary of meteorological conditions during the Arctic mechanisms for the interaction of the surface and atmosphere (AMISA) intensive observation periods.* 1st ed., U.S. Department of Commerce, National Oceanic and Atmospheric Administration, Office of Oceanic and Atmospheric Research, Earth System Research Laboratory, Physical Sciences Division, 57 pp.

Peters, G. P., T. B. Nilssen, L. Lindholt, M. S. Eide, S. Glomsrød, L. I. Eide, and J. S. Fuglestvedt, 2011: Future emissions from shipping and petroleum activities in the Arctic. *Atmos. Chem. Phys.*, **11**, 5305–5320, doi:10.5194/acp-11-5305-2011.

Pincus, R., H. W. Barker, and J.-J. Morcrette, 2003: A fast, flexible, approximate technique for computing radiative transfer in inhomogeneous cloud fields. *J. Geophys. Res. - Atmos.*, **108 (D13)**, doi:10.1029/2002JD003322.

Pithan, F. and T. Mauritsen, 2014: Arctic amplification dominated by temperature feedbacks in contemporary climate models. *Nat. Geosci*, **7**, 181–184, doi:10.1038/ngeo2071.

Pithan, F., A. Ackerman, W. M. Angevine, K. Hartung, L. Ickes, M. Kelley, B. Medeiros, I. Sandu, G.-J. Steeneveld, H. A. M. Sterk, G. Svensson, P. A. Vaillancourt, and A. Zadra, 2016: Select strengths and biases of models in representing the Arctic winter boundary layer over sea ice: the Larcform 1 single column model intercomparison. *J. Adv. Model. Earth Sys.*, **8 (3)**, 1345–1357, doi:10.1002/2016MS000630.

Pithan, F., G. Svensson, R. Caballero, D. Chechin, T. W. Cronin, A. M. L. Ekman, R. Neggers, M. D. Shupe, A. Solomon, M. Tjernström, and M. Wendisch, 2018: Role of air-mass transformations in exchange between the Arctic and mid-latitudes. *Nat. Geosci*, **11**, 805–812, doi:10.1038/s41561-018-0234-1.

Planche, C., 2021: Microphysique des nuages convectifs. Interactions aérosols-nuages-précipitations. *HDR, Université Clermont Auvergne, Clermont Ferrand, France*, 121.

Planche, C., W. Wobrock, and A. I. Flossmann, 2014: The continuous melting process in a cloud-scale model using a bin microphysics scheme. *Quart. J. Roy. Meteorol. Soc.*, **140 (683)**, 1986–1996, doi:10.1002/qj.2265.

Planche, C., W. Wobrock, A. I. Flossmann, F. Tridon, J. Van Baelen, Y. Pointin, and M. Hagen, 2010: The influence of aerosol particle number and hygroscopicity on the evolution of convective cloud systems and their precipitation: A numerical study based on the COPS observations on 12 August 2007. *Atmos. Res.*, **98**, 40–56, doi:10.1016/j.atmosres.2010.05.003.

Possner, A., A. M. Ekman, and U. Lohmann, 2017: Cloud response and feedback processes in stratiform mixed-phase clouds perturbed by ship exhaust. *Geophys. Res. Lett.*, **44**, 1964–1972, doi:10.1002/2016GL071358.

Prenni, A. J., J. Y. Harrington, M. Tjernström, P. J. Demott, A. Avramov, C. N. Long, S. M. Kreidenweis, P. Q. Olsson, and J. Verlinde, 2007: Can Ice-Nucleating Aerosols Affect Arctic Seasonal Climate? *Bull. Amer. Meteorol. Soc.*, **88**, 541–550, doi:10.1175/BAMS-88-4-541,.

Previdi, M., T. Janoski, G. Chiodo, K. Smith, and L. Polvani, 2020: Arctic Amplification : A Rapid Response to Radiative Forcing. *Geophys. Res. Lett.*, **47 (17)**, doi:10.1029/2020GL089933.

Pruppacher, H. R. and J. D. Klett, 1997: *Microphysics of clouds and precipitation.* 2nd ed., Kluwer Academic Publishers, 954 pp.

Qiu, S., X. Dong, B. Xi, and J.-L. F. Li, 2015: Characterizing Arctic mixed-phase cloud structure and its relationship with humidity and temperature inversion using NSA observations. *J. Geophys. Res. - Atmos.*, **120**, 7737–7746, doi:10.1002/2014JD023022.

Ramanathan, V., R. D. Cess, E. F. Harrison, P. Minnis, B. R. Barkstrom, E. Ahmad, and D. Hartmann, 1989: Cloud-Radiative Forcing and Climate: Results from the Earth Radiation Budget Experiment. *Science.*, **243 (4887)**, 57–63, doi:10.1126/science.243.4887.57.

Randall, D., J. Curry, D. Battisti, G. Flato, R. Grumbine, S. Hakkinen, D. Martinson, R. Preller, J. Walsh, and J. Weatherly, 1998: Status of and outlook for largescale modeling of atmosphere-ice-ocean interactions in the Arctic. *Bull. Amer. Meteor. Soc.*, **79**, 197–219, doi:10.1175/1520-0477(1998)079,0197:SOAOFL.2.0.CO;2.

Rangno, A. L. and P. V. Hobbs, 2001: Ice particles in stratiform clouds in the Arctic and possible mechanisms for the production of high ice concentrations. *J. Geophys. Res. - Atmos.*, **106**, 15 065–15 075, doi:10.1029/2000JD900286.

Renfrew, I. A., B. C., A. Elvidge, J. Brooke, C. Duscha, J. King, J. Kristiansen, T. Lachlan, G. Moore, R. S. Pickart, J. Reuder, I. Sandu, D. Sergeev, A. Terpstra, K. Våge, and A. Weiss, 2020: An evaluation of surface meteorology and fluxes over the Iceland and Greenland Seas in ERA5 reanalysis : The impact of sea ice distribution. *Quart. J. Roy. Meteorol. Soc.*, **147 (734)**, 691–712, doi:10.1002/qj.3941.

Rivière, G., L. Raillard, J. Delanoë, S. Bounissou, C. Caudoux, L. Cossalter, K. Huet, C. Cozzolino, O. Jourdan, C. Gourbeyre, C. Aubry, E. Bazile, Y. Seity, V. Douet, J. Trules, J. D. Doyle, F. Pantillon, and M. Wimmer, 2022: Thinice : campagne de mesure aéroportée dédiée à l'étude des dépressions arctiques et des interactions avec les nuages et la banquise. *La Météorologie*, **119 (4-5)**, doi:10.37053/lameteorologie-2022-0074.

Ruiz-Donoso, E., A. Ehrlich, M. Schäfer, E. Jäkel, V. Schemann, S. Crewell, M. Mech, B. S. Kulla, L.-L. Kliesch, R. Neuber, and M. Wendisch, 2020: Small-scale structure of thermodynamic phase in Arctic mixed-phase clouds observed by airborne remote sensing during a cold air outbreak and a warm air advection event. *Atmos. Chem. Phys.*, **20**, 5487–5511, doi:10.5194/acp-20-5487-2020.

Rutledge, S. A. and P. V. Hobbs, 1984: The Mesoscale and Microscale Structure and Organization of Clouds and Precipitation in Midlatitude Cyclones. XII: A Diagnostic Modeling Study of Precipitation Development in Narrow Cold-Frontal Rainbands. *J. Atmos. Sci.*, **41 (20)**, 2949–2972, doi:10.1175/1520-0469(1984)041<2949:TMAMSA>2.0.CO;2.

Ryzhkov, A. V., M. Pinsky, A. Pokrovsky, and A. Khain, 2011: Polarimetric Radar Observation Operator for a Cloud Model with Spectral Microphysics. *J. Appl. Meteorol. and Climatol.*, **50**, 873–894, doi:10.1175/2010JAMC2363.1.

Sand, M., B. H. Samset, Y. Balkanski, S. Bauer, N. Bellouin, T. K. Berntsen, H. Bian, M. Chin, T. Diehl, R. Easter, S. J. Ghan, T. Iversen, A. Kirkevag, J. Lamarque, G. Lin, X. Liu, G. Luo, G. Myhre, T. V. Noije, J. E. Penner, M. Schulz, O. Seland, R. B. Skeie, P. Stier, T. Takemura, K. Tsigaridis, F. Yu, K. Zhang, and H. Zhang, 2017: Aerosols at the poles: an AeroCom Phase II multi-model evaluation. *Atmos. Chem. Phys.*, **17**, 12 197–12 218, doi:10.5194/acp-17-12197-2017.

Savre, J., A. M. L. Ekman, G. Svensson, and M. Tjernström, 2015: Large-eddy simulations of an Arctic mixed-phase stratiform cloud observed during ISDAC: sensitivity to moisture aloft, surface fluxes and large-scale forcing. *Quart. J. Roy. Meteorol. Soc.*, **141 (689)**, 1177–1190, doi:10.1002/qj.2425.

Schwarzenboeck, A., J. Heintzenberg, and S. Mertes, 2000: Incorporation of aerosol particles between 25 and 850 nm into cloud elements: measurements with a new complementary sampling system. *Atmos. Res.*, **52**, 241–260, doi:10.1016/S0169-8095(99)00034-4,.

Schwarzenboeck, A., G. Mioche, A. Armetta, A. Herber, and J. Gayet, 2009: Response of the Nevzorov hot wire probe in clouds dominated by droplet conditions in the drizzle size range. *Atmos. Meas. Tech.*, **2**, 779–788, doi:10.5194/amt-2-779-2009.

Schweiger, A., R. Lindsay, S. Varvus, and J. Francis, 2008: Relationships between Arctic sea ice and clouds during autumn. *J. Climate.*, **21**, 4799–4810, doi:10.1175/2008JCLI2156.1.

Screen, J. A. and I. Simmonds, 2009: The central role of diminshing sea ice in recent Arctic temperature amplification. *Nature.*, **464**, 1334–1337, doi:10.1038/nature09051.

Sedlar, J. and Tjernström, 2017: Clouds, warm air, and a climate cooling signal over the summer Arctic. *Geophys. Res. Lett.*, **44**, 1095–1103, doi:10.1002/2016GL071959.

Sedlar, J. and M. Tjernström, 2009: Stratiform cloud-inversion characterization during the Arctic melt season. *Boundary-Layer Meteorol.*, **132**, 455–474, doi:10.1007/s10546-009-9407-1.

Sedlar, J., M. Tjernström, A. Rinke, A. Orr, J. Cassano, X. Fettweis, G. Heinemann, M. Seefeldt, A. Solomon, H. Matthes, P. T., and S. Webster, 2020: Confronting Arctic Troposphere, Clouds, and Surface Energy Budget Representations in Regional Climate Models With Observations. *J. Geophys. Res. - Atmos.*, **125 (6)**, doi:10.1029/2019JD031783.

Seity, Y., P. Brousseau, S. Malardel, G. Hello, P. Bénard, F. Bouttier, C. Lac, and V. Masson, 2011: The AROME-France Convective-Scale Operational Model. *Mon. Wea. Rev.*, **139 (3)**, 976–991, doi:10.1175/2010MWR3425.1.

Serreze, M. C. and R. G. Barry, 2011: Processes and impacts of Arctic amplification: A research synthesis. *Global Planet. Change*, **77**, 85–96, doi:10.1016/j.gloplacha.2011.03.004.

Serreze, M. C. and J. A. Francis, 2006: The Arctic amplification debate. *Climatic Change*, **76**, 241–264, doi:10.1007/s10584-005-9017-y.

Shaw, G. E., 1982: : Atmospheric turbidity in the polar regions. *J. Appl. Meteor*, **21**, 1080–1088.

Shindell, D. and G. Faluvegi, 2009: Climate response to regional radiative forcing during the twentieth century. *Nat. Geosci.*, **2**, 294–300, doi:10.1038/ngeo473.

Shupe, M. D. and J. M. Intrieri, 2004: Cloud Radiative Forcing of the Arctic Surface: The Influence of Cloud Properties, Surface Albedo, and Solar Zenith Angle. *J. Climate.*, **17**, 616–628, doi:10.1175/1520-0442(2004)017<0616:CRFOTA>2.0.CO;2.

Shupe, M. D., P. Kollias, P. O. Persson, and G. McFarquhar, 2008: Vertical motions in Arctic mixed-phase stratiform clouds. *J. Atmos. Sci.*, **65**, 66–86, doi:10.1175/2007JAS2479.1.

Shupe, M. D., S. Matrosov, and T. Uttal, 2006: Arctic Mixed-Phase Cloud Properties Derived from Surface-Based Sensors at SHEBA. *J. Atmos. Sci.*, **63 (2)**, 697–711, doi:10.1175/JAS3659.1.

Shupe, M. D., M. Tjernström, and P. O. G. Persson, 2015: Challenge of Arctic clouds and their implications for surface radiation. *Bull. Amer. Meteor. Soc.*, **96 (7)**, S130–S131, doi:10.1175/2015BAMSStateoftheClimate.1.

Shupe, M. D., V. P. Walden, E. Eloranta, T. Uttal, J. R. Campbell, S. M. Starkweather, and M. Shiobara, 2011: Clouds at Arctic Atmospheric Observatories. Part I: Occurrence and Macrophysical Properties. *J. Appl. Meteorol. and Climatol.*, **50**, 626–644, doi:10.1175/2010JAMC2467.1.

Shupe, M. D., M. Rex, B. Blomquist, P. O. G. Persson, J. Schmale, T. Uttal, D. Althausen, H. Angot, S. Archer, L. Bariteau, I. Beck, J. Bilberry, S. Bucci, C. Buck, M. Boyer, Z. Brasseur, I. M. Brooks, R. Calmer, J. Cassano, V. Castro, D. Chu, D. Costa, C. J. Cox, J. Creamean, S. Crewell, S. Dahlke, E. Damm, G. de Boer, H. Deckelmann, K. Dethloff, M. Dütsch, K. Ebell, A. Ehrlich, J. Ellis, R. Engelmann, A. A. Fong, M. M. Frey, M. R. Gallagher, L. Ganzeveld, R. Gradinger, J. Graeser, V. Greenamyer, H. Griesche, S. Griffiths, J. Hamilton, G. Heinemann, D. Helmig, A. Herber, C. Heuzé, J. Hofer, T. Houchens, D. Howard, J. Inoue, H.-W. Jacobi, R. Jaiser, T. Jokinen, O. Jourdan, G. Jozef, W. King, A. Kirchgaessner, M. Klingebiel, M. Krassovski, T. Krumpen, A. Lampert, W. Landing, T. Laurila, D. Lawrence, M. Lonardi, B. Loose, C. Lüpkes, M. Maahn, A. Macke, W. Maslowski, C. Marsay, M. Maturilli, M. Mech, S. Morris, M. Moser, M. Nicolaus, P. Ortega, J. Osborn, F. Pätzold, D. K. Perovich, T. Petäjä, C. Pilz, R. Pirazzini, K. Posman, H. Powers, K. A. Pratt, A. Preußer, L. Quéléver, M. Radenz, B. Rabe, A. Rinke, T. Sachs, A. Schulz, H. Siebert, T. Silva, A. Solomon, A. Sommerfeld, G. Spreen,

M. Stephens, A. Stohl, G. Svensson, J. Uin, J. Viegas, C. Voigt, P. von der Gathen, B. Wehner, J. M. Welker, M. Wendisch, M. Werner, Z. Xie, and F. Yue, 2022: Overview of the MOSAiC expedition: Atmosphere. *Elementa: Science of the Anthropocene*, **10**, doi: 10.1525/elementa.2021.00060.

Skamarock, W. C. and J. B. Klemp, 1992: The Stability of Time-Split Numerical Methods for the Hydrostatic and the Nonhydrostatic Elastic Equations. *Mon. Wea. Rev.*, **120**, 2109–2127, doi:10.1175/1520-0493(1992)120<2109:TSOTSN>2.0.CO;2.

Skamarock, W. C., J. B. Klemp, J. Dudhia, D. O. Gill, D. M. Barker, M. G. Duda, X.-Y. Huang, W. Wang, and J. G. Powers, 2008: *A Description of the Advanced Research WRF Version 3*. No. NCAR/TN-475+STR ed., University Corporation for Atmospheric Research, 125 pp., doi:10.5065/D68S4MVH.

Skamarock, W. C., J. B. Klemp, J. Dudhia, D. O. Gill, Z. Liu, J. Berner, W. Wang, J. Powers, M. G. Duda, D. M. Barker, and X.-Y. Huang, 2019: *A description of the advanced research WRF Version 4*. NCAR/TN-556+STR, NCAR Technical note, NCAR, Boulder, CO, USA, 162 pp, doi:10.5065/1dfh-6p97.

Smith, W., C. Hansen, A. Bucholtz, B. E. Anderson, M. Beckley, J. Corbett, R. Cullather, K. Hines, M. Hofton, S. Kato, D. Lubin, R. Moore, M. Rosenhaimer, J. Redemann, S. Schmidt, R. Scott, S. Song, J. Barrick, J. Blair, D. Bromwich, C. Brooks, G. Chen, H. Cornejo, C. Corr, S. Ham, A. Kittelman, S. Knappmiller, S. LeBlanc, N. Loeb, C. Miller, L. Nguyen, R. Palikonda, D. Rabine, E. Reid, J. Richter-Menge, P. Pilewskie, Y. Shinozuka, D. Spangenberg, P. Stackhouse, P. Taylor, K. Thornhill, D. van Gilst, and E. Winstead, 2017: Arctic radiation-icebridge sea and ice experiment (arise): The arctic radiant energy system during the critical seasonal ice transition. *Bull. Amer. Meteor. Soc.*, doi: 10.1175/BAMS-D-14-00277.1.

Solomon, A., G. de Boer, J. M. Creamean, A. McComiskey, M. D. Shupe, M. Maahn, and C. Cox, 2018: The relative impact of cloud condensation nuclei and ice nucleating particle concentrations on phase partitioning in Arctic mixed-phase stratocumulus clouds. *Atmos. Chem. Phys.*, **18**, 17 047–17 059, doi:10.5194/acp-18-17047-2018.

Solomon, A., G. Feingold, and M. D. Shupe, 2015: The role of ice nuclei recycling in the maintenance of cloud ice in Arctic mixedphase stratocumulus. *Atmos. Chem. Phys.*, **15**, 10 631–10 643, doi:10.5194/acp-15-10631-2015.

Solomon, A., M. Shupe, P. Person, and H. Morrison, 2011: Moisture and dynamical interactions maintaining decoupled Arctic mixed-phase stratocumulus in the presence of a humidity inversion. *Atmos. Chem. Phys.*, **11**, 10 127–10 148, doi:10.5194/acp-11-10127-2011.

Solomon, S., D. Qin, M. Manning, Z. Chen, M. Marquis, K. B. Averyt, M. Tignor, and H. L. Miller, 2007: *Climate change 2007: the physical scence basis*. Cambridge University Press, Cambridge, UK.

Sorteberg, A. and J. E. Walsh, 2008: Seasonal cyclone variability at 70°N and its impact on moisture transport into the Arctic. *Tellus. A*, **60 (3)**, 570–586, doi:10.1111/j.1600-0870.2007.00314.x.

Spiga, A., 2008: Dynamique méso-échelle de l'atmophère martienne : Développement d'un modèle météorologique et analyse des observations OMEGA / Mars Express. Ph.D. thesis, Université Pierre et Marie Curie, Paris VI, 292 pp.

Stachlewska, I. S., R. Neuber, A. Lampert, C. Ritter, and G. Wehrle, 2010: AMALi - the Airborne Mobile Aerosol Lidar for Arctic research. *Atmos. Chem. Phys.*, **10 (6)**, 2947–2963, doi:10.5194/acp-10-2947-2010.

Stapf, J., A. Ehrlich, E. Jäkel, C. Lüpkes, and M. Wendisch, 2020: Reassessment of shortwave surface cloud radiative forcing in the Arctic: consideration of surface-albedo-cloud interactions. *Atmos. Chem. Phys.*, **20 (16)**, 9895–9914, doi:10.5194/acp-20-9895-2020.

Stapf, J., A. Ehrlich, E. Jäkel, and M. Wendisch, 2019a: Aircraft measurements of broadband irradiance during the ACLOUD campaign in 2017. *PANGAEA*, doi:10.1594/PANGAEA.900442.

Stapf, J., A. Ehrlich, E. Jäkel, and M. Wendisch, 2019b: Cloud radiative forcing, LWP and cloud-free albedo derived from airborne broadband irradiance observations during the ACLOUD campaign. *PANGAEA*, doi:10.1594/PANGAEA.909289.

Stephens, G. L., 2005: Cloud feedbacks in the climate system: a critical review. *J. Climate*, **18**, 237–273.

Stephens, G. L., D. G. Vane, R. J. Boain, G. G. Mace, K. Sassen, Z. Wang, A. J. Illingworth, E. J. O'connor, W. B. Rossow, S. L. Durden, S. D. Miller, R. T. Austin, A. Benedetti, and C. Mitrescu, 2002: The CLOUDSAT Mission and the A-TRAIN: A New Dimension of Space-Based Observations of Clouds and Precipitation. *Bull. Amer. Meteorol. Soc.*, **83**, 1771–1790, doi:10.1175/BAMS-83-12-1771.

Stephenson, S. R., W. Wang, C. S. Zender, H. Wang, S. J. Davis, and P. J. Rasch, 2018: Climatic Responses to Future Trans-Arctic Shipping. *Geophys. Res. Lett.*, **45**, 9898–9908, doi:10.1029/2018GL078969.

Sterzinger, L. J., J. Sedlar, H. Guy, R. R. Neely III, and A. L. Igel, 2022: Do Arctic mixed-phase clouds sometimes dissipate due to insufficient aerosol? Evidence from comparisons between observations and idealized simulations. *Atmos. Chem. Phys.*, **22 (13)**, 8973–8988, doi:10.5194/acp-22-8973-2022.

Stevens, R. G., K. Loewe, C. Dearden, A. Dimitrelos, A. Possner, G. K. Eirund, T. Raatikainen, A. A. Hill, B. J. Shipway, J. Wilkinson, S. Romakkaniemi, J. Tonttila, A. Laaksonen, H. Korhonen, P. Connolly, U. Lohmann, C. Hoose, A. M. L. Ekman, K. S. Carslaw, and P. R. Field, 2018: A model intercomparison of CCN-limited tenuous clouds in the high Arctic. *Atmos. Chem. Phys.*, **18**, 11 041–11 071, doi:10.5194/acp-18-11041-2018.

Stohl, A., 2006: Characteristics of atmospheric transport into the Arctic troposphere. *Journal of Geophysical Research*, **111 (D11)**, 40–41.

Stonehouse, B., 1989: *Polar ecology*. Blackie, London, 222 pp.

Stroeve, J., M. Serreze, S. Drobot, S. Gearheard, M. Holland, J. Maslanik, W. Meier, and T. Scambos, 2007: Arctic Sea Ice Extent Plummets in 2007. *Science Direct*, **89 (2)**, 13–14, doi:10.1029/2008EO020001.

Stull, R. B., 1988: *An Introduction to Boundary Layer Meteorology*. Springer Dordrecht, Netherlands, 670 pp., doi:10.1007/978-94-009-3027-8.

Tan, I., T. Storelvmo, and M. Zelinka, 2016: Observational constraints on mixed-phase clouds imply higher climate sensitivity. *Science.*, **352**, doi:10.1126/science.aad5300.

Tastula, E., T. Vihma, and E. Andreas, 2012: Evaluation of polar wrf from modeling the atmospheric boundary layer over antarctic sea ice in autumn and winter. *Monthly Weather Review*, **140**, 3919–3935, doi:10.1175/MWR-D-12-00016.1.

Tatarevic, A., P. Kollias, M. Oue, D. Wang, and K. Yu, 2019: User's Guide CR-SIM SOFTWARE v 3.3. *Brookhaven National Laboratory - Stony Brook University - McGill University Radar Science Group (last access: 26 March 2020)*, URL https://www.bnl.gov/CMAS/cr-sim.php.

Taylor, P. C., M. Cai, A. X. Hu, J. Meehl, W. Washington, and G. J. Zhang, 2013: A decomposition of feedback contributions to polar warming amplification. *J. Climate*, **26**, 7023–7043, doi:10.1175/JCLI-D-12-00696.1.

Thomas, M. A., A. Devasthale, M. Tjernström, and A. M. L. Ekman, 2019: The Relation Between Aerosol Vertical Distribution and Temperature Inversions in the Arctic in Winter and Spring. *Geophysical Research Letters*, **46 (5)**, 2836–2845.

Thomas, S. M., A. K. Heidinger, and M. J. Pavolonis, 2004: Comparison of NOAA's operational AVHRR-derived cloud amount to other satellite-derived cloud climatologies. *J. Climate*, **17**, 4805–4822.

Thompson, G. and T. Eidhammer, 2014: A study of aerosol impacts on clouds and precipitation development in a large winter cyclone. *J. Atmos. Sci.*, **71**, 3636–3658, doi:10.1175/JAS-D-13-0305.1.

Thompson, G., P. R. Field, R. M. Rasmussen, and W. D. Hall, 2008: Explicit forecasts of winter precipitation using an improved bulk microphysics scheme. Part II: Implementation of a new snow parameterization. *Mon. Wea. Rev.*, **136**, 5095–5115, doi:10.1175/2008MWR2387.1.

Timmermans, M.-L. and J. Marshall, 2020: Understanding Arctic Ocean Circulation: A Review of Ocean Dynamics in a Changing Climate. *J. Geophys. Res. - Ocean*, **125 (4)**, doi:10.1029/2018JC014378.

Tjernström, M. and R. Graverson, 2009: The vertical structure of the lower Arctic troposphere analyzed from observations and the ERA-40 reanalysis. *Quart. J. Roy. Meteorol. Soc.*, **135**, 431–443, doi:10.1002/qj.380.

Tjernström, M., C. Leck, P. O. G. Persson, M. L. Jensen, S. P. Oncley, and A. Targino, 2004: Experimental Equipment: A Supplement to The Summertime Arctic Atmosphere: Meteorological Measurements during the Arctic Ocean Experiment 2001. *Bull. Amer. Meteorol. Soc.*, **85**, 1305–1321, doi:0.1175/BAMS-85-9-130.

Tjernström, M., C. Birch, I. Brooks, M. Shupe, P. Persson, J. Sedlar, T. Mauritsen, C. Leck, J. Paatero, M. Szczodrak, and C. R. Wheeler, 2012: Meteorological conditions in the central Arctic summer during the Arctic summer cloud ocean study (ASCOS). *Atmos. Chem. Phys.*, **12**, 6863–6889, doi:10.5194/acp-12-6863-2012.

Tjernström, M., C. Leck, C. E. Birch, J. W. Bottenheim, B. J. Brooks, I. M. Brooks, L. Bäcklin, R. Y.-W. Chang, G. de Leeuw, L. Di Liberto, S. de la Rosa, E. Granath, M. Graus, A. Hansel, J. Heintzenberg, A. Held, A. Hind, P. Johnston, J. Knulst, M. Martin, P. A. Matrai, T. Mauritsen, M. Müller, S. J. Norris, M. V. Orellana, D. A. Orsini, J. Paatero, P. O. G. Persson, Q. Gao, C. Rauschenberg, Z. Ristovski, J. Sedlar, M. D. Shupe, B. Sierau, A. Sirevaag, S. Sjogren, O. Stetzer, E. Swietlicki, M. Szczodrak, P. Vaattovaara, N. Wahlberg, M. Westberg, and C. R. Wheeler, 2014: The Arctic Summer Cloud Ocean Study (ASCOS): overview and experimental design. *Atmos. Chem. Phys.*, **14 (6)**, 2823–2869, doi:10.5194/acp-14-2823-2014.

Tobo, Y., K. Adachi, P. J. DeMott, T. C. J. Hill, D. S. Hamilton, N. M. Mahowald, N. Nagatsuka, S. Ohata, J. Uetake, Y. Kondo, and M. Koike, 2019: Glacially sourced dust as a potentially significant source of ice nucleating particles. *Nature Geoscience*, **12 (4)**, 253–258.

Treffeisen, R., R. Krejci, J. Ström, A. Engvall, A. Herber, and L. Thomason, 2007: Humidity observations in the Arctic troposphere over Ny-Ålesund, Svalbard based on 15 years of radiosonde data. *Atmos. Chem. Phys.*, **7**, 2721–2732, doi:10.5194/acp-7-2721-2007.

Tridon, F., A. Battaglia, R. J. Chase, F. J. Turk, J. Leinonen, S. Kneifel, K. Mroz, J. Finlon, A. Bansemer, S. Tanelli, A. J. Heymsfield, and S. W. Nesbitt, 2019: The microphysics of stratiform precipitation during OLYMPEX: Compatibility between triple-frequency radar and airborne in situ observations. *J. Geophys. Res. - Atmos.*, **124**, 8764–8792, doi:10.1029/2018JD029858.

Tunved, P., J. Strom, and R. Krejci, 2013: Arctic aerosol life cycle: Linking aerosol size distributions observed between 2000 and 2010 with air mass transport and precipitation at Zeppelin station, NyAlesund, Svalbard. *Atmospheric Chemistry and Physics*, **13 (7)**, 3643–3660.

Twohy, C., J. Strapp, and M. Wendisch, 2003: Performance of a Counterflow Virtual Impactor in the NASA Icing Research Tunnel. *J. Atmos. Ocean. Technol.*, **20**, 781–790, doi:10.1175/1520-0426(2003)020<0781:POACVI>2.0.CO.

Uttal, T., J. Curry, M. McPhee, D. Perovich, R. Moritz, J. Maslanik, P. Guest, H. Stern, J. Moore, R. Turenne, A. Heiberg, M. Serreze, D. Wylie, O. Persson, C. Paulson, C. Halle, J. Morison, P. Wheeler, A. Makshtas, H. Welch, M. Shupe, J. Intrieri, K. Stamnes, R. Lindsey, R. Pinkel, W. Pegau, T. Stanton, and T. Grenfeld, 2002: Surface Heat Budget of the Arctic Ocean. *Bulletin of the American Meteorological Society*, **83 (2)**, 255–276.

Vaillant de Guélis, T., A. Schwarzenböck, V. Shcherbakov, C. Gourbeyre, B. Laurent, R. Dupuy, P. Coutris, and C. Duroure, 2019: Study of the diffraction pattern of cloud particles and the respective responses of optical array probes. *Atmos. Meas. Tech.*, **12**, 2513–2529, doi:10.5194/amt12-2513-2019.

Vavrus, S., D. Waliser, A. Schweiger, and J. Francis, 2009: Simulations of 20th and 21st century arctic cloud amount in the global climate models assessed in the ipcc ar4. *Climate Dyn.*, **33**, 1099–1115, doi:10.1007/s00382-008-0475-6.

Verlinde, J., J. Harrington, G. McFarquhar, V. Yannuzzi, A. Avramov, S. Greenberg, N. Johnson, G. Zhang, M. Poellot, J. Mather, D. Turner, E. Eloranta, B. Zak, A. Prenni, J. Daniel, G. Kok, D. Tobin, R. Holz, K. Sassen, D. Spangenberg, P. Minnis, T. Tooman, M. Ivey, S. Richardson, C. Bahrmann, M. Shupe, P. DeMott, A. Heymsfield, and R. Schofield, 2007: The Mixed-Phase Arctic Cloud Experiment. *Bull. Amer. Meteorol. Soc.*, **88**, 205–222, doi:10.1175/BAMS-88-2-205.

Vihma, T., T. Kilpeläinen, M. Manninen, A. Sjöblom, E. Jakobson, T. Palo, J. Jaagus, and M. Maturilli, 2011: Characteristics of temperature and humidity inversions and low-level jets over Svalbard fjords in spring. *Adv. Meteorol.*, 1–14, doi:10.1155/2011/486807.

Walden, V. P., S. R. Hudson, L. Cohen, S. Y. Murphy, and M. A. Granskog, 2017: Atmospheric components of the surface energy budget over young sea ice: Results from the N-ICE2015 campaign. *J. Geophys. Res. - Atmos.*, **122 (16)**, 8427–8446, doi:10.1002/2016JD026091.

Wang, S., Q. Wang, R. E. Jordan, and P. O. G. Persson, 2001: Interactions among longwave radiation of clouds, turbulence, and snow surface temperature in the Arctic: A model sensitivity study. *J. Geophys. Res. - Atmos.*, **106 (D14)**, 15 323–15 333, doi:10.1029/2000JD900358.

Wang, W., C. Bruyère, M. Duda, J. Dudhia, D. Gill, M. Kavulich, K. Keene, M. Chen, H.-C. Lin, J. Michalakes, S. Rizvi, X. Zhang, J. Berner, S. Ha, J. D. Beezley, J. L. Coen, J. Mandel, H.-Y. Chuang, N. McKee, T. Slovacek, J. Wolff, and K. Fossell, 2017: Advanced Research WRF (ARW) Version 3 Modeling System User's Guide. *Mesoscale and Microscale Meteorology Division - National Center for Atmospheric Research*, 434.

Warneke, C., R. Bahreini, J. Brioude, C. A. Brock, J. A. de Gouw, D. W. Fahey, K. D. Froyd, J. S. Holloway, A. Middlebrook, L. Miller, S. Montzka, D. M. Murphy, J. Peischl, T. B. Ryerson, J. P. Schwarz, J. R. Spackman, and P. Veres, 2009: Biomass burning in Siberia and Kazakhstan as an important source for haze over the Alaskan Arctic in April 2008. *Geophys. Res. Lett.*, **36**, doi:10.1029/2008GL036194.

Webster, M. A., I. G. Rigor, D. K. Perovich, J. A. Richter-Menge, C. M. Polashenski, and B. Light, 2015: Seasonal evolution of melt ponds on Arctic sea ice. *J. Geophys. Res. - Ocean*, **120 (9)**, 5968–5982, doi:10.1002/2015JC011030.

Wegener, A., 1911: *Thermodynamik der Atmosphare*. Barth ed., Leipzig.

Wendisch, M., D. Handorf, I. Tegen, R. A. J. Neggers, and G. Spreen, 2021: Glimpsing the ins and outs of the Arctic atmospheric cauldron. *Eos*, **102**, doi:10.1029/2021EO155959.

Wendisch, M., M. Brückner, J. P. Burrows, S. Crewell, K. Dethloff, K. Ebell, C. Lüpkes, A. Macke, J. Notholt, J. Quaas, A. Rinke, and I. Tegen, 2017: ArctiC Amplification: Climate Relevant Atmospheric and SurfaCe Processes, and Feedback Mechanisms $(AC)^3$. *Eos*, **98**, doi:10.1029/2017EO064803.

Wendisch, M., A. Macke, A. Ehrlich, C. Lüpkes, M. Mech, D. Chechin, K. Dethloff, C. B. Velasco, H. Bozem, M. Brückner, H.-C. Clemen, S. Crewell, T. Donth, R. Dupuy, K. Ebell, U. Egerer, R. Engelmann, C. Engler, O. Eppers, M. Gehrmann, X. Gong, M. Gottschalk, C. Gourbeyre, H. Griesche, J. Hartmann, M. Hartmann, B. Heinold, A. Herber, H. Herrmann, G. Heygster, P. Hoor, S. Jafariserajehlou, E. Jäkel, E. Järvinen, O. Jourdan, U. Kästner, S. Kecorius, E. M. Knudsen, F. Köllner, J. Kretzschmar, L. Lelli, D. Leroy, M. Maturilli, L. Mei, S. Mertes, G. Mioche, R. Neuber, M. Nicolaus, T. Nomokonova, J. Notholt, M. Palm, M. van Pinxteren, J. Quaas, P. Richter, E. Ruiz-Donoso, M. Schäfer, K. Schmieder, M. Schnaiter, J. Schneider, A. Schwarzenböck, P. Seifert, M. D. Shupe, H. Siebert, G. Spreen, J. Stapf, F. Stratmann, T. Vogl, A. Welti, H. Wex, A. Wiedensohler, M. Zanatta, and S. Zeppenfeld, 2019: The Arctic Cloud Puzzle: Using ACLOUD/PASCAL Multiplatform Observations to Unravel the Role of Clouds and Aerosol Particles in Arctic Amplification. *Bull. Amer. Meteorol. Soc.*, **100**, 841 – 871, doi:10.1175/BAMS-D-18-0072.1.

Wendisch, M., M. Brückner, S. Crewell, A. Ehrlich, J. Notholt, C. Lüpkes, A. Macke, J. P. Burrows, A. Rinke, J. Quaas, M. Maturilli, V. Schemann, M. D. Shupe, E. F. Akansu, C. Barrientos-Velasco, K. Bärfuss, A.-M. Blechschmidt, K. Block, I. Bougoudis, H. Bozem, C. Böckmann, A. Bracher, H. Bresson, L. Bretschneider, M. Buschmann, D. G. Chechin, J. Chylik, S. Dahlke, H. Deneke, K. Dethloff, T. Donth, W. Dorn, R. Dupuy, K. Ebell, U. Egerer, R. Engelmann, O. Eppers, R. Gerdes, R. Gierens, I. V. Gorodetskaya, M. Gottschalk, H. Griesche, V. M. Gryanik, D. Handorf, B. Harm-Altstädter, J. Hartmann, M. Hartmann, B. Heinold, A. Herber, H. Herrmann, G. Heygster, I. Höschel, Z. Hofmann, J. Hölemann, A. Hünerbein, S. Jafariserajehlou, E. Jäkel, C. Jacobi, M. Janout, F. Jansen,

O. Jourdan, Z. Jurányi, H. Kalesse-Los, T. Kanzow, R. Käthner, L. L. Kliesch, M. Klingebiel, E. M. Knudsen, T. Kovács, W. Körtke, D. Krampe, J. Kretzschmar, D. Kreyling, B. Kulla, D. Kunkel, A. Lampert, M. Lauer, L. Lelli, A. von Lerber, O. Linke, U. Löhnert, M. Lonardi, S. N. Losa, M. Losch, M. Maahn, M. Mech, L. Mei, S. Mertes, E. Metzner, D. Mewes, J. Michaelis, G. Mioche, M. Moser, K. Nakoudi, R. Neggers, R. Neuber, T. Nomokonova, J. Oelker, I. Papakonstantinou-Presvelou, F. Pätzold, V. Pefanis, C. Pohl, M. van Pinxteren, A. Radovan, M. Rhein, M. Rex, A. Richter, N. Risse, C. Ritter, P. Rostosky, V. V. Rozanov, E. Ruiz Donoso, P. Saavedra-Garfias, M. Salzmann, J. Schacht, M. Schäfer, J. Schneider, N. Schnierstein, P. Seifert, S. Seo, H. Siebert, M. A. Soppa, G. Spreen, I. S. Stachlewska, J. Stapf, F. Stratmann, I. Tegen, C. Viceto, C. Voigt, M. Vountas, A. Walbröl, M. Walter, B. Wehner, H. Wex, S. Willmes, M. Zanatta, and S. Zeppenfeld, 2022: Atmospheric and Surface Processes, and Feedback Mechanisms Determining Arctic Amplification: A Review of First Results and Prospects of the $(AC)^3$ Project. *Bull. Amer. Meteorol. Soc.*, doi:10.1175/BAMS-D-21-0218.1.

Wesche, C., D. Steinhage, and U. Nixdorf, 2016: Polar aircraft Polar 5 and Polar 6 operated by the Alfred Wegener Institute. *J. Large Scale Res. Facilities*, **2**, doi:10.17815/jlsrf-2-153.

Wesslén, C., M. Tjernström, D. H. Bromwich, G. de Boer, A. M. L. Ekman, L.-S. Bai, and S.-H. Wang, 2014: The Arctic summer atmosphere: an evaluation of reanalyses using ASCOS data. *Atmos. Chem. Phys.*, **14 (5)**, 2605–2624, doi:10.5194/acp-14-2605-2014.

Williams, K. and M. Webb, 2009: A quantitative performance assessment of cloud regimes in climate models. *Climate Dyn*, **33**, 141–157, doi:10.1007/s00382-008-0443-1.

Wilson, A. B., D. H. Bromwich, and K. M. Hines, 2011: Evaluation of Polar WRF forecasts on the Arctic System Reanalysis domain: Surface and upper air analysis. *J. Geophys. Res. - Atmos.*, **116 (D11)**, doi:10.1029/2010JD015013.

Woo, M. and D. Gregor, 1992: *Arctic environment: Past, present and future*. McMaster University, Department of Geography, Hamilton, 164 pp.

Woods, C., R. Caballero, and G. Svensson, 2013: Large-scale circulation associated with moisture intrusions into the Arctic during winter. *Geophys. Res. Lett.*, **40 (17)**, 4717–4721, doi:10.1002/grl.50912.

Xue, J., Z. Xiao, D. H. Bromwich, and L. Bai, 2022: Polar WRF V4.1.1 simulation and evaluation for the Antarctic and Southern Ocean. *Front. Earth Sci.*, **16**, 1005–1024, doi:10.1007/s11707-022-0971-8.

Yang, X., J. A. Pyle, and R. A. Cox, 2008: Sea salt aerosol production and bromine release: Role of snow on sea ice. *Geophysical Research Letters*, **35 (16)**.

Yeo, H., S. Park, B. Kim, M. Shiobara, S. Kim, H. Kwon, J. Kim, J. Jeong, S. Park, and T. Choi, 2018: The observed relationship of cloud to surface longwave radiation and air temperature at Ny-Ålesund, Svalbard. *Tellus B : Chemical and Physical Meteorology*, **70 (1)**, 1–10.

Young, G., P. J. Connolly, H. M. Jones, and T. W. Choularton, 2017: Microphysical sensitivity of coupled springtime Arctic stratocumulus to modelled primary ice over the ice pack, marginal ice, and ocean. *Atmos. Chem. Phys.*, **17**, 4209–4227, doi:10.5194/acp-17-4209-2017.

Young, G., H. M. Jones, T. W. Choularton, J. Crosier, K. N. Bower, M. W. Gallagher, R. S. Davies, I. A. Renfrew, A. D. Elvidge, E. Darbyshire, F. Marenco, P. R. A. Brown, H. M. A. Ricketts, P. J. Connolly, G. Lloyd, P. I. Williams, J. D. Allan, J. W. Taylor, D. Liu, and M. J. Flynn, 2016: Observed microphysical changes in Arctic mixed-phase clouds when transitioning from sea ice to open ocean. *Atmos. Chem. Phys.*, **16**, 13 945–13 967, doi:10.5194/acp-16-13945-2016.

Young, K. C., 1974: The Role of Contact Nucleation in Ice Phase Initiation in Clouds. *J. Atmos. Sci.*, **31 (3)**, 768–776, doi:10.1175/1520-0469(1974)031<0768:TROCNI>2.0.CO;2.

Yu, L., Q. Yang, M. Zhou, X. Zeng, D. H. Lenschow, X. Wang, and B. Han, 2019: The Intraseasonal and Interannual Variability of Arctic Temperature and Specific Humidity Inversions. *Atmosphere*, **10 (4)**, 214, doi:10.3390/atmos10040214.

Zhang, X., T. Schneider, and C. M. Kaul, 2020: Sensitivity of idealized mixed-phase stratocumulus to climate perturbations. *Quart. J. Roy. Meteorol. Soc.*, **146 (732)**, 3285–3305, doi:10.1002/qj.3846.

Zhang, X., T. Schneider, Z. Shen, K. G. Pressel, and I. Eisenman, 2022: Seasonal cycle of idealized polar clouds: Large eddy simulations driven by a GCM. *J. Adv. in Modeling Earth Syst.*, **14 (e2021MS002671)**, doi:10.1029/2021MS002671.

Zhang, X., A. Sorteberg, J. Zhang, R. Gerdes, and J. C. Comiso, 2008: Recent radical shifts of atmospheric circulations and rapid changes in Arctic climate system. *Geophys. Res. Lett.*, **35**, doi:10.1029/2008GL035607.

Zhang, Y., J. Fan, Z. Li, and D. Rosenfeld, 2021: Impacts of cloud microphysics parameterizations on simulated aerosol-cloud interactions for deep convective clouds over Houston. *Atmos. Chem. Phys.*, **21**, 2363–2381, doi:10.5194/acp-21-2363-2021.

Zuo, H., M. A. Balmaseda, S. Tietsche, K. Mogensen, and M. Mayer, 2019: The ECMWF operational ensemble reanalysis–analysis system for ocean and sea ice: a description of the system and assessment. *Ocean Science*, **15 (3)**, 779–808, doi:10.5194/os-15-779-2019.

Title: Study of Arctic mixed-phase clouds observed in June 2017 during the ACLOUD campaign using the WRF atmospheric model.

Abstract:

Different physical processes associated with surface and thermodynamical conditions as well as aerosol concentrations influence the formation and persistence of mixed-phase clouds (MPCs) in the Arctic. Within the framework of the international ACLOUD campaign (Arctic CLoud Observations Using airborne measurements during polar Day), which took place at the North-West of the Svalbard archipelago in spring 2017, two Arctic mixed-phase cloud (MPC) systems with contrasting characteristics were sampled on 17 June 2017 with the MIRAC cloud radar, dropsondes and in-situ microphysics probes deployed on-board the Polar 5 and Polar 6 aircrafts. This work shows how the ACLOUD observations can be used to evaluate the representation of the MPCs properties in the WRF (Weather Research and Forecasting) model, and also investigates how the MPCs properties are impacted by atmospheric thermodynamics conditions, surface types and pollution.

The two MPC systems studied in this work formed either over sea ice or over open ocean permitting to investigate the effect of changing surface. Observations reveal a coupled cloud-surface situation for both cases since the vertical variations of the potential temperature between the surface and the cloud base are lower than 0.5°C. The MPC system observed over open ocean (OO case) was formed in warmer conditions than the one observed over sea ice (SI case). Also, the base of the OO cloud system is lifted, the supercooled liquid water content (LWC) is higher and the ice water content (IWC) is lower than for the SI case. However, a comparative analysis between the reflectivities measured by the cloud radar and those calculated from in-situ microphysics probe measurements highlights the importance of taking into account the degree of riming of the aggregates in the estimation of the ice water content (IWC). The droplet number concentrations are higher in the OO case due to higher concentrations in aerosols with CCN (cloud condensation nuclei) ability observed over the oceanic atmosphere whereas the concentrations in ice crystals are quite similar in both cases. As quite warm temperatures occurred inside the OO cloud system, the ice phase can be only formed via the heterogeneous ice nucleation process whereas the slightly colder temperatures present inside the SI cloud system entail that the ice phase can also be formed via secondary ice processes such as the Hallett-Mossop process.

Comparisons between ACLOUD observations and baseline simulations' results reveal that the performances of the WRF model in reproducing the different cloud properties (such as cloud base, depth, and LWC) are highly dependent on the vertical resolution used within the atmospheric boundary layer for the initial thermodynamic forcing conditions. Thus, using the ERA5 reanalysis data with finer vertical resolution for the model initiation, the WRF capability to reproduce the observed base and depth of both MPC systems is quite well, as well as for their LWC. However, the WRF model underestimates the IWC (especially for the SI case) because the simulated in-cloud temperatures, which are slightly warmer than observed, have an impact on the switch on of the parameterisations representing the ice formation processes. Sensitivity studies of cloud properties to the schemes used to describe the atmospheric boundary layer (BL) and the microphysics (MP) are performed. These tests reveal how the cloud base and depth are dependent on the chosen BL scheme while the LWC and IWC are dependent on the chosen MP scheme, but with different intensities in the two cases. Additional sensitivity studies have been carried out to investigate the impact of the aerosol loading on the distribution of the in-cloud condensed water phases (*i.e.*, LWC and IWC). These latter tests show that the response in the LWC and IWC to the aerosol loadings is not linear. Indeed, there is a critical CCN concentration (not the same for the two cases) from which the atmospheric boundary layer seems to be saturated. Moreover, under quite clean conditions, the formation and the evolution of the MPC are different for the OO case due to changes in the thermodynamics of the lowest levels of the atmosphere.

Keywords:

Arctic mixed-phase clouds, WRF modelling, microphysics, CCN.